THÈSE DE DOCTORAT

Préparée et soutenue publiquement par

Jean Pierre DUFITUMUKIZA

Pour l'obtention du

GRADE DE DOCTEUR DE L'UNIVERSITE DE LILLE

Ecole doctorale des Sciences de la Matière, du Rayonnement et de l'Environnement

Discipline : Énergétique, Thermique, Combustion

Développement des techniques optiques pour la caractérisation in-situ de la suie dans des foyers de combustion à haute pression

Development of optical techniques for in-situ characterization of soot in high-pressure combustors

---

Soutenue le 14 mars 2023, devant le jury composé de :

Iain Stewart BURNS	Professeur, Université de Strathclyde Glasgow	Rapporteur
Mario COMMODO	Directeur de Recherche, CNR Napoli	Rapporteur
Eric THERSSEN	Professeur, Université de Lille, PC2A	Président du jury
Benedetta FRANZELLI	Chargée de Recherche CNRS, EM2C	Examinatrice
Jérôme YON	Professeur, INSA-Rouen, CORIA	Examinateur
Xavier MERCIER	Directeur de Recherche CNRS, PC2A	Directeur de thèse
Cornelia IRIMIEA	Ingénieure de Recherche, ONERA	Co-encadrante de thèse
Nicolas FDIDA	Ingénieur de Recherche, ONERA	Co-encadrant de thèse
Axel VINCENT RANDONNIER	Ingénieur de Recherche, ONERA	Membre invité

Office national d'études et de recherches aérospatiales (ONERA)

&

Laboratoire PhysicoChimie des Processus de Combustion et de l'Atmosphère (PC2A)

This page is intentionally left blank

ABSTRACT

The growth of air traffic urges the combustion research community to get a detailed understanding of the physical and chemical processes occurring in the aircraft engine, with two main objectives: first, to ameliorate the combustion process and second, to lower gaseous and particulate emissions. A solution to the first issue lies in the combustion at higher pressure and temperature, but this can impact the second issue, particularly concerning the production of soot and NO_x emissions. The solution relies on the development of suitable experimental tools for representative combustion conditions of those encountered in aircraft engines to capture their characteristic complex phenomena. As a result, during this research, coupled optical techniques were developed and implemented for characterizing soot particles in aeronautical engine-relevant combustors. Laser Induced Incandescence (LII) is the primary technique on which efforts are directed due to its high sensitivity for detecting soot particles and flexibility to be implemented around semi-industrial combustion installations. In addition, the coupling of LII with other optical techniques presents a high interest in understanding the mechanisms and parameters leading to soot formation. First, Laser Induced Fluorescence (LIF) is added as a complementary technique to detect soot precursors known as polycyclic aromatic hydrocarbons (PAHs). The development of LII/LIF was made in accordance with the application on test rigs and they were first tested on a CH_4/air laminar diffusion flame. The main findings are related to the planar configuration of the LII/LIF systems regarding the correction factors for the use of a laser sheet plane to scan a large region of interest during the measurement. Additionally, two optical configurations (imaging and spectral) proposed for the LII technique were studied to evaluate the uncertainty induced in the conversion step from the recorded LII signal to soot volume fraction. These studies allowed the application of planar LII/LIF and complementary optical techniques on a semi-industrial test rig representative of combustion conditions identified in aircraft combustors. Particle image velocimetry and Mie scattering are used as complementary techniques to LII/LIF. Six operating conditions of the test rig are characterized by the coupled optical techniques to identify the main parameters that affect soot formation in such environment. An exhaustive characterization of the various OC and their correlation with the Landing/Take-Off (LTO) Cycle is proposed. This work narrows down three OC of interest for in-depth studies with sustainable aviation fuels (SAF). These applications are subject to studies on the effect of SAF on soot formation that were evaluated with LII, OH* and Mie scattering. A matrix of three fuels (Jet A-1, 50:50% vol. Jet A 1: Alcohol-to-jet (ATJ) and pure ATJ) was selected to evaluate the fuel impact on soot production for the three selected OC. High-frequency (~ 10 kHz) techniques (OH* and Mie scattering) were implemented to obtain information about the spray dynamics and flame front inside the combustor. The coupled optical techniques identify the parameters leading to soot formation and relate them to the operating conditions or fuel properties.

Keywords: Combustion, soot, optical metrology, laser-induced incandescence/fluorescence, light scattering, particle image velocimetry, OH* chemiluminescence, semi-industrial aeronautic combustor.

RÉSUMÉ

La croissance du trafic aérien pousse la communauté de recherche sur la combustion à vouloir une compréhension détaillée des processus physiques et chimiques qui ont lieu dans un moteur d'avion, avec deux objectifs principaux : premièrement, améliorer le processus de combustion et deuxièmement, réduire les émissions gazeuses et particulaires. Une solution au premier problème réside dans la combustion à une pression et une température plus élevées, mais cela peut avoir un impact sur la seconde problématique, notamment en ce qui concerne la production de suie et les émissions de NO_x. La solution repose sur le développement d'outils expérimentaux appropriés pour des conditions de combustion représentatives de celles rencontrées dans les moteurs d'avion afin de capturer leurs phénomènes complexes caractéristiques. Ainsi, au cours de cette recherche, des techniques optiques couplées ont été développées et mises en œuvre pour caractériser les particules de suie dans des chambres de combustion similaires à celles des moteurs aéronautiques. L'incandescence induite par laser (LII) est la principale technique sur laquelle les efforts sont dirigés en raison de sa haute sensibilité pour la détection des particules de suie et de sa flexibilité de mise en œuvre autour des installations de combustion semi-industrielles. De plus, le couplage de la LII avec d'autres techniques optiques présente un grand intérêt pour la compréhension des mécanismes et des paramètres conduisant à la formation de la suie. Tout d'abord, la fluorescence induite par laser (LIF) est ajoutée comme technique complémentaire pour détecter les précurseurs de suie connus sous le nom d'hydrocarbures aromatiques polycycliques (HAP). Le développement de la LII/LIF a été fait en fonction de l'application sur des bancs d'essai et ont été testés pour la première fois sur une flamme à diffusion laminaire CH_4/air. Les principaux résultats sont liés à la configuration planaire des systèmes LII/LIF concernant les facteurs de correction pour l'utilisation d'une nappe laser afin d'analyser une grande région d'intérêt pendant la mesure. De plus, deux configurations optiques (imagerie et spectrale) proposées pour la technique LII ont été étudiées pour évaluer l'incertitude induite par l'étape de conversion du signal LII enregistré en fraction de volume de suie. Ces études ont permis l'application des techniques LII/LIF planaires ainsi que des techniques optiques complémentaires sur un banc d'essai semi-industriel représentatif des conditions de combustion identifiées dans les chambres de combustion aéronautiques. La vélocimétrie par image de particules et la diffusion de Mie sont utilisées comme techniques complémentaires au couple LII/LIF. Six points de fonctionnement du banc d'essai sont caractérisés par les techniques optiques couplées afin d'identifier les principaux paramètres qui affectent la formation de suie dans un tel environnement. Une caractérisation exhaustive des différents points de fonctionnement et leur corrélation avec le cycle normalisé d'atterrissage/décollage (LTO) est proposée. Ce travail permet d'identifier trois points de fonctionnement d'intérêt pour des études approfondies avec les carburants aéronautiques durables (SAF). Ces applications font l'objet d'études sur l'effet des SAF sur la formation de suie qui ont été évaluées par LII, chemilunescence OH* et la diffusion. Une matrice de trois carburants (Jet A-1, 50:50% vol. Jet A-1:ATJ et ATJ) a été sélectionnée pour évaluer l'impact du carburant sur la production de suie pour les trois points de fonctionnement sélectionnés. Des techniques à haute cadance (OH* et diffusion) ont été mises en œuvre pour obtenir des informations sur la dynamique du spray et le front de flamme à l'intérieur de la chambre de combustion. Les techniques optiques couplées permettent d'identifier les paramètres conduisant à la formation de suie et les relient aux conditions de fonctionnement ou aux propriétés du combustible.

Mots-clés : Combustion, suie, métrologie optique, incandescence/fluorescence induite par laser, diffusion de la lumière, vélocimétrie par imagerie de particules, chimiluminescence OH*, chambre de combustion aéronautique semi-industrielle.

ACKNOWLEDGMENTS

I am incredibly honored and grateful to have had the opportunity to pursue my Ph.D. thesis under the mentorship of my Ph.D. thesis director Xavier Mercier and my supervisors, Cornelia Irimiea and Nicolas Fdida. Their guidance, support, and encouragement throughout my Ph.D. were invaluable. I am deeply grateful for their expertise, patience, and willingness to share their knowledge, which has been fundamental in helping me develop a deep understanding of my research topic. I would also like to express my deepest gratitude for the countless hours they spent reading and commenting on this manuscript and other research works and for their constant availability to discuss my ideas and provide feedback.

I extend my sincere appreciation and thank my thesis committee evaluation jury members, Iain Stewart Burns, Mario Commodo, Eric Therssen, Benedetta Franzelli, Jérôme Yon and Axel Vincent Randonnier for accepting to evaluate this work.

I want to extend my earnest appreciation to my colleagues from ONERA/DMPE/PRA, who have been a constant source of inspiration and motivation. The morning coffee and discussion made my Ph.D. journey incredible. Thank you, David, for all the help on laboratory experiments and fixing my car tires, lamp and battery! Thank you, Arnaud, for the scientific guidance regarding PIV measurements. Thank you, Regis, for all chocolates and for fixing my computer during the Covid period. A big thank you Axel, for all the valuable discussion regarding the operating conditions of the test rigs and their importance. I sincerely thank Ajmal Mohamed for accepting me to be part of the PRA (Air Breathing Propulsion) unit; it was an incredible experience, and based on our last discussion at the Symposium of Combustion in Vancouver, I cannot wait to see how ammonia and hydrogen will change the cards on future combustion science and applications. Also, thanks to my Ph.D. student colleagues Aymeric, Brendan, Jean-Michel, Leonardo, Rafael and Sacha that took the same boat with me. Without your accompaniment, this journey would be hard to pass.

I thank all engineers and technicians in charge of the MICADO test rig: Pascal, Remy, Florian, Samy, for their support throughout my research and during the implementation of optical techniques around the test rig. Providing technical assistance and expertise was crucial to my work success. I also would like to thank Tassadite (our secretary) for her support, ensuring smooth administrative work, and always being available to answer my questions and address any concerns.

I am deeply grateful to my family (Papa, Maman, Janvière, Felix, Alice, Clarisse, uncle Joseph, tante Rose, aunt Jeannette, etc.) for their unwavering love and support throughout these years. Their encouragement and understanding have been a constant source of strength and inspiration, and I would not have arrived at this achievement without their support. My deepest gratitude also goes to my friends Ariane, Benjamin, Christelle N, Christelle R, Doris, Guy, Hubert, Inès, Japhet, Nicole, Philémon, Richard, Sylvie, Taji etc. for being the friends that I was counting on and for providing me the support that kept me going through this arduous-beautiful journey.

Last but not least, I would like to acknowledge the support and contributions of all those who have supported me during my research journey but whom I may not have had the opportunity to mention here. Your contributions have been invaluable, and I am grateful to you all.

This page is intentionally left blank

TABLE OF CONTENTS

This page is intentionally left blank

LIST OF ACRONYMS

2C-LII - Two-Color Laser Induced Incandescence

ALTERNATE - assessment on ALTERNATivE aviation fuels development

A.U - Arbitrary Unity

ASTM - American Society for Testing and Materials

ATJ - Alcohol-To-Jet

ATJ-SPK - Alcohol-To-Jet Synthetic Paraffinic Kerosene

AVG - Average

CCD - Charged Couple Device

CMOS - Complementary Metal Oxide Semiconductor

FF - Flow Factor

FFT - Fast Fourier Transformation

FWHM - Full Width at Half Maximum

GD - Gate Delay

GHG - Green House Gas

GW - Gate Width

HAB - Height Above Burner

HR - TEM - High-Resolution Transmission Electron Microscopy

ICAO - International Civil Aviation Organization

ICCD - Intensified Charge Coupled Device

IR - Infrared

IRZ - Inner Recirculation Zone

LCA - Life-Cycle Assessment

LES - Large Eddy Simulation

LHV - Lower Heating Value

LIF - Laser Induced Fluorescence

LII - Laser Induced Incandescence

LII/LIF - Laser Induced Incandescence/Fluorescence

LTO - Landing and Take-Off

MERMOSE - Measurement and rEsearch on aircRaft eMissiOnS rEactivity

MFC - Mass Flow Controller

MICADO - Investigation Means For Air-Breathing Combustion Using Optical Diagnostic (French acronym: Moyen d'Investigation en Combustion Aérobie à l'aide de Diagnostics Optiques)

NF - Near Field

ORZ - Outer Recirculation Zone

PAH - Polycyclic Aromatic Hydrocarbon

PDF - Probability Density Function

PIV - Particle Image Velocimetry

PM - Particulate Matter

PMT - Photo Multiplier Tube

ppb - Parts Per billion

ppm - Parts Per Million

ROI - Region Of Interest

SAF - Sustainable Aviation Fuels

SHG - Second Harmonic Generation

SL - Shear Layer

S_{LII} - Laser Induced Incandescence Signal

SOPRANO - SOot Process and Radiation in Aeronautical INnovative cOmbustors

STD - Standard Deviation

TEM - Transmission Electron Microscopy

TEM_{00} - Transverse Electromagnetic Mode (Lowest Order)

T_f - Transfer Function

TSA - Towards Sustainable Aviation

UV - Ultraviolet

CHAPTER 1

INTRODUCTION

This page is intentionally left blank

1 INTRODUCTION

1.1 CONTEXT OF THE STUDY

Combustion processes play an essential role in industrialization and transport domains. Despite the massive investment in renewable energy sources, nowadays, about 81% of energy still originates from the combustion processes of fossil fuel [1–3]. The combustion of kerosene-like fuels in aero-engines raises significant problems for emissions of gaseous pollutants such as CO, CO_2, NO_x and carbon-based nanoparticles known as soot [4,5]. Among these pollutant emissions, soot particles are in plain sight of the scientific community due to their adverse consequences on human health [6–9] and the world climate [10,11]. Despite their harmful effects, soot particles have a significant role in the field of nanomaterials, where the engineering of nanocarbon-based materials is interesting for developing medical sensors and tracers, light structures with better flexibility and mechanical properties than metal-based ones, batteries and substrates with controlled physical properties [12–15]. Linked to this work and apart from the environmental context and nanomaterials field, soot particles can have destructive effects when they deposit on the combustor walls inducing higher thermal yield than they can withstand and unwanted wear on the engine parts [16,17]. Due to the increased complexity of soot aggregates and the multitude of parameters that characterize them, it is essential to develop suitable optical diagnostics to measure soot volume fractions in aircraft combustors, from which it is necessary to take into account the *"harshness"* of the combustion environment [16].

The knowledge acquired via experiments is manifold: to identify the regions predominated with soot in combustors, improve combustion efficiency, reduce emissions and engine wear, increase the lifetime of materials and bring information on the mechanisms leading to soot particle formation in such environments [18]. One major problem of combustion in aeronautical chambers is the formation of soot particles, which is, by far, not a well-controlled process due to the high complexity of the combustion chamber geometry, the pressure levels, high turbulence, radiative phenomena, soot chemistry, and the complex composition of the fuel [19–21]. Furthermore, the various physicochemical properties of soot aggregates can be determined, with a certain degree of uncertainty, due to the difficulties encountered in harsh combustion conditions. These facts are significant challenges that require controlling or understanding the combustion, from a kinetic point of view, up to the fluid mechanic equations that explain the turbulent character of the flame. The mechanisms of soot particle formation are subject to numerous questions, and critical gaps exist in experimental data, particularly under harsh combustion conditions characterized by high pressure and temperature values.

The study of soot particles requires additional knowledge of physicochemical parameters that strictly influence their formation: the temperature of the environment, the total flow velocity field, and, most importantly, their molecular precursors [22]. This information is important because the details concerning the transition from molecular precursors in the gas phase (inception process) to the condensed phase (young soot) are still under discussion and partially elucidated [23,24]. Furthermore, these uncertainties require suitable tools for evaluating and characterizing soot particles in aeronautical combustion chambers. For this reason, there is a need to implement and propose a strategy related to fundamental research on combustion in well-characterized laboratory flames

before extending the methodology to applications on more complex aeronautical combustion chambers.

The objective of this Ph.D. thesis is to develop and implement laser-based optical techniques for detecting and characterizing soot particles in harsh combustion conditions. In this work, the difficulties imposed by the combustion environment consist of high pressure, temperature and mass flow rates, and the multiphase character of the flame, such as the coexistence of liquid fuel droplets, particles and the gaseous phase.

Laser-Induced Incandescence (LII) is the main technique on which efforts were focused. LII technique is used due to its high sensitivity for detecting soot particles and flexibility for the implementation around test rig combustors. Furthermore, the coupling of LII with other optical techniques presents a high interest in understanding the mechanisms and parameters leading to soot formation. Notably, Laser-Induced Fluorescence (LIF) is advantageously used as a complementary technique to detect soot precursors such as Polycyclic Aromatic Hydrocarbons (PAHs) and the light scattering is implemented for soot particles and unburnt fuel droplets dynamics. Moreover, OH* chemiluminescence is performed to detect the flame front and heat release. Finally, the PAHs and soot transportation or interactions with the flow field are identified via particle image velocimetry (PIV).

1.2 STRUCTURE OF THE MANUSCRIPT

This thesis is structured into five chapters.

The **first (I) chapter** briefly summarizes the scientific context of the performed work and the motivation behind this study, followed by the state-of-the-art of soot particle formation and some optical techniques used for their characterization in atmospheric laboratory flames and harsh combustion conditions.

The **second (II) chapter**, considered as the pillar of this work, describes the strategy used to develop and implement planar LII (PLII) and LIF (PLIF) techniques on a laboratory laminar diffusion flame (CH_4/air). The first two subchapters present the theoretical working principles of LIF and LII techniques. The third subchapter describes the optical configuration used to characterize a large region of interest (ROI) in the sampling environment. An extensive study was performed to estimate uncertainties induced by the PLII method. Therefore, developing a suitable laser beam-shaping system demands complete knowledge and characterization of the optical system. This section describes how the Gaussian laser beam shaping into a laser sheet affects the LII signal and impacts the results. The laser beam shaping also influences PLIF measurements, which is discussed in the fourth subchapter. This subchapter briefly introduces notions about detecting PAHs in the laminar diffusion flame and their correlation with soot formation. The fifth subchapter describes the methodology used to quantify the LII signal into soot volume fraction by using the auto-compensating LII method.

The **third (III) chapter** of this Ph.D. focuses on the application of planar LII/LIF and complementary optical techniques on a semi-industrial test rig (MICADO), which were reproduced representative combustion conditions similar to those identified in aircraft combustors. PIV and Mie scattering complemented LII/LIF techniques with velocity vector field values and the region of non-vaporized spray. Six operating conditions (OCs) of the test rig were selected to identify the main parameters affecting soot formation in such an environment using coupled optical techniques. Jet A-1 fuel with air was burned with a single swirled configuration of the injection system at pressure values

of the combustor ranging from four to eleven bar. An exhaustive characterization of the various OCs and their correlation with regimes from the Landing/Take-Off (LTO) Cycle is proposed. This work helps to define three OC of interest for in-depth studies with sustainable aviation fuels (SAF).

These studies are subject to the work presented in the **fourth (IV) chapter**, where the effect of sustainable aviation fuel (SAF) on soot formation was evaluated with LII, OH* chemiluminescence and scattering. A matrix of three fuels (Jet A-1, 50:50% vol. Jet A-1: Isopar and neat Isopar) was selected to evaluate their impact on soot formation for the three OCs. High-frequency techniques (OH* and scattering) were implemented to obtain information about the spray dynamics and flame front inside the combustor. The coupled optical techniques are used to identify the parameters leading to soot formation when replacing Jet A-1 with Isopar fuel. The identified phenomena and parameters are related to the OCs and/or fuel properties.

The **last (V) chapter** summarizes the main findings of this work, general conclusions and perspectives.

1.3 STATE OF THE ART

The aircraft industry is responsible for building sustainable flying systems that respond to certification norms on the level of emissions for gaseous and particulate pollutants (emission index limits) on the various fly segments depending on the thrust of the engine and possible adverse effects on the environment [25–27]. These norms are implemented by international organizations such as CAEP [28], which define emission reduction targets in the short and long term, track the progress achieved and re-evaluate the certifications depending on the advancements of instruments [26]. Broadly speaking, turbofan engines emit gaseous and particulate pollutants during defined flight segments based on the engine model, aircraft aerodynamics, burned fuel and load. Figure 1.1 represents the estimation of emissions at different flight stages during aircraft operation demonstrated in the studies of Ranasinghe et al. [26] and Gardi et al. [29]. The aircraft emission inventory is usually calculated based on certificated engine emission indexes provided by the engine manufacturers and reported in the International Civil Aviation Organization (ICAO) [30] engine emission database [31].

A direct impact from the aircraft functioning occurs at high altitudes (emissions and formation of condensation trails) and the ground level (emissions and noise).

The main produced pollutants during various flight segments are carbon dioxide (CO_2), NO_x, unburnt hydrocarbons (UHC), soot (particulate matter – PM) and sulfur oxides (SO_X). CO_2 and NO_x are the targeted pollutants to be reduced, while the other ones are more difficult to certify due to the difficulties encountered in their measurement and quantification.

Nitrogen oxides (NO_X) are unwanted by-products of combustion resulting from the reaction of nitrogen and oxygen from the air in extremely high-temperature conditions (> 2200 K) [26] and eventually pressure [32]. Different formation mechanisms (reactions) of nitrogen oxides have been identified in different studies [33–37], but it is not easy to cover all the complex reaction steps that lead to their formation. The study of Chterev et al. [18] showed that the reduction of emissions in operational conditions of turbine engines is strongly limited and dependent on multiple factors such as the gas phase velocity field, liquid phase fuel distribution, including droplet velocity, sizes, and morphology, heat release, evaporated gas phase fuel distribution, local fuel/air ratios, and key scalar species distributions.

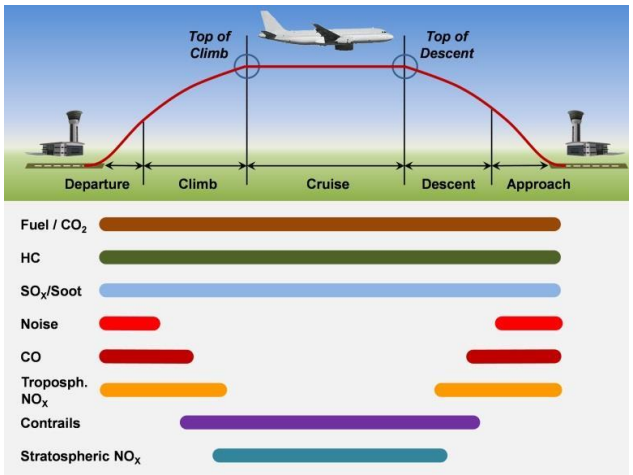

Figure 1.1 Repartition of emissions with associated environmental impact by flight segments associated with the aircraft operation as presented by Gardi et al. [29].

Despite its secondary importance in emissions ranking, the formation of soot particles in aircraft combustors is still a research subject that is not well understood. Soot particles have direct and indirect effects on the environment and are often associated with high toxicity to living beings when emitted in high concentrations at the ground level, depending on their surface chemical composition. Furthermore, after their release into the atmosphere, soot aggregates are known to impact the formation of clouds and trigger a series of chemical processes that induce the formation of secondary organic aerosols (SOA), and recently, they have been considered to play a role in the depletion of the ozone layer due to the increased number of rocket launches, which tenfold the soot concentration in the stratosphere [38–40].

Hence, understanding the soot formation mechanisms in aircraft engines can help transition the combustion processes towards cleaner ones by reducing their emission index at the engine's exhaust and improving turbine cooling as soot particles induce undesired radiative effects. Therefore, this study focuses on soot particle formation in harsh combustion conditions representative of aircraft combustors, particularly in developing necessary metrology tools to detect soot particles in harsh combustion conditions with high detection limits.

1.3.1 Overview of soot formation

In this thesis, the terminology "soot" is often used and is defined as combustion-generated nanoparticles produced after the incomplete combustion of organic compounds. Soot formation is a complex process with different steps regarding its formation in flames. So far, many studies have been conducted on soot morphology and formation mechanism in flames [41–47]. Fundamental studies on soot formation have focused on the combustion of simple hydrocarbons (methane or ethylene) [48–51]. But some studies have extended soot formation to more conventional fuels, like kerosene Jets, gasoline and biofuels [52–55]. To facilitate the study of complex mixtures of liquid fuels that contain thousands of compounds, surrogates made up of simple mixtures of compounds with well-defined thermodynamics and kinetics are used to mimic the behavior of commonly used liquid fuels for specific applications using both theoretical models and experiments [56].

Some terminologies about soot and different steps that participate in their formation are described and detailed in the review of Michelsen et al. [57] and others [15,45,56,58–60]. Soot formation in flames occurs in five major stages: gas phase species, soot particle inception, surface growth, coagulation/agglomeration and oxidation if this step exists. A simplified, sequential picture of the soot formation process in a laminar diffusion flame is depicted in Figure 1.2 [57]. The process before the formation of gas phase species is the high-temperature chemical decomposition of the fuel, also known as pyrolysis. This process is strongly dependent on the composition or type of fuel used, as well as on stoichiometry and the thermodynamic combustion conditions. The first step in soot formation involves the production of gas phase species known as soot precursors. Several species have been suggested as the key gaseous precursors of soot, like polyacetylenes, neutral free radicals, ionic species, common precursors with fullerenes, and polycyclic aromatic hydrocarbons [61,62]. However, most literature studies mentioned that PAHs are the most probable soot precursors [62–65]. The PAHs are organic compounds composed of multiple aromatic rings [63,66]. The simplest PAH is naphthalene which has two aromatic rings, and anthracene-phenanthrene, that have three aromatic rings [67,68]. This study uses the LIF technique to detect soot precursor species.

The second step consists of the inception process. This process is the transition step between gas phase species and the first primary soot particle nuclei. The inception process is identified as the nucleation process. The gas-phase species condense to form the first measurable soot particles, which often are called nuclei [69,70]. However, this term should be used cautiously because of its connotations of physical condensation phenomena [57]. The incipient-formed soot has a spherical shape (mono-mode) with a small size ranging from 1 nm to 10 nm, and it is composed of large organic species with high hydrogen-to-carbon ratios [71,72].

The next step after the inception process is the formation of primary soot particles and surface growth. Surface growth describes the process by which gas-phase species are added to the surface to increase the soot particle mass, which can occur at any stage of soot maturity [57]. In other words, surface growth involves attaching gas-phase species to the surface of the particles and their incorporation into the particulate phase through condensation, adsorption and chemisorption. Soot particle growth from the nuclei stage occurs via coagulation, surface growth, and agglomeration. Coagulation occurs when two particles collide and coalesce to form a larger particle [73]. Based on the definitions given by Michelsen et al. [57], coalescence is the merging of two or more particles into one in a way that removes any boundary between them. Agglomerates are groups of particles loosely held together, and agglomeration is the associated process that forms the agglomerates. The particle growth leads to the production of mature soot particles, defined as particles that have fully evolved at high temperatures. Such particles are refractory and can be heated to the sublimation point of black carbon, known as graphite, which is around 4000 K [57]. Mature soot comprises primary particles of 10 to 50 nm diameter, having a fine structure similar to polycrystalline graphite with low hydrogen-to-carbon (H/C) ratios [72,74–77]. Mature soot aggregates are insoluble in polar and nonpolar solvents, have a molar carbon-to-hydrogen (C/H) ratio ranging from ~8 to ~20 and absorb over a broad wavelength domain spanning the ultraviolet (UV) infrared (IR) range [57,72,78–83].

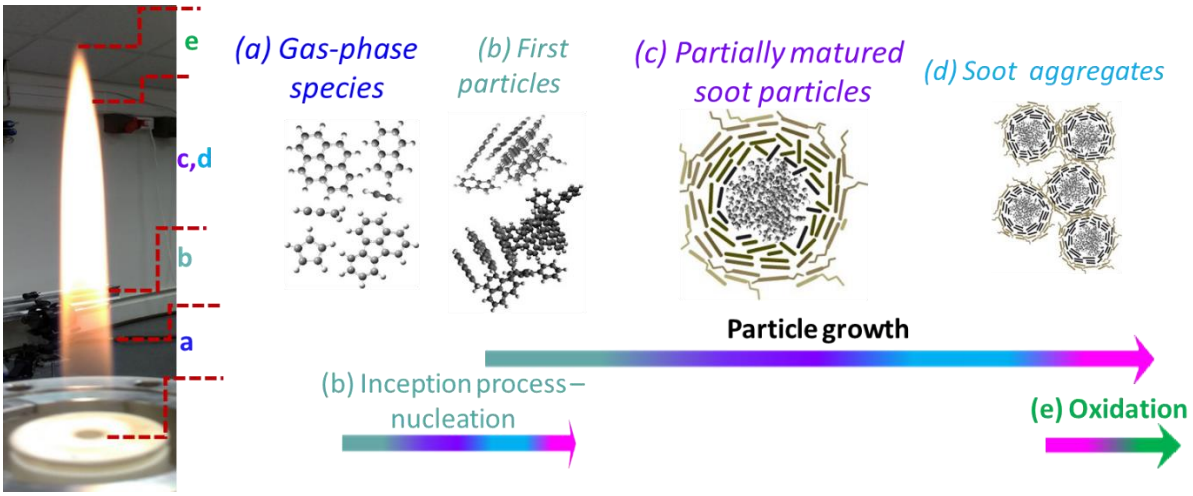

Figure 1.2 A schematic diagram adapted from the study of Michelsen et al. [57] shows the major steps involved in soot formation and the characteristic produced species. The size of these images varies with structures ranging from sub-nanometer scale (a) to ~100 nm (e). The CH_4/Air diffusion flame used in this study is used to show the location of the process into the flame.

The last step of the soot formation mechanism consists of the oxidation process. Oxidation is the conversion of carbon or hydrocarbons to combustion products [73,84]. In soot study, oxidation usually refers to the reaction of O_3, O_2, O or OH with soot particles to form CO, CO_2 and H_20 [57,85,86].

Oxidation of soot particles occurs during all stages of the formation process, from pyrolysis through agglomeration [84]. However, the most active oxidation species depends on the process and state of the mixture at the time [84]; in atmospheric laminal diffusion flame, high soot oxidation takes place on the tip of the flame. Soot oxidation is a temperature-dependent process that begins at a lower temperature limit of approximately 1300 K and increases with increasing temperature [73]. Oxidation reduces soot mass by converting the solid-phase particle to gas-phase products [57]. The study of Sato et al. [87] investigated the effect of temperature on soot formation in a jet-stirred combustor. They found that in a well-stirred reactor, where oxidation and soot formation coincide, peak soot formation rates occur in the temperature range of 1500 – 1700 K.

To conclude, the mechanisms of soot formation are complex; the processes and transitions between one-step to another are not well known yet and likely depend on combustion conditions (temperature, pressure, equivalence ratio) and environment (type of flame). Some effects of pressure and temperature on the soot formation are described in the next section.

1.3.2 Effect of temperature and pressure on soot formation

Soot formation in flames depends on combustion parameters such as pressure, temperature, equivalence ratio, air and fuel flow rate, injection type (diffusion or premixed), fuel types (gaseous or liquid), and turbulence [41,58,88]. As many parameters influence soot particle formation in engines (the case of this study), without their dissociation, it is challenging to predict which combustion parameter directly affects soot particle formation in the combustor and in which way. The characteristic thermodynamic parameters must be tuned simultaneously (pressure, temperature, equivalence ratio etc.) to optimize and stabilize the test rig operability domain and especially to reach the targeted OC. Due to these facts, understanding which physicochemical parameter drives soot formation is not apparent. Therefore, it is challenging to build or imagine a laboratory-scale experiment that can independently account for the effect of the enumerated parameters on soot formation. Some studies have shown the impact of equivalence ratio (Φ) and adiabatic flame temperature on soot and NO_x formation. Figure 1.3 shows an example of the effect of Φ and temperature on soot and NO_x formation in a conventional diesel engine [89]. To limit the formation of soot particles, engines have to operate at a low equivalence ratio which induces an increased local temperature (from ~1700 K to ~2200 K) that results in a higher production yield of NO_x. When the equivalence ratio increases, the flame production of unburnt organic molecules grows, resulting in higher soot particle masses or concentrations.

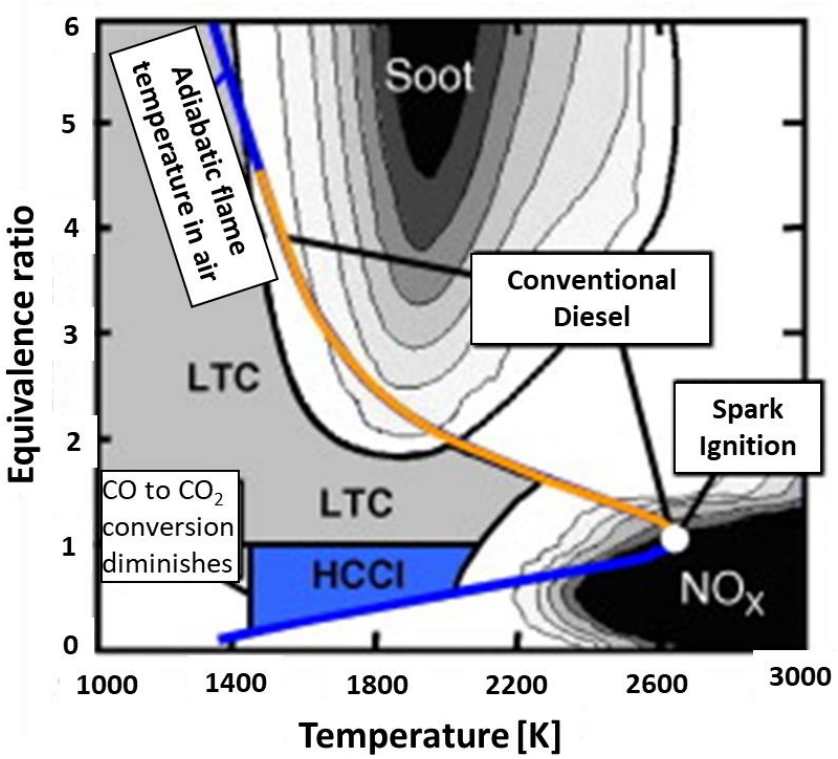

Figure 1.3 Diagram showing the equivalence ratio and temperature ranges for soot and NO_X formation in the case of conventional diesel, SI (spark ignition), HCCI (homogeneous charge compression ignition), and diesel LTC (low-temperature combustion) engines. This figure is from the study of Dec [89].

Their effect on soot particle formation is impacted by pressure and temperature, their effects being among the most studied in the literature. However, most soot studies are carried out on atmospheric laboratory flame conditions (ambient pressure and temperature) as it is easier to access

detailed information on the soot formation mechanism rather than in the operating conditions of engines. Still, some studies have been done at high pressure to deduce the effect of pressure change on soot volume fraction. Among these studies, Omer et al. [90] have investigated the impact of pressure on soot formation in laminar methane-air diffusion flames over the pressure range of 5 bar to 40 bar. They found that the soot volume fraction increases as the pressure increases. In their findings, the carbon peak conversion to soot mass increases with pressure, and that relationship is expressed as:

$$f_s \, \alpha \, p^n \qquad \text{Equation 1.1}$$

p is the pressure value, and f_s is the conversion of fuel carbon content to soot, expressed in percentage, where n equals 1 for p from 5 to 20 bar and n equals 0.1 for p from 20 to 40 bar. Based on that equation correlation, soot formation becomes less sensitive to pressure above 20 bar. For further understanding, Steinmetz et al. [91] studied the soot particle size in laminar nitrogen-diluted ethylene coflow diffusion flames at 4, 8, 12 and 16 atm (1 atmosphere equal to 1.01325 bar). From the key findings, they found that in flames, the local peak soot volume fraction was found to scale with pressure as follows: p^n with n equal to 2.0, 2.3, and 2.2 on the centerline of the flame and the peak soot yield was found to scale as $p^{1.8}$ over the pressure range of 4 to 16 atm. Figure 1.4 a) illustrates an example of the pressure effect on soot yield at different heights above the burner (HAB) in the centerline of the flame [91]. The soot yield is defined as the net amount of soot per gram of fuel [92].

In another study, the dependence of soot production on the pressure also varies with the flame type. In premixed flames, Bönig et al. [93] studied the soot formation in premixed C_2H_4 flat flames at high pressure. They found that PAH concentration increased with the pressure and in parallel to the soot concentration. Additionally, they identified a proportionality between the pressure values and soot volume fractions, where the soot density increases with the pressure nearly proportional to $f_v \sim p^2$ for T ≥ 1700 K and p ≤ 10 bar.

The temperature greatly affects the sooting process by increasing all reaction rates involved in soot formation and oxidation [84]. For example, the study of Xu et al. [94] showed that the high initial temperatures of the airflow mainly cause the high pyrolysis rate of fuel and the rapid formation of PAHs. The study of Mahmoud et al. [95], which investigated the effects of fuel inlet boundary conditions on aromatic species formation in coflow diffusion flames, showed that high initial temperature promotes the nucleation process of soot. The recent study of Chu et al. [96] investigated the effect of elevated reactant temperatures on soot nanostructures in a coflow diffusion ethylene/air flame. Three flame cases were studied with temperature values of the total air mass flow rates of 300 K, 473 K, and 673 K, respectively. Their results showed that increasing the inlet air (fuel temperature had the same value as air temperature) promoted soot formation, as soot volume fraction increased with temperature (Figure 1.4 b). At constant air and fuel mass flow rates among the three selected flames, by increasing the temperature, they also found that as the flame height increased, the soot region extended. Their study also investigated the soot primary particle diameter with LII; they found that elevating inlet temperature yielded larger primary particles, indicating soot surface growth enhancement. However, the change decelerated after 673 K, suggesting a reduction in surface reactivity. The effect of temperature on soot particle formation was also investigated by Qi et al. [97]. They studied the effects of gas preheat temperature on soot formation in co-flow methane and ethylene diffusion flames. They found that the flame peak value of the soot volume fraction was higher as the preheated inlet gas temperature increased.

To conclude, in a flame, the temperature value is critical in the formation of soot particles; high inlet temperature results in a high pyrolysis rate of the fuel and the thermal effect of the additives change the flame temperature, which influences the formation of soot precursors that will lead to soot formation [60].

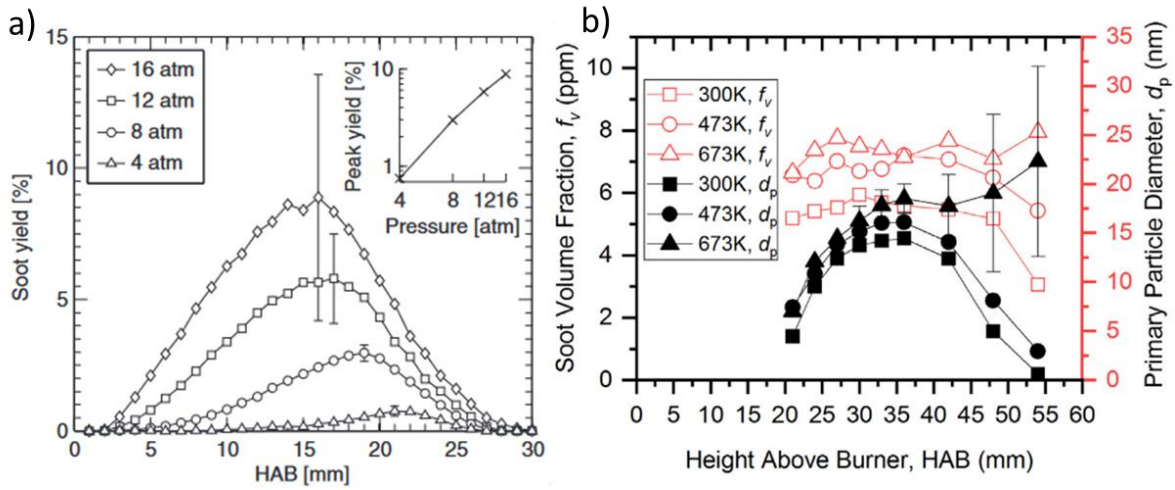

Figure 1.4 a) Soot yield evolution as a function of height above burner (HAB) in nitrogen-diluted ethylene flames from 4 to 16 atm. Inset: Peak soot yield as a function of pressure on a log scale [91]. b) Evolution of soot volume fraction and primary particle diameters in the centerline of coflow ethylene/air laminar diffusion flame for temperatures of the oxidizing air of 300 K, 473 K and 673 K [96].

1.3.3 Soot diagnostic techniques

Due to the complexity of soot regarding characteristic physicochemical parameters at a small scale, it is necessary to use adapted measurement techniques that can give insightful information about soot particles characteristics such as sizes, chemical composition, morphology and structure. Numerous instruments have been developed to measure soot parameters such as mobility size distribution, particle number, concentration, sublimation temperature, volume fraction, density, primary particle size, the chemical composition of the bulk and surface chemical composition [98–101]. Soot diagnostic techniques can be classified into two main categories (Figure 1.5) [102].

The first class of measuring methods are intrusive techniques used to access information about soot particles collected by sampling techniques. Intrusive techniques require physical probing from the flame, exhaust or atmosphere [62,103]. Many techniques rely on sampling probes because they are sophisticated by their nature (like for instance microscopes, spectrometers, etc.), and they cannot perform a measurement directly into a flame. However, these intrusive techniques have disadvantages as the analysis is done outside of the flame, and probing can cause the stagnation of the flow due to the insertion of the probe; this creates more disturbance of the flow and can change the chemical and physical composition of soot molecules between the sample medium and measurement [61].

The second category of instruments is non-intrusive techniques. These techniques are able to measure and detect parameters of interest related to soot without perturbing the environment of analysis (flame) [102]. Non-intrusive techniques can be optical laser and camera-based diagnostics or simply detection methods based on flame self-emission. The advantages of these techniques are that

they do not disturb the analysis volume and provide increased temporal resolution (few ns) and spatial resolution (selection of the sampling volume delimited by the laser beam/sheet). However, the challenges with these techniques rely on their versatility and capability to be implemented around large-scale installations where the ambient conditions are not favorable (fluctuations of temperature, vibrations, dust, etc.).

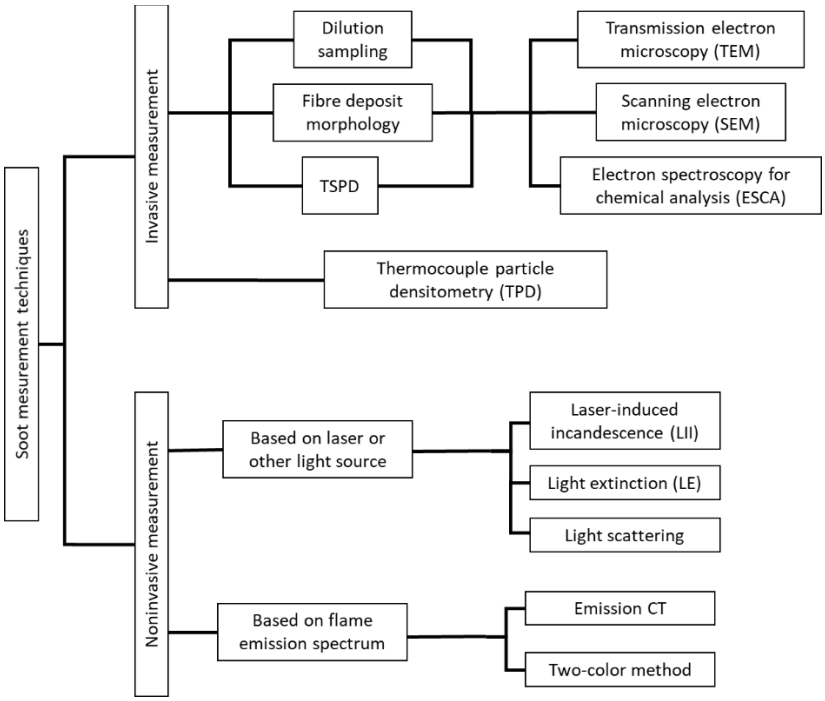

Figure 1.5 Example of intrusive and non-intrusive techniques used for studying soot particles. The diagram was adapted from the study of Lou et al. [102].

Different techniques for studying soot particles are applied based on the soot parameter of interest that need to be measured or determined. The examples of the measurement techniques described in this section are chosen based on four categories:

i. techniques used to determine parameters related to soot particle sizes;
ii. techniques used to determine soot morphology and structure;
iii. techniques used to identify soot chemistry;
iv. techniques used to detect and quantify soot particles in flames.

Additional details on the working principle of different techniques used for studying combustion-generated products can be found in the book of Richard [104].

1.3.3.1 Scanning Mobility Particle Sizer (SMPS)

Scanning Mobility Particle Sizer (SMPS) is used for measuring soot particle size distribution, especially electrical mobility diameter [105]. The working principle of SMPS is based on the mobility of a charged particle in an electric field. First, the particles that enter the system are neutralized. Then, they enter the differential mobility analyzer (DMA), where the particles are classified according to their electrical mobility, with only particles of a narrow range of mobility being counted by a condensation particle counter (CPC) for each bin as delimited by the type of the DMA [106], and resulting in a mobility size distribution that is specific to the majority of the aggregates passing through the system. NanoDMAs

are used to measure size distributions between 2 and 150 nm with high accuracy, with some options that can go to a resolution of 1 nm. A wide range of DMA enables an exhaustive scan from 10 to 800 nm, but intermediary DMA lengths of the column can be selected for increased detection limits to specific mobility particle size ranges.

1.3.3.2 Transmission electron microscopy (TEM)

Transmission electron microscopy (TEM) is a technique (complex instrument) widely used for characterizing the size (mean geometric diameter and primary particle diameter), morphology, and structure of soot particles [42,59,75,107]. This technique is based on thermophoresis probing, where a grid is rapidly inserted into a flame to collect soot aggregates without loading the grid. As the grid passes through the flame, hot soot particles stick to the cold grid surface due to thermophoretic forces. Thermophoresis is the transport force that occurs due to temperature gradient [108,109]. An electron microscope (EM) then analyses the sampled soot particles. In particular, high-resolution TEM (HRTEM) is capable of resolving length scales of a few nanometers [110] and providing important information about incipient soot particle size [111]. A characteristic feature of HRTEM is the high energy of the electron beam [110]. Electrons are accelerated to an energy of more than 100 keV, giving them a wavelength of a few picometers, thus allowing high-resolution imaging [107,111]. However, in practice, the minimum resolution of TEM is limited to around 0.1 nm due to lens aberrations [110,112,113]. Figure 1.6 a and b show examples of soot particle morphology obtained on soot emitted by the SaM146 aircraft engine during the take-off engine cycle. The primary particles (a) are obtained by using HRTEM [114], and aggregates (b) are imaged by TEM [115].

The limitation of these two techniques, regarding the morphology and internal structure of the primary particles, is mainly due to the sampling method. The sampling probe may perturb the flame [116], inducing changes in the soot particles' temperature and concentration and leading to the modification of the sampled particles' chemical composition, which may consequently induce a change in the structure of the crystallites of the primary particles [109].

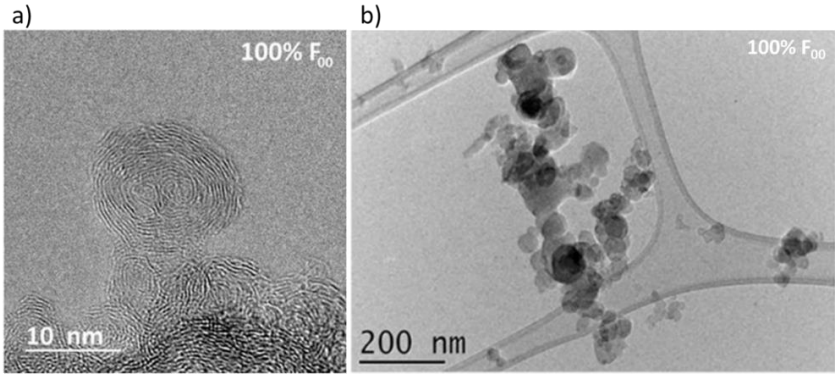

Figure 1.6 a) Soot particles nanostructure (primary particle) obtained by using high-resolution transmission electron microscopy (HRTEM) [114]. b) Morphology of a soot aggregate obtained with transmission electron microscopy (TEM) [115]. All images are obtained on soot emitted from a SaM146 engine during the take-off cycle (MERMOSE project).

1.3.3.3 Scanning electron microscopy (SEM)

Scanning electron microscope (SEM) is a technique mainly used for having information on particle size distributions, morphology, surface topography and elemental chemical composition [117]. SEM is a powerful surface microscopy method that provides high-resolution images over a wide range of samples. Figure 1.7 a) shows an example of the main parts of SEM [118], a focused beam of electrons sweeps across a sample surface, creating an image from the scattered electrons [119]. The beam's position is known at any time, so the properties of the scattered electrons can be mapped in space and obtain the topography of the surface [120]. The SEM technique provides micrographs of soot with high magnification and a satisfactory resolution of a few nm (an example is shown in Figure 1.7 b), that give details on the size of primary particles up to mature particles and especially information about the elemental composition (the content of C, H, O and other elements) which is not easily accessible by other instruments.

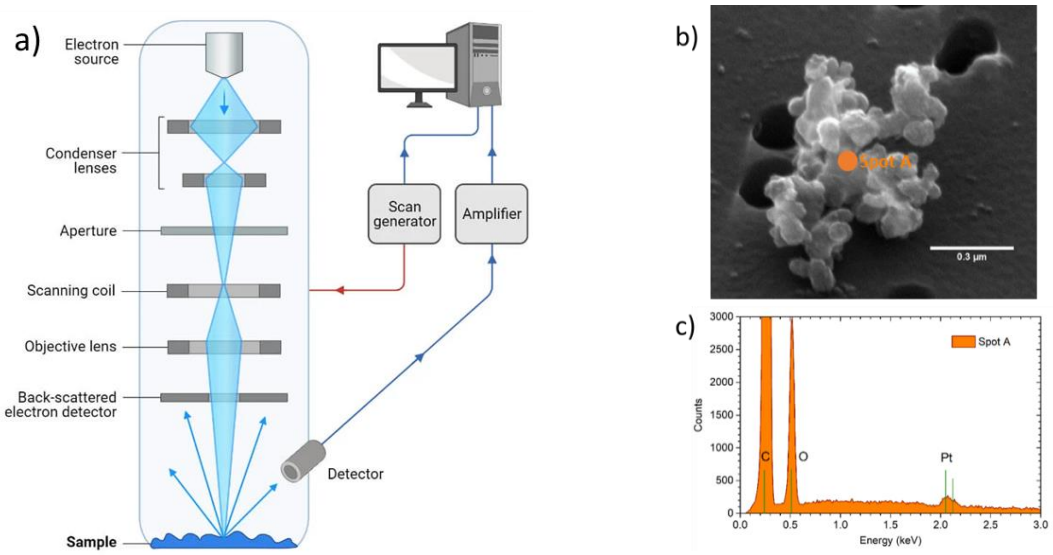

Figure 1.7 a) A schematic illustrating the main parts of the Scanning Electron Microscope (SEM) [118]. b) an example of an SEM secondary electron image showing the soot morphology, c) an Energy Dispersive (EDX) spectrum showing some elementary chemical composition of soot obtained from spot A (marked by the circle on the SEM image) [121].

1.3.3.4 Atomic force microscopy (AFM)

Atomic force microscopy (AFM) is a very high-resolution scanning probe microscope with resolving power on the order of fractions of a nanometer. This technique is mostly used for topography imaging and to determine the chemical structure of molecules (10^{-10} m resolving power), with conventional applications oriented toward analyzing metallic surfaces. The latest advances in technology made it possible to use this technique to study organic compounds, for which, most of the time, this technique was destructive. AFM provided information on the chemical and physical structure of soot particles and especially their precursors [122]. The working principle of AFM consists of a microscale cantilever with a probe at its end that is used to scan the sample surface. The cantilever is typically silicon or silicon nitride with a tip radius of curvature in the order of nanometers. When the tip is brought into the proximity of a sample surface, forces between the tip and the sample lead to a deflection of the cantilever [123].

Depending on the study interest, forces measured with AFM include electrostatic, magnetic or chemical bond forces [123]. Due to this capability of giving information on a molecule structure at its atomic scale, combing AFM with other macroscopy techniques can bring information on the structure of PAHs molecules and incipient soot particles that participate in soot formation. For example, Figure 1.8, taken from the study of Schulz et al. [124], represents a structure of different incipient groups of molecules observed by using STM/AFM. For more details on the use of this technique to understand the mechanism leading to soot formation, the study of Commodo et al. [125] shows the structure of molecules that participate in the early stages of soot formation and the study of Schulz et al. [124] gives insight into incipient soot formation by using AFM.

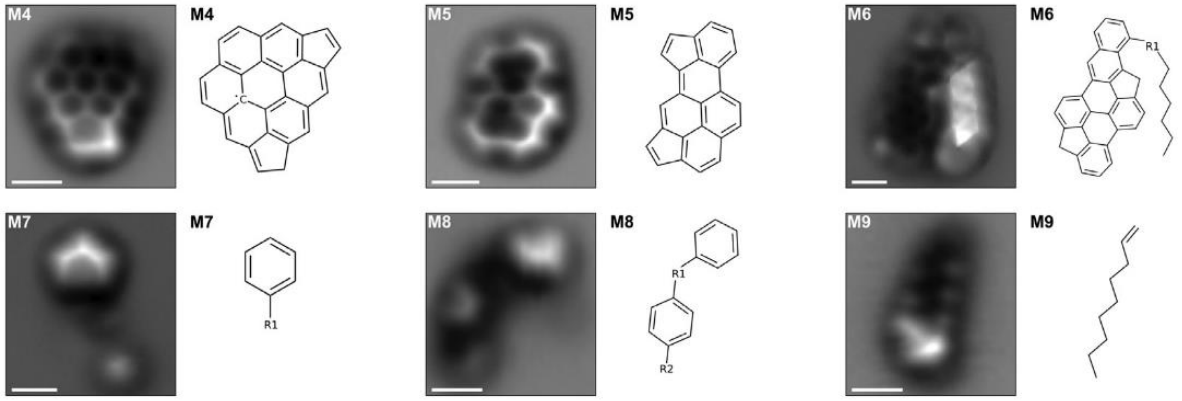

Figure 1.8 Example of AFM images and chemical structure of some representative molecules present in the early stages of soot formation. The figure was taken from the study of Schulz et al. [124].

1.3.3.5 Raman spectroscopy

Raman spectroscopy is an increasingly common experimental method used to characterize soot particles because it can provide structural and chemical information [126]. Raman spectroscopy is used to identify soot molecular structure and crystal orientation based on their vibration modes[126,127]. The working principle of Raman spectroscopy relies on the interaction of molecules with the electromagnetic field produced by a laser [126]. The resulting scattered light (Raman scattering) is electromagnetic radiation emitted at the molecule's vibrational frequency corresponding to vibrational or rotational transitions of a molecule shifted from the incident laser beam frequency [106]. This instrument can analyze soot sampled on filters, and the first-order Raman spectra of carbonaceous materials are generally characterized by two main spectral features, labeled D and G bands, at around 1350 and 1600 cm^{-1}. Soot Raman spectra present at least five deconvolution bands specific to well-defined vibrational modes, but the number of fitted bands can vary to six depending on the study [106]. Information that can be subtracted from Raman spectra is related to the degree of graphitization, disorder and defects in the structure of primary soot particles. Chemical information about the ratio of H/C can also be obtained [128].

1.3.3.6 Light extinction

The light extinction technique is widely used for measuring soot particle concentration (volume fraction) in flames [129,130]. The working principle of this technique is summarized in Figure 1.9, where the light passing through a region of analysis (flame) is partially absorbed by soot particles, and

the ratio of light extinction (attenuation) is used to calculate soot particles concentration/volume fraction along the absorption path [61,94,131]. The ratio of light extinction is determined according to the Beer-Lambert law [102,132,133] expressed as:

$$\tau = \frac{I}{I_o} = \exp(-\int_0^L K_\lambda dl) \qquad \text{Equation 1.2}$$

Where τ is the transmittance; I is the intensity of transmission light; I_0 is the intensity of incidence light; L is the path length traversed by light; K_λ is the absorption coefficient. By considering that a soot particle is spherical and by using particles in the Rayleigh approximation, the soot volume fraction is given by:

$$f_v = \frac{K_\lambda \lambda}{6\pi L E_m(\lambda)} = \frac{\ln(\tau)\lambda}{6\pi L E_m(\lambda)} \qquad \text{Equation 1.3}$$

However, soot is generally present in flames as a form of aggregate structure, and the technique that measures light extinction uses the Rayleigh regime, where a particle is considered spherical or has an equivalent geometry [62,134,135]. Due to this factor, techniques that measure light extinction and use Rayleigh simplification may overestimate the soot concentrations [61]. The limitation of light extinction in flame is mainly based on laser beam steering. Beam steering occurs when the laser beam changes direction due to the environment (density gradient). Some studies have shown how this can affect the results of the soot volume fraction obtained [61,136]. In the targeted application of this research, the flame stabilized on the MICADO test rig is highly turbulent and operated under high-pressure conditions. For this specific application, there is a substantial variation in the optical density gradient over a distance of 100 mm (the cross-section of the combustor).

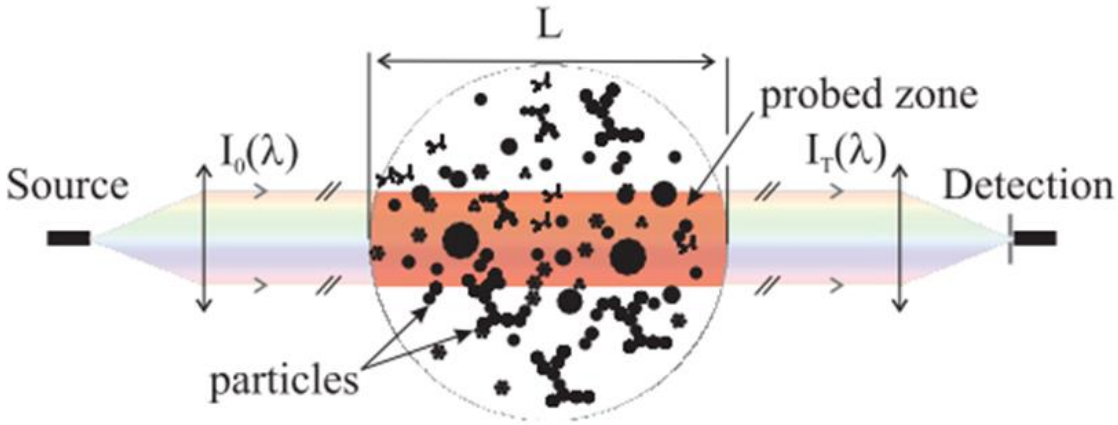

Figure 1.9 Schematic principle of light extinction spectroscopy. Figure taken from the study of Barbosa et al.[137].

This technique is suitable for homogeneous environments in which the concentration of soot particles does not vary significantly along the absorption path (L as shown in *Figure 1.9*). Therefore, this technic is mostly suitable and used for symmetric laminar flames and cannot easily be applicable for turbulent flames, for example, to have absolute quantitative soot measurements. Secondly, the use of specific wavelengths from UV to visible can be tremendous for this technique due to the presence of other molecules on the absorption path. A similar problem can be encountered in the IR domain. Another constraint of this technique is to deduce the value of the soot absorption function index $E_m(\lambda)$, which depends highly on the detection wavelength and temperature. The difficulties of

estimating the value of $E_m(\lambda)$ are also common for the LII technique, some of these difficulties are discussed in chapter 2.

1.3.3.7 Spectral soot emission

The spectral soot emission (SSE) technique measures soot temperature and volume fraction without an illuminating light source [61]. This technique depends on the radiation emitted from soot along a given path. In axisymmetric flames, soot radiation transmitted along a line-of-sight can be detected and spectrally resolved using a spectrometer or other detection systems like cameras [47]. Liu et al. [138] and Snelling et al. [139] have shown the theory behind the SSE technique. The estimation of soot temperature is based on the analysis of radiation from soot transmitted from the flame volume to the detection system. Under the assumption of a line of sight radiation for a symmetrical flame (laminar flame), the intensity detected at a given wavelength λ, and a distance y from the flame center can be expressed as [138]:

$$\mathrm{I_y(y)} = \int_{-\sqrt{\mathrm{R^2-y^2}}}^{\sqrt{\mathrm{R^2-y^2}}} \mathrm{K_{a,\lambda}(x,y)B_\lambda[T(x,y)]} \times \exp\left(-\int_{\mathrm{x}}^{\sqrt{\mathrm{R^2-y^2}}} \mathrm{K_{a,\lambda}(x',y)}\ \mathrm{dx}\right. \qquad \text{Equation 1.4}$$

As illustrated in Figure 1.10, x represents the spatial location along the line of sight under consideration, $K_{a,\lambda}$ is the soot absorption coefficient related to the soot volume fraction f_v, wavelength λ, and the soot absorption function $E_m\ (\lambda)$. The term $K_{a,\lambda}(x,y)B_\lambda$ represents local spectral emission rate $S_\lambda(r)$ and $\exp\left(-\int_{\mathrm{x}}^{\sqrt{\mathrm{R^2-y^2}}} \mathrm{K_{a,\lambda}(x',y)\,dx}\right.$ is the transmission of the local emissions between the flame and the detector. Based on Rayleigh's theory $\mathrm{K_{a,\lambda}}$ is expressed as:

$$\mathrm{K_{a,\lambda}\ (x,y)} = \frac{6\pi\ \mathrm{E_m(\lambda)f_v(x,y)}}{\lambda} \qquad \text{Equation 1.5}$$

By considering that the local spectral emission rate is determined during the experiment and by taking into account the soot absorption function $\mathrm{E_m}\ (\lambda)$ and the spectral emission of a black body [140], the following equation can be expressed:

$$\ln\frac{\mathrm{E_m(\lambda)}}{\mathrm{S_\lambda \lambda^6}} = \frac{\mathrm{hc}}{\mathrm{k\,T\,\lambda}} + C \qquad \text{Equation 1.6}$$

Where h is the Planck constant, c is the speed of light in vacuum, k is the Boltzmann constant, T is soot temperature and C is a constant $(-\ln(12\pi^2\mathrm{hc^2 which\ is\ equal\ to} -40.5))$. The soot temperature can be determined from the slope of Equation 1.7 plot. Equation 1.7 represents the equation of an optical pyrometer applied to a broadband emission spectrum from soot particles.

$$\ln[\mathrm{E_m(\lambda)\ S_\lambda(r)^{-1}\ \lambda^6}]\ =\ \mathrm{f(\lambda^{-1})} \qquad \text{Equation 1.7}$$

$$\mathrm{T} = -\frac{\mathrm{hc}}{\mathrm{K\ slope}} \qquad \text{Equation 1.8}$$

After obtaining the soot temperature, the soot volume fraction can be determined as:

$$\mathrm{f_v} = \frac{\lambda\ \mathrm{S_\lambda}}{6\pi \mathrm{E_m(\lambda)B_\lambda(T)}} \qquad \text{Equation 1.9}$$

Where $\mathrm{B_\lambda(T)}$ Soot emitted intensity depends strongly on the soot optical properties, temperature and detection spectral wavelength.

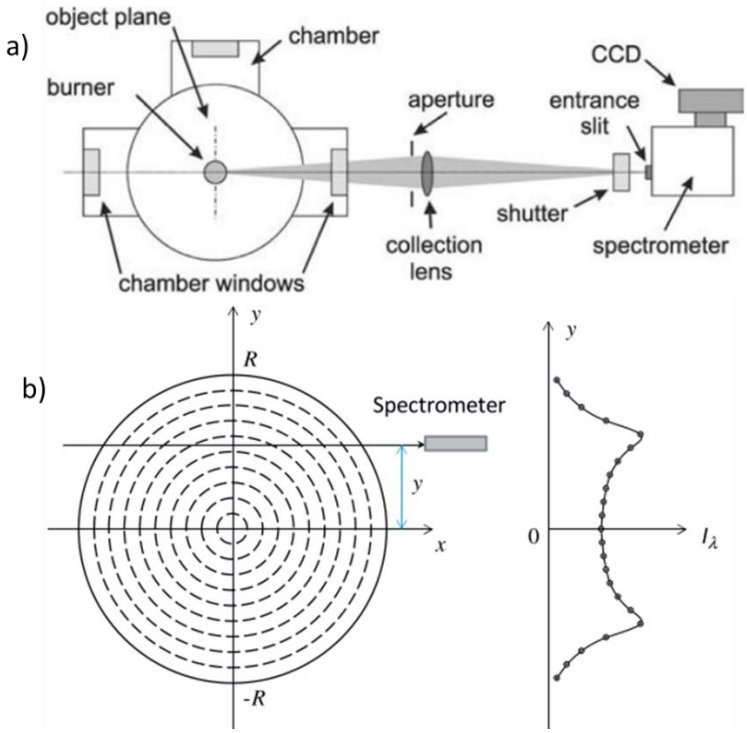

Figure 1.10 a) Typical optical setup for spectral emission-based measurement technique [47], b) schematic of line-of-sight flame emission intensities at a cross-section of a laminar diffusion flame. The figure is taken from the study of Liu et al. [138].

An advantage of SSE is that no additional illuminating source is required for calibration. In addition, for high-pressure applications, optical access is needed only from one side of a high-pressure chamber, simplifying the design of a high-pressure combustion chamber. However, this technique has limited application to turbulent flames due to the difficulties in the deconvolution of the total line-of-sight of emitted signal due to the flame asymmetry with a non-well-defined structure.

1.3.3.8 Laser-induced Incandescence (LII)

Laser-induced incandescence (LII) technique has become prominent in recent decades, providing qualitative and quantitative measurements of soot particles in the flame [76,99,148,149,103,141–147]. In this technique, soot particles are heated around 4000 K by a short-duration high-fluence laser pulse. The energy transferred to the soot after the absorption of the laser light is partly released as quasi-blackbody radiation from soot within the few nanoseconds following the laser pulse. LII radiation is detected with intensified cameras to obtain a 2D image during a short exposure time (few ns) or photomultiplier tubes (PMT) to obtain the LII decay time representative of 1D point measurement [61,102,150–155]. Analyzing the thermal radiation emitted by the particles during their cooling process provides two-dimensional (2-D) distributions of soot volume fraction in the sampled volume [102]. The LII technique presents advantages in studying soot particles, as it is non-intrusive when using a laser fluence below the sublimation threshold.

Furthermore, LII can give information on the primary particle size (from the LII decay time) and soot volume fraction or mass concentration when the density of the particles is known. The LII technique presents some advantages with respect to the other techniques, such as sensitivity for the detection limit (few ppb) [69], selection of the sampling volume with a laser sheet which allows the

separation from the line-of-sight flame emission and versatility around different environments when using separate instruments (laser, camera and optics). Hence, LII is a suitable optical technique for analyzing soot particles in combustors in which stabilized flames are turbulent at high pressure and high mass flow rates. The LII technique has to be custom developed to address the application of soot particle characterization in harsh combustion conditions. More about the LII working principle and theory are specified in chapter 2.

CHAPTER 2

SOOT FORMATION ON ATMOSPHERIC LAMINAR DIFFUSION FLAMES/ DEVELOPMENT OF OPTICAL TECHNIQUE

This page is intentionally left blank

2 SOOT FORMATION ON ATMOSPHERIC LAMINAR DIFFUSION FLAMES / DEVELOPMENT OF OPTICAL TECHNIQUES

This chapter starts with a question:

How can we build an experiment that can be used to detect soot particles with high sensitivity, calibrate detected signals and advance with the status of our understanding of soot particles formation in flames?

No such instrument can answer this necessity; hence, the coupling between optical (instruments) techniques and a laboratory burner that is easily accessible and controllable. For this reason, the work presented in this chapter puts together the development of non-intrusive optical techniques used to characterize soot particles and their precursors on an atmospheric CH_4/air laminar diffusion flame.

A significant part of this work was put into the implementation and development of planar Laser Induced Incandescence (PLII), the optical technique used to detect soot particles, and planar Laser Induced Fluorescence (PLIF), used to detect classes of soot precursors, namely polycyclic aromatic hydrocarbons (PAH). The first two subchapters present the working principle of LII and LIF techniques. The experimental configurations of the LII and LIF are detailed in subchapter 3. A detailed characterization of the selected "planar" optical configuration is presented in subchapter four, and the final subchapter is entirely dedicated to quantifying the LII signal.

2.1 LASER INDUCED FLUORESCENCE (LIF) WORKING PRINCIPLE

Laser-induced fluorescence represents the spontaneous emission from atoms or molecules excited by light or laser radiation, a process known as stimulated emission.

Sir John F. W. Herschel first reported the phenomenon of fluorescence in 1845 [156]. At that time, this intriguing phenomenon attracted the attention of Sir George G. Stokes in 1852, leading to advancements in the understanding of fluorescence and polarization properties of aromatic molecules (quinine). Later in 1935, Alexander Jablonsky proposed a diagram (bears his name) that illustrates the electronic states of molecules under light excitation. Molecules absorb light at one frequency and subsequently emit light at another. The Perrin-Jablonski diagram, Figure 2.1, presents different processes when atoms or molecules absorb light during excitation and emit light during deexcitation. The electronic state mentioned in Figure 2.1 are based on the angular momentum configuration of each state spin. Singlet states are denoted by S (total spin angular momentum is zero), and triplet states by T (total spin angular momentum is one).

S_0 is the singlet ground state of the molecule, S_1 is the first excited singlet state and so on until S_n is the n^{th} excited state. T_1 is the first excited triplet state and T_n is the n^{th} excited triplet state [157]. The vertical arrows correspond to light absorption from the ground electronic state level S_0. Most molecules have S_0 populated with electrons at thermodynamic equilibrium before light absorption ($h\upsilon$). After light absorption, the electrons of the molecule jump from S_0 to one of the vibrational levels of S_1 or S_n depending on the received energy value of the photons (ΔE). The necessary time and energy needed for excitation and the subsequent deexcitation process can be exploited to obtain information about molecules of interest [158]. As mentioned above, for a better understanding of processes involved during fluorescence, the Jablonski diagram illustrates the electronic states with the

vibrational levels, the excitation and deexcitation processes which help differentiate fluorescence from other transition processes (as phosphorescence) that can occur when a molecule has been excited [157,158]. Radiative and non-radiative transitions occur with energy transfer between the electronic states. A radiative transition is a transition between two electronic states where the energy difference is emitted or absorbed by a photon, represented with straight arrows in Figure 2.1. The radiative transition is an intrinsic property of excited species.

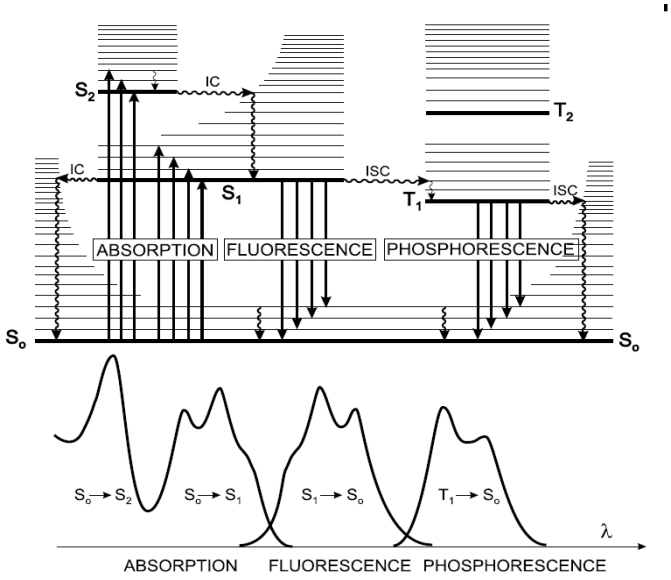

Transition	Characteristic time (sec)
Absorption	10^{-15}
Fluorescence	10^{-10} - 10^{-7}
Phosphorescence	10^{-6} – 1
Intersystem crossing	10^{-10} – 10^{-7}
Vibration relaxation	10^{-12} – 10^{-10}
Internal conversion	10^{-11} – 10^{-10}

Figure 2.1 The Perrin-Jablonski diagram illustrating the electronic states (S_0, S_1 and S_2) with the vibration levels and the phenomena-taking place during the absorption and spontaneous emission, with associated lifetimes. Below the electronic states diagram are represented possible corresponding absorption, fluorescence and phosphorescence spectra. IC stands for internal conversion and ISC for intersystem crossing. This figure was adapted from Bernard Valeur's [158] and Despoina Eleni's [159] work.

In contrast, non-radiative transitions take place without absorption or emissions of photons. This process is sensitive to thermodynamic factors (temperature, pressure and concentrations) of excited molecules or atoms and is presented with wavy arrows in Figure 2.1.

The different transition types are detailed below by considering the duration and energy that allow the process to occur.

1. Absorption is a radiative transition of a molecule from the ground or lower electronic state S_0 to a higher electronic state level (S_1, S_2 or S_n). The absorption process takes about 10^{-15} s and is the fastest transition of the Jablonski diagram [158]. The absorption process is essential as each molecule type can absorb only a specific wavelength equivalent to the energy necessary to shift the electrons

from the ground state to the superior ones. This energy value helps differentiate the various types of molecules coexisting in the same environment or volume. For example, to have information about OH molecules present in a flame, the OH molecule can be excited with a specific wavelength (~283 nm) corresponding to the necessary energy to bring the molecule into an excited state. Multiple absorption lines or bands exist depending on the complexity of the molecule and thermodynamic conditions.

2. Fluorescence is the spontaneous emission of photons (radiative transition) from a high energy level $S_{[1;\,n]}$ to a lower energy level $S_{0,}$ and it occurs on a time scale of 10^{-10} to 10^{-7} s. Due to the loss of energy in the process of vibration and relaxation, fluorescence signal occurs at lower energy than absorption (higher wavelengths) [157,160]. The gap between the peak of the absorption wavelength band and the peak of the fluorescence emission spectrum is called Stokes shift, as he first identified this aspect. Aromatic compounds are complex molecules (they include many atoms in their structure) characterized by broadband absorption spectra. When the emitted photon is more energetic than the absorbed photon, the shift difference is called anti-Stokes shift. For example, Figure 2.2 roughly illustrates broadband absorption and fluorescence emission spectra with the shift between the wavelength band peaks. In general, the Stokes shift is the difference between the position of the broadband absorption peak and the broadband emission spectra of the same electronic transition (mirror effect). This shift can be calculated easily by making a difference in absorption and emission wavelength.

$$\Delta\lambda = \lambda_A - \lambda_F \qquad \text{Equation 2.1}$$

Where λ_A is the absorption (excitation) wavelength domain, λ_F is the peak of the fluorescence emission spectra or detection wavelength and $\Delta\lambda$ is the wavelength shift. The wavelength shift parameter provides information about the molecule's excited states. For example, fluorescent species have a higher yield of fluorescence emission when the Stokes shift is larger [158].

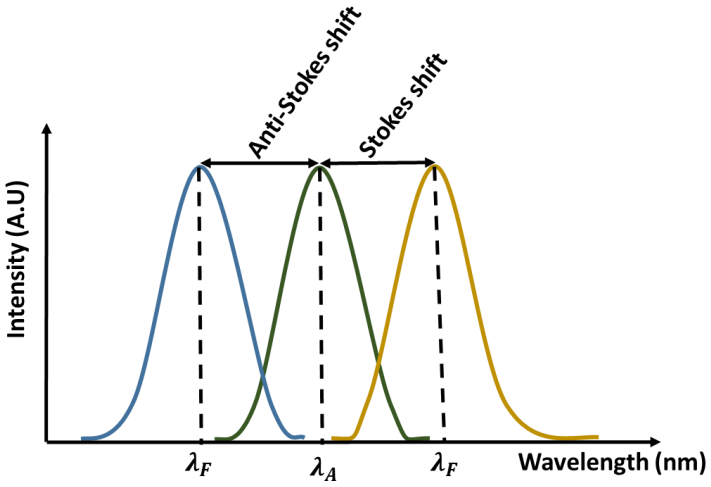

Figure 2.2 Representation of Stokes and anti-Stokes shift in fluorescence emission spectra with respect to absorption spectra. Figure adapted from the book of Joseph [161].

3. Phosphorescence is a radiative transition between two electronic states of different spin multiplicity. In this case, photons are emitted from the excited state T_1 to the lower state S_1. Although the phosphorescence rate is low and therefore occurs at a much longer timescale than fluorescence,

the typical phosphorescence lifetime is between 10^{-6} to 1 s and depends on the molecular chemical structure and thermodynamic conditions.

4. Intersystem crossing (ISC) is a non-radiative transition between two vibrational levels belonging to electronic states with different spin multiplicities. This process is carried out by coupling the excited states S_1 and the iso-energetic vibrational state of triplet state T_1, then by vibrational relaxation until the zero vibration state of T_1. For example, an excited molecule in the vibrational level of the S_1 state can move to the isoenergetic vibrational level of T_n triplet state and then the vibration relaxation brings it into the lowest vibration level. This relaxation is fast, with a lifetime of 10^{-10} to 10^{-8} [158].

5. Vibration relaxation is a non-radiative transition to a lower vibrational level within the same electronic state. After a molecule has been shifted to an excited state by absorption, it is in a non-equilibrium state and will eventually dissipate the energy it gained to return to the ground state. The vibration relaxation occurs rapidly from 10^{-12} to 10^{-10} s and outcompetes all other transitions. Due to this process, fluorescence always involves the transition of the lowest vibrational level of the excited state. Since the space of the emission domain is close, the transition of the vibrational relaxation end in any vibration level of the ground state.

6. Internal conversion (IC) is a non-radiative transition between two electronic states of spin multiplicity. This transition occurs when an intermolecular process of a molecule passes to a lower electronic state without the emission of radiation. It is a crossover of two states within the same multiplicity, meaning singlets to singlet or triplets to triplet. However, the internal conversion rate is inversely proportional to the energy gap between the two electronic states. Internal conversion of the closely spaced higher-lying singlet or triplet excited state will proceed in a timescale of 10^{-11} to 10^{-9} s. The energy gap between the excited state and the ground state is wider and internal conversion between these states occurs at a slower decay time and will compete with other transitions like fluorescence [157].

The lifetime and quantum yield are essential characteristics of fluorescence. Quantum yield is the number of emitted photons relative to the number of absorbed photons. Molecules with the most significant quantum yields have the highest emission intensity. The lifetime or decay time is also essential as it determines the time available for molecules to interact with or diffuse in their environment and can reveal information about their physical or chemical properties.

Equation 2.2 illustrates a method for calculating the lifetime of fluorescence. It is considered a concentration [A*] of molecules (expressed in mol/L), excited with a short pulse laser light. At time t_0 (the molecules are in equilibrium), the energy intake brings a certain number of molecules A to the excited state S_1 by absorption of a photon. These excited molecules return to the ground state S_0 through the radiative or non-radiative transitions. In nominal conditions, the rate of disappearance of signal or decay time of excited molecules is expressed by the following expression [158]:

$$-\frac{d[A^*]}{dt} = (k_r^s + k_{nr}^s)[A^*] \qquad \text{Equation 2.2}$$

where k_r^s is the constant for radiative deactivation from the excited state S_1 to the ground state S_0 during the fluorescence emission.

k_{nr}^{S} is the rate constant for non-radiative deactivation of intersystem crossing from T_1 to the ground state S_0; this rate consists of the sum of the rate constant of internal conversion from the excited state to the ground state and the rate constant of other non-radiative deactivation crossing the state.

By integrating Equation 2.2, the time evolution and the concentration of excited molecules [A*] at time t_0 resulting from the pulse of the laser excitation can lead to:

$$[A^*](t) = [A_0^*] \exp\left(-\frac{t}{\tau_s}\right) \quad \text{Equation 2.3}$$

Where τ_s is the lifetime of the excited state given by

$$\tau_s = \frac{1}{k_r^s + k_{nr}^s} \quad \text{Equation 2.4}$$

The fluorescence intensity is defined by the number of photons (directly proportional with the concentration, in mol) emitted per unit time (s) and per volume of molecules (L) and can be simplified in this reactional equation:

$$A^* \xrightarrow{k_r^s} A + \text{photon} \quad \text{Equation 2.5}$$

The fluorescence intensity i_F at time t after the excitation with a short laser pulse at time t_0 is proportional, at any time, to the instantaneous concentration of molecules in an excited state [A*]. The proportionality is the rate constant for radiative deexcitation k_r^S in this case. Therefore, fluorescence intensity at a given time can be expressed as:

$$i_F(t) = k_r^S[A^*] = k_r^S[A^*]_0 \exp\left(-\frac{t}{\tau_s}\right) \quad \text{Equation 2.6}$$

i_F (t) is the fluorescence decay time characterized by an exponential function. The quantum yield of fluorescence ϕ_F, is the fraction of excited molecules that return to the ground state after the emission of fluorescence photons and this quantum yield can be expressed as:

$$\phi_F = \frac{k_r^S}{k_r^S + k_{nr}^S} = k_r^S \tau_s \quad \text{Equation 2.7}$$

In other words, the fluorescence quantum yield is the ratio of the number of emitted photons (over the whole duration of the decay) to the number of absorbed photons. If there is an external perturbation, the fluorescence quantum yield can remain proportional to the lifetime of the excited states of molecules.

The fluorescence intensity can be decreased or increased by various parameters like thermodynamic factors (temperature and pressure), pH and the presence of other molecules, particularly oxygen [159]. As this study focuses on the fluorescence of PAHs, it is worth pointing out that the main quenchers for PAHs are oxygen and nitro-compounds molecules (e.g., nitromethane) [162]. Moreover, when considering the flame aspects, temperature and pressure significantly impact the fluorescence signal. The temperature increase generally leads to a decrease in the fluorescence quantum yields and lifetime due to non-radiative processes, thermal agitation or collision, that are more efficient at high temperatures [158,161].

The planar laser induced fluorescence (PLIF) technique has been used in the combustion domain to provide qualitative or quantitative measurements of molecules such as NO, CO, OH, PAHs and temperature [143,163–166]. This study uses LIF to characterize and detect classes of PAHs that participate in soot particle formation in the flame. In general, organic compounds have high absorption and quantum yields. Therefore, it is advantageous to use LIF for studying PAHs. Still, this technique is limited for combustion applications as the fluorescence signal can interfere with other molecules that absorb or emit in the same wavelength domain. PAH can be excited and detected in a broadband wavelength domain spanning the UV-visible range. Bejaoui et al. [12] reported on a diagram the wavelength spectral ranges of the lower excitation transitions (S_1<--S_0) and corresponding emission domains for different classes of PAHs, as shown in Figure 2.3 a. Upon UV excitations, the fluorescence emission wavelength from PAHs shifts to longer wavelengths until near-infrared with increasing molecular size or the number of aromatic rings. Figure 2.3 b shows the variation of the absorption and emission wavelength domains for a few PAHs at ambient temperature and expected at high temperature (flame temperature). These diagrams showed that the absorption wavelength domain increased for the same selected molecules while the emission wavelength domain remained the same when the temperature increased, with the peak of the fluorescence emission shifting towards red [12]. This observation is because the vibrational excited states are already thermally populated, leading to a broadening of the absorption wavelength domain.

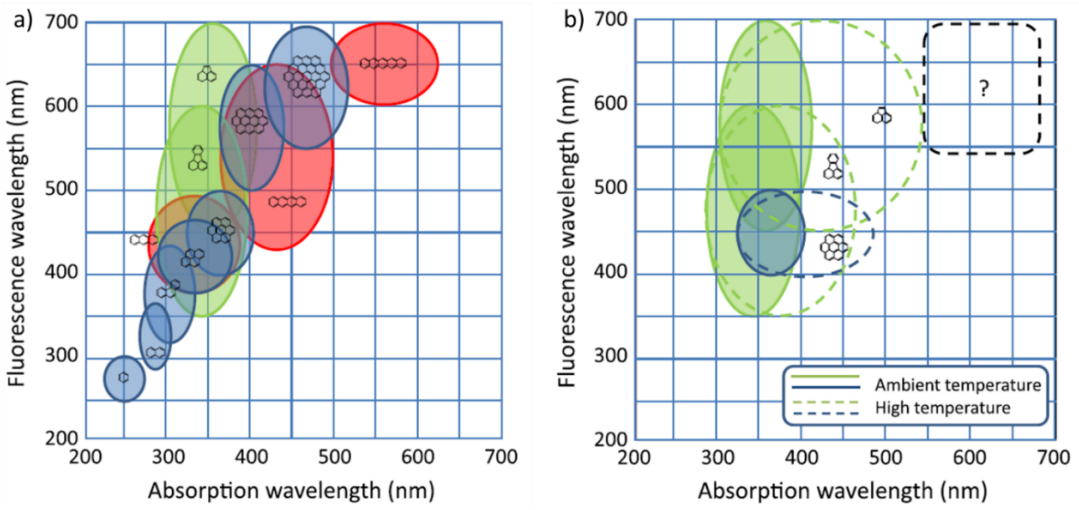

Figure 2.3 a) Fluorescence and absorption wavelength spectrum of several PAHs formed in the premixed sooting flame of methane/oxygen/nitrogen and stabilized McKenna burner at atmospheric pressure. b) The absorption and fluorescence emission wavelengths domain of coronene, acenaphthylene and fluoranthene under ambient and high temperatures [167].

Numerous studies attribute UV fluorescence emission to aromatic species with 2 or 3 rings. In contrast, the broadband fluorescence in the visible domain is generally assigned to PAHs with more aromatic rings or higher molecular weight [168–170]. Based on the molecular weight, it can be possible to selectively detect a given type of PAHs by varying the excitation and detection wavelength. Based on the type and region of the flame, PAHs molecular weight can change. In a premixed flame, where the pool of PAHs fluorescence is significant, the UV excitation leads to broadband spectra, therefore, identifying PAH classes is not straightforward without a complementary technique such as mass spectrometry (MS) [171]. In a diffusion flame, which offers a stratification of different classes of PAHs,

the spectral shift can be observed by increasing the height above the burner (HAB) [167,172]. This variation can be connected to the size and growth of PAHs along the flame. A low laser fluence regime has to be used to activate the fluorescence signal without the interference of LII in the UV visible excitation wavelength domain. PAHs in flames have been shown to highlight absorption spectral features from UV to 680 nm [167]. Although the exact nature of the species at the origin of the absorption and related fluorescence signals observed for excitation wavelengths higher than 450 nm is not well defined in the literature, these signals are clearly related to aromatic gaseous precursors of soot particles and, therefore, characteristic of the species at the origin of the soot formation.

In this study, PAHs *in situ* measurements are conducted on an atmospheric CH_4/air laminar diffusion flame and turbulent diffusion flames stabilized on the MICADO test rig, with a 532 nm excitation wavelength.

2.2 LASER INDUCED INCANDESCENCE (LII) WORKING PRINCIPLE

In 1977, Eckbreth was the first scientist to recognize the interaction between laser and carbon particles [173]. However, the real pioneer of the laser induced incandescence technique was Melton [174]. Melton was the first to exploit its potential as a powerful diagnostic tool for soot concentration measurement and particle sizing. In 1995, Roth [175] used the LII technique to investigate in-situ ultrafine particle sizing by combining pulsed laser heat-up and particle sizing thermal emission in an optical diesel engine. Since then, the technique has continually been improved and implemented for different conditions. Laser-Induced Incandescence has evolved over the last two decades into a particularly attractive technique that offers the possibility of accurate and spatially resolved soot volume fraction and particle size measurements. This technique has been developed for spatially and temporally resolved *in situ* measurements of soot concentration and has been applied to different conditions, from laboratory flames to relevant industrial application scale engines [174]. This optical technique is based on the incandescence signal induced by high energy laser radiation. By heating particles with a short laser pulse, particles interact with the laser, they absorb the energy, their temperature increase and they emit radiation according to Planck's law [72]. From the enhanced thermal radiation (LII signal), it is possible to determine primary particle size, temperature or volume fraction [176].

One of the advantages of LII is the particular sensitivity to soot particles that absorb laser radiation at different excitation wavelengths in the UV-IR spectral range [177]. A detectable LII signal is obtained if the particles are heated not beyond the sublimation point of black carbon (around 4000K) [72]. The emitted radiation is recorded by a fast-gated intensified photodetector immediately after the laser pulse. Depending on the detection system, the LII signal can be recorded either as the decay time with a photomultiplier tube or prompt detection (during a few ns) on a 2D image. In most cases, the temporal decay of the LII signal is used for soot primary particle size measurements.

In contrast, the 2D spatial distribution of the LII signal (image mode) gives information on the distribution of soot particles in a sampled volume [178]. In both cases, optical filters are used to select a narrow spectral band of the emitted broadband spectrum. The incandescence signal emitted by soot particles corresponds to the broadband radiation of a grey body, an emission governed by Planck radiation law [72]. Figure 2.4 illustrates the spectral density of the electromagnetic radiation emitted by a black body in thermal equilibrium for a few given temperatures between 3500-5500 K [179]. LII offers many advantages compared to other soot measurement techniques as absorption and scattering. On the positive side, LII is essentially non-intrusive, so it does not interfere with the combustion process and enables highly resolved temporal and spatial measurements [176]. This technique also has some limitations, which depend on the type of measured particles and analysis environment. Also alternative methods as sampling probe methods can be used to measure soot volume fraction. However, these methods lack high temporal and spatial resolution and require an intrusive probe that can perturb the combustion process and change the properties of soot. With careful experimental design and appropriate calibration, LII measurements of soot volume fraction and mass concentration can be made without a detailed heat-transfer model or the understanding of all the fundamental processes. However, the fundamental basic understanding is essential for determining accurate soot particle concentrations through a good practice of implementation of the instrument/technique to the analysis environment. Further, the theory for the energy-mass balance equation is presented for a soot aggregate irradiated by laser radiation.

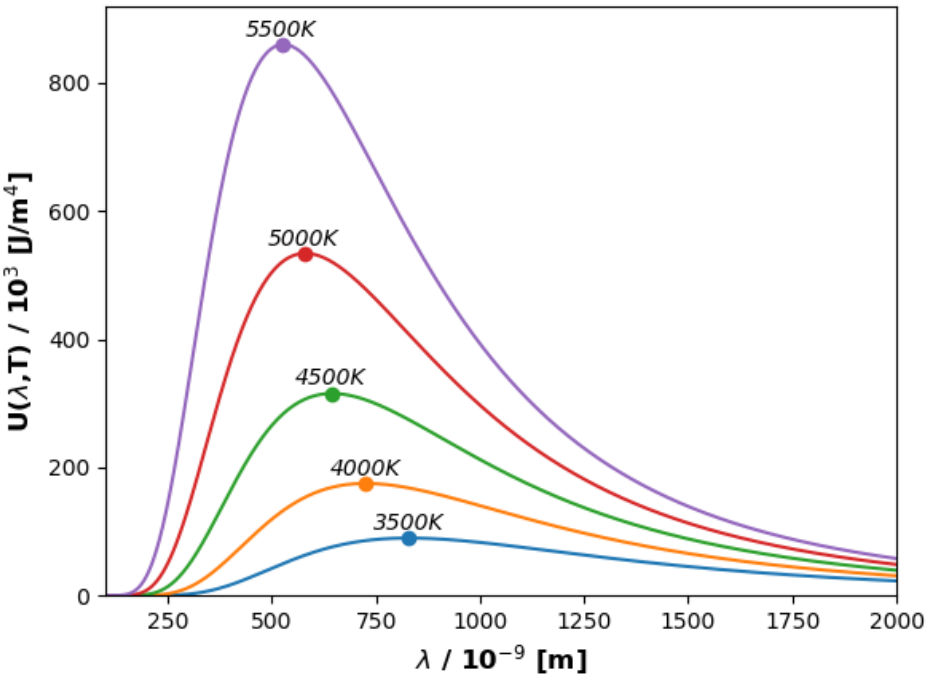

Figure 2.4 Planck curves, which describe blackboard radiation, show the possible radiation intensity at different wavelengths by changing temperature.

2.2.1 Energy and mass balance equation

As mentioned above, the LII technique is based on the heating of the soot particles with a laser to induce the soot incandescence signal [180]. Under certain conditions, a number of processes can be initiated and have a significant impact on the LII signal. A significant volume of research focused on understanding these processes and models capable of predicting the LII signal [180–185].

At the bottom of Figure 2.5.b. the processes influencing the temperature and mass of a particle during LII-signal induction and collection are illustrated. First, particles are heated by the absorption of laser radiation and, to a lesser extent, by oxidation and annealing. Under most conditions, particles cool down through conduction to the surrounding gas and sublimation and, to a lesser extent, by thermionic and radiative emission. Under certain conditions, particles cool down by conduction and sublimation, and to a lesser extent, by thermal emission and radiation. Particles lose mass by sublimation and oxidation [72]. The LII signal is derived from radiative emission from the particle.

To summarize Figure 2.5, soot particles absorb laser radiation to a given extent. Under most conditions, particles cool down by conduction to the surrounding gases. Sublimation appears in the case of higher laser energy than the sublimation point of soot; in this case, the particles lose mass. After these processes, the signal is produced by radiative phenomena that give the final incandescence signal [72].

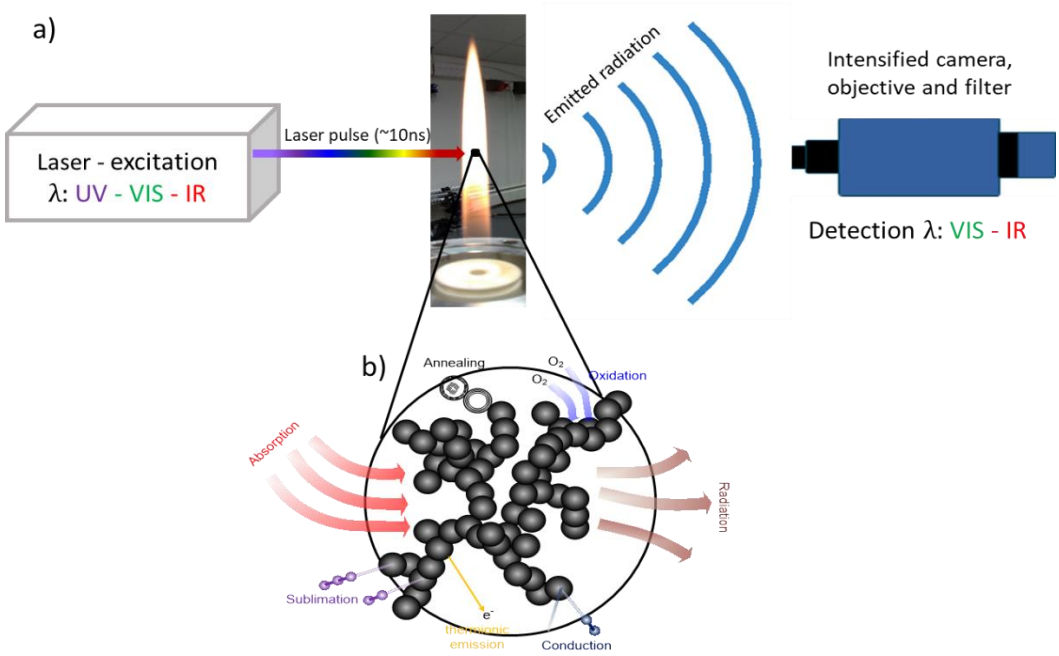

Figure 2.5 a) Example of LII in a simplified configuration b) A zoom of what happens at a nanometric scale of soot particles during absorption of the laser energy until the emission of radiation. b) is adapted from the article of Michelsen [72].

To study the temporal evolution of the temperature and diameter of primary soot particles, the energy conservation equation has to be resolved by considering the mechanisms leading to soot formation. All details that demonstrate the processes that occur during and after the absorption of laser radiation by the particle are adapted from the work of Michelsen [72]. The energy balance equation for a soot aggregate can be summarized as follows:

$$\frac{dU_{int}}{d_t} = \dot{Q}_{abs} + \dot{Q}_{rad} + \dot{Q}_{cond} + \dot{Q}_{sub} + \dot{Q}_{ox} + \dot{Q}_{ann} + \dot{Q}_{therm} \qquad \text{Equation 2.8}$$

Where U_{int} is the internal energy of the particle, t represents the time, $\dot{Q}_{abs}$ is the absorptive heating rate for a single primary particle, $\dot{Q}_{rad}$ is the radiative cooling rate, $\dot{Q}_{cond}$ is the conductive-cooling rate, $\dot{Q}_{sub}$ is the evaporative cooling rate, $\dot{Q}_{ox}$ is the oxidative heating rate, $\dot{Q}_{ann}$ is the heating rate from annealing and $\dot{Q}_{therm}$ the thermionic cooling rate.

1. Internal energy

Internal energy is the energy accumulated by soot particles. During this process, the rate of internal energy variation is expressed by:

$$\frac{dU_{int}}{dt} = \rho_s c_s \frac{\pi d_p^3}{6} \frac{dT}{dt} = M c_s \frac{dT}{dt} \qquad \text{Equation 2.9}$$

Where ρ_s is the particle density, c_s is the particle-specific heat, d_p is the primary-particle diameter, T is the particle temperature, and M is the primary-particle mass. The study of Hiers et al. [186] derived a modified expression with an additional term that accounts for losing some ability to store sensible heat when the particle's mass is reduced. This term is canceled in Equation 2.8 by

additional terms introduced in similar expressions of terms for sublimation and oxidation. Substituting Equation 2.9 into Equation 2.8 and solving for temperature yields:

$$\frac{dT}{dt} = \frac{1}{Mc_s(T)}\left(\dot{Q}_{abs} + \dot{Q}_{rad} + \dot{Q}_{cond} + \dot{Q}_{sub} + \dot{Q}_{ox} + \dot{Q}_{ann} + \dot{Q}_{therm}\right) \qquad \text{Equation 2.10}$$

Where M is the particle mass and T is the particle temperature. The equation below is the expression used for calculating the mass loss:

$$\frac{dM}{dt} = \left(\frac{dM}{dt}\right)_{sub} + \left(\frac{dM}{dt}\right)_{ox} \qquad \text{Equation 2.11}$$

The mass loss is related to the particle diameter via the density according to:

$$d_p = \left(\frac{6M}{\pi\rho_s}\right)^{\frac{1}{3}} \qquad \text{Equation 2.12}$$

where ρ_s is the density of the primary particles.

As the mass loss is related to the particle diameter, this phenomenon is used to determine the LII decay time based on the diameter of the particle [69,187]. Figure 2.1 is extracted from the study of Mansmann [188]. He simulated the LII temperature decay on various soot particle diameters in the flame environment at 1700 K ambient gas temperature after heating with a pulsed laser to 3600 K at t=0. Small particles (small diameter) cool down quickly during a few nanoseconds, while the larger ones (larger diameter) need hundreds of nanoseconds to reach the thermal equilibrium with the temperature environment. Besides the diameter of the particle, other processes can influence the decay time of soot particles, like the quenching process caused by the surrounding environment at high-pressure conditions.

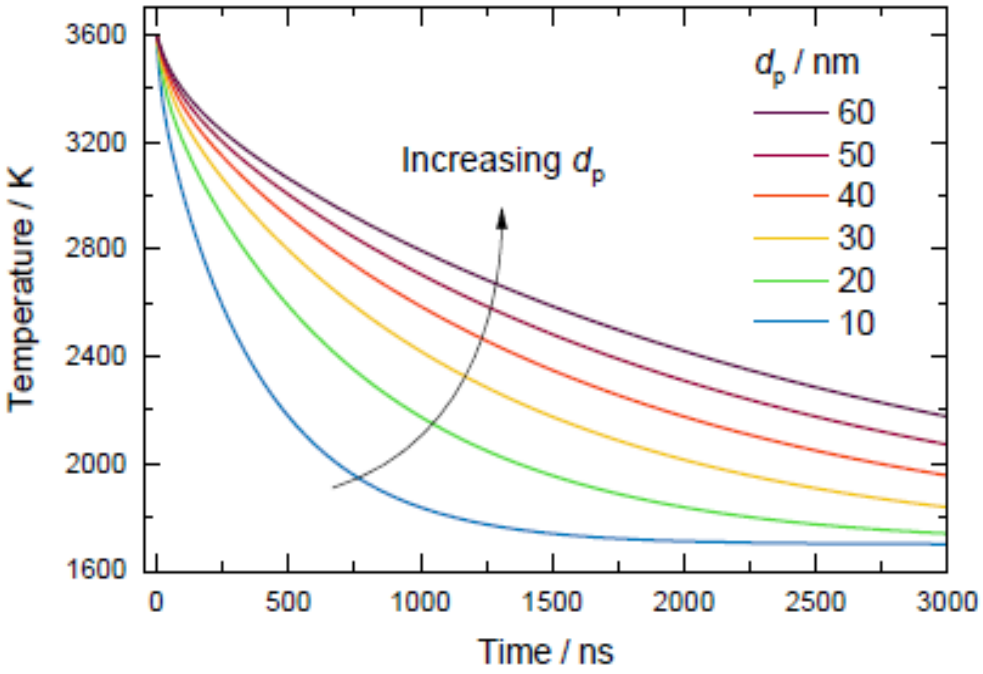

Figure 2.6 Simulated temperature decay time for different soot particle diameters [188].

2. Laser absorption and radiation

The initial step of the LII technique is the heating of the soot particle by absorption of incident laser light [72]. Based on the Kirchhoff's law, the emissivity of soot particles is equal to the absorption coefficient and depends on particle diameter, refractive absorption index and the wavelength used. The emissivity is given in the Rayleigh approximation regime, where $d_p << \lambda_L$, by:

$$\varepsilon_\lambda = \frac{4\pi d_p E_m}{\lambda} \qquad \text{Equation 2.13}$$

Where m is the complex index of refraction and E_m is the refractive index function for absorption. The E_m depends on the wavelength and is based on Kirchhoff's law, which also describes the emission properties of a particle. The LII signal is usually calculated over a narrow or broadband wavelength range in the ultraviolet, visible, or near-infrared spectral regions [186].

Heating the soot particles with a laser causes the soot temperature to rise rapidly during the laser pulse duration. For a primary particle in the Rayleigh regime, $d_p << \lambda_L$ where λ_L is the laser wavelength, the absorption cross-section (σ_{abs}) of a particle is given by:

$$\sigma_{abs} = \frac{\pi d_p^3 E_m}{\lambda_L} \qquad \text{Equation 2.14}$$

The flux density of the laser beam depends on the normalized temporal distribution of the laser energy balanced by the local energy density. The absorption cross-section can change if the particle size or the refractive index and E_m change. Absorption cross section for small particles scales with volume. The cross-section changes if the particle size changes, which refers to the change of the absorption refractive index function E_m [72].

The absorptive heating rate is then calculated according to the following equation:

$$\dot{Q}_{abs} = \sigma_{abs} E_e(t) \qquad \text{Equation 2.15}$$

Where $E_e(t)$ is the time-dependent irradiance of the incident laser.

The rate of thermal radiation is calculated based on the Planck's law of radiation over all wavelength domain [72,186]. When there is non-wavelength dependence to E(m), the radiative cooling rate is expressed as [189]:

$$\dot{Q}_{rad} = \frac{\pi^3 d_p^3 (k_b T)^5 E_m}{h(hc)^3} \qquad \text{Equation 2.16}$$

where k_b is the Boltzmann constant, h the Planck constant and c the speed of light. A more complex expression of $E_m$considers the wavelength dependence [186]. The radiative cooling rate usually is significantly smaller than the other cooling rates, such as the conductive cooling at atmospheric pressure and above and the evaporative cooling rate at high laser fluence. This heat radiation mechanism is the dominant cooling mechanism for low laser fluence is used (laser energy per surface) [72].

3. Conduction

Understanding heat transfer by conduction is necessary for inferring primary particle sizes from pulsed-LII decay rates. Conductive cooling also competes with absorptive heating on time scales relevant for continuous wave (CW) LII detection and can limit the minimum detectable particle size using this approach [72,190]. Considerable work has been devoted to identifying an appropriate conductive-heat-transfer mechanism for LII applications. In the free-molecular-flow regime (where the mean free path is significantly higher than the particle diameter), the conductive-cooling rate can be expressed as [72,186,189]:

$$\dot{Q}_{cond} = -\frac{\pi\, d_p^2\, \alpha_T\, P_0}{R\, T_0}\left(\frac{R\, T_o}{2\pi\, W_a}\right)^{\frac{1}{2}}\left(C_p - \frac{R}{2}\right)(T - T_0) \qquad \text{Equation 2.17}$$

Where P_0 is the ambient pressure, T_0 is the ambient temperature, R is the universal gas constant, W_a is the molecular weight of air, C_p is the heat capacity of air at constant pressure, and α_T is the thermal accommodation coefficient. A more detailed version of this expression, which accounts for the temperature dependence of the heat capacity, is given by:

$$\dot{Q}_{cond} = -\frac{\pi\, d_p^2\, \alpha_T\, P_0}{R\, T_0}\left(\frac{RT_0}{2\pi W_a}\right)^{\frac{1}{2}}\int_{T_0}^{T} C_p(T')dT' + \frac{R}{2}(T - T_0) \qquad \text{Equation 2.18}$$

Where C_p is the heat capacity of air at constant pressure, and α_T is the thermal air coefficient. With respect to conductive cooling, part of the current work focuses on understanding the effect of aggregate size, primary particle polydispersity, bridging between primary particles, aggregate morphology, and particle maturity on conduction energy [185,191–193].

4. Sublimation and vaporization mechanisms

Evaporative heat loss is a significant cooling mechanism when a high laser fluence is used [72]. More importantly, sublimation and other vaporization mechanisms lead to rapid decreases in the LII signal because of mass loss during the laser pulse. These mechanisms are the most poorly understood of all processes that have a strong influence on LII signal. Most LII models and experiments cannot reproduce the rapid signal decay attributable to the evaporative-mass loss or the plateau in the peak temperature at high fluence. The cooling evaporation rate is written for the majority of LII models as follows:

$$\dot{Q}_{sub} = \frac{\Delta H_V}{W_V}\left(\frac{dM}{dt}\right)_{sub} \qquad \text{Equation 2.19}$$

where ΔH_V is the enthalpy of formation of the sublimated carbon atoms/or latent heat of soot sublimation, W_V is the average molecular weight of the sublimated carbon atoms. Therefore, the rate of mass loss is:

$$\left(\frac{dM}{dt}\right)_{sub} = -\frac{\pi d_p^2 W_V \alpha_M P_V}{RT}\left(\frac{RT}{2\pi W_V}\right)^{K} \qquad \text{Equation 2.20}$$

where α_M is the mass accommodation coefficient, P_V is the average saturation partial pressure of the sublimed carbon clusters, and K is a constant that is typically equal to 0.5 but is sometimes given a value of 0.4 to account for non-idealities of the bath gas and desorbed clusters [72].

5. Oxidation

The oxidation process has the particularity of being able to lead to two phenomena of heating and loss of mass of the particles, but it is less rapid and significant than the previous processes. In classical laminar diffusion flame, oxidation occurs at the flame tip when the mature soot mass or concentration starts to reduce. Sometimes this mechanism is neglected in LII methods, although it can impact the size of the primary particles. The heating oxidation rate is expressed in the work of Michelsen [72] as follows:

$$\dot{Q}_{ox} = \frac{\Delta H_{ox} + \alpha C_p^{CO}}{W_1} \left(\frac{dM}{dt}\right)_{ox} \qquad \text{Equation 2.21}$$

where ΔH_{ox} is the enthalpy of the reaction $C + \frac{1}{2} O \rightarrow CO$ at a reference temperature T_{ref}, which is equivalent to the enthalpy of formation of CO, C_p^{CO} is the heat capacity of CO, and W_1 is the molecular weight for a carbon atom.

The rate of mass loss through oxidation can be expressed according to:

$$\left(\frac{dM}{dt}\right)_{ox} = -\frac{\pi d_p^2 W_1 2 k_{ox}}{N_A} \qquad \text{Equation 2.22}$$

where N_A is the Avogadro constant, and k_{ox} is the rate constant for $2C + O_2 \rightarrow 2CO$. Of course, under combustion conditions, concentrations of radical species OH and O can be significant, and rates of oxidation by these species may contribute substantially to overall oxidation rates [72].

6. Annealing

Annealing is perceived as an exothermic phenomenon that heats the particle. A more significant contribution from this process is its potential influence on all other processes because it changes the physical structure of the particle at the fine-scale. Little is known about this mechanism, its rate, its energetics, and how it affects other physical parameters, such as the particle optical properties. Although this mechanism could significantly impact LII signal, it is disregarded in most LII models and experiments because so little is known about how to take it into account. The heating rate for this mechanism can generally be expressed as follows:

$$\dot{Q}_{ann} = \frac{\Delta H_{ann} k_{ann} N_d}{N_A} \qquad \text{Equation 2.23}$$

where ΔH_{ann} is the enthalpy for annealing, k_{ann} is the rate constant for annealing, and N_d is the number of defect sites in the particle. The model that includes annealing assumes that the particle anneals at low temperatures by the migration of interstitial atoms that combine with defects within the graphite planes [72].

7. Thermionic emissions rate

This rate has less influence on the study of particle emissions and is, therefore, neglected for the LII measurements. However, it can be taken into account to understand and predict the particle surface changing caused by laser heating. This ratio, based on an approximation made by Dushman [194], is expressed as:

$$\dot{Q}_{therm} = -\frac{4\phi m_e \left(\pi d_p k_B T\right)^2}{h^3} \exp\left(\frac{-\phi}{k_B T}\right) \qquad \text{Equation 2.24}$$

where ϕ is the work and m_e is the mass of an electron [9.1093837×10^{31} kg].

Table 1 provides an overview of the effects of different mechanisms involved in the particle energy and mass balance for soot aggregates during LII [72]. The mechanisms that impact the energy balance the most are laser absorption for heating, conduction and sublimation for cooling and sublimation for mass loss. These mechanisms with corresponding effects are considered when using a pulsed laser for LII measurement during the induction process (few ns). For mature soot at flame temperatures and atmospheric pressure, the usually used laser fluence in most studies is below 0.15 J/cm^2 at 1064 nm, but some measurements use higher fluence values [141,181]. The laser fluence ranges used during LII mainly depend on the fuel type (liquid or gaseous), combustion conditions (pressure and temperature) and particle morphology. Conductive cooling and oxidation are less important during sublimation or vaporization. The timing for sublimation depends on particle morphology, size, composition, and laser irradiance. Sublimation becomes predominant when the particle reaches the sublimation temperature. The sublimation point of graphite at atmospheric pressure lies between 3900 and 4050 K, and it is seldom considered a reference for LII [72,190,195]. On the other hand, the sublimation point for soot strongly depends on its structure, morphology, coating and environment, although the sublimation point varies between 4000-4500 K.

Mechanisms	**Main effects**	**Fluence range**
Heating mechanisms		
Laser absorption	Peak LII, rise time	All fluences
Oxidation	LII decay rate	Low fluences
Annealing	Optical properties	All fluences
Cooling mechanisms		
Conductions to air	LII decay rate	Low fluences
Sublimation	Peak LII, the decay rate	High fluences
Radiation	Minor, unless low pressure	All fluences
Thermionic emission	Minor	All fluences

Table 1 Contribution of the energy loss mechanisms extracted from the study of Michelsen [72].

8. Laser Induced Incandescence signal

The LII signal represents the detected enhanced thermal radiation from soot particles in the measurement volume. The LII signal $S_{LII}(T, \lambda)$ for a particle with d_p diameter is calculated using the Planck function, which considers the deviation of a soot aggregate from a perfect blackbody. The thermal emission of a black body is expressed by:

$$R(T,\Delta\lambda) = \int_{\lambda_1}^{\lambda_2} \frac{2\pi hc^2}{\lambda^6} \frac{1}{\exp\left(\frac{hc}{\lambda k_B T}\right) - 1} d\lambda \qquad \text{Equation 2.25}$$

Where:

$M(T,\Delta\lambda)$: Emittance or spectral radiance expressed in power per unit solid angle and per unit of area normal to the propagation ($Wsr^{-1}m^{-3}$)

$\Delta\lambda$: Emission spectral range or detection wavelengths (m), ($\Delta\lambda = \lambda_2 - \lambda_1$)

T: Absolute temperature of the black body (K)

h: Planck constant ($6.6256 \times 10^{-34}\ JHz^{-1}$)

c: Speed of light in a vacuum($3 \times 10^8\ ms^{-1}$)

k_B: Boltzmann constant ($1.3805 \times 10^8\ JK^{-1}$)

The LII signal can be expressed based on the equation of Planck by approximating that the soot particles are a black body where their temperature $T_{(t)}$ changes as a function of time. By also supposing that soot particles are spherical with a radius r_p, the emitting surface that has to be taken into account is:

$$S_p(t) = 4\pi r_p^2\ (t) \qquad \text{Equation 2.26}$$

By taking into account the number of primary particles N_p in the sampling volume, the LII signal (S_{LII}) is represented as:

$$S_{LII}(T,\lambda) = \int_{\lambda_1}^{\lambda_2} N_p \frac{2\pi hc^2 E_m(\lambda)}{\lambda^5} \left[\frac{1}{\exp\left(\frac{hc}{\lambda k_B T}\right) - 1}\right] 4\pi r_p^2\ (t) d\lambda \qquad \text{Equation 2.27}$$

In reality, soot particles are not black bodies. Instead, they are considered grey bodies. Therefore, only a part of the laser light they absorb is reemitted as a signal. By taking into account the emissivity $\dot{Q}_{em}$, with values comprised between 0 and 1, the LII signal becomes:

$$S_{LII}(T,\lambda) = \int_{\lambda_1}^{\lambda_2} Q_{em}\ N_p \frac{2\pi hc^2}{\lambda^5} \frac{1}{\exp\left(\frac{hc}{\lambda k_B T}\right) - 1} 4\pi r_p^2\ (t) d\lambda \qquad \text{Equation 2.28}$$

By taking into account Kirchhoff's law, which establishes the relationship between the ability to emit and absorb electromagnetic energy by any physical body, it is possible to deduce the approximation that heated soot particles are in thermodynamic equilibrium with encountered radiation. In that case, Q_{abs} absorptive heating rate is equal to the emissivity radiation (Q_{em}), and it gives:

$$Q_{abs} = 4E_m \frac{2\pi r_p(t)}{\lambda_{abs}} = 4\ E_m \frac{2\pi r_p(t)}{\lambda_{em}} = Q_{em} \qquad \text{Equation 2.29}$$

Where λ_{abs} is the particle absorption wavelength and λ_{em} is the particle emission wavelength. By considering all number of primary particles, the expression of the LII signal becomes:

$$S_{LII}(T,\lambda) = \int_{\lambda_1}^{\lambda_2} 4E_m \frac{2\pi r_p(t)}{\lambda_{em}} N_p \frac{2\pi hc^2}{\lambda_{em}^5} [\frac{1}{\exp\left(\frac{hc}{\lambda k_B T_{(t)}}\right) - 1}] 4\pi r_p^2 (t) d\lambda \quad \text{Equation 2.30}$$

By rearranging the Equation 2.30 becomes:

$$S_{LII}(T,\lambda) = \int_{\lambda_1}^{\lambda_2} 64\, E_m \frac{\pi^3 hc^2}{\lambda_{em}^6} [\frac{1}{\exp\left(\frac{hc}{\lambda k_B T_{(t)}}\right) - 1}] N_p\, \pi r_p^3 (t) d\lambda \quad \text{Equation 2.31}$$

As described in previous equations, the LII signal depends on the number of primary particles and their cross-section. Therefore, based on these equations, the soot volume fraction is calculated as:

$$f_v = \frac{4}{3}\pi r_p^3 (t)\, N_p \quad \text{Equation 2.32}$$

By introducing Equation 2.32 into Equation 2.31, the LII signal becomes:

$$S_{LII}(T,\lambda) = \int_{\lambda_1}^{\lambda_2} 48E_m \frac{\pi^2 hc^2}{\lambda_{em}^6} [\frac{1}{\exp\left(\frac{hc}{\lambda k_B T_{(t)}}\right) - 1}] f_v (t) d\lambda \quad \text{Equation 2.33}$$

It has to be considered that the LII signal is collected from a solid detection angle and corrected by the efficiency of the detection system, which is the transfer function of the optical chain. Therefore, by taking into account the effect of the detection angle and transfer function, the LII signal can be expressed as:

$$S_{LII}(T,\lambda) = \int_{\lambda_1}^{\lambda_2} 12E_m \frac{\pi hc^2}{\lambda_{em}^6} [\frac{1}{\exp\left(\frac{hc}{\lambda k_B T_{(t)}}\right) - 1}] V_m \Omega \beta f_v(t) d\lambda \quad \text{Equation 2.34}$$

Where:

V_m: Volume of analysis given by the laser sheet size (m^3)

Ω: Solid angle given by the position of the detection system (Sr)

β: Transfer function obtained from the optical chain (pulse/watt)

The measured LII signal (SLII) represents the integrated emission over a defined spectral wavelength range. The detected signal depends on the temperature at which soot particles are heated, the morphology of soot particles (young, mature or oxidized), detection wavelength and soot refractive index E_m (λ, T). The E_m (λ, T) can affect the shape of the LII emitted intensity over a broadband emission spectrum and effective soot temperature.

2.3 MAIN PARTS OF THE LII CONFIGURATION – EXPERIMENTAL SETUP

This subchapter describes the general LII experimental configuration used in the laboratory. The experimental setup consists of three main parts. The first one is the source of combustion, which includes a coaxial laminar diffusion flame at atmospheric combustion conditions, with methane and

air. The second part consists of a Nd:YAG laser as an excitation source. Most of the lasers used to induce incandescence have a Gaussian cavity; therefore, the Gaussian characteristic is inherited by the laser beam. The theory for the propagation of the Gaussian beam is discussed and presented since it has to be taken into account when shaping the laser beam into a laser sheet. The last part of the LII consists of the detection system with an intensified camera coupled with lenses and filters.

2.3.1 Source of combustion – coaxial burner with CH_4/air laminar diffusion flame

Laboratory flames are studied because they present some advantages with respect to pressurized-turbulent flames. These advantages include the laminar aspect of the flow, which does not impact the variation of the combustion conditions from one image to another. Some laminar diffusion flames present a stratification between various classes of PAHs and soot, which results in the possibility of following the *"combustion chemistry"* and the growth of soot particles along the flame axis (radial or axial).

In this study, the used atmospheric laminar CH_4/air diffusion flame is similar to the one described by Santoro et al. [196] and other researchers [197–199]. A flow of methane is injected through the central part of the burner using a cylindrical injector with an internal diameter (ID) of 9 mm surrounded by a coaxial airflow. The empty volume of the burner surrounding the central injector was filled with glass beads placed on a layer of sintered material for airflow homogenization. The flame was stabilized with a 47.5 L/min air shield and 0.546 L/min CH_4. These conditions resulted in a laminar non-smoking diffusion flame with a height of ~ 116 mm and a 10 mm diameter near the injector. The exit fuel velocity is 0.12 m/s and 0.23 m/s for air with Reynolds numbers of 106 (CH_4) and 1154 (Air). The flame tip was slightly flickering due to exposure to ambient conditions. A chimney with four quartz windows was added to stabilize the flame and to confine it from the surrounding air.

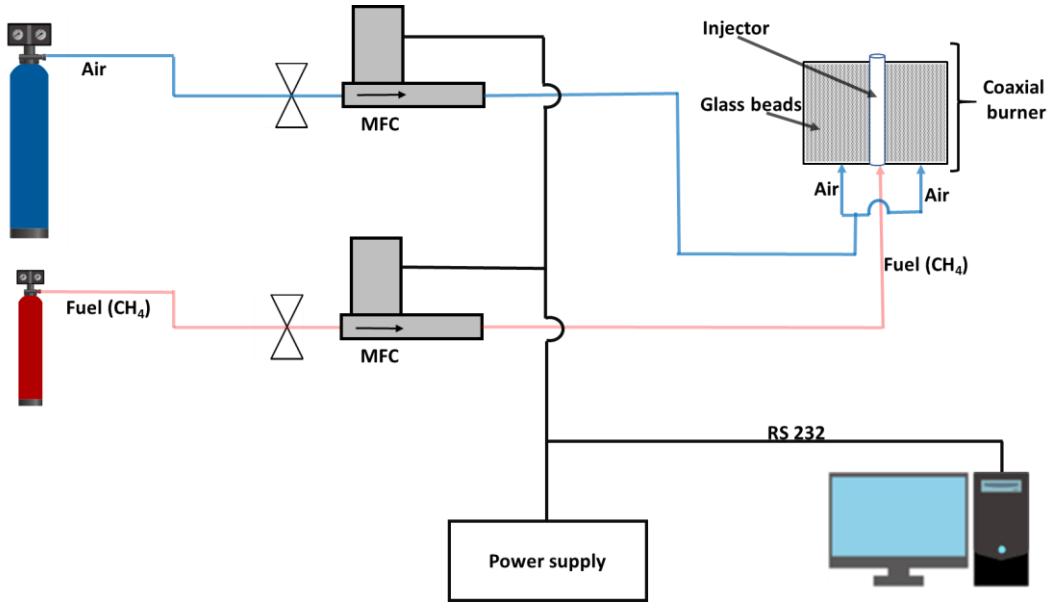

Figure 2.7 Overview of experimental configuration used for the coaxial burner with the CH_4/air laminar diffusion flame. The figure represents the fuel/air supplying lines, their control and the burner.

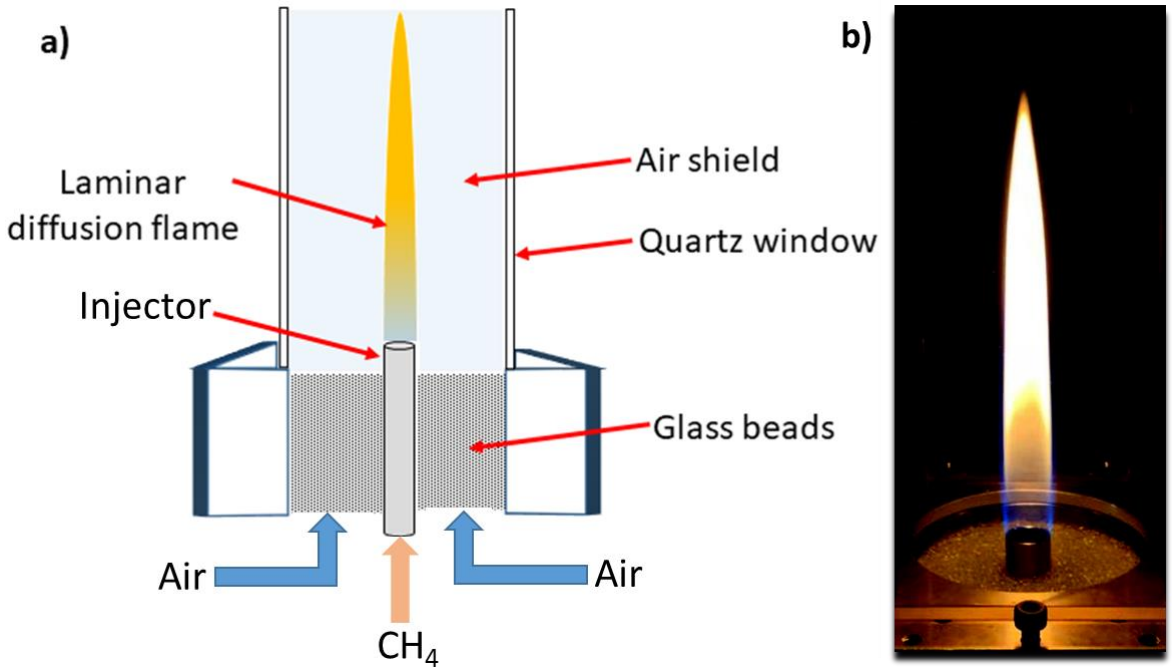

Figure 2.8 a) Schematic of coaxial burner with the laminar diffusion flame (b) Image of the stable CH_4/air laminar diffusion flame used in this study.

2.3.2 Laser excitation source

Laser technologies have been developed to answer various complex application fields. Due to their unique properties, lasers have occupied a significant place in combustion and fluid mechanics applications. The excitation source used in this study is a pulsed Litron laser (Nd:YAG) TRLiG 850 model. This laser type is one of the most frequently used high-power pulsed solid-state lasers and it was selected because it has the corresponding technical requirements in terms of fluence, pulse duration and divergence. The working principle of the Nd:YAG lasers is detailed in Annex 0.

This Litron laser has a pulse duration of 5-7 ns at the full-width half maximum (FWHM) of the laser peak and is lasing at 10 Hz. The maximum laser energy per pulse is 1 J for the fundamental excitation wavelength of 1064 nm. The diameter of the laser beam is 9 mm in the near field (NF) at the laser exit. The laser is equipped with a motorized energy attenuation module that helps modify the laser output energy without perturbing the laser beam characteristics (size, divergence, polarization) and a frequency-doubling module (2ω) that can generate 532 nm.

2.3.2.1 Gaussian beam propagation

The Gaussian characteristic of the beam plays a role in its propagation and shaping. The M^2 factor, namely the beam propagation factor, is a quantitative indicator of the laser beam quality [200]. M^2 indicates how close to an ideal beam the laser beam is propagating. In addition, it shows the deviation of the implied beam from a theoretical Gaussian beam. Mathematically M^2 is defined as the ratio between the beam parameter product (BPP), which is equal to the beam waist radius (W_o) multiplied by the half-angle divergence (θ) of the measured beam with the theoretical Gaussian beam. Thus, for a single-mode ideal TEM_{00}theoretical Gaussian beam, the M^2 factor equals 1. Also, the beam

parameter product of the laser beam, represented by the product of the laser beam divergence angle (half-angle) and the beam radius at its narrowest point (the beam waist), is always equal to or more significant to the ideal beam parameter product. Therefore, an M^2 value close to 1 indicates excellent beam quality. This laser beam characteristic is associated with low divergence and a good ability to focus.

The beam waist is the location along the beam propagation axis where the beam radius reaches its minimum value when focalized with a lens. For example, for a theoretical Gaussian beam, the beam radius W_{th} (Z) at any Z position along the beam axis is given by the following equation:

$$W_{th}(Z) = W_{0th}\sqrt{1+\left(\frac{\lambda z}{\pi w_{0th}^2}\right)^2} \qquad \text{Equation 2.35}$$

Where λ is the laser wavelength and W_{oth} is the theoretical beam waist radius.

As depicted in Figure 2.1, the theoretical Rayleigh length Z_{rth} is the distance along the propagation axis between the beam waist and the position where the beam radius is $\sqrt{2}$ times larger than the beam waist (double cross-section). A laser beam with a small divergence is privileged for applying laser-based techniques, which require a laser sheet (plane) in the combustion process. For LII measurement, it is essential to have a homogeneous beam, as it is privileged to heat soot particles at the same temperature in the sampling volume.

In this study, the system used to characterize the laser sheet width contains an sCMOS sensor. The used beam profiler is a Gentec-EO Beamage 4M series. It has a variable exposure time between 0.06 and 200 ms. In addition, it can withstand a maximum laser fluence of 30 $\mu J/cm^2$ on the sensor with a laser exciting in IR. Neutral filters or laser beam attenuators were used to reduce the laser fluence value.

For laser beam/sheet size measurement, the beam-profiling camera was positioned at the center of the injector before each measure. Furthermore, the neutral density filters were added in front of a beam profiler to reduce laser power below the damage threshold.

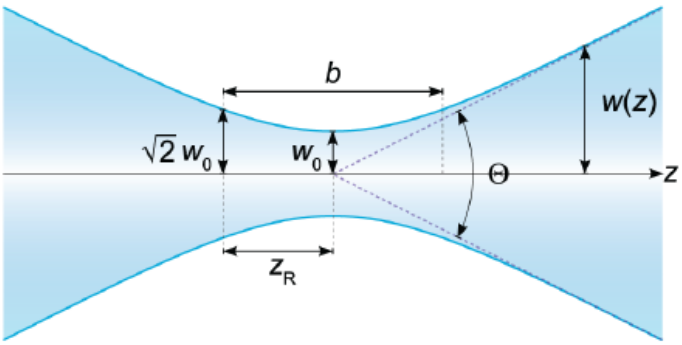

Figure 2.9 A diagram representing the parameters of interest that characterize a Gaussian laser beam during propagation [201].

2.3.3 Detection system

A suitable detection system is needed for the LII technique configuration to record the LII emitted signal. For point measurements, a Photomultiplier Tube (PMT) is often employed, and a Charge Couple Device (CCD) or a scientific Complementary Metal Oxide Semiconductor (sCMOS) coupled with an image intensifier is mainly used for 2-dimensional measurements [202]. In this work, intensified cameras are used for detecting induced incandescence and fluorescence signals. The induced signal is collected on the sensor either with image relay lenses or an optical fiber bundle, depending on the camera type. The image sensor consists of arrays of pixels (a matrix), which record the amount of incident light.

For the LII signal acquisition, a LaVision sCMOS camera is used. The maximum recording frequency at the full frame is 50 Hz. The inter-frame time for the sCMOS detector is 120 ns (for double-frame acquisition mode) and a few ms for single-frame acquisition mode. An Intensified Relay Optics (IRO) system is placed in front of the sCMOS, which allows recording light signals with a minimum opening gate width (GW) of 10 ns.

The IRO system comprises a photocathode, a Micro Channel Plate (MCP) comprised of electron multipliers and a phosphor screen. The photocathode has the role of converting photons into electrons. An S20 photocathode, which covers the UV-visible wavelength domain but has high detection sensitivity in UV, equips this IRO. The electrons are then multiplied by the MCP and arrive on the phosphor screen that transforms the electron image into a photon image in the visible domain. The IRO system contains a P43 Phosphor screen with a characteristic signal decay time of 1 ms. Relay optics then transfer the photons to the sCMOS detector. The sCMOS sensor contains pixels of 6.5 µm size, arranged on a 2560 x 2160 matrix.

Canon lenses with a focal length of 135 mm focus the region of interest (ROI) onto the camera system. The aperture is adjustable to select the sampling depth at the focal point. In addition, a binocular system from LaVision can be added in front of the lenses to capture on the detector two images at different wavelengths at the same; this is equivalent to the split of the sensor in two. Narrow-band filters centered at 450 nm, 580 and 650 nm, with a wavelength bandwidth of 10 nm, are added on each side of the binocular system to select the spectral area of interest.

In this study, the LII signal comes from a laminar diffusion flame at atmospheric pressure. The LII signal is recorded after the peak of the laser pulse for a few ns (50 ns). It is necessary to work with a double-frame camera on test rigs to subtract the flame emission from the total emitted signal. In order to collect the LII signal, the gate of the intensifier must be synchronized with the laser pulse (the Q-Switch or the flash lamp signal) of the excitation source. A trigger is sent from the laser to the camera, allowing the collection of an LII image at each laser pulse. For this specific case, the laser and the camera are synchronized with a photodiode that has a rise time of 2 ns and a broadband spectral response between 200 and 1100 nm. The synchronization between the camera gate and the laser pulse was monitored on an oscilloscope. The images collected with the camera are sent to a computer for processing and storage.

2.3.4 Choice of LII excitation and detection wavelengths

LII detection and excitation wavelengths have been extensively studied over the last decade as they directly affect the induced signal. Given that soot particles have broadband absorption and emission spectrum (Planck type emission) and especially due to the presence of various complex PAHs and other simple molecules in flames, it is judicious to analyze the possible advantages and disadvantages of various LII configurations. The challenge is to choose adapted wavelengths for induction and detection of the signal, which do not produce interference due to the interaction between the flame/matter and the laser, which the detection system can consequently record.

Due to technical and practical reasons, the detection of LII is seldom performed in the visible wavelength domain. This is mainly due to the temperature, around 4000 K, at which soot particles are heated. A peak emission spectrum in visible is expected when heating soot particles to their incandescence temperature. Existent detection systems also play a role in detecting soot particles in a 2D image. Accessible intensified cameras give range to various applications, mostly with detection sensitivity in the UV-near IR wavelength domain. In this account, it is established to select the inducing wavelength which is not inducing other phenomena (fluorescence, scattering, vaporization) and the detection domain on the LII peak, without interference from other combustion self-excited molecules or self-emission of the flame.

The chosen IR laser delivers sufficient output energy that can heat soot particles to incandescence. A laser with an IR excitation wavelength (1064 nm) is seldom used for LII. The Nd:YAG harmonic wavelengths (532, 355 or 266 nm) or other wavelengths, such as 283 nm, can also induce fluorescence from PAHs or interfere with other molecules (for instance, OH), as shown in different studies [164,203,204]. In combustion-related applications, the advantage of inducing incandescence of soot with 1064 nm relies on eliminating fluorescence interference when the detection is set for the visible wavelength domain.

The generation of an electronically excited C_2 Swan band at red-shifted excitation wavelengths is less pronounced with a well-adapted laser fluence (J/cm^2). However, the C_2 Swan band can still interfere with the LII signal at high laser fluence beyond the sublimation point, as demonstrated in the study of Bengtsson et al. due to the vaporization of soot particles [205]. Moreover, the interference of C_2 or other species might change with the increasing pressure of the combustor. To discriminate C_2 signal, it is recommended to use detection wavelengths that have low C_2 band emission. Figure 2.10 shows the emission spectrum for Swan carbon molecules.

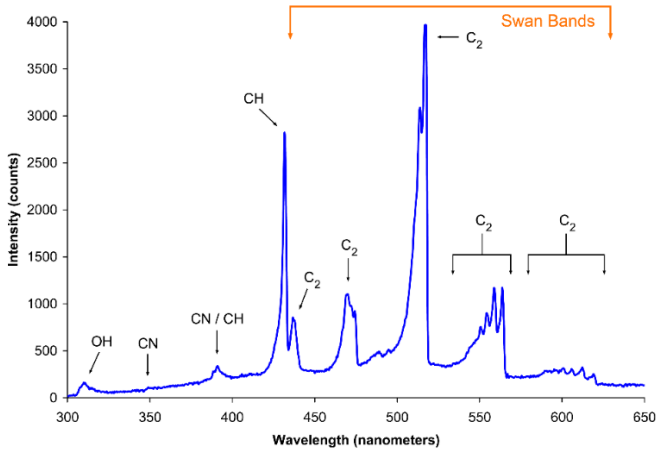

Figure 2.10 Spectrum of the blue flame from a butane torch showing excited molecular radical band emission and Swan bands [206].

The elastic scattering of soot is predominant when the LII signal is excited in the visible domain. However, IR scattering cross sections are much smaller than visible cross sections, making IR scattered light easier to discriminate when IR excitation and detection in the visible are employed. Additionally, many photodetectors used in LII have weak or no response at 1064 nm, limiting the interference with the scattering signal. However, when one wants to perform measurements of both LII and elastic light scattering, the combined use of 532 nm will be favored over the use of 1064 nm.

If the laser source is below the infrared domain, it is possible to discriminate fluorescence signal during detection from the LII by adding a delay of some nanoseconds. However, the disadvantage of delaying the LII can bias the quantification of the LII signal into soot volume fraction since the decay time depends on the size of the primary particles; this means that detected LII is sensitive to larger soot particles. Therefore, 1064 nm is used in this work to limit mentioned challenges and reduce the errors. Furthermore, this excitation wavelength is also advantageous for broadband detection of the LII spectra.

It is challenging as well to select the detection wavelength of interest. Due to the change of soot optical properties at different wavelengths, a detection wavelength that is near-IR or infrared is preferred over the visible wavelength domain detection. The near-IR wavelength domain detection scheme minimizes the influence of variation in the soot absorption index function (E_m (λ, T)) from different soot types and for broadband LII detection.

However, for the application of LII on highly emissive flames, as is the case of test rig applications, it is preferred to improve the discrimination of the LII signal from the flame luminosity. Furthermore, flame emissivity is high in the infrared domain for harsh combustion conditions flames. Hence, a compromise must be found on the detection wavelength for LII.

Suppose two-color LII (2C-LII) is used for the measurement. In that case, the detection wavelength couple has to be chosen wisely, as this highly affects the obtained soot effective temperature (T_{eff}) and, consequently, the volume fraction. The selection of the two detection wavelengths differs substantially from one research group to another and is worth mentioning. Table 1 summarizes the excitation and detection wavelengths used by the different research groups. The selection of the two detection wavelengths must be mainly made to maximize the signal-to-noise ratio

using the detectors at hand while avoiding interference from other emissions and acceptable precision of T_{eff} [207].

Reference	$\lambda_{exc.}$	$\lambda_{det.}$	Observations
Liu et al. 2022 [208]	1064 nm	λ_1: 420 nm, λ_2: 560, λ_3: 680 nm and λ_4: 790 nm.	- Effects of detection wavelength pairs on soot volume fraction using the AC-LII technique. - The effective soot temperature was derived over three pairs of LII signals, namely [420, 560 nm], [560, 680 nm], and [680, 790 nm].
Potenza et al. 2014 [187]	1064 nm	λ_1 = 488 nm and λ_2 = 635 nm	- Two-dimensional measurements of primary soot diameter in diffusion flames by 2D-LII
Michelsen et al. 2007 [185]	532 nm	λ_1: 400 nm and λ_2: 650 nm	- Modeling of soot particles by using 2C-LII techniques
Iuliis et al. 2006 [153]	1064 nm	λ_1: 500 $\pm$10 nm and λ_2: 647 $\pm$9 nm	- 2D soot volume fraction imaging in an ethylene diffusion flame by two-color laser-induced incandescence (2C-LII) technique and comparison with results from other optical diagnostics
Snelling et al. 2005 [209]	532 nm	400 $\pm$45 nm and 780 $\pm$20 nm	- A calibration-independent LII technique for soot measurement by detecting absolute light intensity
Török et al. 2021 [210]	1064 nm and 532 nm	λ_1: 575 $\pm$25 nm and λ_2: 684 $\pm$24 nm	- 2C-LII used to estimate absorption efficiency of differently matured soot
Mouton et al. 2013 [155]	1064 nm	- UV–Visible PMT (150–650 nm) - Spectrometer (500-625 nm)	- Laser-induced incandescence technique to identify soot nucleation and very small particles in low-pressure methane flame

Table 2 Examples of some detection and excitation wavelengths used for LII in the literature, λ_{exc} stands for excitation wavelength and $\lambda_{det.}$ is the detection wavelength.

2.4 LASER SHEET CHARACTERIZATION: 532 NM AND 1064 NM

Using lasers to probe combustion environments implies the mastery of the laser beam shaping with respect to the sampling volume, propagation axis and detection system. Therefore, developing an adapted laser beam-shaping system demands an in-depth understanding and characterization of lenses that convert the circular Gaussian laser beam profile into a planar laser sheet.

This sub-chapter describes how the lenses used for laser sheet generation can affect the LII signal and its interpretation. Different lens settings are used for generating planar laser sheet configurations that are investigated on the CH_4/air laminar diffusion flame, described in section 2.3.1.

2.4.1 Optical configurations

Firstly, the Litron Nd:YAG laser equipped with a SHG module (2ω, 532 nm) that generates a Gaussian beam was used and the final configuration of selected lenses was applied to the shaping of 1064 nm laser beam as well. These tests resulted in three main optical configuration settings.

The main characteristics of 1064 nm laser beam are as follows: divergence < 0.5 mrad, M^2 <2 and 0.6% energy variation from one laser pulse to another. These characteristics are necessary to estimate the divergence of the laser sheet in the focal point while using various sets of lenses for shaping the laser beam.

The schematic representation **of the first experimental setting** is displayed in Figure 2.11. A set of three mirrors directs the laser beam into a series of lenses used to generate a laser sheet. The laser sheet generator consists of three lenses. Other configurations of laser sheet generators can be identified in the literature [211–213]. The first lens (L1) is a negative cylindrical lens with a focal length of either -15 or -19 or -25,4 mm, used for expanding the circular laser beam on one axis. The second positive cylindrical lens (L2) with a focal length of 200 or 300 mm collects the diverging laser beam to convert it into a parallel one, on one propagation axis only (one dimension). The last lenses (L3) consist of positive cylindrical lenses with a focal length of 500 or 1000 mm that focus the generated laser sheet into the region of interest (center of the flame), and make it parallel on the second propagation axis. These two lenses were set orthogonal to the L2.

A beam splitter window, which transmits 90% of the laser beam and reflects 10%, was positioned in the focal point of the laser sheet at the same position as the center of the flame. The reflected 10% were directed on a laser beam profiler placed at 90° of the beam splitter and 90% were transmitted into a power meter. However, the reflected laser sheet still contains a high energy density due to high laser energy, which can damage the beam profiler. To avoid this, neutral density filters with optical density (OD) of 1.3 and 0.4 are added in front of the detector.

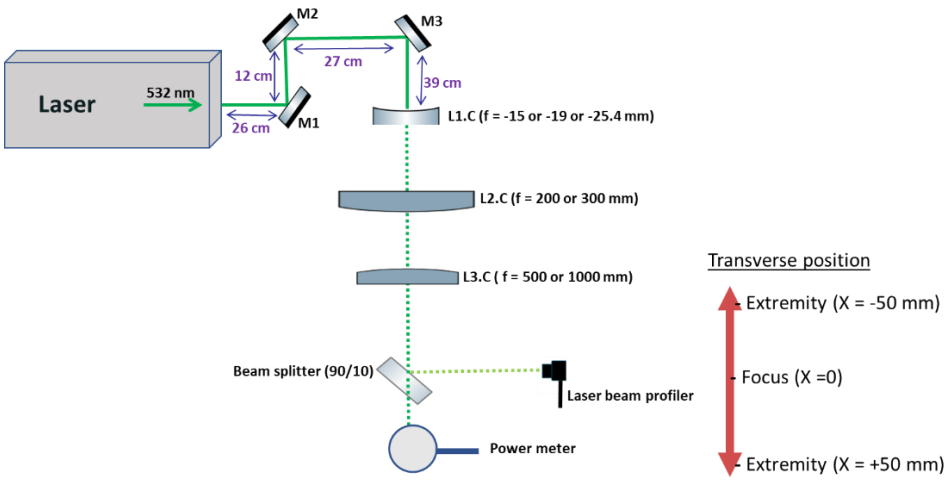

Figure 2.11 Schematic representation of first studied optical laser sheet configurations, the lenses used for generating laser sheet were changed based on lens focal point. In addition, the visible Laser is used for better alignment. L1.C: first plano-concave cylindrical lens, L2.C: second plano-convex cylindrical lens, L3.C: third plano-convex cylindrical lens and X: different point in the transverse position of laser sheet propagation (e.g., X = 0 mm is in the focal point).

The **second tested optical configuration** (Figure 2.12) consists of the same set of mirrors and the first negative cylindrical lenses. However, the last two positive cylindrical lenses were replaced with spherical lenses with a focal length of 500 or 1000 mm. The detection system was the same as the first optical configuration.

Figure 2.12 shows the second tested configuration where the last lens used is spherical. Despite being a more robust optical configuration, the inconvenience consists of limited flexibility in the alignment of the last lens when the distance between the lenses and the sampling volume is limited. For example, this problem can show up for complex measurements around test rigs with limited space.

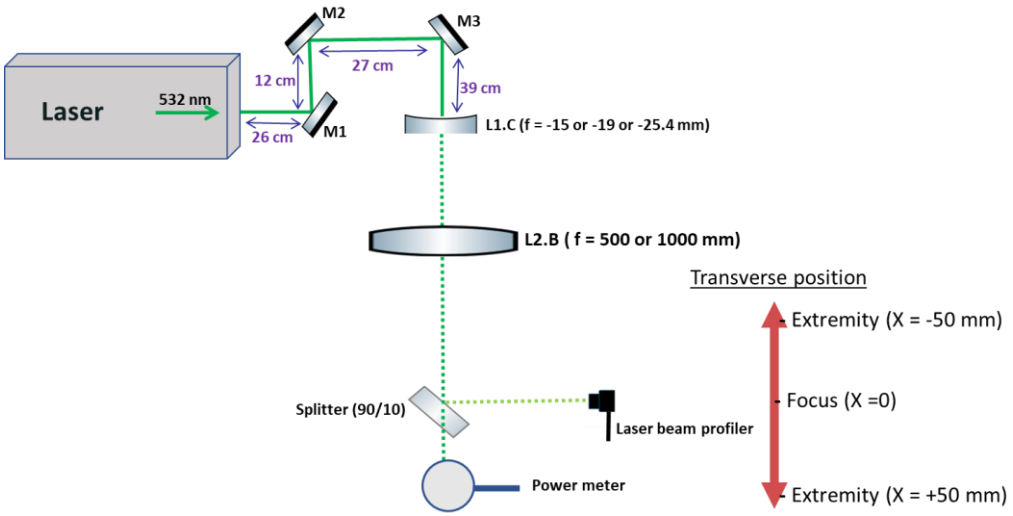

Figure 2.12 Schematic of the experimental layout for the second studied optical laser sheet configuration. L2.B: second bi-convex cylindrical lens or spherical lens.

A **third optical configuration** was performed with lenses suitable for 1064 nm wavelength. Lenses selected with 532 nm were used in this case.

2.4.2 Characteristics of the laser sheet propagation

Presented optical configurations were used to determine the quality of the laser beam before being used for the LII/LIF techniques. To have information on the width of different generated laser sheets, lenses used for the sheet generator were moved from the focal point (X= 0 mm) to the extremities (X= + 50 and - 50 mm) on the propagation axis of the laser beam with a high precision manual translation stage.

The Gentec beam profiler was used to record 20 images that were subsequently averaged for each optical setting of the lenses in the established positions along the laser beam propagation axis. The obtained laser line sheets are approximated with a semi-top hat profile, as shown in Figure 2.13. The selected width was measured at the FWHM of the profile in the central part of the generated laser sheet. The height of the generated laser sheet is 10 cm. Just a few measurements scanned the height of the laser sheet to ensure that it was homogenous on the selected height, while the recorded measurements were performed in the central part of the laser sheet.

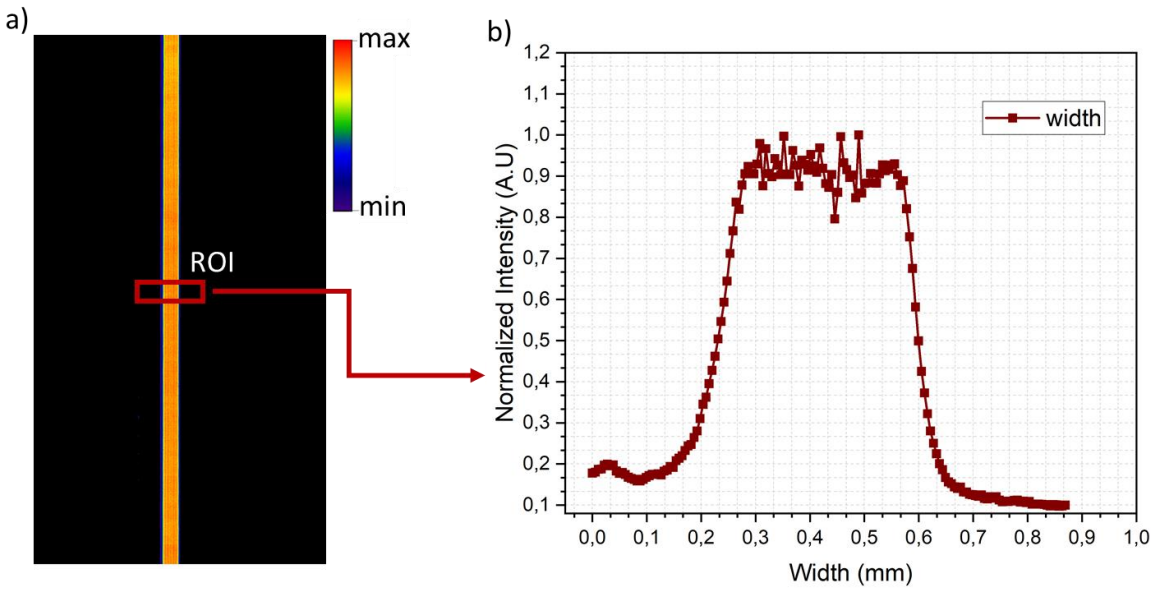

Figure 2.13 a) Averaged energy distribution of the laser beam, b) profile of the normalized energy distribution in the selected ROI.

Table 3 summarizes the selected optical laser sheet configurations (from C1 to C6) with the corresponding laser sheet widths for the three selected points in the propagation axis. In addition, a further in-depth analysis was performed for each laser sheet lenses configuration.

Configuration	f1 L1.C (mm)	f2 L2.C (mm)	f3 L3.C (mm)	f4 L2.B (mm)	w X = -50 mm	w X = 0 mm	w X = 50 mm
C1	-25.4	-	-	500	0.61	0.43	0.55
C2	-19	-	-	500	0.58	0.36	0.51
C3	**-25.4**	**200**	**1000**	-	**0.54**	**0.36**	**0.53**
C4	-19	200	1000	-	0.49	0.34	0.50
C5	-15	200	1000	-	0.71	0.46	0.76
C6	-25.4	200	500	-	0.8	0.20	0.83

Table 3 Six tested optical laser sheet configurations (C1-C6), f is focal length and w is laser sheet width.

By changing the transversal distance from the focal point to the extremities over 160 mm around the focal point, the results indicate a non-negligible effect of laser sheet divergence. Figure 2.14 shows that the laser sheet width changes from the focal point to the extremities of the propagation axis for the six selected configurations. For all tested laser sheet configurations, the laser sheet width increases from the focal point to the extremities of the propagation axis. The sixth configuration (C6) shows that the focal point of the laser sheet width is narrow (0.2 mm) for the optical configurations in which the focal length of the last lens is small (500 mm). These lens configurations are of use when analyzing a small region of interest. The high divergence at the extremity of the laser sheet compared to the other configurations indicates that these options are unsuitable for our application on the test rig, where the cross-section of the combustor is 100 mm. For configuration five (C5), the laser sheet width is 0.46 mm at the focal point and is large compared to the other studied configurations. This configuration can induce errors while studying the incandescence of soot particles

as it can highly affect the LII signal in the sampling volume due to laser fluence difference along the laser sheet propagation axis.

For our application on aeronautical test rigs, configurations three and four (C3 and C4) are the best choice due to the lower divergence towards the extremities of the laser propagation axis from the focal point.

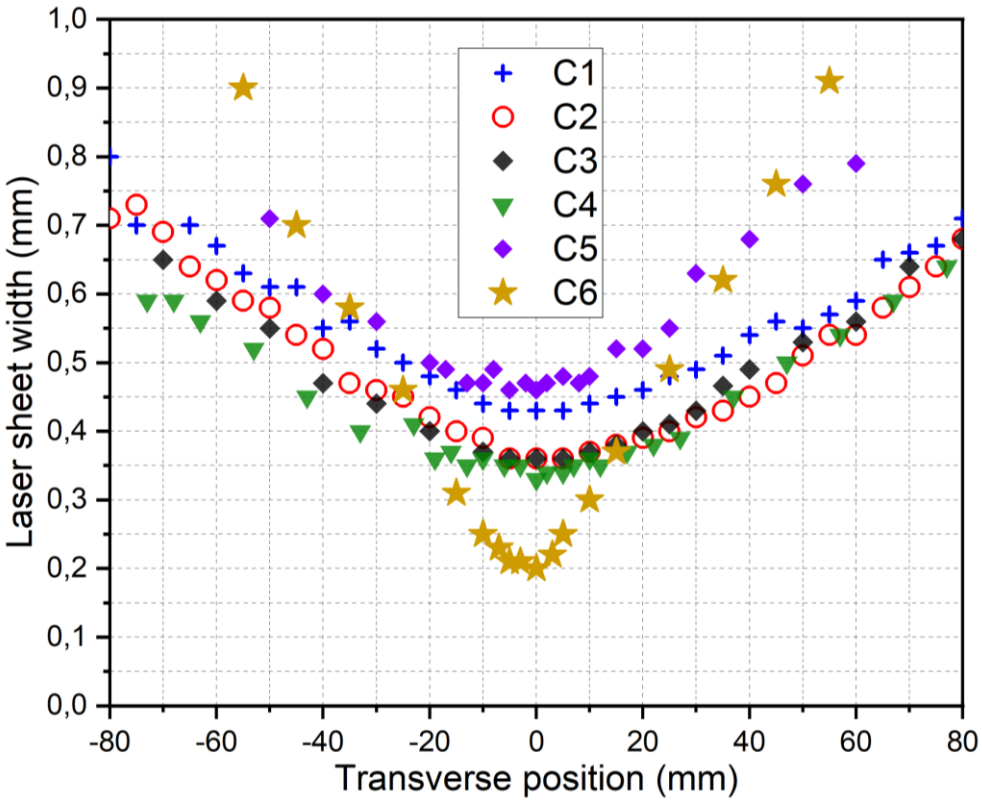

Figure 2.14 Evolution of laser sheet width of different tested configurations at different transversal positions. The obtained width is averaged over 20 laser pulses.

The selected laser sheet configuration was also applied to the IR laser beam (1064 nm), since this wavelength is used for LII. The divergence of the laser beam wavelength changes when doubling the frequency of the laser, and the obtained results confirm this observation, as shown in Figure 2.15. It is found that the green laser wavelength (532 nm) has a slightly smaller laser sheet width (W = 0.28 mm) at the focal point (x= 0 mm) compared to the one of a 1064 nm laser, which is 0.317 mm. However, the 532 nm laser is more divergent in the extremities of the laser sheet compared to the 1064 nm wavelength. Besides the advantage of using a 1064 nm laser for studying the incandescence of soot particles and discriminating the interfering signals, with this excitation wavelength, the laser sheet divergence is reduced compared to the visible wavelength, as illustrated in Figure 2.15.

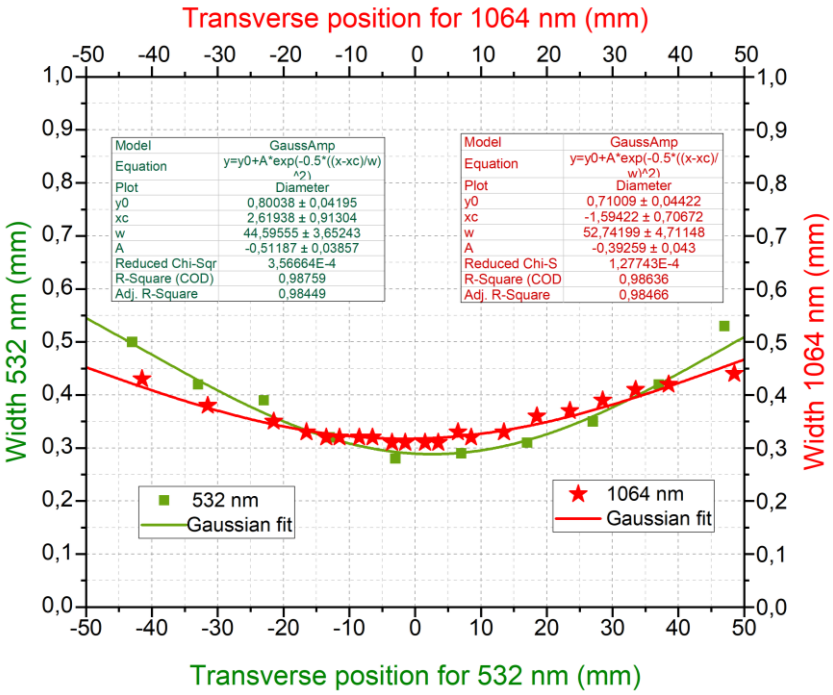

Figure 2.15 Comparison of the laser sheet width values for 1064 and 532 nm on the propagation axis with the associated Gaussian function fit and corresponding parameters.

The laser energy also changes with transversal position along the propagation axis of the laser sheet. Figure 2.16 illustrates that at the same position around the focal point of the laser sheet, the obtained energy at different transversal points changes. The displayed energy was measured on a 50 mm height of the laser sheet, corresponding to the diameter of the energy sensor detector. The laser energy is higher in the laser sheet focal point (0 mm) and decreases towards its extremities (+50 and -50 mm). The energy/pulse peak shows a Gaussian character of the laser sheet. With this configuration, it is observed that the laser fluence in the focal point of the laser sheet is two times higher than the value on the extremities of the laser sheet. These values impact the LII/LIF signals differently because a different phenomenon is at the basis of each technique. This consideration must be considered when trying to calibrate the LII signal into the soot volume fraction since the relationship between the LII signal and the soot volume fraction is not linear.

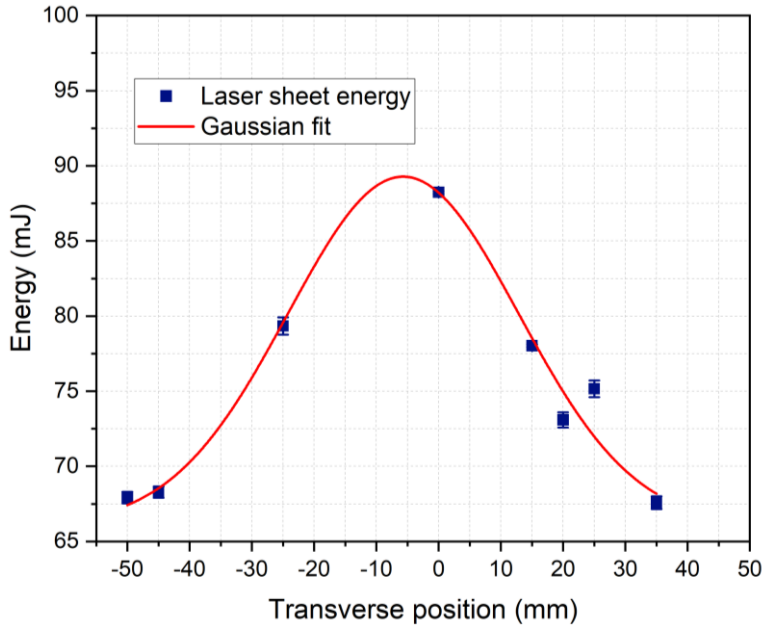

Figure 2.16 Measured energy/pulse corresponding to 50 mm height and the associated width from Figure 2.15 for different transversal axial positions. The excitation wavelength is 1064 nm.

2.4.3 LII and LIF variation with the laser sheet propagation axis

After characterizing the parameters (width and energy/pulse) of the laser sheet on a propagation distance of 10 cm around the focal point, the main objective is to investigate the evolution of the LII and LIF signals at different locations in the laser sheet. The CH_4/air laminar diffusion flame was used for this experiment, as displayed in Figure 2.13. The laser beam profiler was replaced with the intensified sCMOS camera to detect the LII and LIF signals. The intensified camera was equipped with a binocular system that split the detector into two, allowing the detection of induced signals at two wavelengths simultaneously. Various sets of filters were placed in front of the image doubler[214]. The power meter monitored the laser energy during the measurement on the side of the flame, while the energy at each location on the laser sheet was measured without the flame. The laser sheet generator was translated on the axis of propagation of the laser beam for measuring induced signals at different positions in the laser sheet.

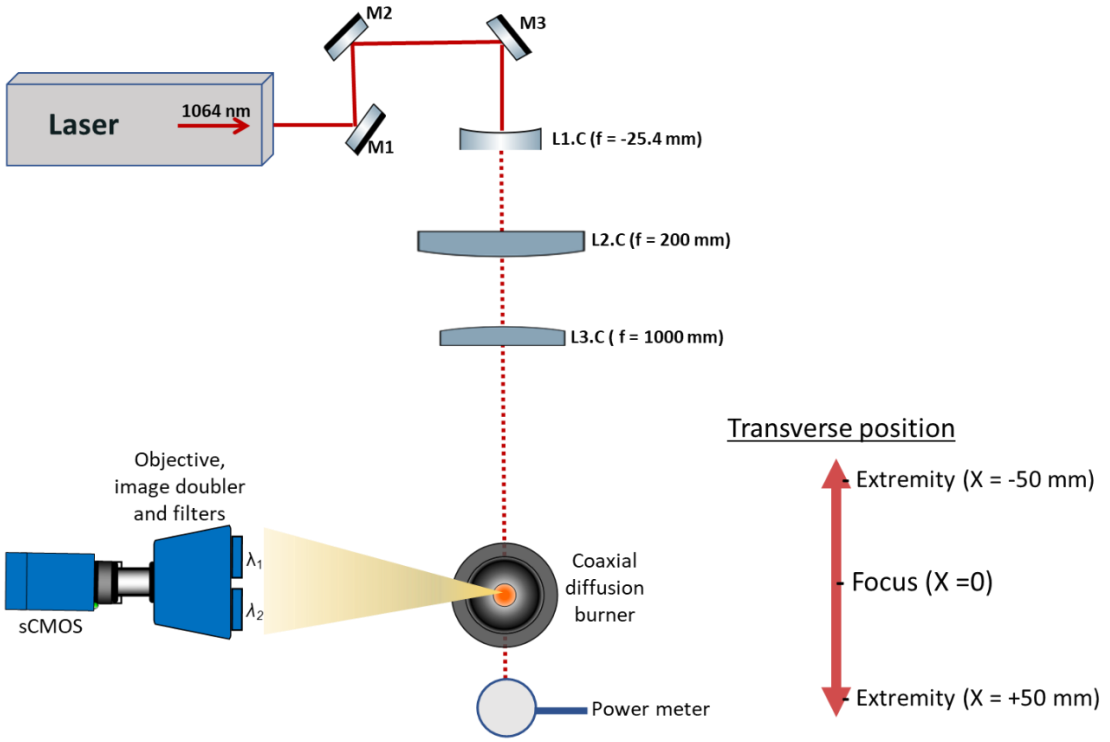

Figure 2.17 Schematic representation of the optical setup used to study the effect of the laser sheet divergence on the LII/LIF signals.

2.4.3.1 Variation of the LII signal

Firstly, the effect of laser fluence on the LII signal (1064 nm inducing wavelength) was evaluated at different axial positions. Figure 2.18 b, shows the measured variation of the LII signal for various laser fluences at the laser sheet focus (0 mm) to the 50 mm extremity of the laser sheet.

When comparing the LII signal in the focal point with the signal on the extremity of the laser sheet for various fluence values, the observed LII signals vary with the spatial location on the propagation axis, as obtained in Figure 2.18. At higher laser fluence after the peak of the LII signal (soot sublimation threshold), when moving away from the laser sheet focal point, the incandescence signal increases. This phenomenon can be due to the expansion of the laser sheet or the increased sampling volume. This observation was also observed in the study of Shaddix et al. [213]. Where they found that, for lower laser fluence, before the initial peak of the LII signal, moving away from the laser sheet focal point results in a lower LII signal due to the lower local fluence, such that the soot particles are heated to a lower temperature and emit less signal. The study of Smith et al. [215] also showed that the LII generation for the Gaussian sheet is relatively constant with the fluence level; once a suitable level has been reached, if the fluence at the focal point is high enough, moving away from the focal point will result in more significant LII signal, as a broader region of soot is heated by the laser pulse and therefore contributing to increased LII signal. For the LII detected at 450 nm, the signal obtained in the focal point reaches a plateau due to sublimation, after which it decreases and slightly increases while the laser fluence increases to 0.8 J/cm^2. This observation can be due to the fact that in the focal point, the soot starts to evaporate after 0.4 J/cm^2 and what is observed is the interference of the background from the Swan carbon signals.

By changing the LII detection wavelength to 650 nm, a similar behavior of LII obtained at 450 nm was observed. Still, in the case of laser sheet focus, the LII signal at the plateau region decreased slightly after reaching the sublimation point. This is due to the reduced C_2 Swan band background that is not well detected in the near-infrared domain.

In Figure 2.18, it is worth noticing that the obtained LII signals are noisy due to the jitter of the used system, which is higher than 10 ns. A system from LaVision was used for these first measurements and it was concluded that prompt detection plays an essential role in detecting LII and LIF signals. The detection system was changed for further experiments with an equivalent camera that did not require a PTU (programmable timing unit) synchronizing unit for the camera.

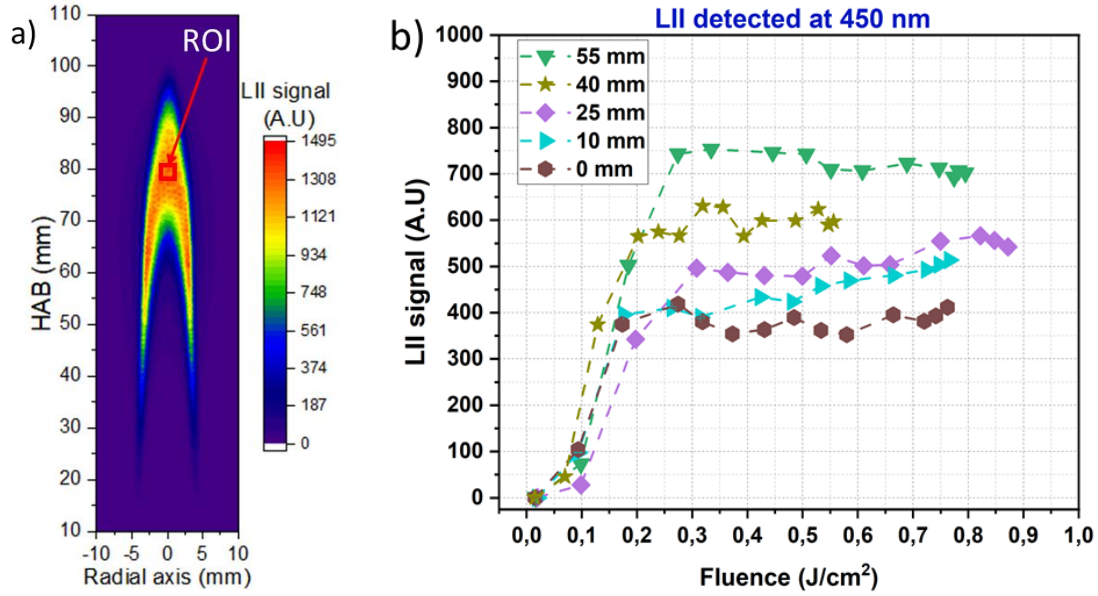

Figure 2.18 a) Averaged LII signal map detected at 450 nm in the focal point of the laser sheet (X= 0 mm). The underlined ROI represents the averaged intensity at HAB= 80 mm, used to determine the fluence curve represented in b. The averaged signal map was obtained over 100 images. b) Variation of LII signal in function with laser fluences at different transversal position axis; the signals were recorded at prompt detection.

The observed behavior of the LII signal after reaching the sublimation point was also described in Bodh and Bengtsson [216]. They found that with an extended laser sheet, the signal should increase up to the sublimation point, decrease slightly around 30% from the peak of LII, and start to increase again on the plateau region. After the sublimation, high laser fluence induces Swan carbon and other organic molecules, and LII interferes with other species.

Figure 2.19 shows the evolution of the LII signal at different heights above the burner at different transversal positions (X= 0 and +50 mm). The signal profiles are taken in the centerline of the flame by taking the region of interest of a square of 8 pixels. The LII signal started to appear at the HAB of 38 mm; from that height, up to 65 mm is supposed to be the region with primary soot particles. The maximum LII signal was obtained in the 72 - 84 mm HAB range, a region that contains mature soot. The increase of LII signal observed on the extremity (X = +50 mm) of laser sheet propagation is due to the increase of the sampling volume with respect to the focal point.

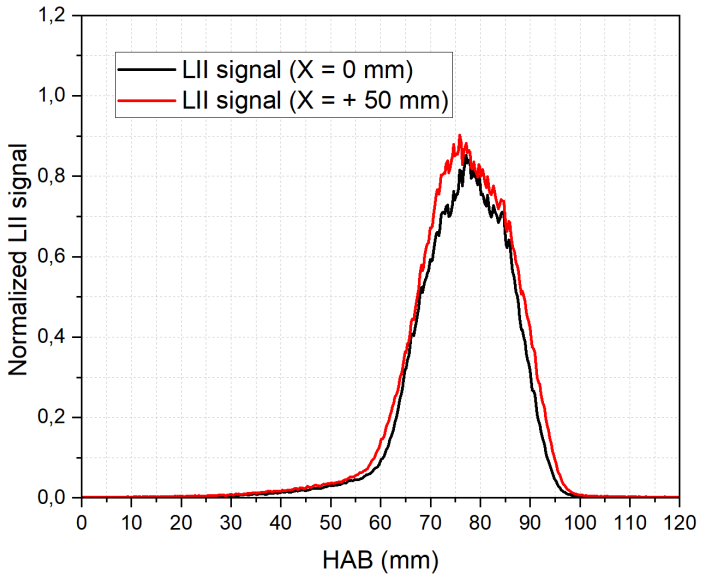

Figure 2.19 LII signal evolution, obtained in the centerline of the flame at a different height above the burner. The signal was recorded at the prompt detection of GW of 30 ns using a laser fluence of 0.2 J/cm^2. The signal corresponds to the profiles taken in the centerline of the flame.

From the dependence of the LII signal with the laser fluence, it is possible to calculate the variation of the LII signal with the position relative to the nominal laser sheet focal point. By using the same laser energy, the soot signal changed by a factor of two from the focal point to the extremities (+50 or -50 mm). This phenomenon observation has to be considered when analyzing the LII signal, particularly on the MICADO test rig where the ROI extends over a cross-section of 100 mm.

Based on the LII signal obtained in the focal point of the laser sheet, the correction factor needed to obtain the same LII signal away from the focal point can be calculated as follows:

$$\Gamma(x) = \frac{S_{LII}(x)}{S_{LII}\,(X = 0)} \qquad \text{Equation 2.36}$$

Where $S_{LII}(x)$ is the LII signal obtained at a given transversal position (mm) from the focal point and $S_{LII}\,(X = 0)$ is the LII signal obtained in the focal point (0 mm) of the laser sheet. This correction factor estimates the correct LII obtained signal when the laser sheet passes through the extended analysis volume. Figure 2.20 shows the evolution of the LII signal at different transversal positions for four values of the laser energy/pulse. The needed correction factor for the LII signal obtained near the focal point is small compared to the correction factor obtained at the far extremities. By changing the laser energy, there is a non-symmetric change in the needed correction factor. An insignificant change was observed in the correction factor by changing the LII detection wavelength from 650 nm to 450 nm.

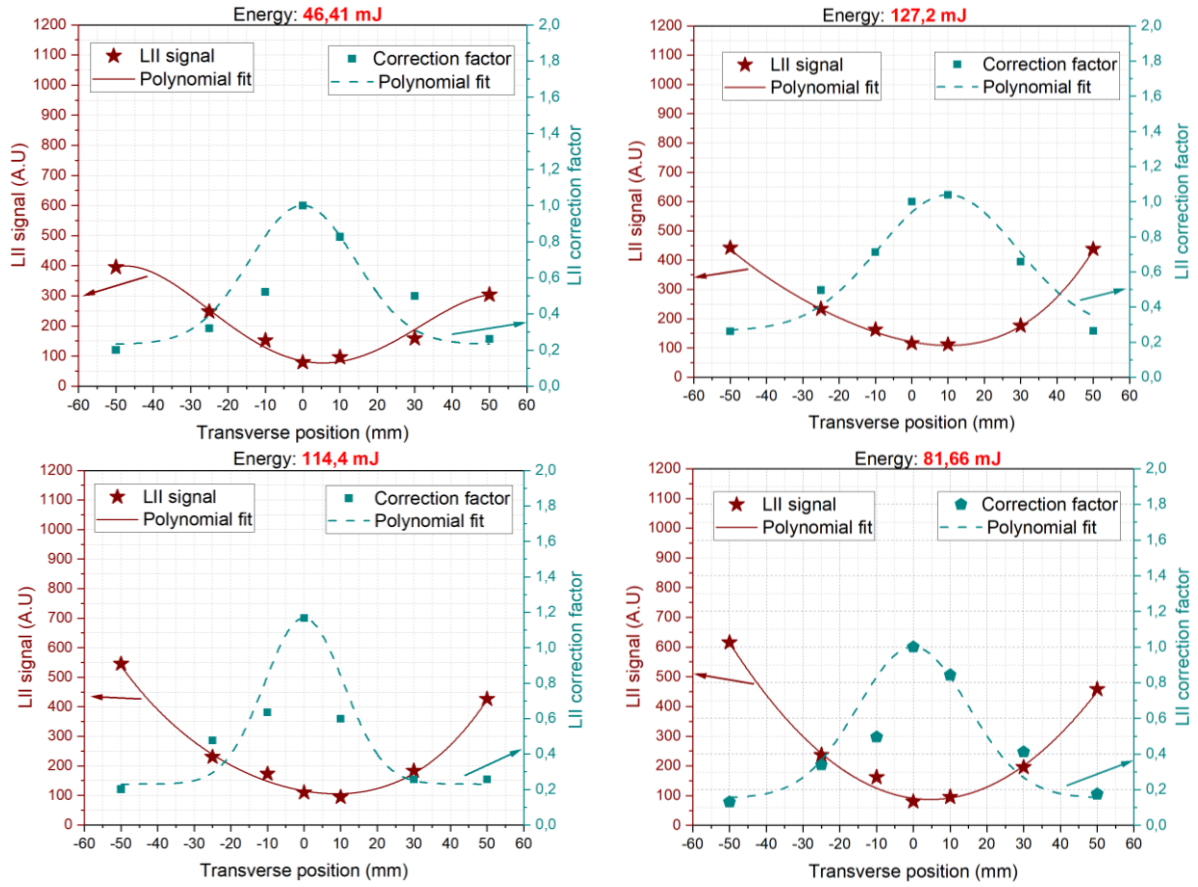

Figure 2.20 LII signals and their corresponding correction factor were obtained using different laser energy in the selected points in the propagation direction of the laser sheet. The LII signal was detected at 650 nm. The signal corresponds to the averaged LII from the flame centerline at 80 mm HAB.

2.4.3.2 Variation of the LIF signal

For the measurement of the fluorescence of PAHs induced with visible light, the LIF signal was detected at two wavelengths, 450 and 580 nm, in prompt detection with a GW of 30 ns. In front of each detection wavelength, a Notch filter that cut the 532 nm radiation was added to avoid the interference of the soot-scattered signal with the LIF signal. The selected laser fluence is 37.98 mJ/cm^2. With a laser of 532 nm, it is possible to activate the LII signal as well after a certain threshold. Therefore, tests were performed by delaying the detection of the camera to determine the low fluence mode, in which the LII signal was not induced with 532 nm. Figure 2.21 illustrates the evolution of the visible-induced fluorescence signal at different HAB. In the centerline of the flame, the LIF signal starts to be activated at the HAB of 52 mm and peaks at 65 mm. The signal disappeared after reaching the HAB of 77 mm. Some signal appeared at the flame tip in the oxidized soot region. This signal is attributed to some LII interference since removing it entirely with this laser fluence is impossible. For the edges of the flame, the fluorescence signal started to appear at the HAB of 22 mm and the maximum was recorded at the HAB of 42 mm and disappeared at the HAB of 66 mm.

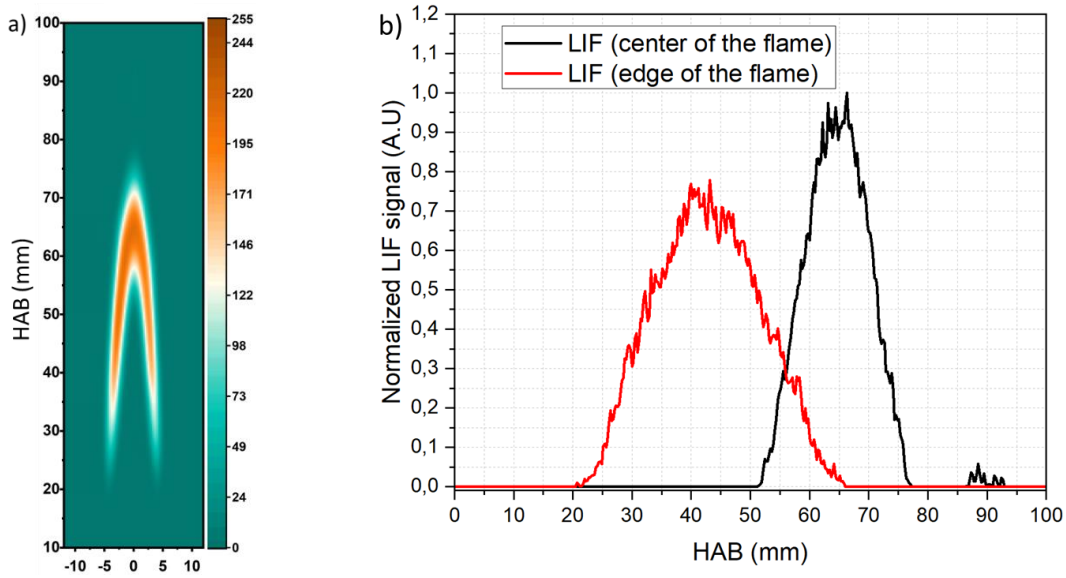

Figure 2.21 a) Vis-LIF map detected at 580 nm, b) Evolution profile of normalized LIF signal detected on the left edge and centerline of the flame. The signal was recorded at the prompt detection of GW of 30 ns.

The laser sheet divergence was also tested on LIF measurements, the Equation 2.36 is used for calculating the LII correction factor, where also used for the LIF signal. Figure 2.22 shows the evolution of the LIF signal detected at 450 and 650 nm wavelengths and their corresponding correction factor. For both wavelengths, the LIF signal is lower in the focal point of the laser sheet and higher in the extremities of the laser sheet. This increase can be based on the analysis volume; in the focal point (0 mm), the laser sheet is small, leading to a lower quantity of sampled PAHs. Moving away from the focal point (+50 or -50 mm), increases the analysis volume, which leads to a higher LIF signal than the one detected at X=0 mm. The signal detected at anti-Stokes detection (450 nm) was higher than at Stokes detection (650 nm). Most of the time LIF signal is higher in Stokes detection mode, but this difference can be caused by the camera's quantum efficiency, which is decreasing towards IR. The observed difference indicates having different PAHs that participate in LIF detected at 450 nm and the one detected at 650 nm. A ratio between the LIF detected on the edges of the laser sheet and the focal point at the two wavelengths is a good indicator that LIF detected at different wavelengths comes from various classes of aromatic compounds.

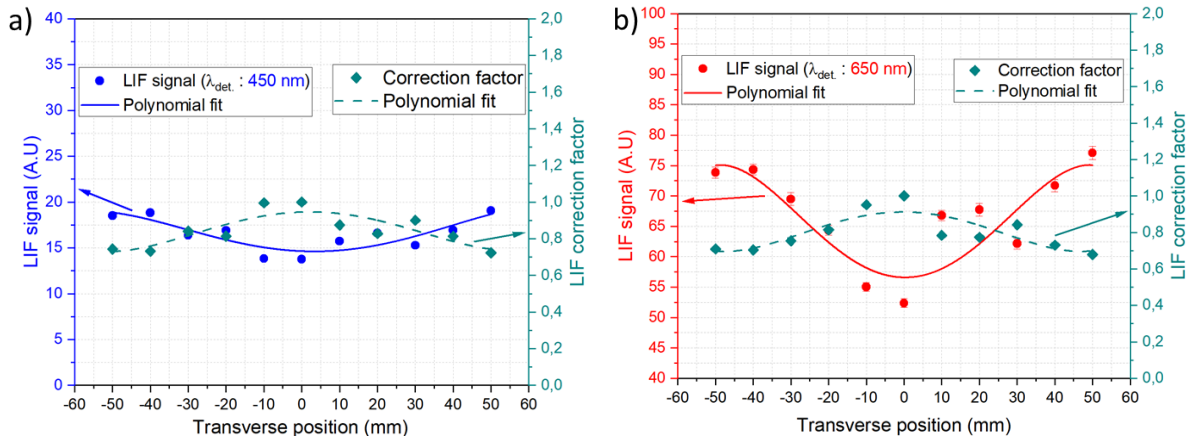

Figure 2.22 Evolution of PAHs fluorescence at different transversal positions detected at two different wavelengths. The presented signal corresponds to the ROI of 8 pixels square averaged intensity in the centerline of the flame at the HAB of 66 mm.

2.4.4 Summary of the subchapter

An in-depth characterization of the laser sheet is essential as the sheet divergence can affect the Incandescence and Fluorescence signal. For this reason, this subchapter investigated the effect of laser sheet expansion on the LII and LIF signals. A couple of laser sheet generator configurations were studied to see the effect of used optical lenses on the laser sheet width on a specific propagation distance (±50 mm) from the focal point. All results showed that the laser sheet width increased by moving from the focal point to the extremities of the laser sheet propagation. From all tested laser sheet configurations, a set of one negative lens (f1= -25.4 mm) and two positive lenses (f2= 200 mm and f3 = 1000 mm) was chosen as it provides a laser sheet with a size that fits the need of our measurement applied on the aeronautical combustor and the lowest divergence from the focal point. The effect of laser excitation wavelength on sheet divergence was also discussed, and it was observed that the laser exciting in the visible domain (532 nm) has a slightly higher divergence compared to the IR laser (1064 nm).

The variation of the LII signal as a function of the laser sheet position relative to its focal point was also investigated. The soot particles were induced by a laser exciting at 1064 nm and were detected at 450 and 650 nm. The obtained fluence curves show that the LII signal increases as the fluence increases until a plateau region (sublimation point) and the LII signal increases from the focal point (X=0 mm) towards the extremities of laser sheet propagation (X = ±50 mm). The increase of the LII signal on the laser sheet extremities is due to the increase in the sampling volume. After all, a correction factor is proposed for correcting the LII signal detected along the 100 mm propagation axis of the laser sheet. The signal change due to the laser sheet divergence can induce the error in calculating effective soot temperature and quantifying LII signal into soot volume fraction. Further details on the effect of laser sheet divergence on effective soot temperature are discussed in chapter 2.5.7.

For LIF, the PAHs were excited at 532 nm and detected at 450 and 580 nm. The obtained LIF signal showed that based on the detection wavelength, different PAH classes are detected. The fluorescence signal detected at 650 nm (Stokes detection) has a higher contribution compared to the

one detected at 450 nm (anti-Stokes detection) at the selected HAB of 66 mm. Based on the detection wavelength, different correction factors were proposed and this can be associated with the efficiency of LIF detection before and after the excitation wavelength. A nonlinear correlation was observed between the correction factor and the sampling volume variation used for the LIF signal detection, as at 650 nm, a slightly higher correction factor is needed compared to the signal detected at 450 nm. This can be based on the absorption/de-excitation processes taking place during LIF at this ROI into the flame, the gas phase concentration and temperature. The main conclusion is that caution has to be paid when applying a correction factor for fluorescence measurements, as the correction factor does not vary linearly with the sampling position and is strongly dependent on various parameters characteristic of the ROI. This criterion is not respected by most of the commercial setups for LIF. This experiment also demonstrates that 532 nm excitation for LII, with anti-Stokes detection, is not suitable for combustion-related experiments due to the interference of the anti-Stokes fluorescence, which is considered negligible in many studies.

2.5 QUANTIFICATION OF LASER INDUCED INCANDESCENCE SIGNAL INTO SOOT VOLUME FRACTION

This subchapter focuses on the methodology and steps used to quantify the LII signal into soot volume fraction (f_v). First, a priori information about the soot refractive index function $E_m(\lambda,T)$ and the effective temperature (T_{eff}) has to be determined to convert the LII signal (raw recorded data) into f_v with reasonable accuracy. Multi-wavelength optical pyrometry or 2C-LII is a common measurement technique used to obtain the T_{eff} of soot particles and the soot mass concentration or volume fraction when a calibrated optical chain with a known spectral radiance is used. Different research groups used this technique for quantifying LII signals into soot volume fractions [191,209,217,218]. Despite this volume of research, it is acknowledged that 2C-LII has some technical points that need to be clarified and studied to reduce the accuracy of the calibration step. With this in mind, two LII measurement configurations, such as image and spectral modes, are tested and described in this work while focusing on the steps used to obtain the T_{eff} of soot. CH_4/air equivalent flame temperature-specific parameters are determined from the self-emission of soot particles and the H_2O water vapors. Additional information about the flame environment can provide valuable insight into the processes responsible for soot production. Flame characteristic parameters are equally crucial for the interpretation of LII-detected signals. Finally, the obtained soot volume fraction is discussed for LII image and spectral configurations.

2.5.1 Two-color laser-induced incandescence (2C-LII)

Two-color laser-induced incandescence (2C-LII), also known as auto-compensating LII, is a measurement technique commonly used to calculate the effective soot temperature [219]. The LII signal is detected at two or more wavelengths (broadband) and the ratio between detected signals is used to determine the T_{eff} of soot during a short time. Depending on the T_{eff} of soot, the absolute soot incandescence emission and the shape of the emission spectrum can change. Assuming that the absolute spectral radiance of soot is quantifiable, it is possible to calculate the effective temperature of soot particles in the sampling volume by measuring the irradiance at two or more wavelengths [176]. Assuming that the absolute spectral radiance of soot is quantifiable, it is possible to calculate the effective temperature of soot particles in the sampling volume by making the ratio of soot incandescence signal (Equation 2.33 in subchapter 2.2.1) detected at two or more wavelengths. To obtain T_{eff} of soot, it is necessary to assume that the condition from Equation 2.37 is accomplished.

$$\exp\left(\frac{hc}{\lambda\, k_B T_{(t)}}\right) >> 1 \qquad \text{Equation 2.37}$$

For example, a black body with $\exp(hc/\lambda\, k_B T_{(t)}) > 170$ for wavelengths in the range of 400 - 700 nm, T is between 1500 to 4000 K [176]. By simplifying this exponential ratio of Equation 2.37 and rearranging different parameters, the final soot effective temperature is expressed as:

$$T_{eff}\,(Em,\lambda) = \frac{hc}{k}\frac{\left(\frac{1}{\lambda_1}-\frac{1}{\lambda_2}\right)}{\ln\left(\frac{E_m(\lambda_1)}{E_m(\lambda_2)}\frac{S_{LII}(\lambda_2)}{S_{LII}(\lambda_1)}\left(\frac{\lambda_2}{\lambda_1}\right)^6\right)} \qquad \text{Equation 2.38}$$

The effective soot temperature depends primarily on soot refractive index function $E_m(\lambda)$ and detection wavelength range; these factors are described in section 2.5.5. Therefore, the LII signal

detected at these two wavelengths must be corrected by a transfer function of the detection system obtained from a calibrated emission source.

2.5.2 Comparison of imaging and spectral configuration mode – advantages and disadvantages of selected optical configurations

In this chapter, a focus is made on the development of the LII signal based on the sampling volume and detection measurements system. This is because different configurations can induce specific errors inherent to the laser beam/sheet shape and detection systems.

Imaging and spectral configurations of LII are classified depending on the sampling volume (laser sheet or beam) and the detection of the induced signals (camera or spectrograph with camera).

2.5.2.1 Sampling volume for imaging and spectral configurations of LII

In this study, imaging LII configuration corresponds to measurements performed with an extended laser sheet. The advantage of using an extended laser sheet is that it has a large sampling volume, which is suitable for obtaining a soot map for the corresponding ROI. Nevertheless, such configuration measurements do not allow the heating of soot particles at the same temperature overall sampling volume. These factors can induce errors in quantifying LII into soot volume fraction. Another source of error is the E_m (λ), which changes with the wavelength domain and soot properties [129,220–222]. It is difficulty to associate the types of soot, such as mature or incipient, corresponding to a specific ROI from the sampling volume in a turbulent environment.

The second configuration used is spectral LII. The reduced laser beam was shaped into a top-hat profile with this mode. The advantage of this configuration is that the laser beam divergence is less significant due to the reduced number of optics used to shape the laser beam. Therefore, deducing the optical properties of soot particles can be accessible with minor errors compared to the extended laser sheet. The disadvantage of this configuration is that it has a small sampling volume which is not advantageous to implement in test rig environments where there is a limited time for the measurement and no time to scan the ROI. Constructing a soot map in turbulent combustion conditions with point measurements can be challenging.

Figure 2.23 shows the differences in the sampling volume between the two configurations: a) represents the extended laser sheet measurement where the volume of the analysis is [L=100 × W_0=0.35 × l=100] mm^3 and b) represents the reduced laser beam that generated a volume of analysis of [L=100 × d_{01}=1.04 × d_{02}=1.04] mm^3.

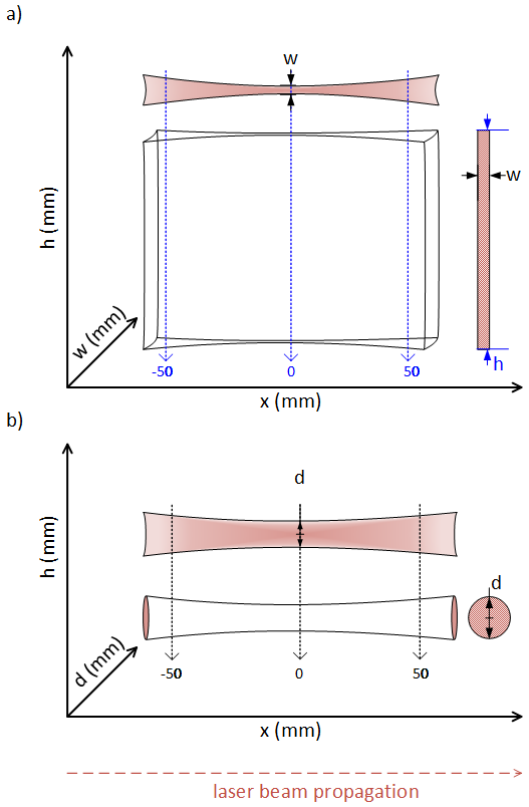

Figure 2.23 Schematic laser sheet/beam mapping configurations: a) extended laser sheet configuration used in imaging mode b) top-hat laser beam configuration used for spectral mode.

2.5.2.2 Detection for imaging and spectral configurations of LII

The first detection configuration (**image mode**), including measurements performed with an extended laser sheet, consists of an intensified camera coupled with Canon lenses, a binocular system and optical filters. This configuration has the advantage of detecting the entire volume illuminated by the laser sheet, but it has the disadvantage of only detecting the LII signal at two wavelength domains.

The second detection configuration (**spectral mode**) consists of a spectrometer coupled with an intensified camera and lenses for light collection. This optical configuration detects the broadband emitted signal for a reduced ROI delimited by the laser beam.

2.5.3 Experimental setup

This section gives details of the experimental setup used for the 2C-LII calibration method applied to CH_4/air diffusion flame. The flame used in this study is the same flame described in previous studies [223,224] and has the same configuration as the one used for laser sheet characterization. The experimental configuration (laser, cameras and spectrographs) was changed due to the jitter of the first implemented configuration presented in subchapter 2.3.

2.5.3.1 Excitation source and laser sheet

The excitation source is a Nd:YAG pulsed laser (Quantel Q-Smart) with a pulse duration of 6 ns at full-width half maximum (FWHM). The repetition rate is 10 Hz with maximum energy of 850 mJ/pulse at 1064 nm. This laser is equipped with a frequency doubling module (2ω) to generate 532 nm. As established with the previous configuration (Section 2.3.4), 1064 nm was used to induce LII and 532 nm was used to induce LIF of PAHs. In addition, a beam attenuation module (BAM) was added to control the laser energy. Laser beam/sheet size was measured by a beam profiler camera positioned at the center of the injector before each measurement (the same as described in the previous section). The laser energy was monitored with a power meter, as described in subchapter 2.4. The laser sheet and beam were shaped on the two established configurations as follows:

For extended laser sheet configuration (Figure 2.26), the 1064 nm laser beam is directed on the optical path with a set of mirrors and lenses to create a vertical laser sheet of h=100 × W=0.35 × l=100 mm^3. First, the laser sheet was generated with the C3-lenses configuration as selected in subchapter 2.4. This configuration of lenses consists of a negative cylindrical lens (f = - 25.4 mm) and two positive cylindrical lenses (f_1 = 200 and f_2 = 1000 mm); the configuration was chosen to minimize the divergence of the laser sheet. The laser fluence in the focal point (W_0) is 177 mJ/cm^2 and is selected because this value represents the sublimation threshold of the LII for mature soot detected in the CH_4/air flame.

For the spectral configuration (Figure 2.25), mirrors are used to direct the laser beam through a pinhole with a diameter of 1 mm. Afterward, the beam was shaped into a circular top-hat profile of 1.04 mm diameter at FWHM using a diaphragm positioned at 2f (40 cm) before a spherical lens (f= 20 cm). The lenses are placed at two times the focal length distance(2f) between the pinhole and the burner to avoid diffraction patterns produced by the Gaussian beam [223,224]. In imaging mode, the formed laser sheet scans the whole height of the flame at once, whereas, in spectral mode, the laser beam scans the flame at each 2 mm.

2.5.3.2 Detection system

A 16-bit intensified PIMAX-IV (GEN III intensifier) camera with maximum quantum efficiency in visible to near IR (Annex 2), is used to detect the LII signal in the image mode configuration. This camera has an acquisition frequency of 3.33 Hz at full frame. The CCD detector contains a pixels array of 1024 × 1024. This camera was coupled with Canon lenses with a variable focal length between 28-300 mm. For detecting LII at two wavelengths, an image doubler system from LaVision is added in front of the lenses, allowing to capture two images at different wavelengths simultaneously. The LII/LIF signal was selected with ten nm bandwidth filters centered at 450, 580 and 650 nm. The filters were interchanged among them to detect LII or LIF at the three selected wavelengths. The selection of detection wavelengths has to be chosen wisely as they affect the final obtained LII signal.

The LII signal was recorded in prompt detection with a GW of 50 ns. Figure 2.24 shows the schematic representation of the entire experimental setup used for the imaging configuration. The setup was adapted to measure LIF of PAHs with 532 nm in the low laser fluence (30 mJ/cm^2) excitation regime to limit the activation of the LII signal. The lenses used in the first configuration (LII) were changed to coated lenses adapted to the visible domain. The fluorescence signal was detected at 450 and 580 nm with 10 nm bandwidth filters. In addition, a notch filter with OD7 that cuts 532 nm was added to remove soot scattering. The fluorescence was recorded with a GW of 30 ns. A series of 200

images were recorded on each measurement (LII/LIF). Fluorescence measurements were performed only in imaging configuration mode.

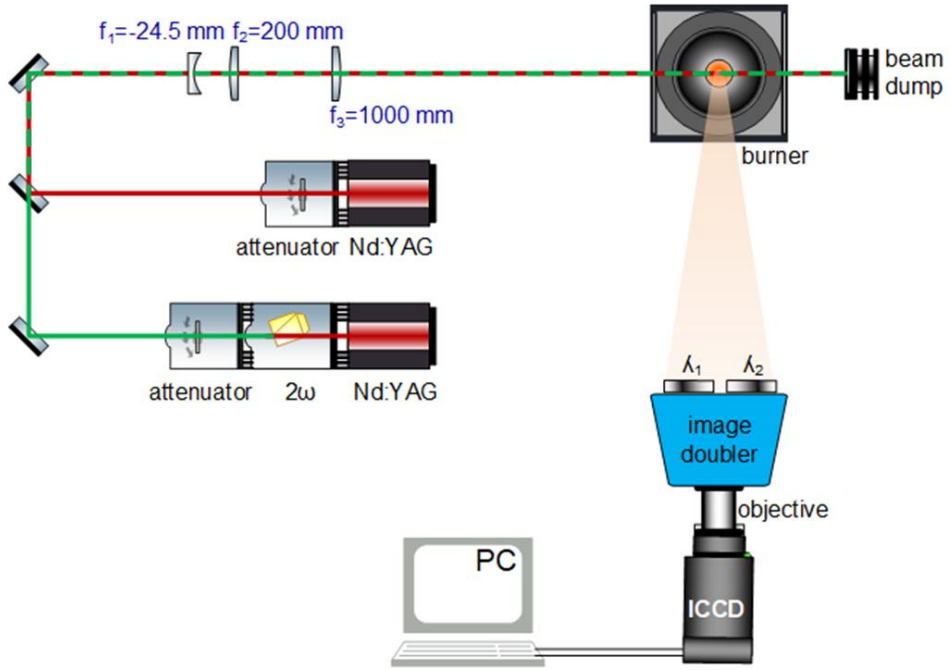

Figure 2.24 Schematic representation of the LII or LIF system implemented for the image mode measurements.

For LII measurement made in spectral configuration (Figure 2.24), the detection system used for imaging mode was replaced by an acquisition system placed at 90° with respect to the laser beam propagation axis through the flame. An achromatic lens doublet (f1 = 40 cm and f2 = 20 cm) is used to direct and focus the LII signal onto the slit of the spectrograph. Spectral LII images and flame emission were collected with a spectrograph with a focal distance of 30 cm. The entrance slit is adjustable between 12.5 and 2000 µm. In this study, the entrance slit was set at 1000 µm, the same as the height of the sampled volume (diameter of the laser beam) with the laser beam. The spectral resolution is defined by the opening of the slit together with the focal length of the spectrograph. Two diffraction gratings are used: the first is 150 groves/mm blazed at 400 nm and the second is 150 groves/mm, blazed at 680 nm. The diffraction gratings are mounted on a motorized turret, allowing the selection of the wavelength domain of interest for the measurement. The spectrograph has two outputs to collect the signal, from which one is dedicated to a photomultiplier tube (PMT) and the other to the intensified camera. In this case, the LII signal was recorded by a 16-bit intensified CCD camera (PiMAX II, GEN II intensifier (annex 2)) coupled to a spectrograph with a spectral detection range between 300 - 1500 nm. The LII signal was detected at prompt detection with a GW of 50 ns. Two series of 200 hundred images were recorded for each measurement. The first series contains LII and flame emissions signal and the second one contains only the flame emissions. Before each measurement, a dark image (background) was recorded.

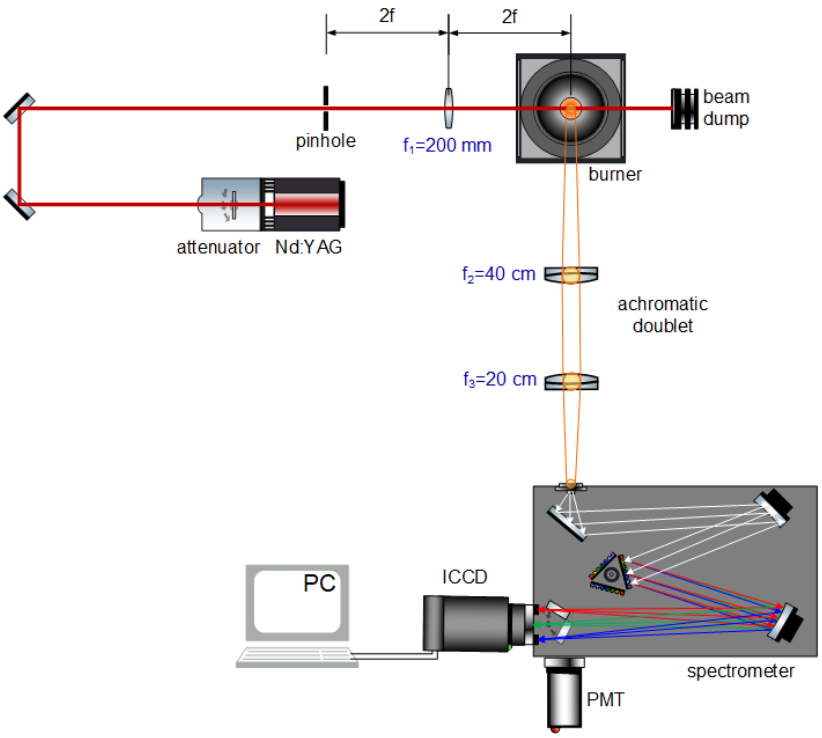

Figure 2.25 Schematic representation of the LII system implemented for LII spectral measurement mode.

Figure 2.26 shows the laser beam energy density distribution profile for a) the laser sheet configuration at W_0 position in the propagation axis and b) the laser beam in the focal point "0" as displayed in Figure 2.24.

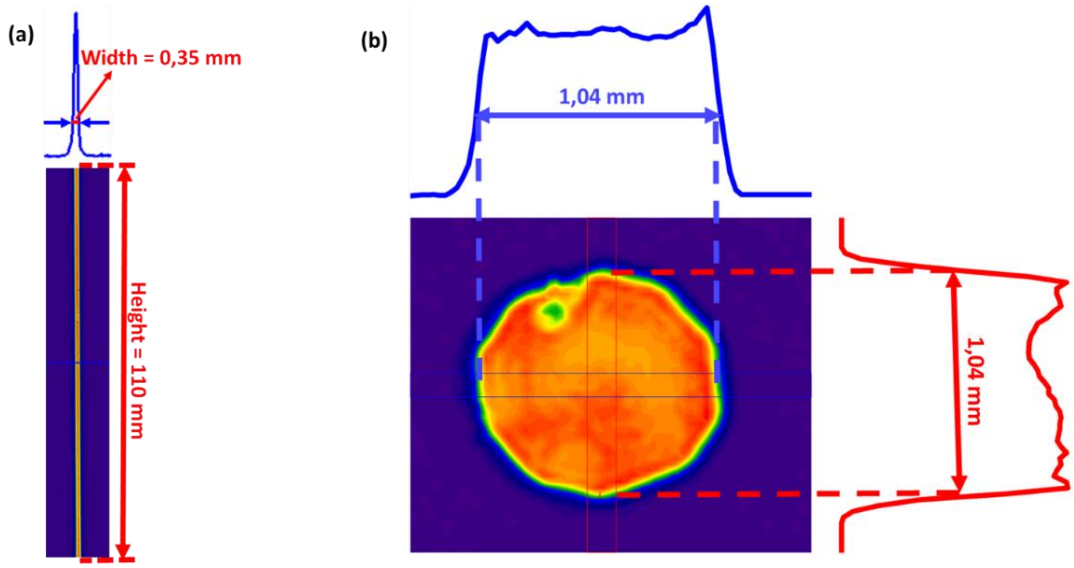

Figure 2.26 Energy density distribution profile generated with 1064 nm for the a) extended laser sheet used for imaging measurement configuration and b) circular laser beam used for spectral measurement configuration.

2.5.4 Calibrated optical sphere

The LII signal can be calibrated directly with a calibration source or indirectly via other techniques. Indirect calibration methods include external measurement techniques like line-of-sight attenuation (LOSA), gravimetric sampling, or cavity ring-down spectroscopy. These enumerated techniques have some drawbacks related to soot particle properties that vary with the combustion conditions, which therefore increase the uncertainty of the calibration method [224–227]. The 2C-LII method used in this study is calibrated with a known source of light. The working principle of this method consists in calibrating the detection system against a source with known irradiance [224].

In this study, to better interpret the obtained LII signal and convert it into soot volume fraction, it is necessary to determine and apply a correction factor (transfer function) to the optical response of the measurement system, which consists of two lenses, a spectrometer and an intensified camera for spectral measurements, and intensified camera coupled with lenses and image double for imaging measurements.

To do that, an integration sphere from Sphere-Optics CSTM-LR-6-M is used. The sphere is placed at the same position as the flame to respect the same optical path for the detection system used for LII measurements. The sphere consists of a lamp placed inside a cavity covered by a white Lambertian substrate. It emits black body-type radiation with a tunable temperature between 2000 and 3300 K by adjusting the voltage of the external power supply module. The same parameters used to record LII signals are used for recording the emitted light from the sphere. Figure 2.27 shows the optical setup for absolute light intensity calibration used for imaging and spectral measurements. The sphere emits a known irradiance (light flux/area) calibrated by NIST. The emitted irradiance at different settings of the voltage (temperature) is recorded by a spectrometer via an optical fiber coupled to the sphere. The setup was all calibrated as a unit with a source of known spectral irradiance. The calibration file is applied to any measurement of spectral irradiance made with this unit to convert the recorded signal with the spectrometer into spectral irradiance.

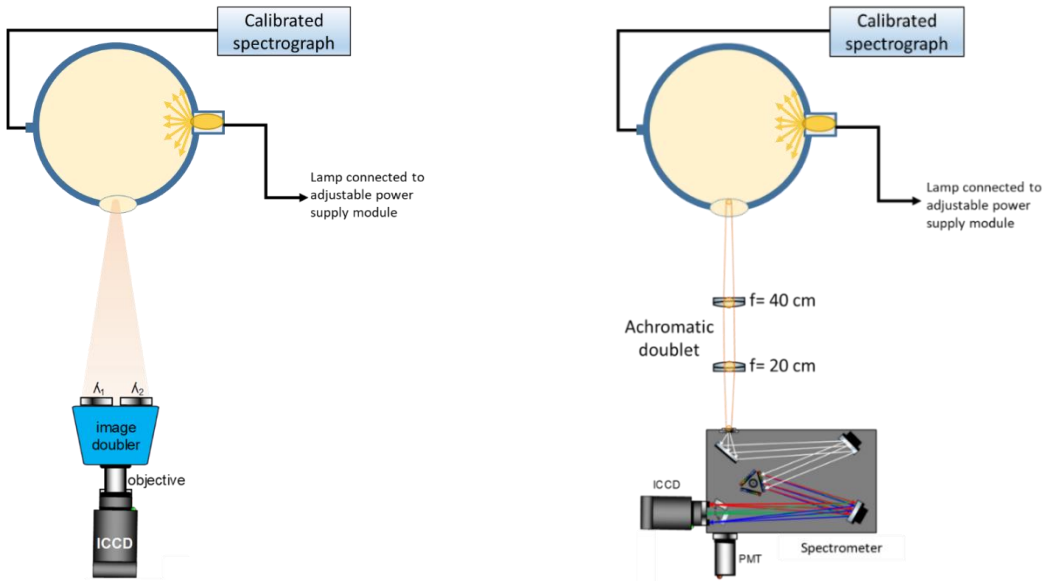

Figure 2.27 Optical configuration used to determine the optical response of the measurement, namely the transfer (T_f) function of the system.

The spectral irradiance of the sphere, taking into account the solid angle, depends on the detection wavelength used, and it can be expressed as:

$$R = \frac{2\pi hc^2}{\lambda_{em}^5}\left[\frac{1}{\exp\left(\frac{hc}{\lambda k_B T_{(t)}}\right)-1}\right]\frac{1}{2\pi}\Delta\lambda \qquad \text{Equation 2.39}$$

The irradiance is expressed in ($W.m^{-3}.Sr^{-1}$). Equation 2.40 looks almost the same as Equation 2.25. Figure 2.1 illustrates the emitted sphere signal in the wavelength range 360 nm - 1000 nm for a corresponding temperature of 2700 K. The temperature is tuned using an external power supply module connected to the lamp. After the calibration procedures, the transfer function of the detection system is calculated as the ratio between the signal obtained from the sphere during the experiment and the signal of reference. The equation for calculating the transfer function can be expressed as:

$$T_f = \frac{I_{exp}(\lambda)}{I_{ref}(\lambda)} \qquad \text{Equation 2.40}$$

Where T_f is the transfer function, $I_{exp}(\lambda)$ is the intensity measured during the experiment and $I_{ref}(\lambda)$ is the reference intensity given by the calibration sphere.

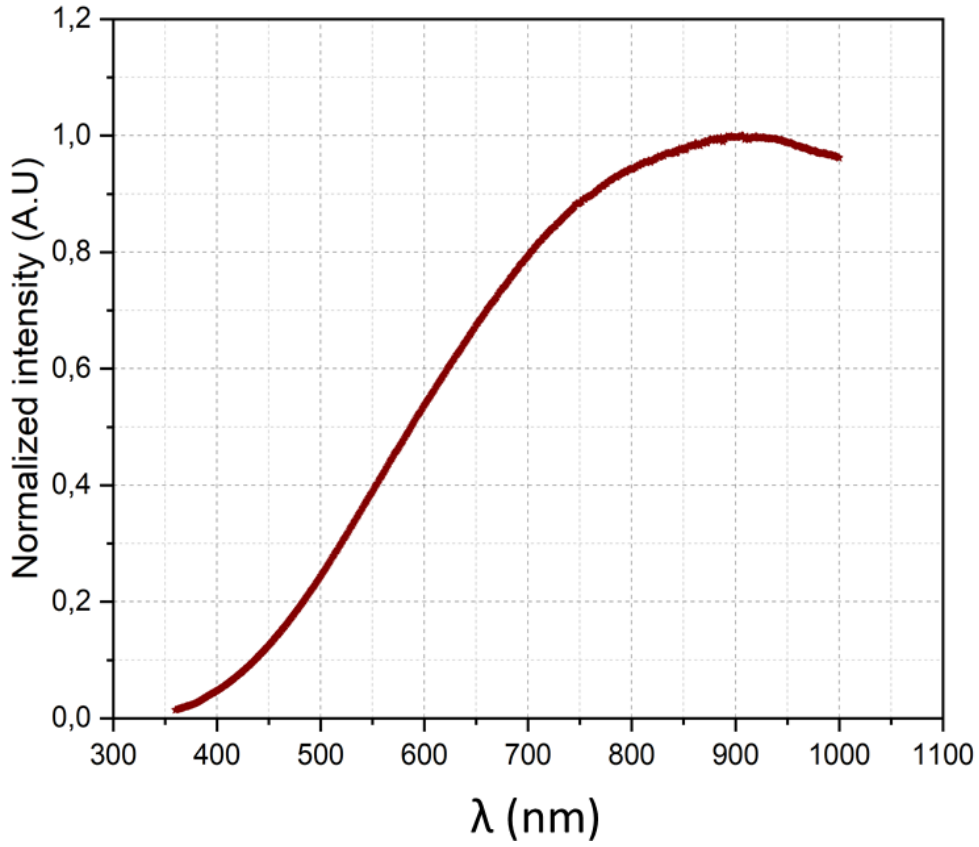

Figure 2.28 Evolution of emitted sphere intensity function of the wavelength. Emitted spectrum corresponds to the 2770 K temperature of the filament.

2.5.5 Results

This section describes the results obtained by the two measurement configurations of LII: image and spectral. In addition, soot effective temperature and volume fraction were derived.

2.5.5.1 Imaging measurements configuration

2.5.5.1.1 Fluence curves

A fluence curve represents the evolution of the LII signal as a function of the laser energy/pulse (fluence). This curve indicates the fluence threshold at which soot particles (at the given sampling conditions) start to sublime. It is crucial to determine the value of the laser fluence necessary to sublime the soot particles because this value may change with soot maturity [228], temperature and pressure [229]. The laser fluence that heats soot particles below their sublimation threshold varies from one flame to another and is influenced by the spatial homogeneity of the laser beam and its temporal profile. With a top-hat laser beam profile, the LII signal first reaches a peak, followed by a decrease in intensity with the laser fluence increase due to the soot evaporation.

Figure 2.29 shows the evolution of the LII map signal obtained in the CH_4/air laminar diffusion flame for 22 different laser fluence values. The LII is activated at the fluence of 68 mJ/cm^2, the intensity increases exponentially up to ≈ 250 mJ/cm^2 and after this fluence value, the LII signal reaches a plateau region. At lower fluence, the peak of LII intensity rises monotonically with the laser fluence as the particle temperature increases. For the LII configuration using 1064 nm inducing laser wavelength, it is recommended to use laser fluence values between 120 and 250 mJ/cm^2. The disadvantage of using these values of the laser fluence is mainly for the detection of small soot particles or incipient soot. Less energy is necessary for reaching the sublimation threshold of soot particles when using ultraviolet (UV) or visible (VIS) inducing wavelengths. The shape of the fluence curves is similar to the one obtained with IR-inducing wavelength. When using different excitation wavelengths (1064 nm, 532 nm or 266 nm), the fluence curves can help deduce soot absorption properties like Em [171]. The origin of the changing behavior in the fluence curves for different soot particles is partially understood [181,190,205]. These changes are related to variations of soot optical properties, morphology and structure, organic coating or local temperature variations in the sampling environment [230–232].

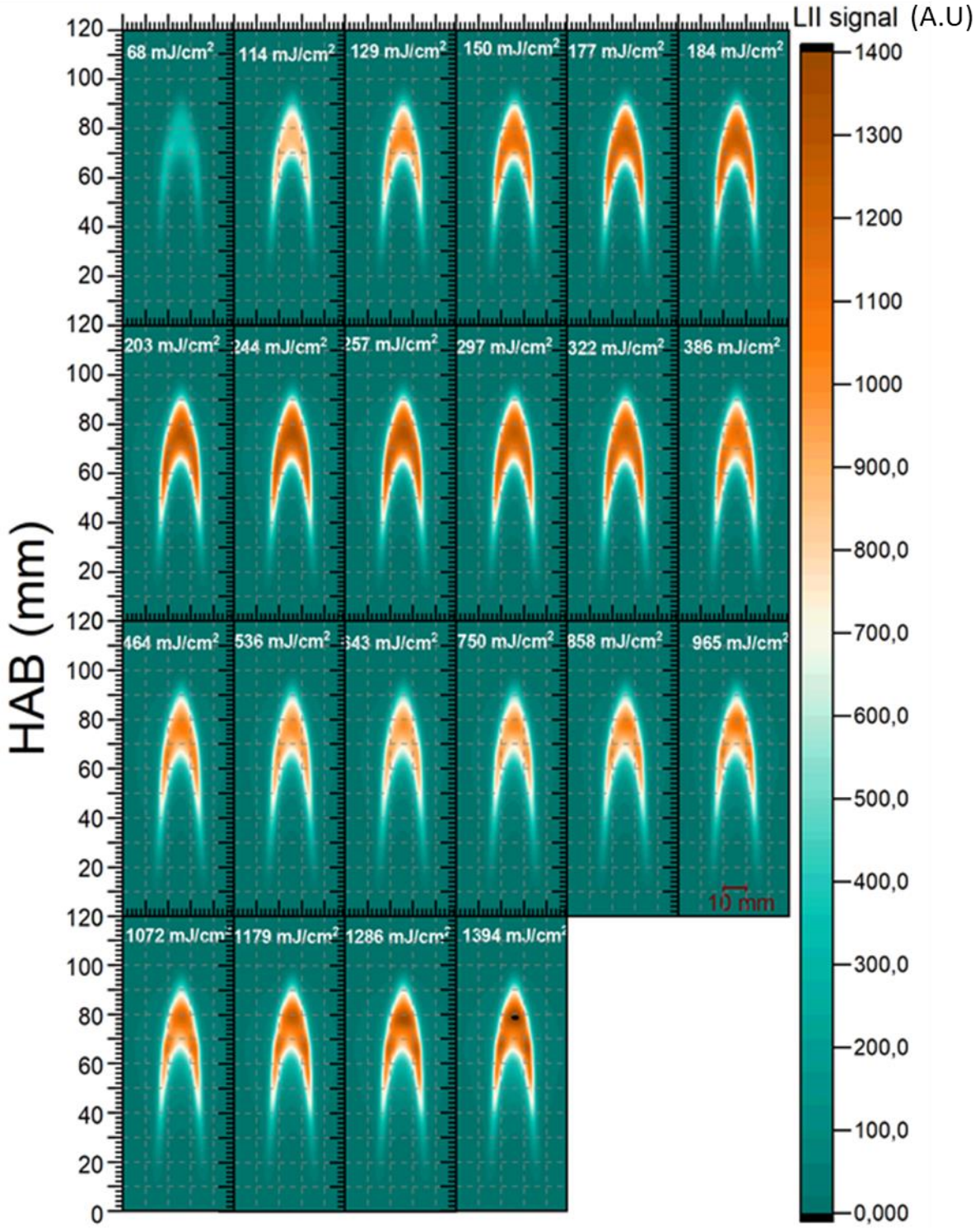

Figure 2.29 Soot maps obtained for the CH_4/air laminar diffusion flame in the focal point of the laser sheet. The maps represent the spatial evolution of the LII signal with the laser fluence. The fluence of 177 mJ/cm^2 was chosen for the experiments - the fluence before the sublimation point for mature soot.

For the fluence curves, small regions of interest are selected at different HAB of the flame. The HAB of 68 mm was chosen as considered representative of incipient soot particles, the HAB of 80 mm was chosen as it was estimated to be the region with mature soot and the HAB of 90 mm for oxidized

soot. Figure 2.30 illustrates the evolution of the LII signal with the laser fluences for the three selected HAB. It is observed that the sublimation point of mature soot is near 210 mJ/cm^2. After increasing the laser fluence beyond the sublimation point, soot evaporates and loses mass, and the LII signal decreases. After that decrease, at the fluence of 305 mJ/cm^2, LII reached a plateau region until the fluence of 750 mJ/cm^2. Then, the LII signal increased again with increasing fluence. This increase can be due to the interference of the incandescence signal with other evaporated organic compounds or C_2 Swan carbon bands.

On the other hand, incipient or primary particles need higher laser fluence to reach the sublimation point, the sublimation point is around 250 mJ/cm^2, and there is a shift of around 30 mJ/cm^2 compared to the sublimation point of mature soot. In the literature, excitation laser fluence within the plateau region has been preferred for soot volume fraction measurements to avoid laser attenuation or fluctuation; these measurements also provide information on incipient soot particles [233]. However, this method can induce errors as it sublimates mature soot particles, a process that is impossible to evaluate. In this study, a compromise was made between the necessary fluence for incipient soot and mature soot. A fluence of 177 mJ/cm^2 was chosen for all further measurements. This fluence avoids the sublimation of mature soot and induces LII signal from some nascent soot particles at the same time. Also, it is recommended to use this fluence if the results are compared with numerical models, as most models do not consider the sublimation process [233].

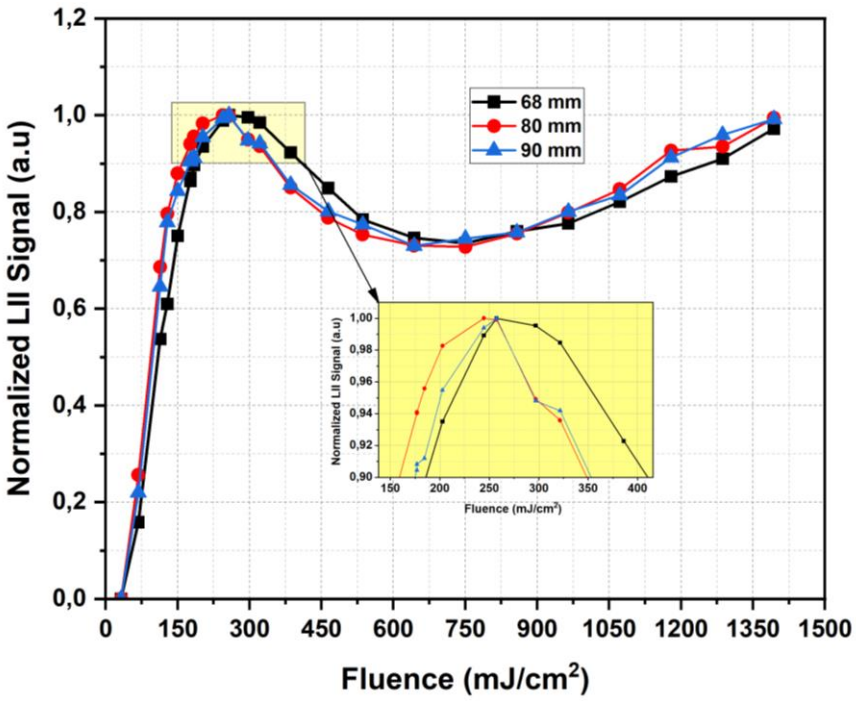

Figure 2.30 Normalized LII fluence curves selected in the center of the CH_4/air laminar diffusion flame for three HABs. Laser sheet measurements in the focal point of the laser sheet.

2.5.5.1.2 LII signal

Before recording the LII signal, the camera background (dark image) was recorded using the same exposure time and gain for recording the incandescence signal. The importance of that background is

to remove the electronic noise and intensity that is not due to the emitted signal. Most intensified cameras have a background level known as dark noise. In the flame, the Incandescence signal is recorded simultaneously with flame emission, and the second step consists of recording the flame emission that is subtracted from the raw incandescence signal. Attention has to be taken during the subtraction of flame emission because the background is already in the flame emission. As processing steps, it is possible to either subtract the background from the flame emission and raw LII signal or independently or subtract only flame emission directly from the raw incandescence signal. The response of the pixels for intensified camera technology is not homogeneous, especially with the aging of the detector. Therefore, a flat field correction (or white field correction) is needed to correct the response of the pixels on the sensor. This abnormality in different pixels' response can be due to: variable pixel gain, detector aging, vignetting and dust [234]. It is recommended to apply a flat field correction step when the quantification of the LII signal into soot volume fraction is performed. The image of a homogeneously white source (pannel) that illuminates the detector entirely is recorded for a flat field correction. The obtained LII image signal (after background subtraction) is divided by the flat field image for correction. Two hundred images were recorded for each LII measurement. Figure 2.31 resumes the steps implemented for LII image analysis and the corresponding flat field, flame emission and LII signal images.

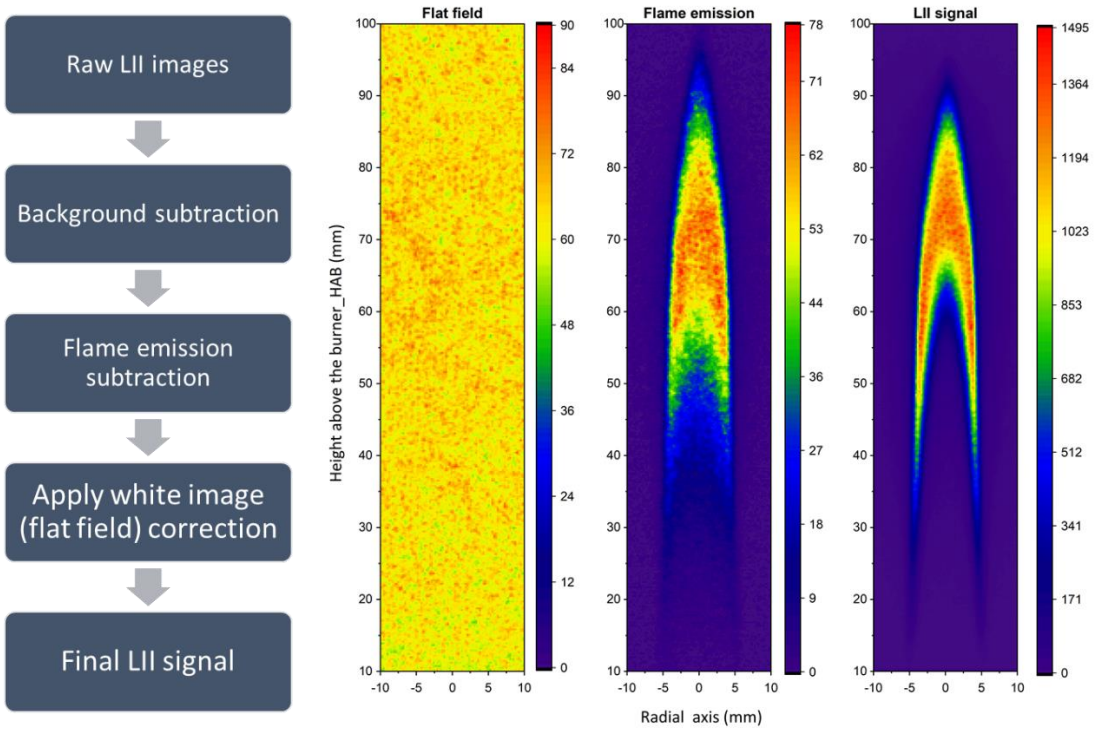

Figure 2.31 Different steps used for LII image data analysis. One example of a flat field, flame emission and corrected LII signal image.

As the binocular system is being used, the camera detector is divided into two regions of interest to record two images simultaneously at different emission wavelengths. A target with a known resolution was used before each measurement to measure the resolution of detected images. For imaging configuration, the image resolution was 4.1 pixel/mm. After resizing both images detected at two wavelengths, the obtained image has a size of 98 pixels in the radial position and 479 pixels in the axial position, resulting in a map of 23.41 mm × 116.82 mm.

Figure 2.32 shows the LII signal detected at the three selected wavelengths: 450, 580 and 650 nm. The signal is low at 450 nm due to the low quantum efficiency of the Pi-MAx 4 camera at that wavelength domain. The intensities obtained on 580 nm and 650 nm are close, with slightly higher intensity at 580 nm compared to 650 nm. It is interesting to detect soot particles in the near-infrared and infrared zone as the soot absorption index is supposed to be constant in that detection region [235]. In the centerline of the flame, the LII signal appears approximately at the height of 40 mm from the injector. High fluence can induce an incandescent signal at 30 mm HAB, but this signal is within the error bars of the detected LII signal. On the edges of the flame, the LII signal appears at 18 mm HAB, it increases with the height increase and shifts towards the center of the flame. Finally, the incandescence signal diminishes around 87 mm due to soot oxidation. By taking a profile on the axial direction in the centerline of the flame, the predominant soot region is between 78-82 mm HAB.

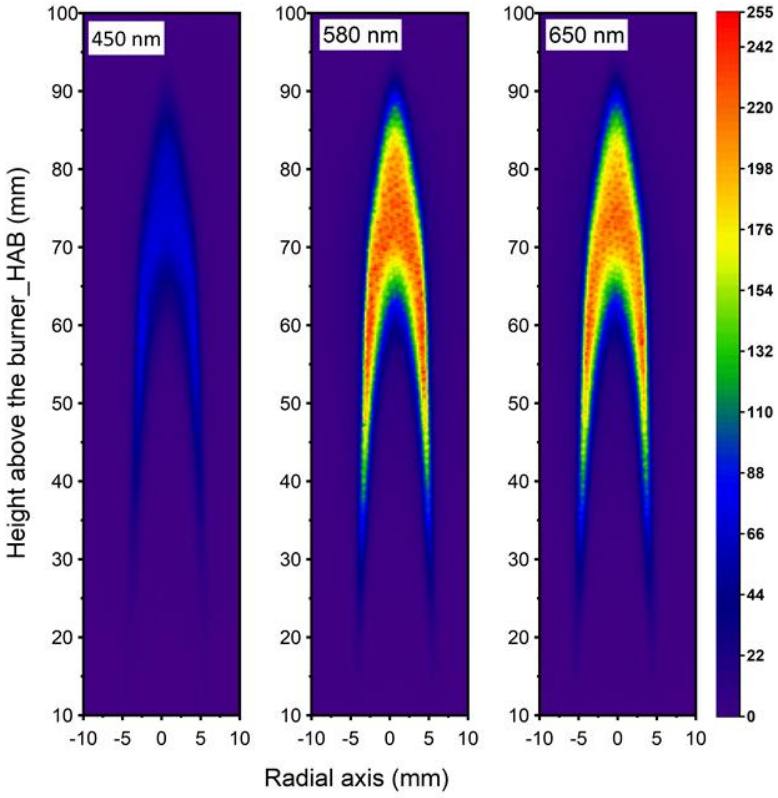

Figure 2.32 LII averaged signal maps obtained in imaging mode after the intensity was corrected for flame emission, background and flat field. LII soot maps were detected at 450, 580 and 650 nm.

After all image corrections, the final obtained signal maps have a pattern due to the optical fiber connection between the detector and intensifier module. A gaussian filter is applied to remove this pattern (Figure 2.33). For LII images, a low-pass filter is applied. The low pass filter blocks the frequency components above a specified cut-off frequency, allowing only the lower frequencies to pass [236]. A 10% Fourier pixel cut-off filter was selected to remove the honeycomb pattern from the LII soot maps, shown in Figure 2.33.

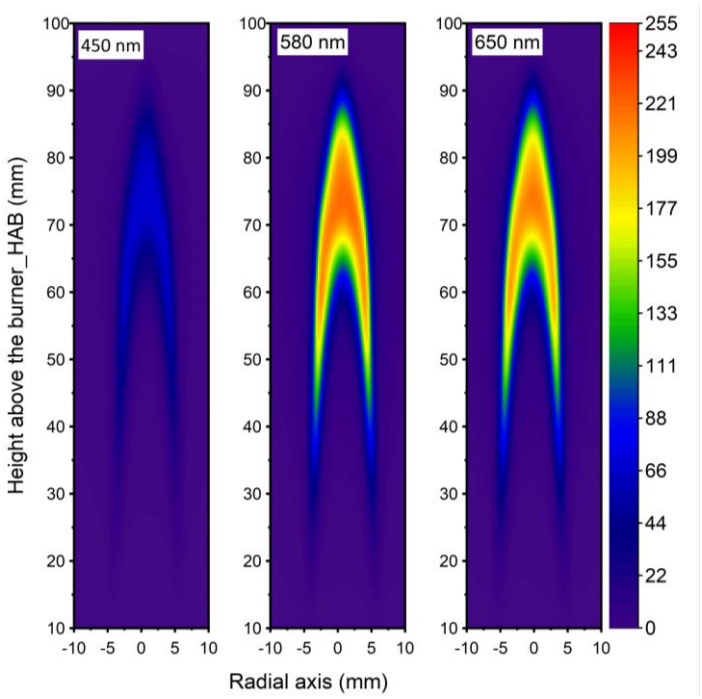

Figure 2.33 LII averaged signal maps obtained in imaging mode after applying a 2D FFT Gaussian filter to remove the honeycomb pattern observed in Figure 2.32.

The evaluation of measured LII signal can strongly be affected by the response of different optical configurations used for detection. As mentioned in section 2.54, the LII signal has to be corrected by the transfer function obtained from a calibrated optical system. Figure 2.34 shows the evolution of the LII signal in the centerline of the flame at different HAB before and after applying the transfer function. Before applying the transfer function, the LII signal is higher for 580 nm and 650 nm compared to the signal detected at 450 nm. After applying the transfer function, the detected signal at 450 nm becomes closer to the signal obtained at 580 nm and 650 nm.

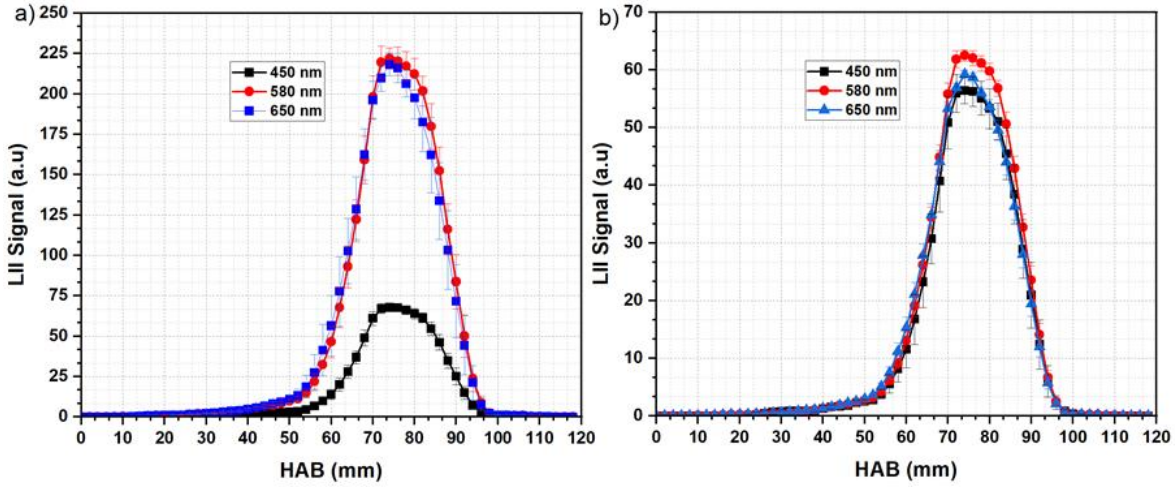

Figure 2.34 a) LII signal at different HAB in the centerline of the flame, the signal was obtained on an 8 pixels square region of interest; b) LII signal at different selected HAB after transfer function correction in the center of the flame.

The detection wavelength is one main factor that influences the obtained LII signal, as discussed in section 2.3.4. The LII signal ratio between different detection wavelength couples is an indirect indicator of obtaining an accountable effective temperature of soot. Figure 2.35 shows the signal ratio variation against the HAB for different couples of the three detection wavelength pairs. Based on the definition of the signal ratio $S_{LII1}/S_{LII2,}$ by assuming that the $S_{LII1}<S_{LII2}$ in general, the signal ratio remains less than 1. It is observed that the ratio of LII signal for detection couple of 450_580 nm and 450_650 nm increases as the HAB increases. Nevertheless, for the detection wavelength couple of 580_650 nm, the slope of LII is slightly constant with high standard error variation. This change follows the results of effective soot temperature described in section 2.5.6.

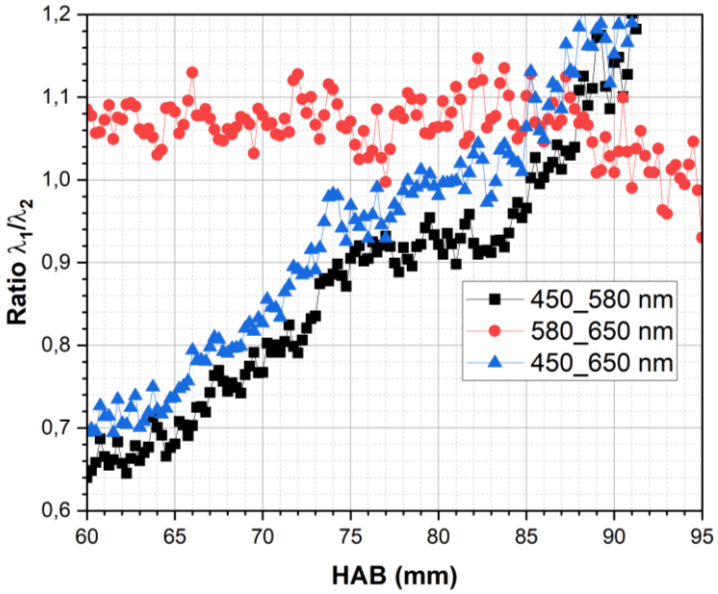

Figure 2.35 Variation of the signal ratio with the HAB in the center of the flame for three different couples of detection wavelengths: 1) 450_580 nm, 2) 450_650 nm and 3) 580_650 nm.

2.5.5.1.3 Soot refractive index (Em)

The soot refractive index is dependent on the optical properties of the soot. This parameter is of great significance in calculating the magnitude of absorption and emission of soot (soot temperature and volume fraction) [237]. The challenge is that Em varies with the detection wavelength, temperature, morphology, structure or organic content of soot [238]. The challenge comes in estimating the type of detected soot (mature or incipient) in the reactive combustion process, which brings a high uncertainty in estimating the real value of Em. The morphology depends on the fuel type, oxidizer, flame position, pressure, etc. The general equation that has been used for estimating Em is expressed by:

$$E_m(\lambda, T) = -Im\left(\frac{m^2 - 1}{m^2 + 2}\right) \qquad \text{Equation 2.41}$$

Where m is the complex index of refraction. To estimate the value of Em, it is important but not necessary to know the complex index of refraction m. In literature, significant variability has been demonstrated in measurements of the soot refractive index [221,239–243]. There is a considerable amount of published work where light extinction methods have measured the spectral dependence of Em, with correction for light scattering and gravimetric determination of soot concentration. Most

literature data estimate that Em is constant throughout the near-infrared to infrared wavelength domain, as shown in Figure 2.36.

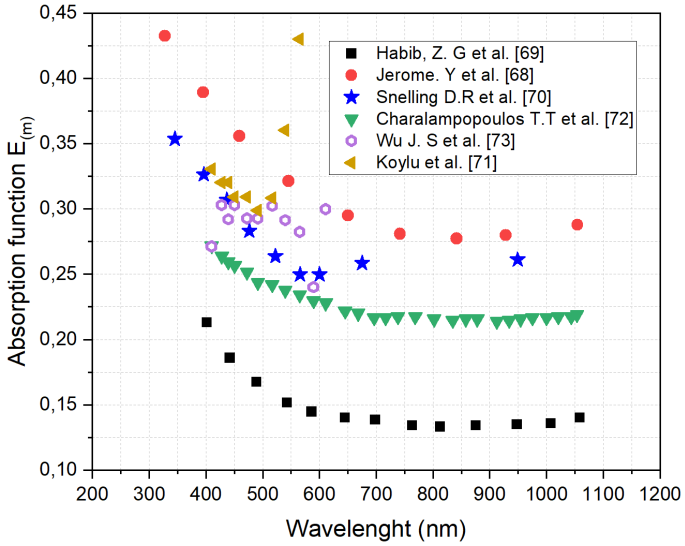

Figure 2.37 Comparison of different studied soot absorption refractive index function Em with detection wavelength [221,239–243]. The data were collected by using a web plot digitizer for better comparison.

In the study of Irimiea [244], the relative values of Em with the HAB in the CH4/air laminar diffusion flame (the same flame as this study) were estimated from the plot of the LII emission spectra at each HAB with a polynomial function. The incipient soot has a higher organic fraction compared to the mature soot. Figure 2.38 a) illustrates the evolution of the Em function at different detection wavelengths obtained in the work of Irimiea for the 550-780 nm wavelength domain [244]. A larger detection wavelength domain was used in this work. Hence, the obtained functions from the work of Irimiea [244] were extrapolated to the 440-760 nm wavelength domain, as shown in Figure 2.38 b.

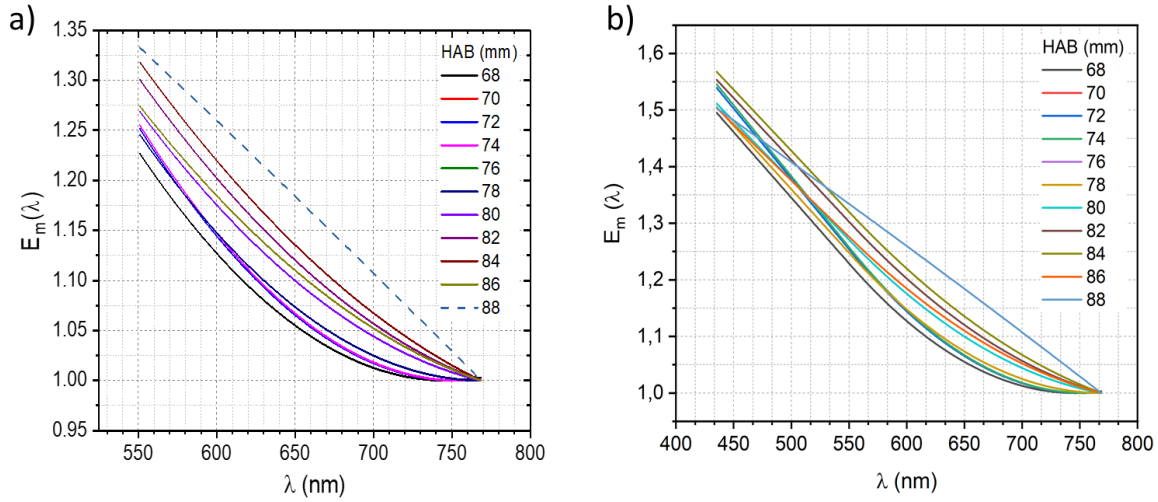

Figure 2.38 a) Relative Em (λ) function deduced from the LII spectral profiles on the centerline of the CH_4 - air laminar diffusion flame b) Extrapolated relative Em (λ) function deduced from the LII spectral profiles in the centerline of the CH4 - air laminar diffusion flame [244].

The value of the refractive index plays an important role in estimating the soot-effective temperature and, subsequently, the volume fraction. Its effect on obtained results is described in section 2.5.6.

2.5.6 Spectral measurements mode

The second LII configuration mode is spectral. For this mode, the first sequence of recorded images was the flame luminosity, and the second was for the LII signal with flame luminosity. The same steps used in imaging mode are followed for spectral mode data. As previously presented, the first thing is to determine the necessary laser fluence or the measurements. Figure 2.39 shows the evolution of normalized LII signal with the laser fluence, obtained laser beam size of (1.04 X 1.04 X 10) mm. The fluence curve was obtained at 76 mm HAB, corresponding to the region with mature soot particles. The fluence curve shape can change from one point to another in the flame as soot maturity changes. In this study, the LII signal starts to be activated at the laser fluence of 0.05 mJ/cm^2, and it increases as the fluence increases until the sublimation point at approximately 220 mJ/cm^2. The laser fluence used for further measurement is 188.46 mJ/cm^2; this value was chosen because it is before the sublimation point of soot and can also activate incipient soot particles. The entire flame height was scanned every 2 mm.

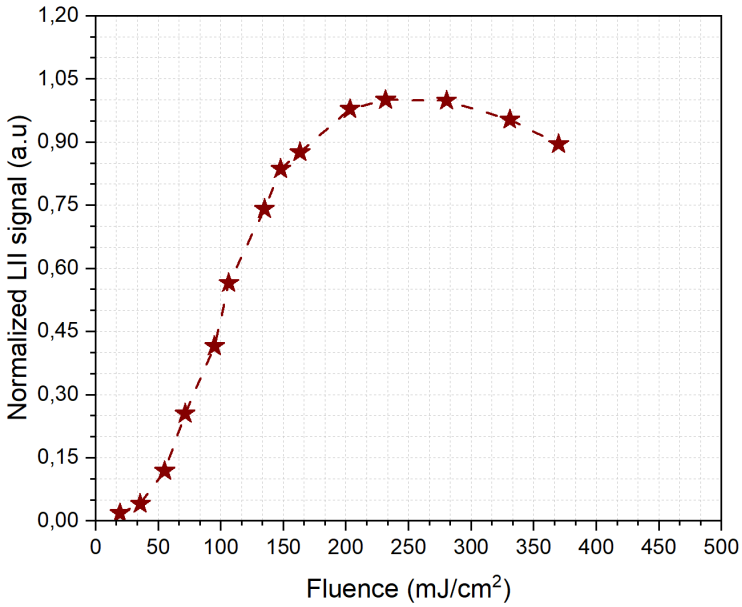

Figure 2.39 Fluence curve obtained at HAB of 76 mm. The signal was detected at 650 nm and summed over $10\ nm$. One point represents an average over 200 images for the selected ROI of 2 mm.

The shape of the fluence curves of the top hat laser beam and extended laser sheet is slightly different but the sublimation point for mature soot is similar. A slight difference is observed in the rising part of the fluence curve, representative of the low fluence regime. This difference can be attributed to the different sampling volumes between the laser beam and the laser sheet.

The LII soot map obtained in spectral mode looks similar to the one in imaging mode for the CH_4/air laminar diffusion flame. For both LII configurations, in the central axis of the flame, the incandescence signal starts at 40 mm HAB and fades at 90 mm HAB. The high sooting region in the

centerline is estimated to be between 70 – 86 mm. In the radial axis, the soot profile is estimated to be 8 mm in diameter, and the incandescence signal starts to appear at the height of 18 mm on the edges of the flame. Figure 2.40 shows the cartographies of LII soot signal obtained in a) spectral and b) imaging measurement configurations. The sooting region looks the same for both configurations, which can help predict some properties of soot.

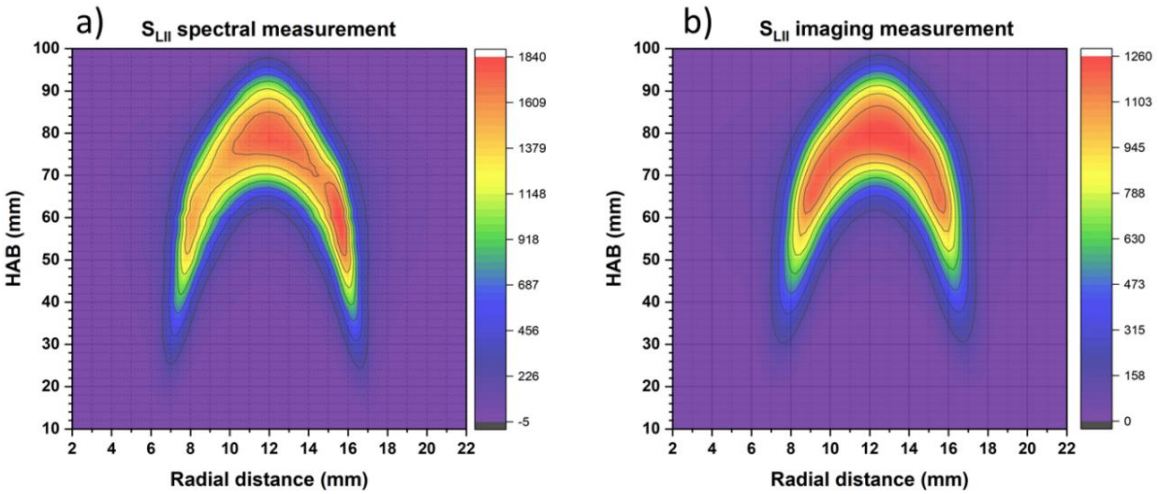

Figure 2.40 a) Cartography of LII signal obtained by using spectral measurement mode, b) Cartography of LII signal obtained with image measurement mode for the CH_4/air laminar diffusion flame. LII was detected at 650 nm and summed over 10 nm.

2.5.7 Soot effective temperature (T_{eff})

Soot particles in the detection volume generally have different effective temperatures due to their characteristic properties and the local environmental conditions. The thermal radiation intensity displays different temperatures depending on the wavelength detection domain. The effective soot temperature inferred from the ratio of laser-induced incandescence (LII) signals in the auto-compensating LII (2C-LII) technique depends on the detection wavelengths and affects the measured soot volume fraction [208]. In the characterization of soot particles, the effective temperature is a parameter needed to quantify the soot incandescence signal into volume fractions. Using the 2C-LII technique described in the previous section makes it possible to calculate the temperature from the detection of LII at two wavelengths. Soot effective temperature is obtained from the following equation plot:

$$\ln\left(\frac{LII(t_0,\lambda)\,\lambda^6}{E_m(\lambda)}\right) = -\frac{hc}{kT\lambda} + \ln(48\,\pi hc^2 f_v) \qquad \text{Equation 2.42}$$

The effective temperature is calculated from the slope obtained in Equation 2.42. Therefore the effective temperature is:

$$T_{eff} = \frac{h.c}{K.slope} \qquad \text{Equation 2.43}$$

Where K corresponds to all known constant values from Equation 2.42.

The value of Em has a considerable effect on the obtained T_{eff}. In this study, a comparison is made to show the effect of Em on obtained T_{eff}. Until now, there is still a lack of appropriate techniques for measuring the soot Em function. Therefore, it is necessary to estimate T_{eff} with an approach that can minimize the effect of Em on the obtained results.

In the imaging measurement method, Figure 2.41 illustrates the slope used for calculating the soot T_{eff} by using different detection wavelengths and values of Em ratios at the detected wavelengths of LII.

It is found that the soot T_{eff} obtained from the couple of two closest wavelengths (580_650 nm) is elevated (around 5000 K, Figure 2.41) with a significant error (standard deviation). The soot T_{eff} values obtained with Em constant are high (around 4500 K) compared to the soot sublimation temperature threshold. Therefore, it is deemed necessary to use either Em values identified in the literature or the polynomes presented in the thesis of Irimiea [244] for the same flame. The value of soot T_{eff} obtained by applying the relative Em ratios used in the study of Irimiea [244] lowers the T_{eff} to values closer (3890 K) to soot sublimation temperature. Realistic soot T_{eff} values (around 4100 K) were obtained as well when applying the soot Em function from the work of Jerome et al. [245].

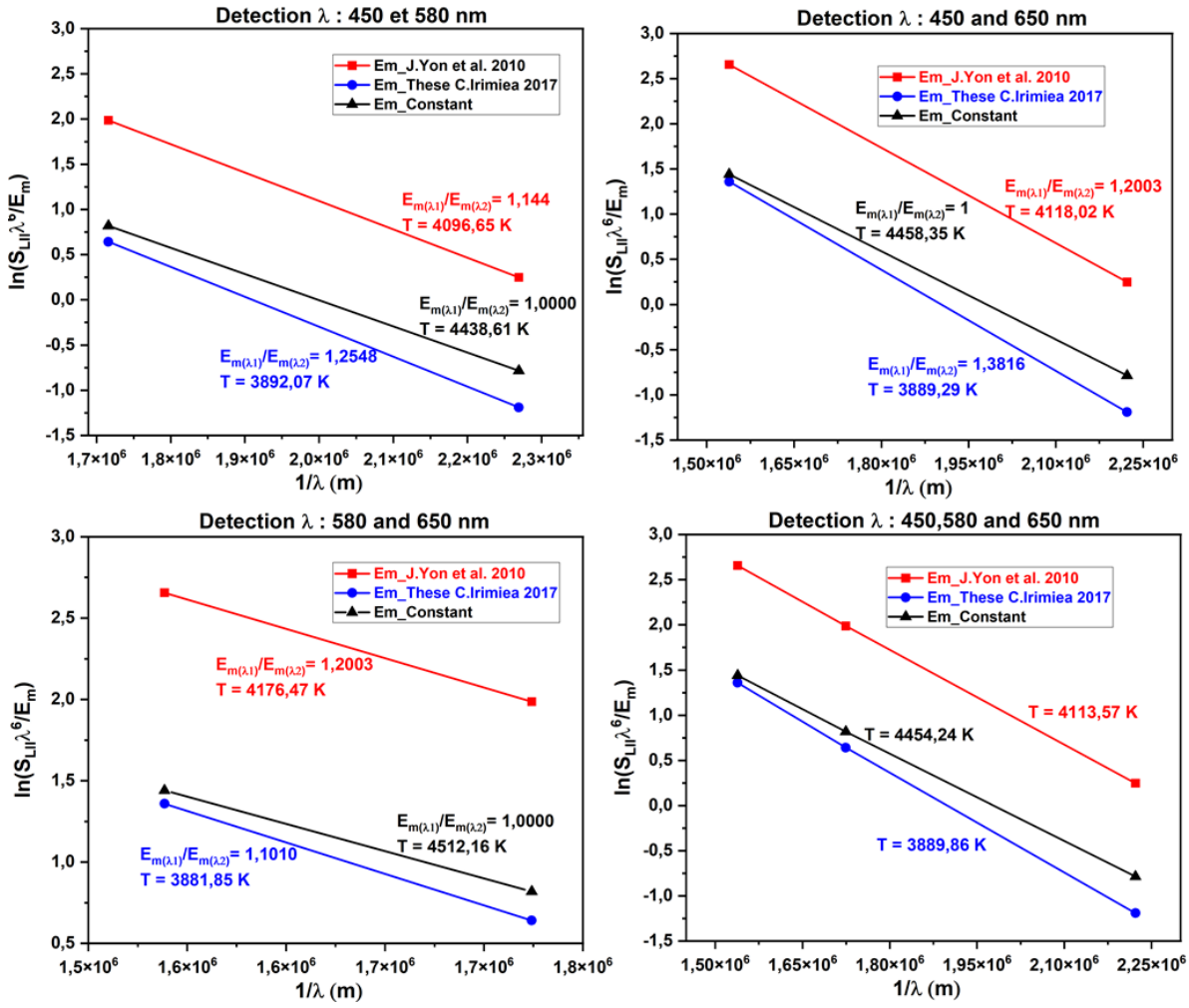

Figure 2.41 Examples of the slopes used for calculating soot T_{eff} in imaging LII mode at different detection wavelengths couples using different values of Em ratios.

Figure 2.42 illustrates how T_{eff} changes at different HAB when $E_m(\lambda)$ ratio is considered constant (Em_1/Em_2=1) for the selected pairs of wavelength. T_{eff} values were obtained on the axial profile of the flame by using detection wavelength couples of 450_580 nm, 450_650 nm, 580_650 and 580_450_650 nm. The approximation of T_{eff} in the low-sooting region (low incandescence signal) is difficult due to the diminished signal values and high noise.

The T_{eff} increases as the HAB increases in the sooting region of the flame where mature soot is expected (55 – 85 mm), for all wavelength detection pairs except 580_650 nm. For the detection wavelengths couple 580-650 nm, there is a high variation of T_{eff} between one point to another, even in the region with mature soot due to the narrow detection wavelength. A broader detection wavelength domain is recommended when using the pyrometry technique for higher precision in the determination of soot T_{eff}.

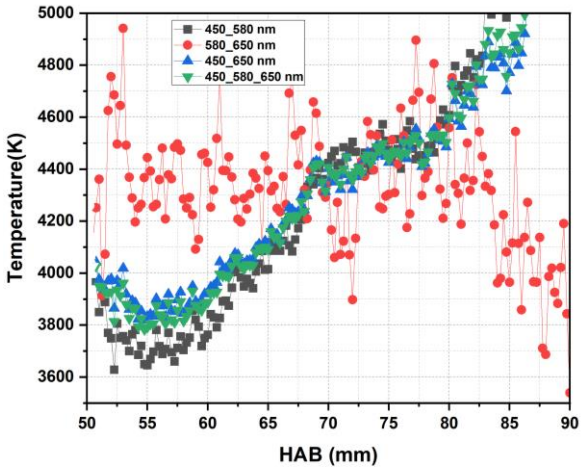

Figure 2.42 Soot effective temperature in the centerline of the flame, calculated with constant Em (Em_1/Em_2= 1).

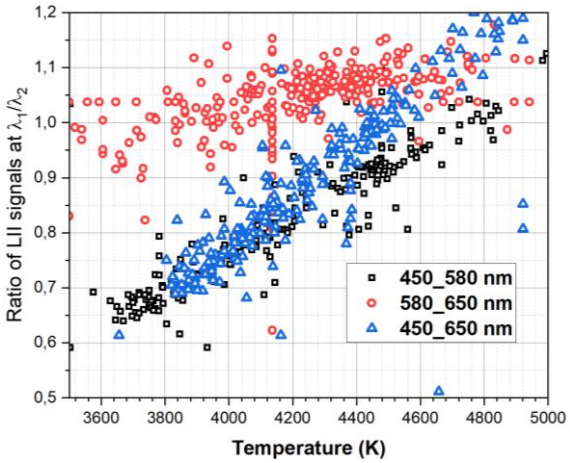

Figure 2.43 Variation of the LII signal ratio *as a* function *of the* soot T_{eff} for the temperature range 3400 to 5000 K.

To see the dependence of the incandescence signal with the obtained T_{eff}, Figure 2.43 shows the variation of the ratio of the LII signal detected at two wavelength pairs with the temperature. For detection wavelength couple of 450_580 nm and 450_650 nm, when the T_{eff} increases, the intensity ratio between the two signals increases. However, for the detection wavelength of 580_650 nm, the ratio between two signals varies significantly from one point to another. The ratio values can be used as a filter when processing 2D images.

The observation obtained in Figure 2.43 also depends on the type of sampled soot with LII. Figure 2.44 shows the correlation between different detection wavelengths with their obtained soot Teff. The correlation coefficients measure the strength of the relationship between two variables (R2). A correlation between variables indicates that one variable can change in value, and the other tends to change in a specific direction (+ or -). The possible range of values for the correlation coefficient is -1 to 1 if the data is standardized. A correlation of -1 indicates a perfect negative correlation, and a correlation of 1 indicates a perfect positive correlation. If the correlation coefficient is greater than zero, it is a positive correlation. Conversely, if the correlation is less than zero, it is a negative correlation. A value of zero indicates that there is no relationship between the two variables. As one variable increases, there is no tendency for the other variable to either increase or decrease.

Nevertheless, there is a negative correlation between the soot T_{eff} obtained on detection wavelength couple of 580 – 650 nm with all other detection wavelengths. The highest correlation factor is obtained for the three-wavelength couple (R^2=0.99) and the broader detection wavelength domain, with an R^2 of 0.98. High R^2 means reduced uncertainty for the calculation of T_{eff}.

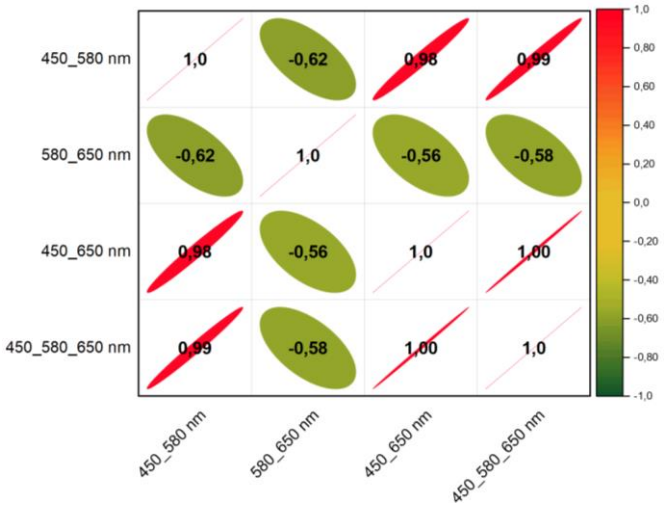

Figure 2.44 The correlation coefficient between different detection wavelengths based on the soot $T_{eff.}$ The Em function was considered constant in this case.

The importance of using 2C-LII is to deduce 2D soot-effective temperature map. Figure 2.45 shows an example of 2D soot T_{eff} map obtained for detection wavelength couple of 450_580 nm. From the height of 52 mm, the T_{eff} is around 500 K, which increases until the HAB of 60 mm, where the T_{eff} is around 4000 K; this region consists mainly of primary particles. From the height of 64 mm, the T_{eff} is almost constant until 87 mm. This region is estimated to have mature soot. With 2C-LII, if the soot particles are heated at the same temperature and have the same morphology, the T_{eff} should be the same. From the height of 90 mm, the T_{eff} starts to decrease, and this region consists mainly of oxidized soot.

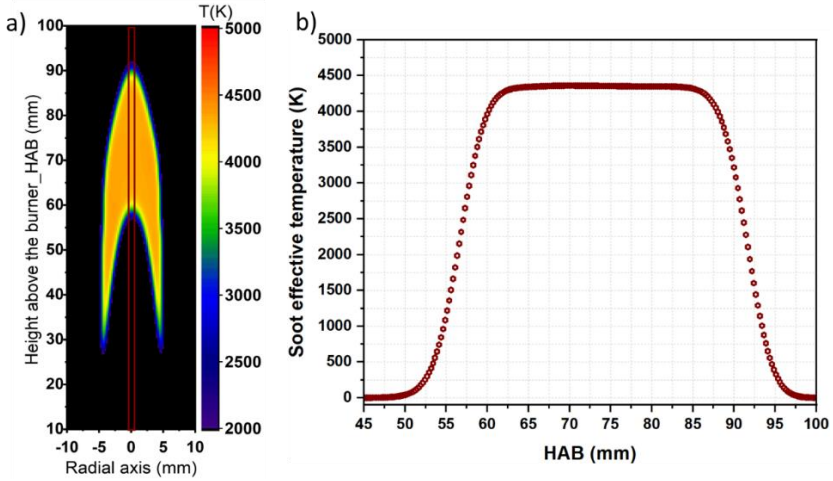

Figure 2.45 a) Soot T_{eff} map obtained on detection wavelength couple of 450_580 nm by considering Em_1/Em_2 ratio constant, b) Evolution of soot T_{eff} profile with HAB, taken on 4 pixels in the centerline of the flame.

Besides the temperature map obtained at the focal point of the laser sheet, also there is a variation of T_{eff} at different transversal positions from the focus (± 50 mm) to the extremities of the laser sheet propagation. Figure 2.46 shows how the T_{eff} map changes from the focal point to the extremities of the laser sheet. The average temperature map in the focal point is slightly higher than the temperature obtained on the extremities of the laser sheet propagation due to a higher fluence value than on the extremities. The change of effective temperature can be high in turbulent environments, not only due to the laser fluence that can change outside of the laser sheet focal point but also due to the combustion environment than can absorb the laser sheet.

Figure 2.47 shows the soot T_{eff} profiles taken in the centerline of Figure 2.46. In the lower region of the flame (below 50 mm), the temperature values are similar for the three sampling measurement points. The temperature increases at 52 mm HAB - region with incipient soot particles. The temperature increases until the region with mature soot. In the mature soot region, the soot T_{eff} is constant for all 3 propagation axis profiles. The average temperature in this region for the case of laser sheet focus (0 mm) is around 280 K higher than the one obtained away from the focus (+50 mm and 50mm). This information is useful in estimating soot T_{eff} on test rig application. For example, on MICADO test rig, the laser sheet propagates around 90 mm from the entrance to the exit of the windows. Without considering other combustion phenomena, it can be noted that if the soot T_{eff} is estimated in that environment, it can have a high variation from the focus of the laser sheet to the exit or entrance of the combustion chamber. This change is better controlled for laboratory diffusion flame, but with turbulent combustion, it can be difficult as other combustion conditions influence (adiabatic flame temperature, pressure and turbulence) the obtained soot T_{eff}.

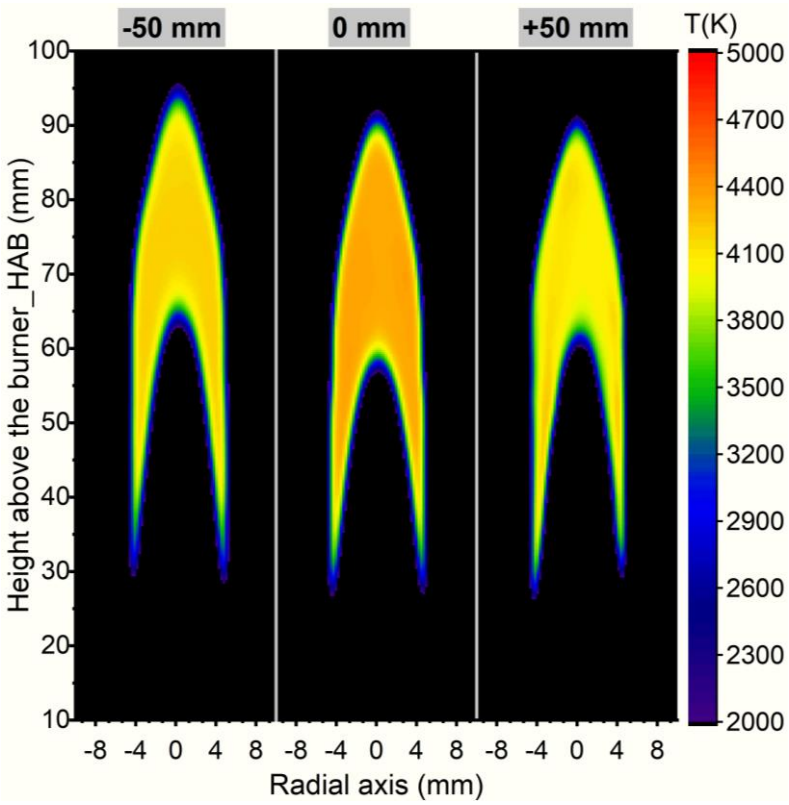

Figure 2.46 2D profile of soot effective temperature obtained with the detection wavelength pair 450_580 nm by considering Em_1/Em_2 ratio constant.

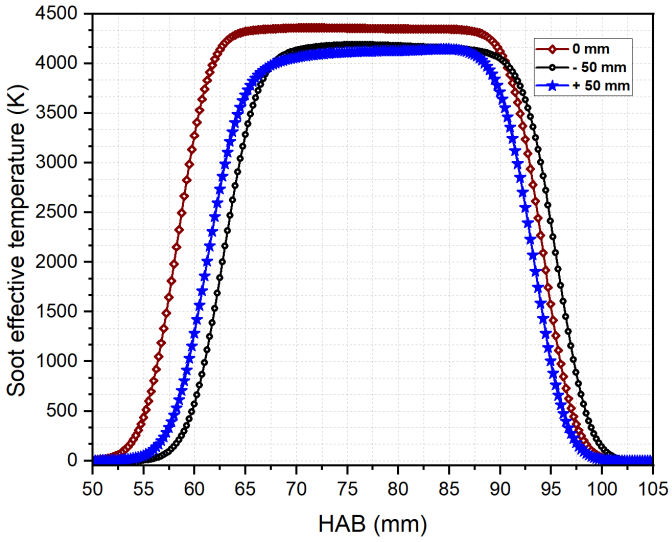

Figure 2.47 The evolution of soot effective temperature profiles at different HAB with different laser sheet propagation positions (+50, 0, +50 mm). The temperatures were obtained on the axial centerline of the flame and averaged over 4 pixels.

The second step of T_{eff} calculation obtained by imaging mode is to consider the values of Em interpolated from the work of Irimiea [223]. In this case, the soot T_{eff} values are low compared to the values obtained considering the Em constant. Figure 2.48 shows the T_{eff} obtained with different detection wavelengths at different HAB. The T_{eff} obtained with the selected detection wavelengths varies between 3750 K to 3980 K between 66 and 90 mm HAB.

For detection wavelength couple 450_580 nm, the mean value of effective temperature in the 68 – 88 mm HAB is 3870 K with a standard deviation of 39 K corresponding to a spread of 1.01 %. After a polynomial fit on obtained temperatures, the observation and the predicted values have an R^2 of 0.88.

By changing the wavelength detection couple to 450_650 nm, the averaged effective temperature in the sooting region is 3850 K with a standard deviation of 38 K and an R^2 of 0.97 of the polynomial fit.

By taking into account the three detection wavelengths, the effective mean temperature is 3854 K with a standard deviation of 38 K. After applying a polynomial fit, the soot T_{eff} fit has an R^2 of 0.99 which is better than the one obtained by using only two detection wavelengths. The average effective temperature detected for all wavelength couples shows that the small average temperature is 3780 K at the HAB of 68 mm with a standard error deviation of 1.64%. The temperature increases until the region with mature soot, where the temperature is 3874 K at the HAB of 80 mm with a standard error deviation of 0.17%. As the HAB increase, the effective temperature also continues to increase, but after passing the HAB of 82 mm, the standard error deviation increases. The averaged temperature in the region with mature soot has a lower standard error deviation compared to the temperature obtained for incipient and oxidized soot zones.

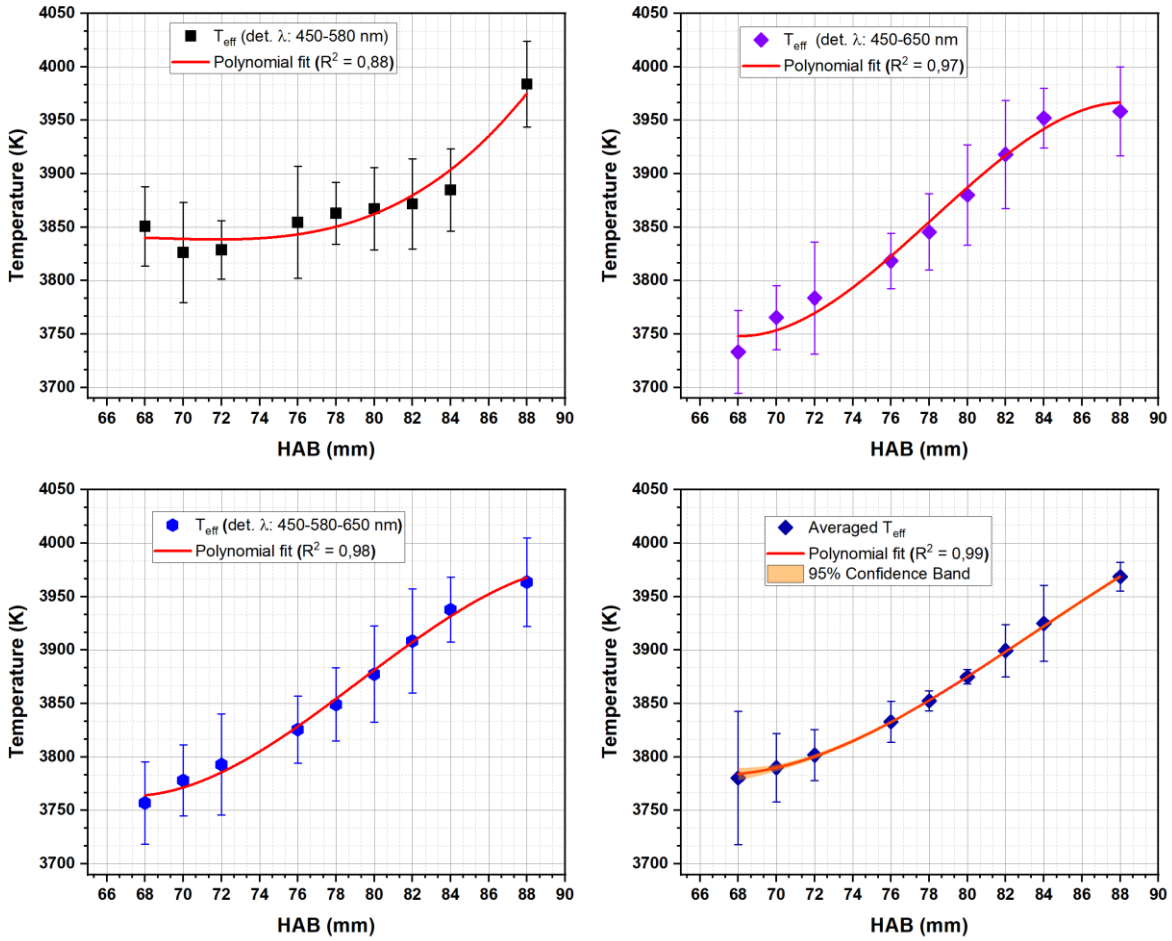

Figure 2.48 Evolution of soot effective temperature with different HAB by applying the soot absorption index Em for the three pairs of detection wavelengths.

Estimating the Em factor in the incipient and oxidized soot regions is challenging, as the morphology, absorption and emission behavior of soot change dramatically and therefore increase the uncertainty for the estimation of soot T_{eff}.

After the data analysis on imaging mode results, the second step consists of determining the soot T_{eff} on spectral images. The advantage of spectral mode for soot T_{eff} calculation, instead of calculating a slope of two or three detection wavelengths, is in the increased confidence of the fit over the selected spectral domain, which is not possible with the detection of LII at two wavelengths as shown in Figure 2.49. The soot T_{eff} value obtained in one spectral range can change when measured on another domain due to the variation of Em function.

Initial soot effective temperature was calculated by considering the soot Em function constant over the detection spectrum range. The slope was calculated in two spectral domains, one in the visible domain (440 -638 nm) and the second in the near-IR domain (660 – 739 nm). LII signal was detected in the spectral range of 300 – 900 nm, with a step and glue option (two recordings were necessary for obtaining this wavelength domain).

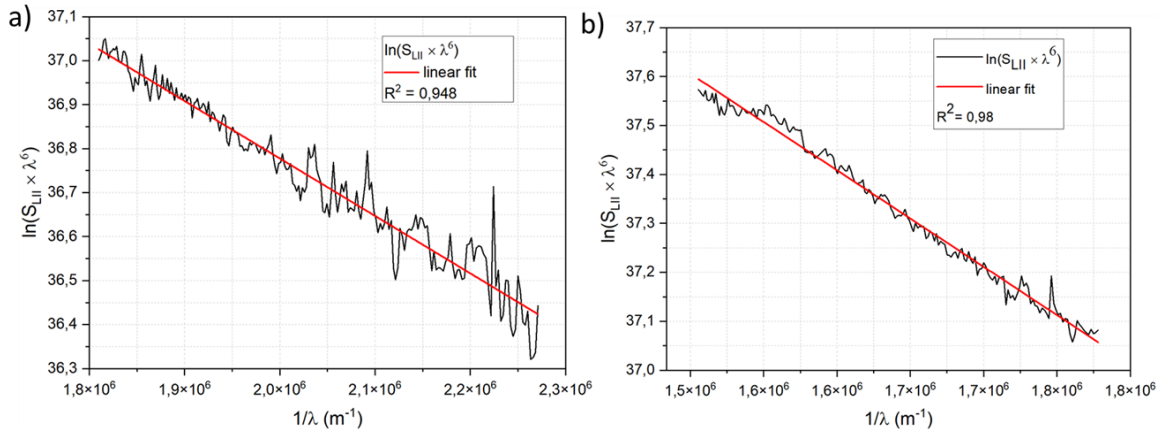

Figure 2.49 Representation of the slope of LII signal obtained in spectral measurement mode. a) a slope for the detection spectrum range in the visible domain 440 – 638 nm, b) a slope obtained in the detection near-IR domain (660 – 739 nm).

In spectral mode, the same measurement with the same configurations was made in the study of Irimiea [244]. It is noticed that the temperature obtained without Em correction is higher for young soot, with almost a 1000 K difference between the visible and infrared domains. For spectral data, the temperature difference decreases once it arrives in the zone of mature soot and takes over when it arrives in the oxidation zone. This was similar to the effective temperature obtained with imaging mode.

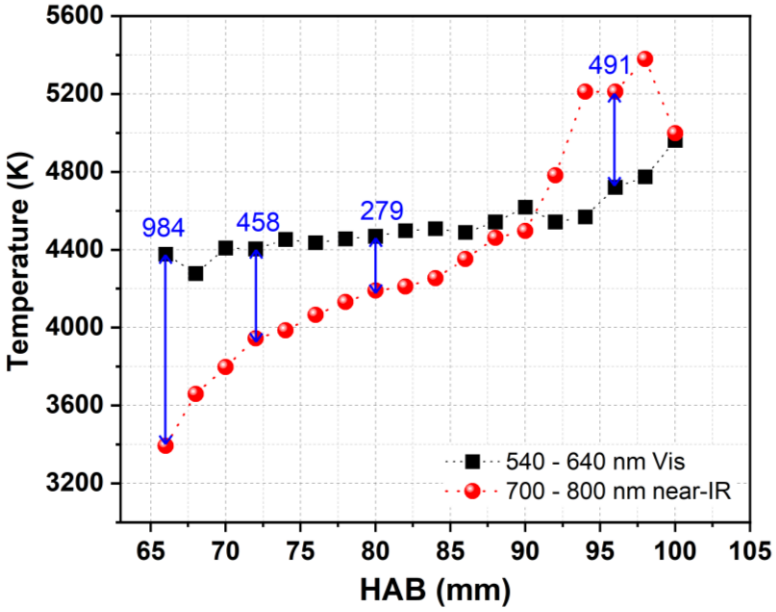

Figure 2.50 Evolution of soot effective temperature at different HAB detected in visible and near-IR domains using spatial measurement mode with constant Em [244].

By applying the Em factor from Irimiea [244], on obtained soot T_{eff}, with imaging, it was observed that in the region with mature soot, Em minimizes the errors. The LII emission spectra in the incipient and oxidized soot zones have an increased signal-to-noise ratio, but despite this, it is possible to estimate a confidence error bar of the fit.

Figure 2.51 shows the evolution of soot effective temperature obtained by considering the Em values from the interpolation of the Em functions obtained in the work of Irimiea [244] and for the selected spectral domain of 660 – 739 nm. The soot T_{eff} values increase with the HAB from 3650 K for primary soot to 3820 K for mature soot. These findings were approximately in the same range as in the imaging mode. By using the same laser fluence, the effective temperature increased with the maturity of the soot. In most atmospheric laminar diffusion flame, the maturity of soot increases when the HAB increases in the centerline of the flame.

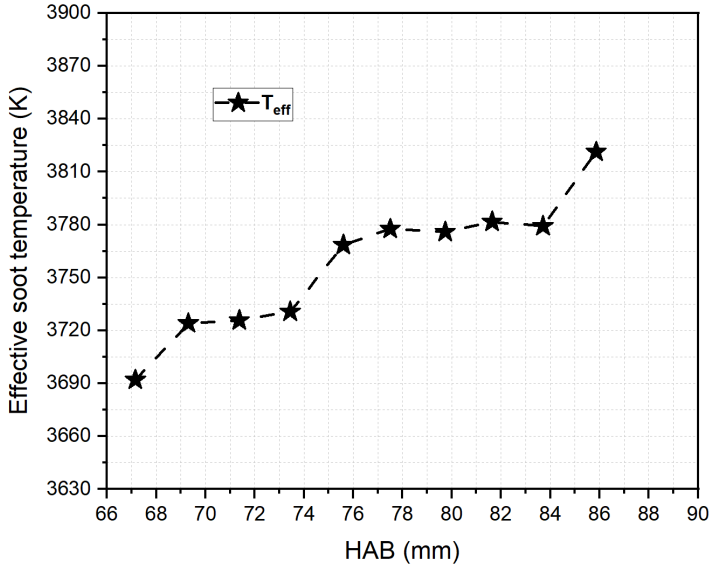

Figure 2.51 Obtained soot T_{eff} at different HAB by considering the Em function polynomials for the selected spectral domain 660 – 739 nm.

The milestone of this study was to compare the response of the incandescence signal obtained in imaging mode with the one of spectral mode. Figure 2.52 illustrates the soot T_{eff} comparison at different HAB by considering the Em variation polynomials. Generally, the soot T_{eff} obtained in spectral mode (1D) is lower than in imaging mode (2D). This can be due to the laser fluence; in spectral measurement mode, the chosen laser fluence was 188.46 mJ/cm^2, whereas in imaging mode was 177 mJ/cm^2.

Another factor that can impact the T_{eff} is the sampling volume variation from spectral mode to image mode. The increased sample volume in the spectral mode can have a higher impact on the T_{eff} uncertainty since various soot particles can contribute to the signal. A reduced volume increases the spatial resolution of the sampled soot particles and therefore affects less the obtained soot T_{eff}; increased confidence of the fit.

At the height of 68 mm, the difference in the obtained soot T_{eff} between the imaging and spectral modes is 158.9 K, but with a high standard error deviation (60 K). The temperature difference decreases as the HAB increases until the zone with mature soot. This observation is due to the uncertainty on the soot Em function for incipient soot region, where the soot particles are heated in the low fluence regime.

The temperature difference is around 90 K in the region with mature soot, which starts to increase when approaching the oxidation zone. A high-temperature difference of 204 K was observed at 86 mm HAB.

The confidence band of 95% is applied to the obtained temperature in both imaging and spectral data to see for which HAB domain the soot T_{eff} can change. The confidence band for spectral data is lower than the imaging mode data, especially for the regions of the flame where soot is either oxidized or in the inception zone.

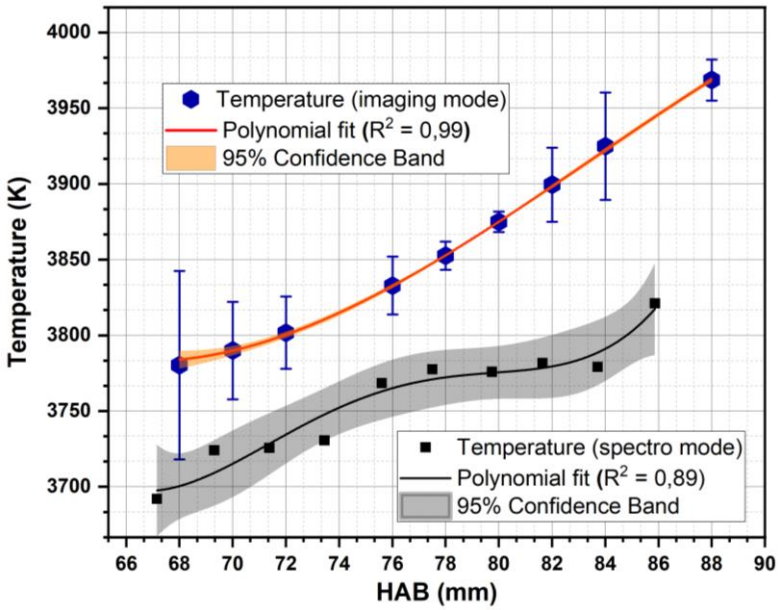

Figure 2.52 Comparison of soot effective temperature obtained in imaging and spectral measurement mode.

2.5.8 Flame temperature (T_{soot} and T_{H2O})

Gas temperature and radiative properties are essential parameters influencing the soot behavior in a combustion process. In addition, the temperature gradient in the surrounding soot environment can bring information about the soot properties. In this work, different techniques are used to calculate the flame temperature.

The first way to establish the spatial variation of the temperature is based on the pyrometry method applied to flame self-emission; the images subtracted from the LII signal images with the flame emission interference. The advantage of pyrometry is that it is non-intrusive, but it records the light-of-sight emission of the flame. Figure 6.6 shows the flame emission signal obtained for the three selected wavelengths in imaging mode. The recording system used for LII imaging mode measurement mode was used for flame emission detection. The second method used in this work is Tunable Diode Laser Absorption Tomography (TDLAS) for the H_2O vapors [246,247]. TDLAS working principle is based on the Beer-Lambert law that describes the attenuation of laser beam intensity for a particular wavenumber range when it crosses an environment with the molecules or particles that can absorb that wavelength [248].

2.5.8.1 Soot self-emission temperature (T_{soot})

Data processing steps identified for the LII techniques are applied to the images with flame emission. First, the images with the flame emission are background and flat field corrected. After that, the transmission function of the optical chain is applied. The flame emission spectrum is predominant in the near-infrared and infrared domains for temperatures of the flame at around 1800 K in the sooting zone. An example of the flame emission at the three detected wavelengths is shown in Figure 6.6 (annex 2).

A 2D reconstruction of the 2D line-of-sight flame emission is necessary for retrieving the local temperature of soot in the central axis of the flame. As the spatial field of the emitted signal is axi-symmetric, the method used for the deconvolution of flame-emitted signal to a symmetric field is Abel transform. The Abel transformation has two main types of applications. The first one is the forward transformation when the integrated emitted signal along a ray with the closest distance from the center of the flame. The second type (used in this work) is inverse transformation, which considers axial symmetry from the center of the flame toward its edges and is used for reconstructing radial or axial symmetrical volume intensity. The axis of the flame (from the fuel injection center) is vertical. The Abel transformation requires the position of the symmetry axis for calculation. This results in a separation line on the obtained reconstructed image, as shown in Figure 2.*53*. This reconstruction effect brings difficulties in estimating the temperature in the centerline of the flame.

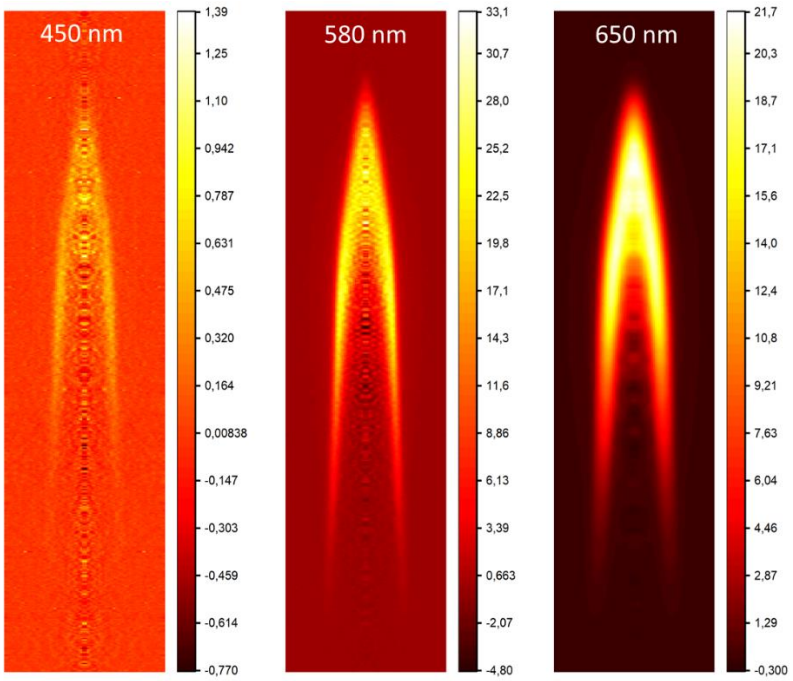

Figure 2.53 Reconstructed flame emission profiles after the inverse Abel transformation applied on soot flame emission signal detected at the three wavelengths.

The images are 2D FFT-filtered as the pyrometry is sensitive to the low signal noise from one pixel to another. The resultant de-noise images are displayed in Figure 2.54. Although this filter help to reduce noises, it works well on images detected at 580 and 650 nm as they have higher intensity, but the signal distribution on images detected at 450 nm has an overall low signal, and the filtering method does not change much the distribution profile obtained after Abel transformation.

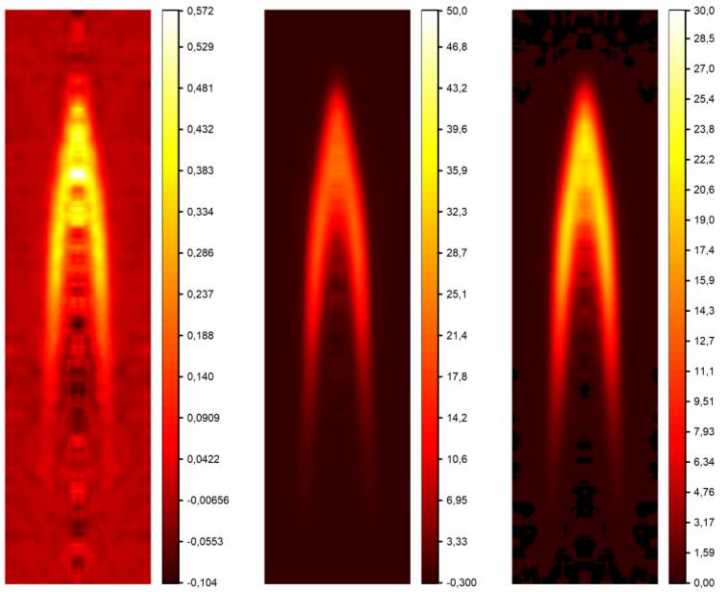

Figure 2.54 Final deconvoluted soot flame emission signal obtained after applying the 2D-FFT filter. The soot maps correspond to the three selected wavelengths.

A series of rectangular grids of 16 × 8 pixels (4 × 2 mm) are used on the central axis of the flame to obtain the temperature at a given HAB in the flame. This ROI was selected based on the quality of the obtained final images.

Based on the used detection wavelength couple, the soot temperature (T_{soot}) measured by using 450_580 nm is lower than the one obtained with the couple 450_650 nm. The high confidence of the fit is assured by the three-wavelength detection range of the flame emission; hence this data is considered for the discussion.

The measurable T_{soot} is possible only in regions where soot particles are present. It is observed that T_{soot} increased from 30 mm to 46 mm HAB, a region in the flame height considered to contain young soot. The T_{soot} in the region with mature soot increases to almost 2000 K and slowly decreases to 1400 K toward the tip of the flame. This temperature change depends on many factors like properties of soot present in each stage (incipient, mature and oxidized), flame local conditions and sensitivity of the technique in that region. The study of Naegeli et al. [249] showed the effect of flame temperature on relative soot concentration. They found that the relative soot concentration increases if the flame temperature increases. It is also estimated that a high flame temperature coincides with the highest soot volume fraction region for the CH_4/air laminar diffusion flame used in this study. This assumption can be valid only for laminar diffusion flames, while in turbulent diffusion flames typical of gas turbine combustor, the temperature dependence on soot formation is difficult to assess, presumably due to the increased importance of competing of soot precursors and other molecules that can be present in the flame [249].

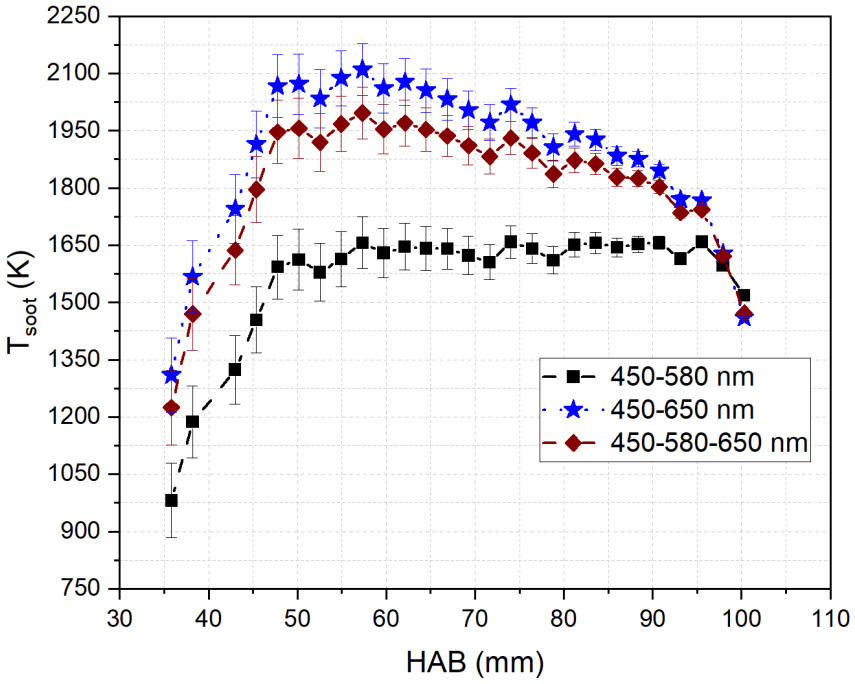

Figure 2.55 Axial profile variation of T_{soot} with the HAB. Values obtained from the reconstructed flame emitted signal from the CH_4/air laminar diffusion flame.

2.5.8.2 H_2O vapor temperature (T_{H2O}) - TDLAS

The implementation of the TDLAS experiment was performed in the framework of another work, as described in Annex 6.1.6. Therefore, only obtained results are presented for the discussion. The working principle of TDLAS is also based on the reconstruction of the absorption signal across the flame radial profile, which can introduce a significant error in the reconstruction of the temperature of water vapors (T_{H2O}) at each radial position of the flame. The resultant T_{H2O} can be associated with the gas temperature in the flame.

The water vapor temperature (T_{H2O}) is measured at each two mm of the flame height. The flame was scanned in the axial and radial profile with TDLAS to obtain the absorption spectra, which were reconstructed for the middle axis of the flame to get the T_{H2O}.

The T_{H2O} is around 300 K in the lower flame region near the injector at 0 – 5 mm HAB. After that, the T_{H2O} increases until 30 mm HAB to 1450 K. Between 35 – 95 mm HAB, the T_{H2O} is constant with an average of 1660 K and a standard deviation of 15 K (~ 1%). From 95 mm HAB toward the tip of the flame, the T_{H2O} values vary considerably, with a 300 K difference.

Figure 2.56 summarizes the values of the T_{H2O} and T_{soot} measured with the two presented techniques, plus the temperature measured with an S-type thermocouple as presented in the work of Elias et al. for the same flame [250]. Figure 2.57 shows the measured temperature in this flame obtained with the thermocouple, PLIF-NO and PLIF-OH [250].

For the temperature measurement techniques used in this work, the obtained results trends have more or less the same behavior, but it does not have to be excluded the fact that the uncertainty of each measurement is inherent to the system used for the measurement, the sampled molecules or

particles and the processing of the data with associated corrections. By comparing Figure 2.56 and Figure 2.57, it is observed that there are some differences in the obtained temperature values in the selected flame from the multiple techniques used in this work and a complementary one [250]. It is worth mentioning that the precision of the T_{soot} is directly related to the quantity of soot detected in the analyzed volume and the inversion technique. Therefore, the overestimation of the temperature obtained from the T_{soot} is within the acceptable range. It is worth mentioning that the T_{soot} catches as well the increase of the flame temperature near the oxidation zone. The T_{H2O} values are closer to the ones obtained with the thermocouple measurements in the region with mature soot and underestimated values in the region near the injector. The underestimation of T_{H2O} next to the injector may be due to reduced water vapor concentration at this HAB.

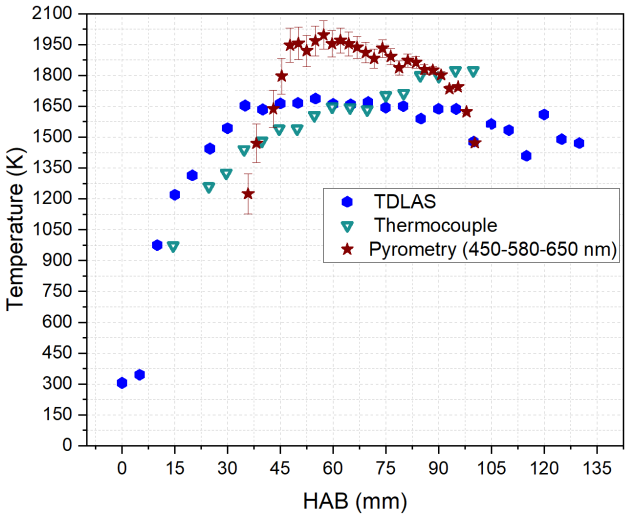

Figure 2.56 Comparison of temperature profiles obtained on the vertical central axis of the CH_4/air laminar diffusion flame using pyrometry and TDLAS. Thermocouple measurements performed in the work of Elias et al. [250] are shown for comparison.

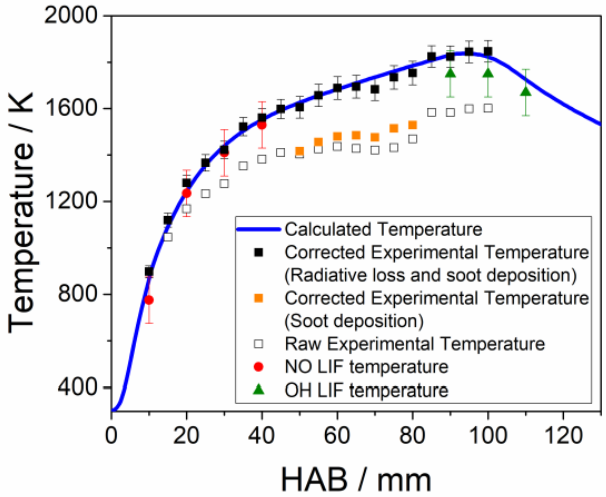

Figure 2.57 Measurements of the temperature profiles performed in the work of Elias et al. [250] for the vertical central axis of the CH_4/air laminar diffusion flame used in this study.

Since temperature is one of the leading parameters in the formation of soot particles, a brief discussion of the flame temperature impact on soot formation is provided. In the literature, the high pyrolysis rate of fuel and rapid formation of PAHs are mainly caused by high initial temperature [94].

Also, a high initial temperature promotes the nucleation process of soot [95]. The study of Qi et al. [97], investigated the effect of gas preheat temperature on soot formation. They found that the effective soot temperature increased with gas preheat temperature, leading to more soot formation and oxidation. Davis et al. [50] investigated the effect of temperature on soot formation on laminar diffusion flame; their findings show that the PAHs were reduced with the increase in the flame temperature. Their observation may hold because some classes of PAHs participate in the first stages of the nucleation process of soot, or they are converted to another class of PAHs as higher flame temperature promotes the carbonization of soot particles and the formation of PAHs with higher planarity, allowing PAHs to stack [251]. An interesting conclusion from our study is related to the TDLAS temperature (T_{H2O}), which starts to increase at 35 mm HAB, where it is actually suspected to have the first incipient particles in this flame. An increase in the H2O concentration is an indicator of the first stages of soot particle formation, which does not have to be neglected since the LII signal detected in the image mode suggests that some soot may be present at this HAB.

After this discussion, it is necessary to make a parallel comparison between the different values of the temperature measured in the CH_4/air flame and the T_{eff} obtained from the imaging mode LII measurements. Figure 2.58 shows the comparison of different temperatures obtained in this study. The results obtained in the region with mature soot 60-90 mm show a relationship between soot T_{eff} obtained with 2C–LII method and the flame temperature measured by the other techniques. When the flame soot emitted temperature (FE) increases, the soot T_{eff} increases. The temperature profiles obtained from TDLAS measurement have a different trend and it can be due to the H_2O vapor content, which starts to decrease when the oxidation process of soot starts.

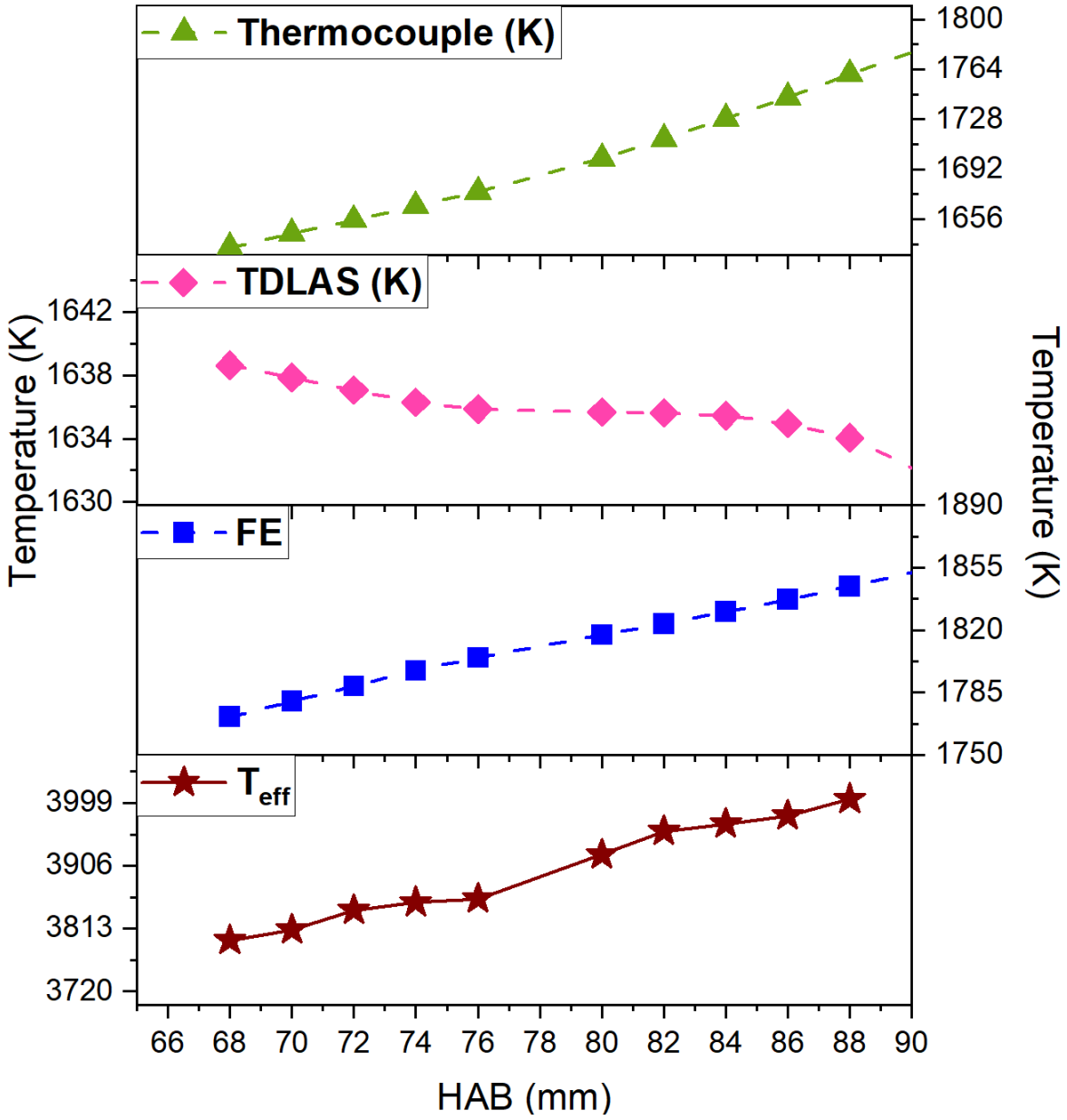

Figure 2.58 Evolution of temperature between 68 and 90 mm HAB. From top to bottom, the curves represent first the thermocouple-measured temperature, T_{H2O} obtained with TDLAS, T_{soot} obtained from the flame emission and T_{eff} obtained from the LII signal. Both T_{eff} and T_{soot} were calculated from the detection wavelengths of (450_580_650) nm.

2.5.9 Soot volume fraction (f_v)

The luminance measured by a calibrated source of light (described in section 2.5.4) was used to derive the soot volume fraction (f_v) on the vertical central axis of the CH_4/air laminar diffusion flame. The luminance shows the intensity per unity light area at a given angle or direction. In this work, the luminance is expressed in [W/m^3Sr], which depends on the detection wavelength. The luminance was calculated in imaging mode for three detection wavelengths (450, 580 and 650 nm). For each wavelength, the luminance was averaged over $\Delta\lambda$ of 10 nm. For the wavelengths of 450, 580 and 650 nm, the obtained luminance values are 1.01×10^8, 3.84×10^8 and 5.41×10^8 W/m^3Sr respectively. The

luminance increases as the wavelength increases due to the temperature of the lamp, which was set to 1800 K. The luminance is expressed as the spectral irradiance of the calibration sphere. The spectral irradiance from the calibration sphere is obtained by the detection system (Pi-MAX camera) for each pixel in the selected wavelength domain. As also demonstrated in the Ph.D. thesis of NGO [224], the spectral irradiance can be calculated as:

$$S_{CDD} = \frac{2\pi hc^2}{\lambda^5} \frac{1}{\exp\left(\frac{hc}{\lambda k T_{lamp}}\right) - 1} \frac{1}{2\pi} \Delta\lambda \, S_{1\,pixel} \, \Omega \, \beta \qquad \text{Equation 2.44}$$

Where S_1 pixel is the surface area [m^2] of the corrected image in the space corresponding to one pixel on the camera, Ω [sr] is the solid collection angle, β is the transmission coefficient, which depends on the setup of the experiments and the detected wavelength range. T_{lamp} is the temperature of the lamp. The product value of $\Omega \times \beta$ expressed in [counts.sr/W] is calculated from a flat field corrected LII signal over the power emitted on each pixel [W/sr]. The final f_v was calculated based on this equation:

$$f_v = S_{LII} \left[\frac{1}{\exp\left(\frac{hc}{\lambda k T_{(t)}}\right) - 1} \right] \Delta\lambda \, E_m \, V_m \, \Omega \, B \qquad \text{Equation 2.45}$$

The V_m [m^3] is the volume of analysis, which depends on the volume sampled by the laser sheet and its size on one camera pixel.

From Equation 2.45, the soot volume fraction depends on the soot Em function and the inverse of the soot T_{eff}. It is recalled that polynomial soot Em functions were used for calculating soot T_{eff} (Figure 2.32.b).

2.5.9.1 F_v image mode configuration

Figure 2.59 represents the evolution of the f_v detected at 650 nm in the vertical centerline axis of the flame with the HAB for different Em values, constant over the selected HAB. The soot absorption function affects the obtained f_v. Selected Em values span the 0.30 - 0.42 absolute value domain. The results show that increasing the Em value decreases the f_v soot detected at various HABs in the flame. But there is no constant ratio between the f_v detected at each HAB, which is in good agreement with the polynomial functions proposed in Figure 2.32.

For Em equal 0.32 the lowest soot volume fraction is 0.302 ppm at 68 mm and it increases until the height of 76 mm where the maximum f_v is 0.611 ppm. The highest f_v was obtained in the 76 – 81 mm range. After 81 mm the f_v started to decrease until 93 mm HAB where the signal was undetectable.

These results show the impact of the Em function on the soot volume fraction values. A constant Em impacts mostly the results obtained for incipient and oxidized soot particles. If the proposed polynomial functions are correct, it can be concluded that a constant Em function underestimates young soot particles and overestimates the soot volume fraction of oxidized soot particles.

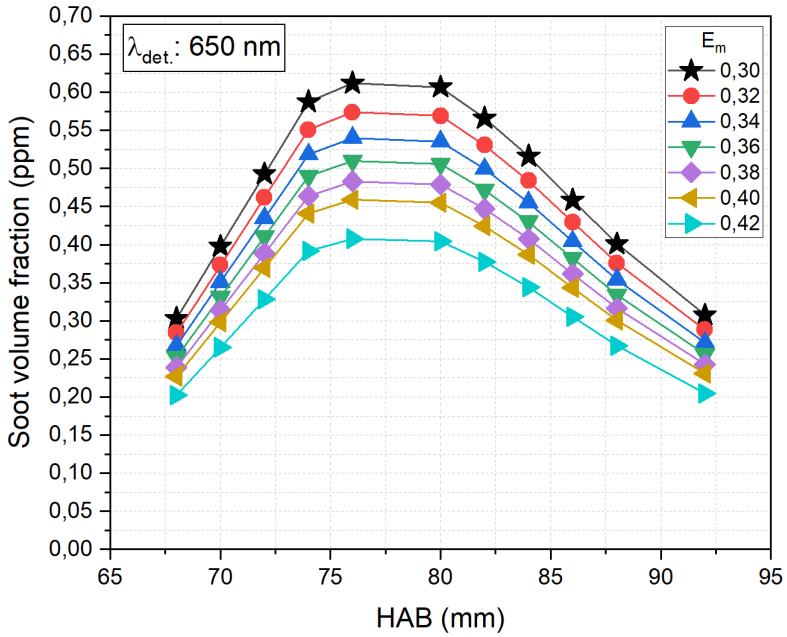

Figure 2.59 Soot volume fraction obtained in vertical profiles in the central axis of the CH_4/air flame for the LII signal detected at 650 ± 5 nm. The soot f_v was calculated by using different Em functions.

The soot Em function changes with the detection wavelength, as shown in Figure 2.61. The soot volume fraction for the selected vertical axis in the center of the flame is represented in Figure 2.60 for the three detection wavelength domains: 450, 580 and 650 nm with an Em constant value of 0.36.

The soot volume fraction obtained at 450 nm is 2.98 times lower than the soot volume fraction obtained at 580 nm, and this gap decreases approximately 3.93 times for the f_v at 650 nm at the HAB of 80 mm. This difference is lower for detection wavelengths of 580 nm and 650 nm. The f_v determined at 580 nm in the region with incipient soot is 1.53 lower than that at 650 nm. In the region with maximum f_v, the soot volume fraction is 1.28 lower than 650 nm.

These findings show that the lower detection wavelength (450 nm) has a strong influence on the upper detection wavelengths (580 and 650 nm) on the sensitivity of soot volume fraction, and it was also obtained in the study of Liu [207].

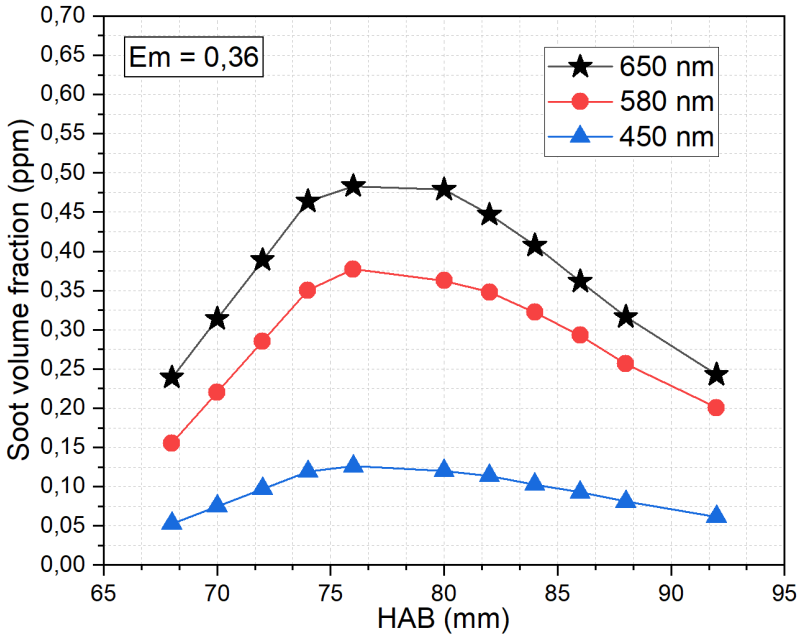

Figure 2.60 Effect of the wavelength detection on f_v at different HAB when using an Em value constant of 0.36.

A variable Em value was used for determining the soot volume fraction at 580 and 650 nm. For example, at the detection wavelength of 650 nm, if Em is 0.40, the minimum volume fraction is 0.227 ppm, and the maximum is 0.458 ppm with averaged soot volume fraction of 0.357 ppm with a standard error deviation of 23.75 %. On another side, at the detection wavelength of 580 nm, when considering the Em value of 0.32, the minimum soot volume fraction is 0.184 ppm, the maximum is 0.447 ppm, and the average volume fraction is 0.342 ppm with a standard error deviation of 25.25 %.

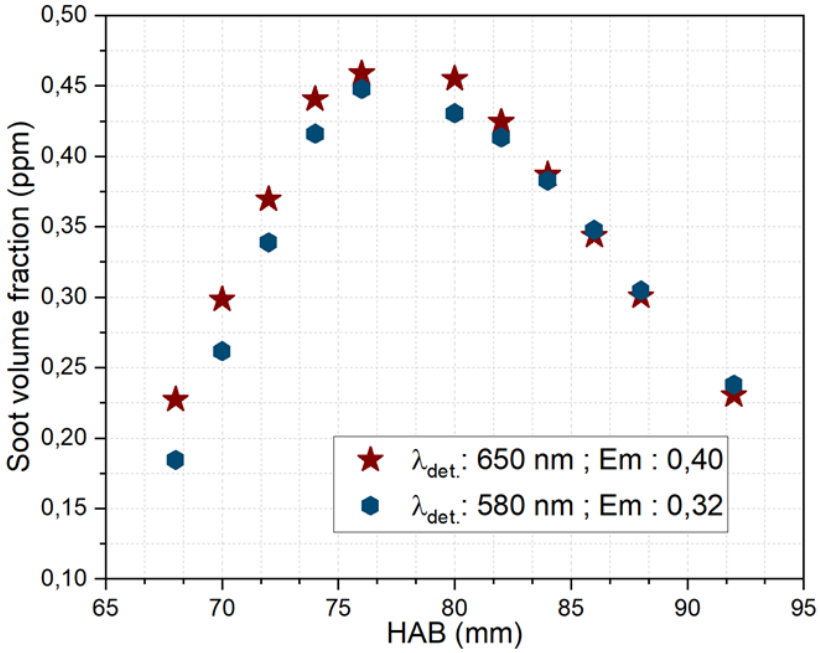

Figure 2.61 Evolution of the soot volume fraction with different HAB obtained with detection at 580 and 650 nm and with different Em values.

During this study, the temperature was measured with different techniques. In literature, different studies investigated the effect of temperature on soot formation. The study of Wey et al. [252] investigated the effect of temperature on the sooting behavior in a diffusion flame. They found that as the flame temperature increased, soot began to be formed earlier in the flame. At the same time, the soot loading at a given HAB increases. This more extensive sooting at higher temperatures was found to be due to larger soot agglomerates that, in turn, are formed partially by the size of spherules and partially by the degree of agglomeration that can also depend on the residence time of soot. The study of Glassman et al. [252] explained the differences in sooting trends with temperature in the premixed and diffusion flame in terms of competing pyrolysis and oxidation reaction in the pre-sooting zones. They found that in the premixed flame, the oxidation rate of soot precursors is accelerated more by an increase in temperature than their formation via pyrolysis reactions, leading to the reduction of soot concentration. However, for the diffusion flame, they found that non-oxidation occurred during pre-heating, leaving only the pyrolysis reaction, which read to the increase in soot concentration with the temperature. All these measurements were made only to see the effect of temperature on soot concentration without considering the soot optical properties.

2.5.9.2 Fv image and spectral configuration modes comparison

The aim of this study was to make a comparison of soot volume fraction obtained by using imaging and spectral measurement mode. Figure 2.62 compares the soot volume fraction obtained on both configurations at different HAB. For imaging mode, the presented results are obtained with 580 nm detection wavelength using an Em value of 0.36. The soot volume fraction was calculated in the spectral range of 660 – 739 nm with spectral measurement mode. This range was chosen to minimize the standard deviation of the fit. The same Em (0.36) value was considered for the soot volume fraction calculation. For both configurations, the soot volume fraction increases as the HAB increases until the region with mature soot. For example, at 70 mm HAB, for both configurations, the volume fraction is 0.227 ppm. The difference was obtained in the region with mature soot where the maximum volume fraction for imaging is 0.398 ppm at the height of 76 mm, whereas the maximum for spectral data mode is 0.305 ppm obtained at the HAB of 78 mm. The difference in volume fraction for both configurations can be due to the different wavelength detection range used to obtain the slope for the soot T_{eff}. The averaged soot volume fraction in the spectral mode in the range of 75 – 85 mm is 0.294 ppm which corresponds to the standard deviation of 2.6 %, whereas for imaging mode in the region of 74 – 84 mm HAB, the averaged soot volume fraction is 0.371 ppm with standard error deviation of 5.75%. The difference between averaged volume fraction in the region of mature soot, the volume fraction obtained in imaging mode is 1.263 times higher than the one obtained in spectral measurement mode.

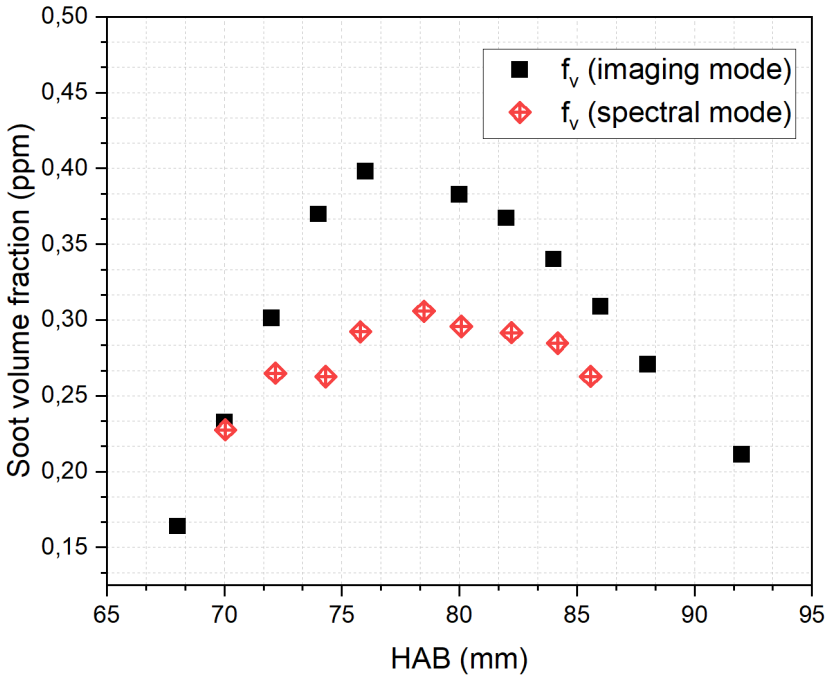

Figure 2.62 comparison of soot volume fraction obtained in imaging and spectral measurement mode at different HAB. The volume fraction obtained in imaging mode was detected at 580 nm and for spectral was detected in the range of 660 – 739 nm. Both volume fractions were calculated by using an Em value of 0.36.

2.5.10 Sources of errors and limitations in the quantification of LII signal into f_v

One of the main challenges of the LII technique is quantifying the measured LII signal into soot volume fraction. This subsection details the sources of errors and their importance in determining the soot effective temperature and volume fraction.

The LII uncertainty increases due to the calibration procedures, signal correction (background and flat field), self-absorption of LII signal due to the presence of soot in the detection pathways and the variability or instability of the flame.

The non-homogeneity of the laser beam and the laser sheet are also sources of errors because soot particles in the analysis volume are not heated at the same temperature. Liu et al. [105] studied the effects of laser fluence non-uniformity on ambient-temperature soot measurements using the AC- LII technique.

Another error source is the laser source jitter that can occur from one laser pulse to another. This jitter can induce errors when detecting the LII signal at prompt detection. The limitation based on the laser source are mostly due to the manufacturer – the typical jitter for the lasers used in this work is below 1 ns.

There is a limitation in LII measurements at high frequency (kHz), because it is difficult to have a high-frequency laser that can give the necessary energy needed for heating soot particles or have a homogeneous laser beam profile. Nevertheless, the use of a high-frequency laser is interesting in highly turbulent environments.

Soot absorbs and emits in a broadband wavelength domain. Choosing a laser excitation wavelength has to be done carefully, as this parameter can play an important role in soot characterization. In most studies, soot particles are heated by an Nd:YAG laser with an excitation wavelength of 1064 nm exciting at the frequency of 10 Hz with a pulse duration of approximately 7 ns [178,240].

The other source of error in LII measurement can be due to the used optics due to undesired reflection or absorption.

The detection system used in LII measurement has to be established based on the sooting environment to be analyzed. In this study, intensified cameras are used. Some research groups prefer to use photodetectors. In the visible domain, the flame self-emission can interfere with the LII signal, and in this region, soot has a considerable change in optical properties. In near-infrared and infrared, the optical properties of soot do not change much due to the wavelength detection, but the flame emission is considerably high for LII detection, mostly in harsh combustion conditions.

In quantifying the LII signal by using the auto-compensating (2C-LII) method, care has to be taken on the detection wavelengths as they can bring high uncertainty in obtained results. An extensive study is necessary to understand how the selected detection wavelengths affect soot temperature and soot volume fraction calculations. To improve the design of a 2C-LII detection system for soot temperature and soot volume fraction measurements, in this study, in imaging mode measurements, the wavelength detection is performed at three wavelengths to increase the precision of the fit. Therefore, attention must be paid to the selected detection wavelength, not only for a better signal-to-noise ratio but also for a more accurate soot effective temperature and volume fraction estimation, as illustrated in the previous section of the results. General factors that should be considered in the selection of two detection wavelengths include effective soot temperature detection range, the signal noise ratio, the system sensitivity, the spectral response of the detector and laser scattering interference. But also, based on the laser fluence, choosing the appropriate detection wavelength can avoid interference from other laser-induced emissions like Swan Carbon emission (C_2) or PAHs fluorescence [207].

For converting the LII signal into soot volume fraction and calculating effective soot temperature, the primary parameter affecting obtained results is the soot refractive index function Em. In literature, different techniques are used for determining the Em value. The challenge with Em is that it depends on the morphology of soot particles, which is linked to the fuel type and combustion environment. It also depends on the detection wavelengths used. Due to these factors, it is difficult to establish a method to estimate the absolute value of the Em function in turbulent combustion. Most studies show that the Em function changes between 0.2 to 0.4 in most cases [221,239,242,243]. In general, the soot refractive index Em variation dominates the total measurement uncertainty because of its high uncertainty and influence on the measured soot effective temperature and volume fraction.

2.6 SUMMARY OF THE CHAPTER

The primary purpose of this chapter was the development of LII/LIF techniques on atmospheric CH_4/air laminar diffusion flame.

The first subchapter was dedicated to the characterization of the laser sheet. The obtained results showed that LII and LIF signals depend on the shaping mode and expansion of the laser sheet configuration along the propagation axis. An LII correction factor is proposed to help correct the signals detected on the extremities of the laser sheet with respect to the focal point.

The second subchapter consists of detailing the steps for the calibration of the LII signal into soot volume fraction. The LII auto-compensating method is used for calculating the soot effective temperature and volume fraction. Two main measurement configurations are used; the first is the imaging configuration mode, where the laser beam is shaped into a laser sheet of 100 mm × 100 mm × 0.35 mm to map the region of interest. An ICCD coupled with lenses, binocular system and filters are used to detect emitted 2D LII signal. Different detection wavelength couples were tested within this configuration. It is found that the measured soot temperature and soot volume fraction depends on the selected couples of detection wavelengths.

The second used configuration is spectral or point measurement mode (0D), where the laser beam is shaped into a top hat laser beam with a diameter of 1.04 mm. The detection system was made by a spectrograph coupled with an ICCD camera. The values of soot effective temperature and volume fraction obtained with this configuration are slightly lower than those obtained in imaging mode. In the region of mature soot, there is approximately a gap of 21% in soot volume fraction at the HAB of 80 mm between the two configurations. These values can change based on the maturity of soot.

Measurements of LII at multiple wavelength bands showed that soot temperatures and volume fraction are subject to significant uncertainties, and improvements to this technique should be prioritized. In addition, it was found that different two-color ratios do not yield the same soot temperature and volume fractions. This could be explained by uncertainty on the optical properties of soot Em function. Therefore, the insight into how this value can be estimated can reduce the uncertainty in the conversion of LII signals into soot volume fractions.

CHAPTER 3

SOOT FORMATION IN AERONAUTICAL SEMI-INDUSTRIAL TEST RIG, IMPLEMENTATION OF LII/LIF AND COMPLEMENTARY OPTICAL TECHNIQUES

3 SOOT FORMATION IN AERONAUTICAL SEMI-INDUSTRIAL TEST RIG, IMPLEMENTATION OF LII/LIF AND COMPLEMENTARY OPTICAL TECHNIQUES

This chapter presents data about the characterization of soot particles on a semi-industrial aeronautical test rig, with additional metrology techniques that can help understand the formation of soot particles in such combustion conditions. The LIF technique developed on the CH_4/air laminar diffusion flame was applied together with LII (in collaboration with DLR Stuttgart) to swirl-stabilized kerosene/air flames on the MICADO test rig. The complexity of this flame increased compared to the laminar flame, which is why the necessity to add complementary techniques for characterizing these environments. PIV and light scattering (collaboration with CORIA laboratory) are complementary techniques to LIF/LII and give information on flow field velocity vectors, spray and soot dynamics. This work represents the first step regarding the application of the LIF/LII techniques on large-scale installations. The idea behind this work was to develop suitable optical techniques which can capture experimental parameters necessary for understanding soot particles formation, an extremely complex phenomenon that cannot be explained by only detecting soot particles. An outcome of already being able to detect soot particles and quantify the measured signal into soot volume fraction directly helps to predict the impact of heat transfer through radiation effect. Another advantage of performing these measurements is obtaining an experimental database that covers operating conditions (OC) of high-pressure turbulent combustion representative of aero-engine combustors, which can be used to validate numerical models.

The main objective of this work covers two main scientific subjects.

1. To investigate combustion conditions representative of aircraft combustors with in-situ optical techniques.
2. To conduct an in-depth characterization of soot particles emitted by a modern combustor at engine-relevant operating conditions and increased pressures.

This chapter focuses on implementing coupled LIF and LII experiments for detecting soot particles and soot precursors on the MICADO test rig. These two *In situ* techniques were chosen as they can provide spatially and temporally resolved information about soot and polycyclic aromatic hydrocarbons (PAHs) in flames [177]. PIV results bring information on the transportation phenomena, mixing, residence time and interaction of soot with PAHs. As the fuel used is liquid (Jet A-1), light scattering is used to get information on the spray dynamics, vaporization and possible soot particle scattering.

The studies presented in this chapter have been conducted in the framework of the European project SOPRANO (Soot Process and Radiation in Aeronautical inNOvative combustors) [253] and the ANR (French National Research Agency) project Astoria (Accounting for soot particle morphology in flame thermal radiation and optical diagnostics in complex systems) [254].

3.1 MICADO COMBUSTOR CONFIGURATION

Aero-combustor testing requires facilities capable of simulating aero-thermodynamic conditions at the inlet of the combustion chamber (e.g., downstream from the compressor). Chamber pressure, inlet temperature and injection system global equivalence ratios are the governing parameters to be respected for representative experiments or simulations of the combustion chemical reactions inside the combustor [143,255]. To answer this matter, ONERA developed test rigs capable of operating in conditions similar (input airflow and pressure) to those found in relevant aircraft engines [255]. MICADO is a French acronym for “Investigation Means for Air-breathing Combustion using Optical diagnostics”; MICADO is one of ONERA’s aeronautic test rigs on which tested combustion conditions are representative of the ones identified in single- or multi-sector aeronautical engine combustors [25,256]. This research platform ensures realistic operating conditions inside the chamber in terms of Reynolds, Damköler and Karlowitz numbers.

The combustion chamber has a 100 mm x 100 mm square section with three optical accesses of 89 mm x 88 mm. The combustor can be fed with gaseous (H_2, CH_4) or liquid (e.g., Jet A-1) fuel and air as an oxidant. Air and fuel enter the combustor through an axial single-swirl injector. Fuel is injected either through the main (premixed) or pilot (non-premixed) flow paths. A sampling probe for the combustion of gaseous and particulate pollutants is placed 140 mm downstream of the combustor dome. The pressure in the combustion chamber is adjusted using an exit nozzle equipped with a throttling plug. The combustion chamber has a water cooling system temperature and pressure sensors that monitor thermodynamic parameters inside the combustion chamber [255].

The operating conditions domain of the MICADO combustor goes as high as:

1. Air mass flow rate: $\dot{m}_{air} \leq 4$ kg/s
2. Air temperature: $T_{air} \leq 800$ K
3. Combustion chamber pressure: $p_{ch} \leq 40$ bar
4. Flame global equivalence ratio: $0.5 \leq \Phi \leq 0.8$

These values allow the reproducibility of combustion with operating conditions (OC) similar to those identified for the Landing and Take-off cycles (LTO) and various other condition values outside the LTO. Figure 3.1 presents a schematic of the feedthrough airline with the Venturi tube (3 m upstream from the injection's plane), the injector, the combustion chamber, the burned gaseous pollutants and particulate matter sampling probe, the exit nozzle with its throttling plug, and the exhaust pipe. The pressure in the combustion chamber (p_{ch}) is controlled with an exit nozzle and adjustable throttling plug.

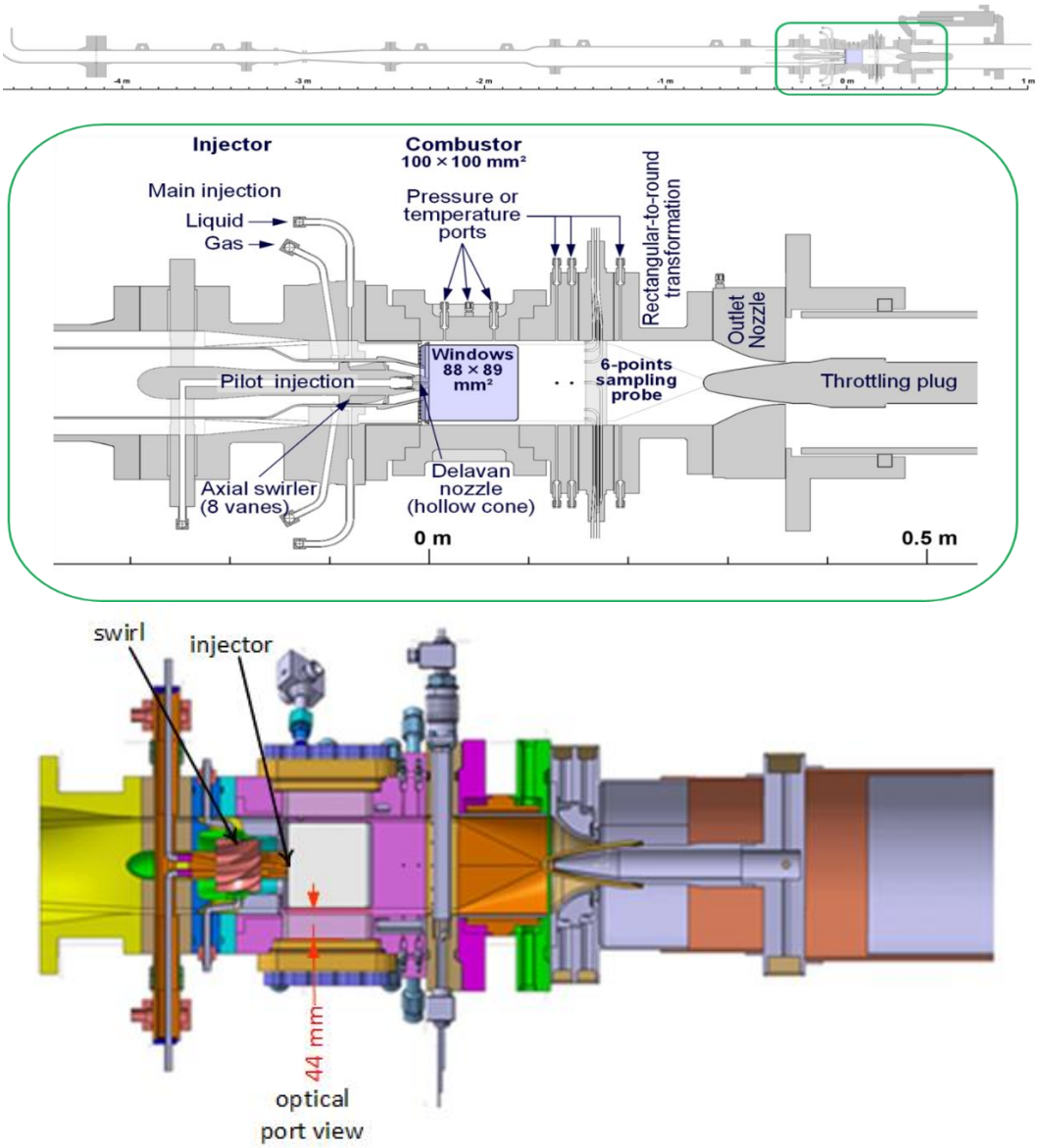

Figure 3.1 Top figure: 2D Schematics of the MICADO combustion chamber with the fuel and air supply lines. The bottom figure shows a 3D cross-section of the combustor. The air-flow stream is from the left-hand side to the right-hand side.

The bottom part of Figure 3.1 displays a cross-section of the MICADO combustion chamber which underlines the optical accesses port views (44 mm thickness) used for inserting the laser beams/sheet or visualization. Due to the limited space around the combustion facility, lasers, computers and other diagnostics setups are placed in a dedicated optical laboratory. The optical path from the exit of the laser to the combustor roughly ranges between 3 to 5 meters. The operation and monitoring of the combustor are carried out from a control room detached from the test rig. All instruments are remotely controlled while the test rig is operational.

3.1.1 Test rig operating conditions (OCs)

During the measurements campaign, different operating conditions (OCs) were studied. The OCs are classified based on the working parameters of the test rig, which include the total air and fuel mass

flow rates, the temperature of the air, and the pressure in the combustor. A referenced flow factor (FF) value is selected to stabilize a targeted operating condition. The FF is deduced from the ratio between the total air mass flow rate multiplied by the square root of the temperature and the chamber pressure (Equation 3.1).

$$FF = \frac{\dot{m}_{air} \times \sqrt{T_{air}}}{p} \qquad \text{Equation 3.1}$$

The MICADO-referenced FF is relative to the CFM 56 engine FF (FF_{ref}). The FF_{ref} is 19 kg s^{-1} $K^{0.5}$ MPa^{-1}. Noteworthy, FF is related to the flow velocity in the combustor. Consequently, a special care should be taken when comparing measurements obtained at different OC as, for given pressure and air inlet temperature, changing air mass flow dramatically changes the aerodynamics and residence time in the combustor. The total air mass flow rate for a single sector engine can therefore reach 4 kg/s, considering the air mass flow rate dedicated to the cooling of the combustion chamber walls (up to 30 % of the total air mass flow rate), or about 2.5 kg/s without wall cooling. The inlet air temperature depends on the engine's OPR (Overall Pressure Ratio), its polytropic efficiency (η_p), and the temperature of the air inlet (288 K at ground level, 217 K at cruising altitude) and is determined by the following equation:

$$T_{air(2)} = T_{air(1)} \times \left[\frac{P_2}{P_1}\right]^{\frac{1}{\eta_P}\frac{\gamma-1}{\gamma}} \qquad \text{Equation 3.2}$$

Where $T_{air\,(2)}$ is the air temperature at the exit of the compressor, $T_{air\,(1)}$ is the air temperature at the inlet of the compressor, P_2 is the pressure at the exit of the compressor, P_1 is the pressure at the inlet of the compressor, γ is the ratio of thermal capacities at constant pressure and volume, and η_P is the polytropic efficiency which varies between 0.8 up to 0.95.

The MICADO test rig is designed to operate continuously for a few hours, depending principally on the total air and fuel volumes necessary for spanning planned OC.

The global equivalence ratio (Φ) is calculated based on fuel and air injection mass flow rates. To simplify calculations, consider that the fuel used has a formula of C_xH_y. Then, the global equivalence ratio at the injection point can be expressed as:

$$\Phi = \frac{\left(x+\frac{y}{4}\right)\cdot\frac{\dot{m}_{fuel}}{M_{fuel}}}{n_{O_2}} = \frac{x+\frac{y}{4}}{X_{O_2}}\cdot\frac{M_{air}\cdot\dot{m}_{fuel}}{\dot{m}_{air}\cdot M_{fuel}} = \frac{x+\frac{y}{4}}{12{,}011\cdot x+1{,}008\cdot y}\cdot\frac{M_{air}\cdot\dot{m}_{fuel}}{\dot{m}_{air}X_{O_2}} \qquad \text{Equation 3.3}$$

Where M is the molar mass (fuel or air), x and y represent the carbon and hydrogen composition (content) in the fuel, X_{O2} is the volumic fraction of O_2 in air, n_{O2} is the number of moles of O_2, $\dot{m}_{air}$ and $\dot{m}_{fuel}$ are the mass flows of air and fuel.

Figure 3.2 shows the MICADO achieved operating conditions (red dots) as the FF variation with the pressure inside the combustor. The OC domain for the MICADO test rig is underlined with red, while the FF CFM56 OC points are represented with orange dots. These tested conditions are representative of single or multi-sector jet engine combustors and civil helicopter engines in terms of

pressure and reduced air mass flow rate. The corresponding cycle is color-coded from blue (Relight) to red (Take-Off).

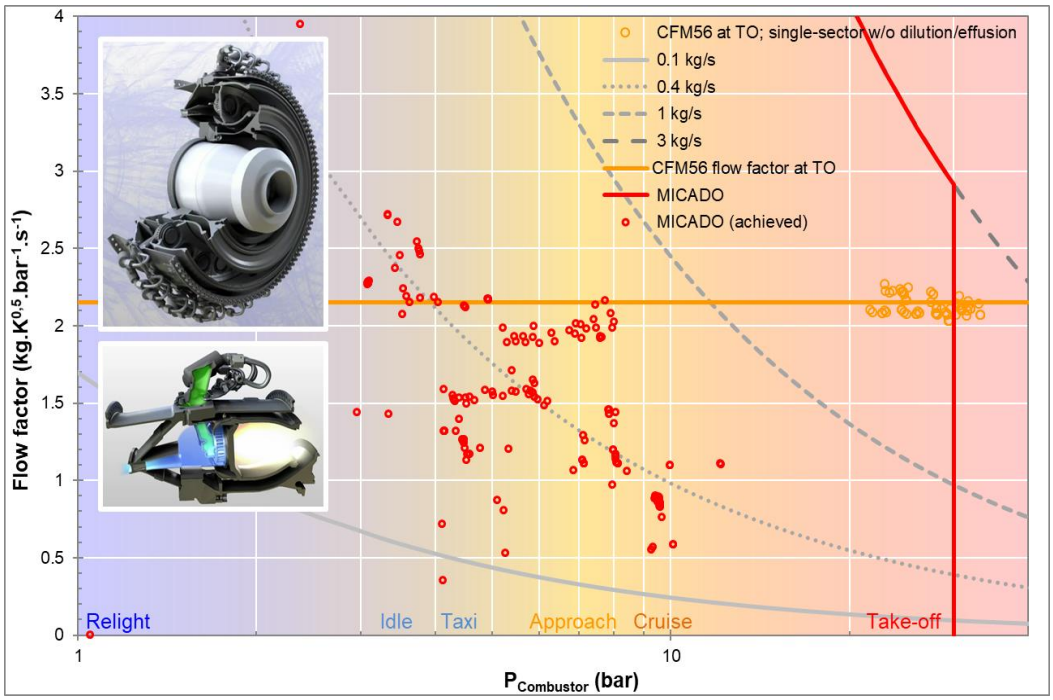

Figure 3.2 MICADO operating conditions domain represented as the flow factor variation with combustor pressure.

The injector used for MICADO is swirled, with a swirl number of one. Figure 3.3 shows a global schematic representation of the flow field inside the MICADO combustor. The following terms describe and interpret the results obtained in this chapter: ORZ stands for Outer Recirculation Zone, SL: Shear Layer and IRZ: Inner Recirculation Zone, often called central recirculation zone. The advantage of this injector is that it provides a high spray area-to-volume ratio, which can lead to the required level of atomization without large penetration lengths and improve atomization and mixing efficiency [257,258]. The dynamic of the flow (flame) is mainly based mainly on the swirl number, which defines as the ratio of the axial flux of angular momentum to the axial flux of linear momentum that is expressed as:

$$S_w = 2\frac{G_\theta}{G_x D} \qquad \text{Equation 3.4}$$

Where G_θ is the axial flux of the tangential momentum, G_x is the axial momentum of the tangential momentum and D is the combustor diameter or chamber cross-section for a square chamber. For more details, the book of Grinstein et al. [259] describes swirl injector types and their advantages.

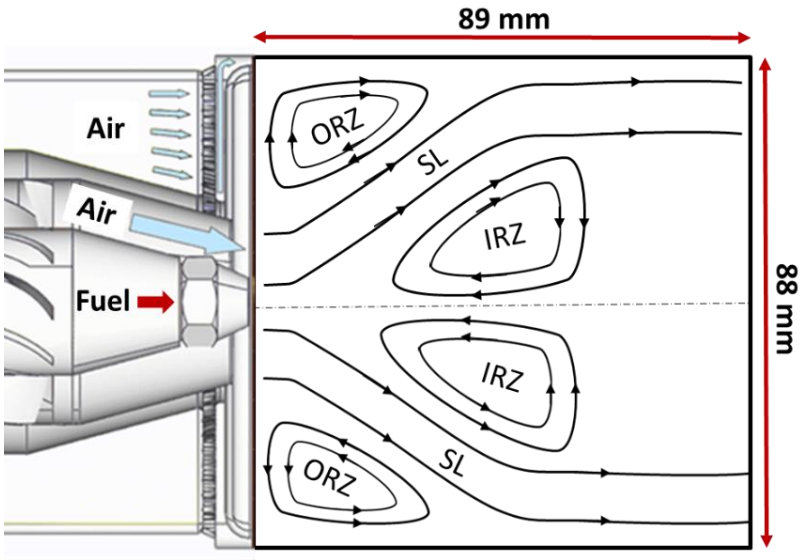

Figure 3.3 Schematic of MICADO swirled injector and flow field notation: ORZ Outer Recirculation zone, SL - Shear Layer, IRZ - Inner recirculation zone.

3.2 IMPLEMENTATION OF LASER-INDUCED INCANDESCENCE AND FLUORESCENCE (LII/LIF) ON MICADO TEST RIG

Laser-induced incandescence and fluorescence are implemented on the MICADO test rig to detect soot particles and precursors. However, these non-intrusive techniques are difficult to implement around combustors with such complexity. The difficulties are caused, on the one hand, by the restricted available room around the test rig and remote control of the instruments, and on the other hand, by the high variations in the density gradients of temperature and pressure inside the combustor [260,261]. These experiments were carried out in a joint collaboration with DLR Stuttgart in the framework of the SOPRANO project [253].

Table 4 lists six studied operating conditions with LII and LIF measurements. These six operating conditions (simulating the approach and cruise cycles) were selected because there is a high interest in knowing how much soot is formed at cruising altitudes and towards the descent flight segments. This information is relevant for explaining the formation of contrails. In addition, selected points ensure well-stabilized combustion, favorable to the acquisition of laser-based measurements in the volume of the combustion chamber. The last column of Table 4 shows an example of the instantaneous image of the stabilized flame on each OC.

Operating conditions	p_{ch} (bar)	Φ	$T_{air\ inlet}$ (K)	$\dot{m}_{air}$ ($kg \cdot s^{1}$)	$\dot{m}_{fuel}$ ($kg \cdot s^{-1}$) (pilot)	$\dot{m}_{fuel}$ ($kg \cdot s^{-1}$) (main)	Pilot: main	FF/FF_{ref} (%)	Instantaneous flame image
OC 1	8,08	0,77	542	0,399	0,021	0	100:0	60	
OC 2	7,85	0,704	548	0,486	0,0234	0	100:0	76	
OC 3	9,39	0,788	547	0,351	0,0189	0	100:0	46	
OC 4	10,08	0,788	544	0,25	0,0135	0	100:0	30	
OC 5	7,1	0,784	546	0,341	0,0183	0	100:0	59	
OC 6	7,14	0,796	547	0,336	0,0099	0,0084	54:46	58	

Table 4 Selected MICADO operating conditions during the SOPRANO project (LII/LIF measurements).

Figure 3.4 illustrates the variation of characteristic parameters such as the pressure, FF/FF_{ref}, global equivalence ratio, inlet air temperature and air and fuel flow rate of each OC represented in Table 4. Five OCs (from one to five) used only pilot injection of the fuel, and one OC (six), used simultaneous pilot and main injection of the fuel. Pilot injection refers to fuel injection through the central nozzle of the injector (diffusion flame). In contrast, the main fuel injection represents the premixed fuel and air injection through the swirl (premixed). The ratios between the two injection modes are varied with the OC. For the selected OC, the pressure of the chamber varies between 7.1 to 10.08 bar, FF/FF_{ref} spans the 30-76% domain, the equivalence ratio is between 0.704 and 0.796, the temperature is almost constant at 546 K, the total air mass flow rate is between 250 and 486 g/s, and the total fuel mass flow rate is between 13.5 and 23.4 g/s.

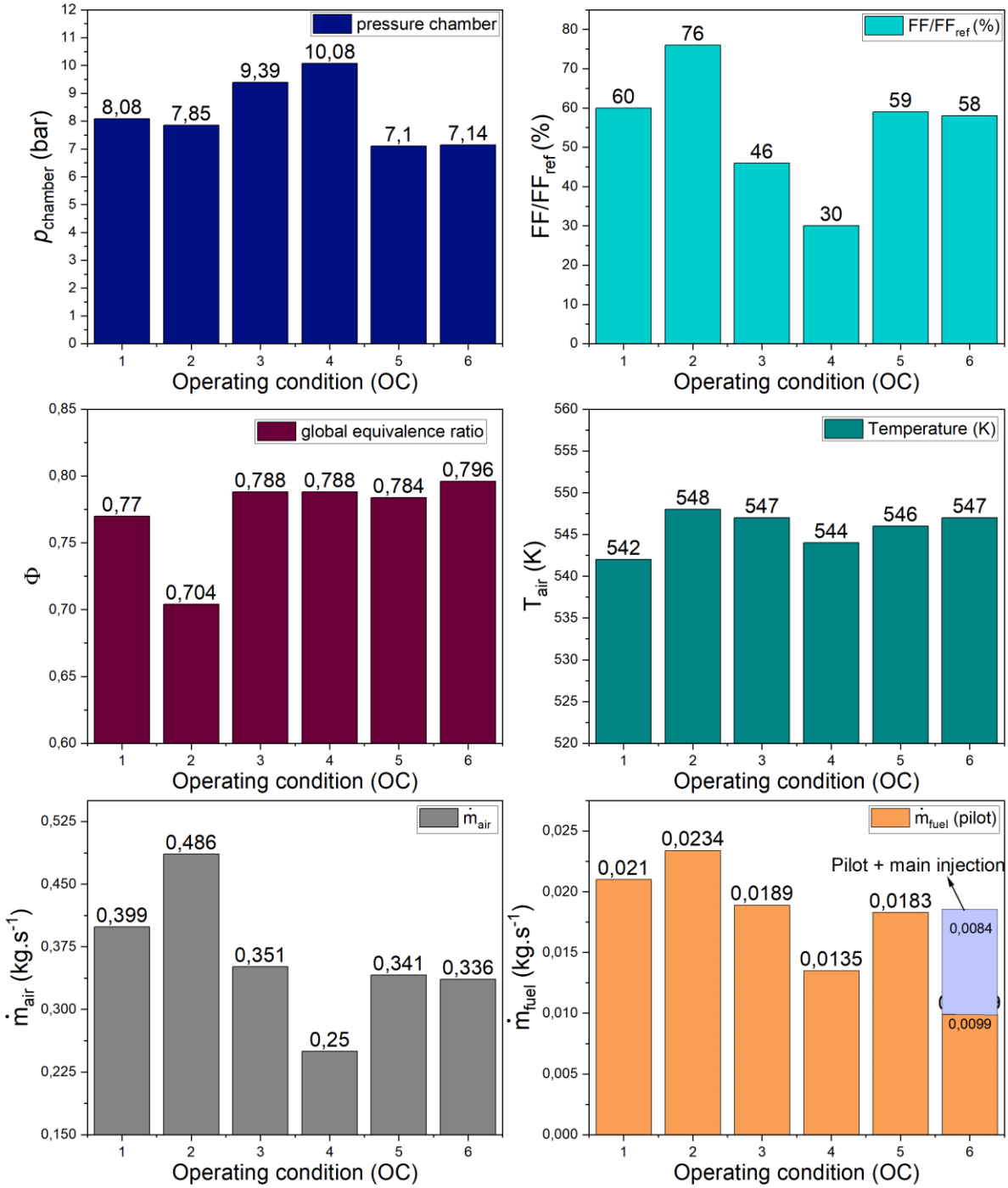

Figure 3.4 The variation of characteristic parameters for each operating condition studied with LII and LIF measurements.

3.2.1 Optical experimental setup

Optical experimental materials used in this study are performed with two Nd:YAG laser sources, a specific set of mirrors and lenses required for the laser sheet generation, and two intensified cameras for the acquisition systems. Two different lasers are used for the simultaneous measurements of incandescence and fluorescence images recorded by two synchronized intensified cameras. The two

measurements were classified based on the optical technique that was implemented. Their descriptions are described below:

1. For LII, the same optical configuration used in the work of Geigle et al. [55] was adapted near the combustor. The excitation source is a fundamental Nd: YAG laser (Brilliant B Quantel), λ = 1064 nm, with a pulse duration of 7 ns and a repetition rate of 10 Hz. A set of IR-coated mirrors are used to direct the generated laser beam from the optical room to the combustion chamber room. For generating an extended laser sheet, a first cylindrical (f = −50 mm) lens is used for expanding the laser sheet and a second spherical (f= 1000 mm) lens is used for focusing the generated laser sheet in the center of the combustion chamber. A laser sheet of 50 mm in height and 0.3 mm thickness was inserted transversally in the combustor, aligned with the nozzle of the fuel injector. The laser sheet energy in the focal point was 60 mJ/pulse (50 mm diameter size of the detector head). An image intensifier coupled with a dual-frame intensified CCD camera equipped with a Nikon f/2.5 lens recorded the induced LII signal. A double flame recording mode was selected to record the self-flame emission on the first image and the LII signal plus the self-emission of the flame with a short time difference between them. The flame emission and LII signals were recorded with independent gate widths of 20 ns with an inter-frame time of 200 ns. A temporal spectrogram between the laser pulses and camera recordings is shown in Figure 3.5. LII signals were collected perpendicularly to the laser sheet through a bandpass filter centered at $\lambda = 450 \pm 50$ nm. The LII camera recorded an image with a scale of (512 x 432) pixels and a spatial resolution of 5 pixels/mm. A schematic representation of the experimental setup around the combustor is displayed in Figure 3.6.

2. The second experimental configuration consists of the LIF setup (Figure 3.6). Based on the literature, it is known that most PAHs have strong absorption bands in the UV range (200 – 300 nm) and that their fluorescence emission spectra shift to higher wavelengths with an increase in PAH size [3,11]. To induce LIF from large PAHs, excitation can be shifted from the UV to the visible range; large PAHs are commonly considered to fluoresce upon excitation in the visible domain [262]. In this study, PAH-LIF measurements were performed using an Nd:YAG laser from Quantel (ULTRA Compact Folded Resonator 200) coupled to a second harmonic generator (SHG) module that generates a 10 Hz laser pulse of 10 ns at 532 nm excitation wavelength. A 70 mm x 1 mm laser sheet is formed using a negative cylindrical lens with f = -10 mm, an afocal system composed of two spherical lenses and a positive cylindrical lens with f = 1000 mm. Before the combustion chamber entrance, the LIF laser sheet is aligned (superposed) with the IR laser sheet via a laser beam combiner M2 (Figure 3.6). The laser pulse energy of 20 mJ was measured at the focus point of the laser sheet set in the middle of the combustor. This laser fluence was chosen to avoid the activation of the LII signal; to do this, different laser energies were tested before the measurement. The acquisition system used for LIF contains the sCMOS camera, which has an exposure time between µs to a few ms. An IRO (Intensified Relay Optics) is used to detect the LIF signal, with a GW of 50 ns and focus it on the sCMOS. Canon lenses with a focal length of 135 mm focus the region of interest (ROI) onto the sCMOS detector. A narrow-band filter centered at 580 nm with a bandwidth of 10 nm is added in front of the lenses to select the spectral bandwidth. The PAHs-LIF camera recorded an image of 2560 x 2160 pixels and a resolution of 26.4 pixels/mm. The resolution of both cameras was determined with a calibration target placed near the injector's nozzle.

Figure 3.5 shows a synchronization diagram between LII/LIF cameras with their corresponding laser pulses. The LII camera recorded flame-emitted (FE) and LII combined with flame-emission signals. The LIF camera was only recording emitted PAHs-LIF signal. A delay of 1 µs is set between LII and LIF

signal detection to avoid signal interferences. For each measurement (operating condition), a set of 800 images was recorded by each camera.

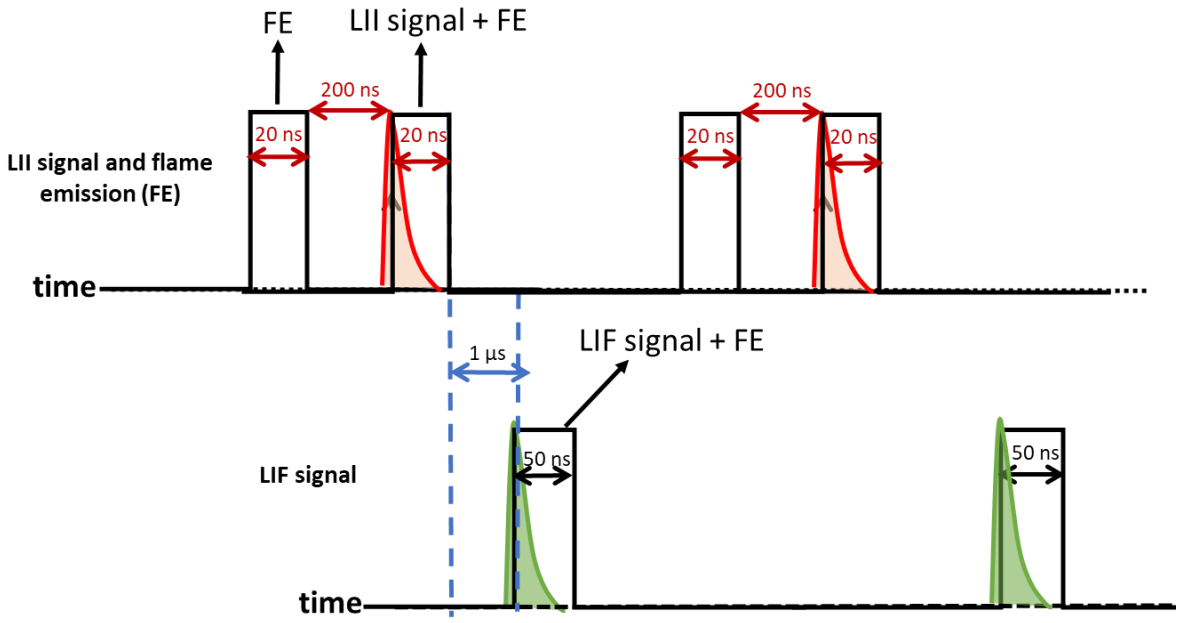

Figure 3.5 A diagram showing the synchronization between LII and LIF measurement. Both signals were recorded at 10Hz. FE stands for flame emission.

Figure 3.6 shows the LII/LIF optical configuration implemented around the MICADO combustion chamber. The optical configuration was set up in collaboration with DLR via the SOPRANO project [253]. DLR implemented LII to detect soot particles and ONERA added in parallel LIF for the quasi-simultaneous detection of soot precursors. The two lasers were installed in the optical room on the top of the combustion chamber. The two-laser beams are directed towards the combustion chamber room using different mirrors and are shaped into the described two laser sheets. Mirror 1 (M1) sends the generated laser sheet for LIF measurements into the combustor. Mirror M2 reflects the generated laser sheet for LII into the combustor and transmits the LIF-generated laser sheet (laser sheet combiner). A UV-visible high transmission mirror (M4) is placed below the combustion chamber to reflect the signals on the corresponding detectors. A dichroic mirror (M5) with a cut-off wavelength of 500 nm was used to direct LII and LIF signals onto their corresponding detection systems, placed at 90° one from each other. The wavelength domain 400 - 500 nm was directed toward the LII intensified camera, while wavelengths between 500 - 750 nm were reflected on the LIF intensified camera. Lasers and diagnostics controllers were placed in separate control rooms, while the laser sheet monitoring and detection devices were positioned near the combustor.

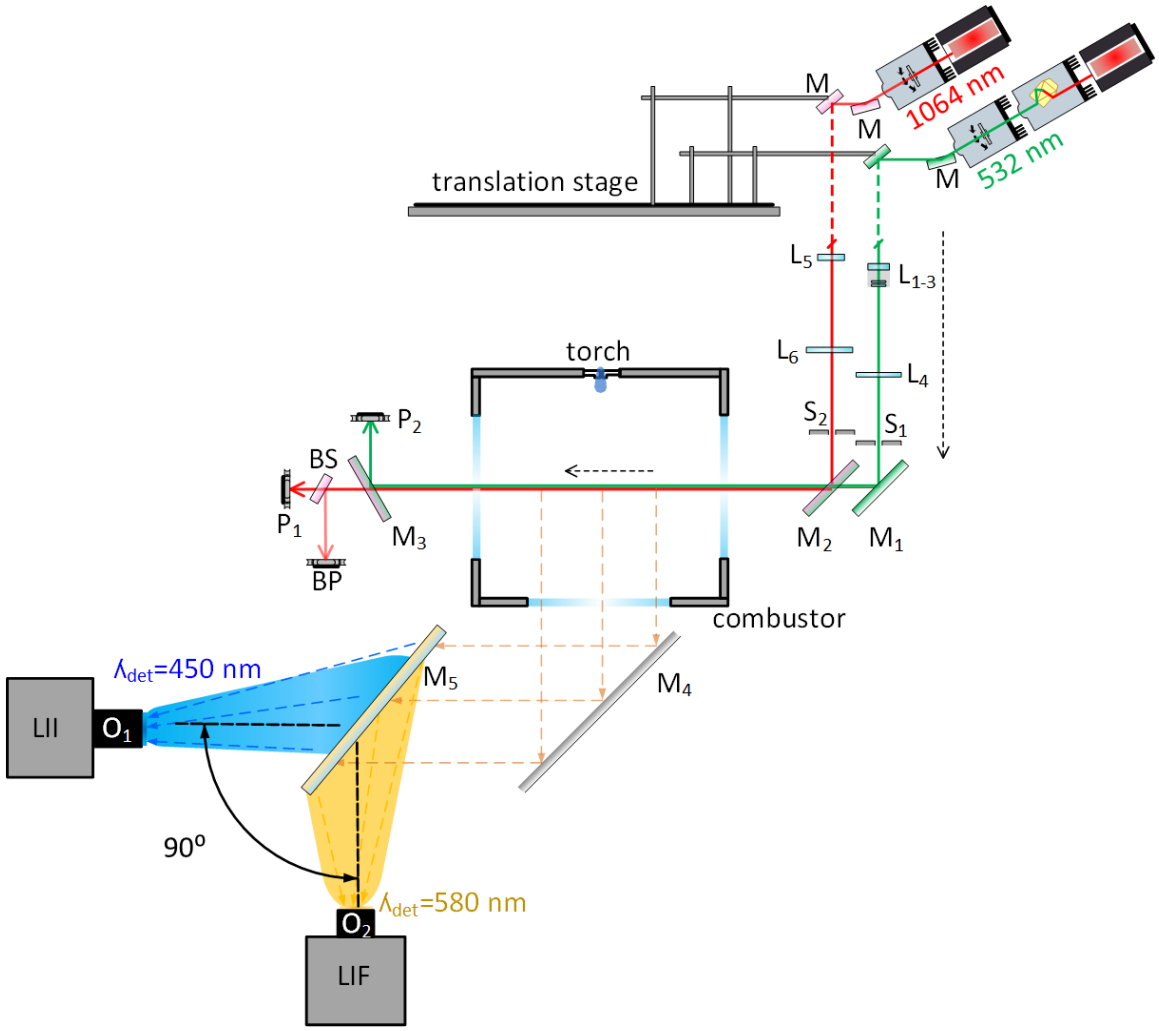

Figure 3.6 Experimental sketch of LII/LIF techniques installed on MICADO. L – lens, S – slit, M – mirror, P – power meter, BS – beam splitter, BP – laser beam profiler, F – filter, O – lenses, LII/LIF – intensified camera for LII and LIF.

Figure 3.7 illustrates the MICADO combustion chamber after installing all-optical techniques around the combustors. Implementing different optical technics in this environment is challenging as there is limited space behind the combustion chamber to install all optical components. The other limitation is the high radiative temperature and vibrations, which can damage some materials like the intensified cameras or defocus the laser sheet inside the combustion chamber.

The laser sheets' widths do not cover the entire cross-section of the combustion chamber. For this, two measurement positions are set to cover the entire field of view given by the optical access to the combustion chamber. For soot particles, the first position (P1) allows the laser sheets to irradiate a 50 mm transversal plane near the injector, while the second position (P2) is translated 44 mm downstream of the injector (towards the sampling probe). The LIF laser sheet covers 65 mm at position 1 and 34 mm at position 2. A remotely controlled translation stage was used to shift the LII/LIF excitation and collection optics to perform measurements at these two positions and obtain the complete map of soot particles and precursors inside the combustion chamber.

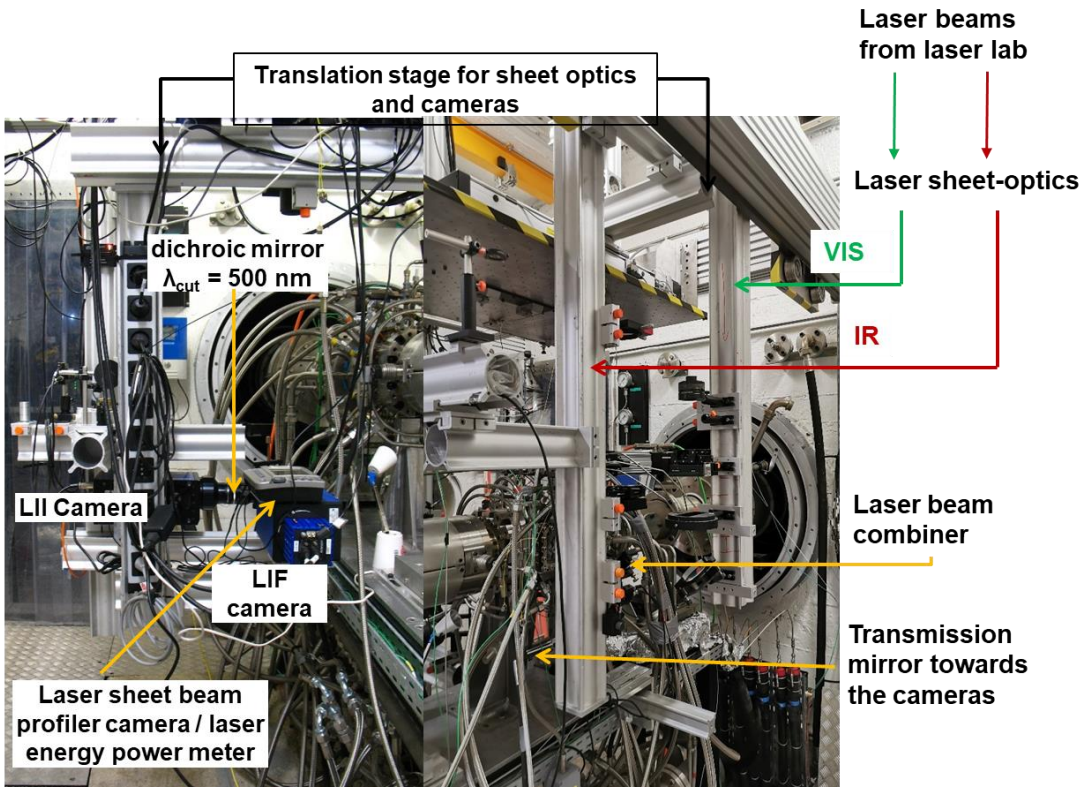

Figure 3.7 Schematic view of MICADO test rig after installing the coupled optical setup during LII/LIF measurement. The detection system is on the left-hand side picture and the optics for the laser sheet generation and coupling are shown on the right-hand side picture.

Figure 3.8 (a) illustrates the optical port view of the MICADO combustor with the ROI covered by LII/LIF when the translation stage is at position P1. Figure 3.8 (b) shows an example of an instantaneous image of the turbulent flame stabilized in OC6 (mixed pilot and main injection of the fuel, $\dot{m}_{air}$ = 336 g/s, $\dot{m}_{jet\ A\text{-}1}$= 18.3 g/s, p_{ch}= 7.14 bar and Φ = 0.796).

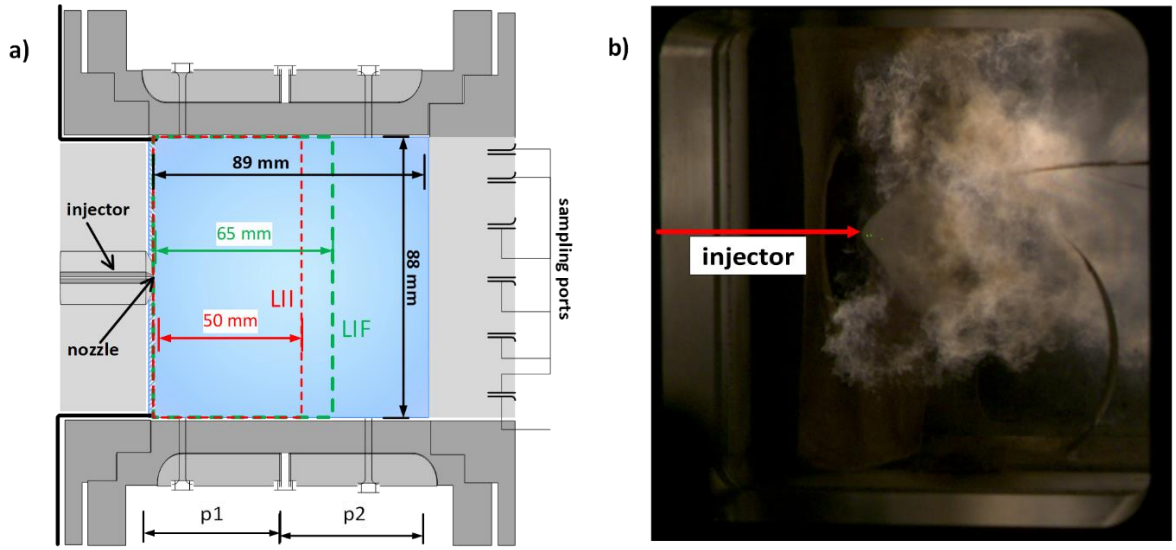

Figure 3.8 a) Cross section of the configuration of MICADO combustion chamber, showing the area covered by LII (red rectangle)/LIF (green rectangle) laser sheets in P1. b) Example of the flame inside the combustion chamber for OC 6.

After obtaining LII and LIF signals, different data processing steps are followed to obtain the final signals. For each measurement, a set of 800 images was recorded. During image analysis, the first step was background (electronic noise) subtraction. The camera's background image is recorded when the camera's aperture is closed. A background image intensity is subtracted from the recorded LII signal to obtain the images without a background. The second step consisted of separating flame emission from LII and LIF signals. The first recorded sequence of the LII camera was the flame emission, and the second was the LII signal combined with flame emission signals. The flame emission signals were subtracted from the combined LII and flame emission recorded signal to separate these signals. With the intensified cameras, applying a white image (flat field) correction is essential, as described in the previous chapter. The third step consists of using a flat field or white image correction to ensure the homogeneity of all pixels. The last step consisted in resizing the region of interest from the final obtained LII and LIF signal. The signals recorded by both cameras cover a substantial ROI, larger than the volume determined by the size of the laser sheet. Both cameras do not have the same image size.

A calibration target image with a known pattern size was recorded before each measurement and used to resize all images. As the signals were recorded at two positions, the images near the injector (P1) were cropped, considering a reference point of 2 mm from the injector. The images taken downstream of the injector were also resized, considering the right-hand-side limit of the optical access as the reference point. The LIF images were resized to be the same size as the one of LII, as the flame emission recorded by the LII camera has to be subtracted from the LIF-detected signal. The image size of the LIF signal was larger than the one of the LII signal, so a compression factor of 4 × 4 was applied to the LIF images.

3.2.2 Soot precursors and soot maps

This section describes the LIF/LII results obtained on MICADO six selected OCs. Soot formation in turbulent combustion flames is challenging to study due to the high intermittency, variation of local parameters and short residence times [263]. The soot formation is known to be heavily influenced by pressure and turbulence, but at such a scale, it is impossible to identify the parameters that affect soot formation when coupled [61]. Therefore, it is admitted that caution has to be paid when interpreting the experimental data obtained from highly turbulent combustion environments.

Nevertheless, implementing non-intrusive techniques like LII/LIF on MICADO test rig flame meets additional challenges due to fouling of the optical port views or damage during the measurement. This impacts the visualization inside the combustion chamber, changes the optical refractive index of the combustor windows and can worsen the quality of the laser sheet. The presented results show a shadow on the side near the exit of the combustor; this shadow is due to the window crack. Another challenge is the attenuation of the laser sheet due to the dense environment. The unburned liquid fuel can absorb the laser sheet, and this can bring difficulties in measuring soot particles and precursors in the volume of interest. The last challenge is based on the sensitivity and uncertainty of the chosen optical techniques, which are cumbersome to determine.

The response of the optical techniques in high-pressure and temperature flames is not well studied due to the technical limitations and the costs of such studies [264]. LIF is a good candidate for detecting soot precursors (PAHs) due to their high absorption coefficient and quantum yields [168,177]. Most of the challenges impacting the LII technique measurements are also encountered in

the LIF technique. However, considering that different phenomena are at the basis of LII and LIF, it is expected to have different variations of the LII and LIF signals based on the high pressure, the density of the environment and the temperature [177]. Even if a specific detection selectivity can be achieved for PAH fluorescence, making measurements in turbulent flames remains challenging due to the unresolved and broad-band structures of PAHs fluorescence and the lack of sufficient spectroscopic data at high-pressure and temperature flames [177]. Even so, it is interesting to have such information because it helps identify the soot formation regions, the evaporation rate of fuel and if there is a complete combustion.

The first step of implementing the LII technique on the MICADO test rig was measuring the needed laser fluence. In dense environments, there is quite an uncertainty on total pulse energy caused by scatter losses from the spray or particles while the laser sheet crosses the combustion chamber path of 100 mm. The laser sheet absorption within these combustion conditions is high compared to the laboratory laminar diffusion flame described in chapter 2. The laser fluence used for LII was established based on some tests performed at the beginning of the measurement campaign. The LII signal variation with the laser fluence was measured for OC 1. The value of the LII laser fluence was selected at the beginning of the plateau of the LII fluence curve.

On the other hand, the LIF laser fluence was selected based on measurements performed on the laboratory flame. The LIF laser fluence for test rig measurements was slightly increased with respect to laboratory measurements. LII signal was not detected on the delayed measurements for LIF. The LII absence from delayed LIF images may be either due to no LII signal interference or the fact that the LII decay time is shorter for harsh combustion conditions. Another way to double-check this interference was by inspecting the LIF/LII images, which did not contain similar structures of soot and PAH regions.

The six OCs are classified based on the flow factor FF, where three categories are identified:

- 1st category comprises the OC 1 and OC 2 with **$FF/FF_{ref} > 60\%$**
- 2nd category comprises the OC 5 and OC 6 with **$60\% < FF/FF_{ref} < 50\%$**
- 3rd category comprises the OC 3 and OC 4 with **$FF/FF_{ref} < 50\%$**

In this chapter, the presented result focuses on understanding and discussing the combustion parameters that impact soot formation among the six selected OCs.

The **LIF results** are presented first since they hold information on soot formation regions. Figure 3.9 shows an example of the detected instantaneous images of the PAHs LIF signal obtained for operating condition OC 1. The presented images were obtained after applying all correction parameters (flat field correction, flame emission and background subtraction) on row LII/LIF detected signals. This OC is characterized by FF/FF_{ref} of 60%, where the pressure inside the combustor is 8.08 bar, and the global equivalence ratio is 0.770 and pilot injection of the fuel.

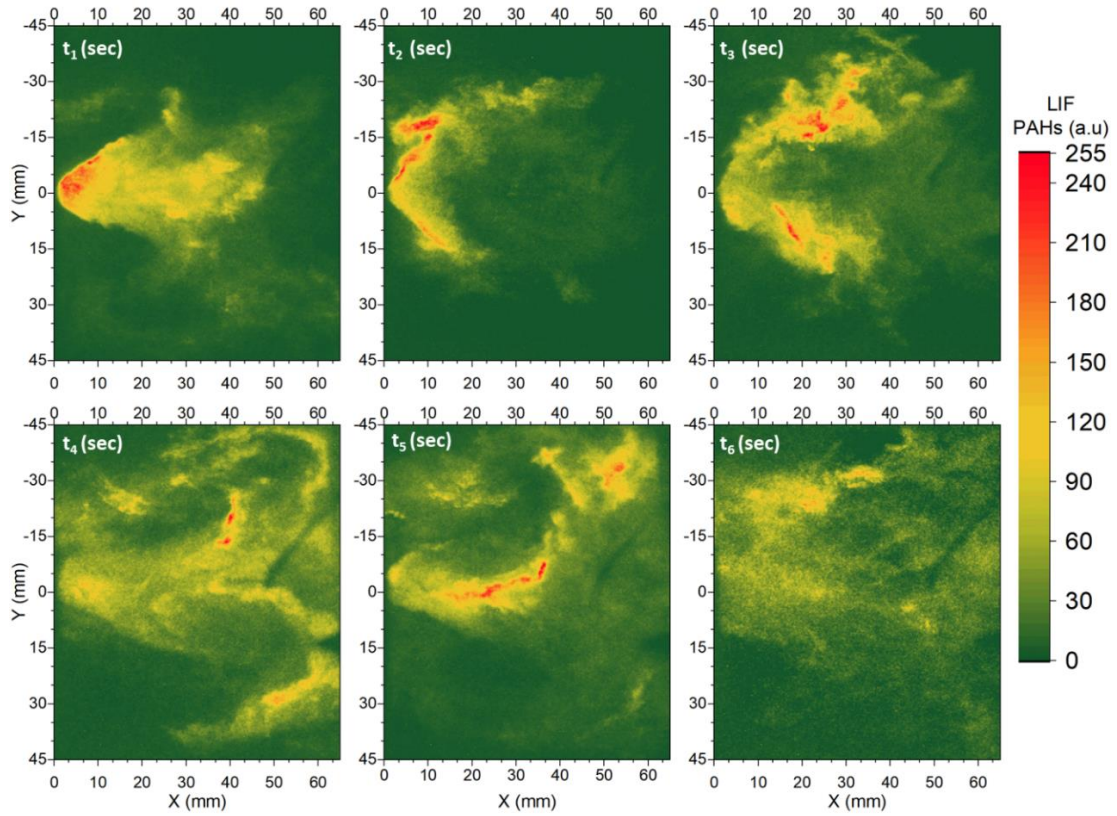

Figure 3.9 Example of six selected instantaneous images with LIF from PAHs obtained for OC 1.

The PAHs fluorescence signal changes from one image to another. In these types of flames, it is difficult to conclude the behavior (e.g., localization, types of PAHs) of PAHs molecules inside the combustor by only looking at the instantaneous signal recorded at 10 Hz. For all images, the PAH signal is distributed all over the combustion chamber with predominant intensity in the zone near the injector. As can be seen, the distribution of the signal fluctuates and can move either toward the IRZ or the ORZ due to the dynamics of the swirled flow.

The zones containing gas phase soot precursors have well-defined structures (edges) on the instantaneous images. As mentioned before, gas phase PAHs formed in aeronautical combustors are challenging to be attributed to a chemical formula. The detected PAHs can have pyrogenic and petrogenic origins as well. From their predominance near the spray region, it can be assumed that this category belongs to the vaporized fuel, while the PAHs transported towards the combustor exit belong to the gas phase combustion.

Figure 3.10 illustrates averaged LIF signals over 800 laser shots with their corresponding standard deviation at different operating conditions. In most cases (From OC 1 to OC 6), the averaged maximum intensity is found near the injector. Considering the pressure inside the combustion chamber, the averaged LIF signal increases with the pressure increase for all OCs with the pilot injection mode. The highest LIF intensity signal is observed near the injector, signals that are strongly reduced towards the combustor exit. The V shape of averaged signals looks almost similar to their corresponding standard deviation (std). However, some differences are observed in the opening of the V shape. OC 3 and OC 4 (category 3) have high PAH LIF intensity compared to the other tested conditions. These conditions are characterized by high pressure in the combustion chamber and low FF/FF_{ref} (46% for OC 3 and 30% for OC 4).

The OC 2 shows the lowest averaged PAH LIF signal; this condition is characterized by a pressure value of 7.85 bar with the highest FF/FFref of 76 %. By changing the injection mode from the pilot to the combined pilot-main injection on OC 6, the obtained PAH LIF signal highlights a moderated intensity with a high opening angle compared to the other tested condition.

OC 5 and OC 1 have intermediate values of LIF signal detected near the injector region and it seems that the two OCs have similar openings in the spray region.

The 2D mapping of the fluorescence signals is essential in depicting the distribution of the PAHs inside the combustor for particular operating conditions giving different modes and extending the factors affecting the soot precursors formation. In turbulent flame, different PAH species have significant differences in optical properties like molecular energy level absorption and absorption cross-section. They span a wide concentration range, and their absorption and emission features are broadened due to the collisional quenching of fluorescence based on local gas composition, temperature and pressure variation [177,265]. Therefore, only sampling and analytical techniques can allow a detailed analysis of the PAHs formed in sooting flames.

From all recorded LIF images on different operating conditions, information about the physical phenomena of soot precursors formation and interaction with the flow is obtained. The 2D mapping of average images is obtained by calculating the mean value of a pixel from N images and its standard deviation (std) from N images that depends on the LIF signal with a relation of $S_{LIF}(x, y, t)_i$. In addition, various radial and axial distribution profiles can be extracted from these images for further analysis and comparison.

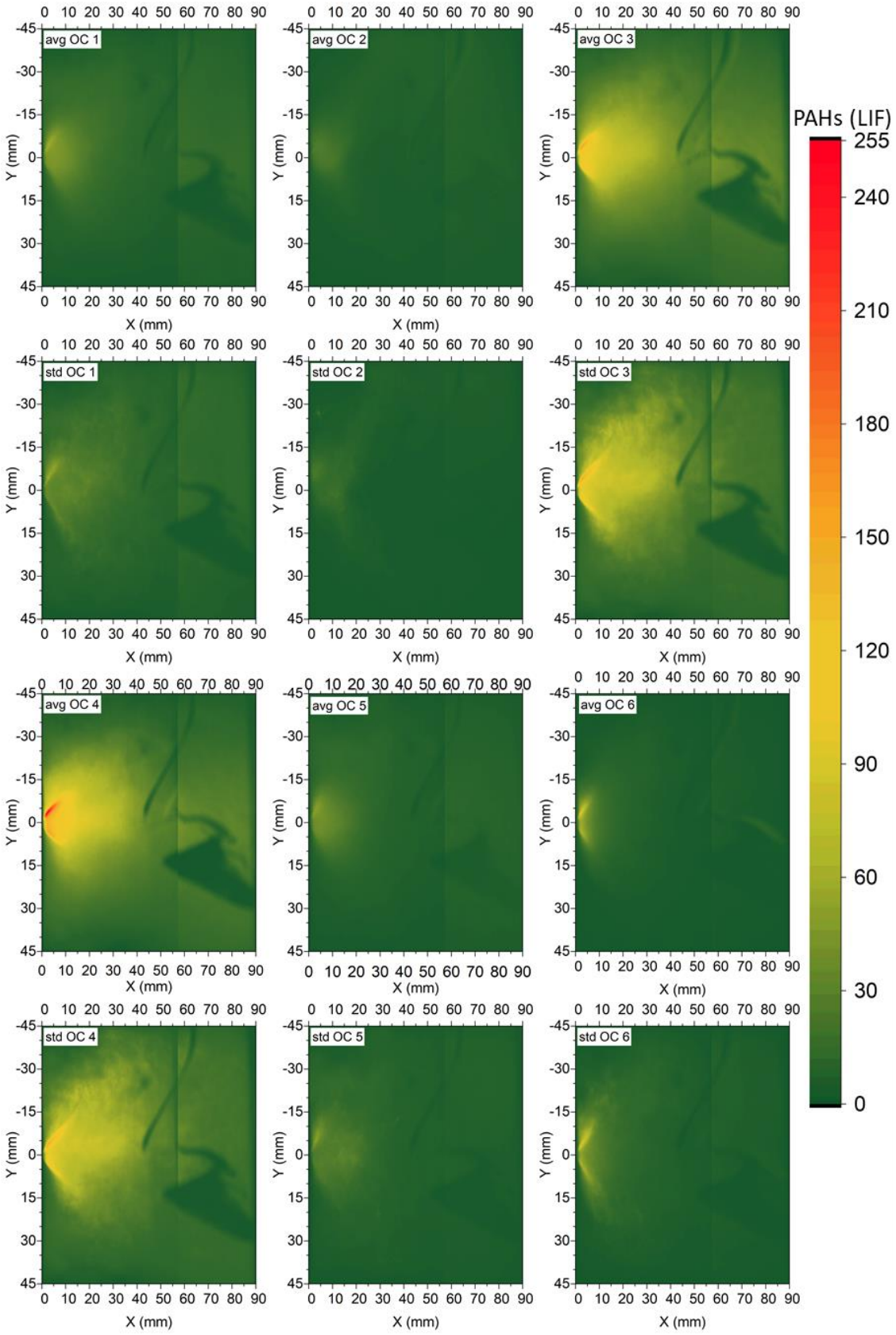

Figure 3.10 Averaged PAHs fluorescence signal with their corresponding standard error deviation for the six operating conditions. These averages are obtained from 800 images recorded at 10 Hz.

To see the details on the evolution of PAH molecules inside the combustor, Figure 3.11 shows the profiles of the LIF signal recorded upon the different tested operating conditions. These profiles were taken on a radial position at a given distance from the injector to the exit of the combustion chamber. For all tested operating conditions, the maximum fluorescence signal was obtained at a distance of 5 mm from the injector and the intensity decreased as the distance from the injector increased. Annex 3.6, Figure 3.31 shows the LIF evolution at different positions in the combustion chamber for all studied OCs.

For OC 1, the fluorescence signal has intermediate values compared to the other working condition. The second operating condition OC 2, has the lowest global equivalence ratio of 0.704 and the highest FF/FF_{ref}. This condition has the lowest signal profiles at all selected distances compared to the other studied operating condition. From this, it can be seen that the PAH molecules also depend on the proportionality of fuel and air used. The maximum intensity profiles were obtained on OC 3 and OC 4. These two OCs have the highest tested pressure (9.39 and 10.08 bar). At high pressure, the fluorescence decay time decreases due to the significant signal quenching. In literature, different studies have shown the impact of pressure on the formation of soot particles and precursors but mostly with UV-inducing wavelengths [43,49,266].

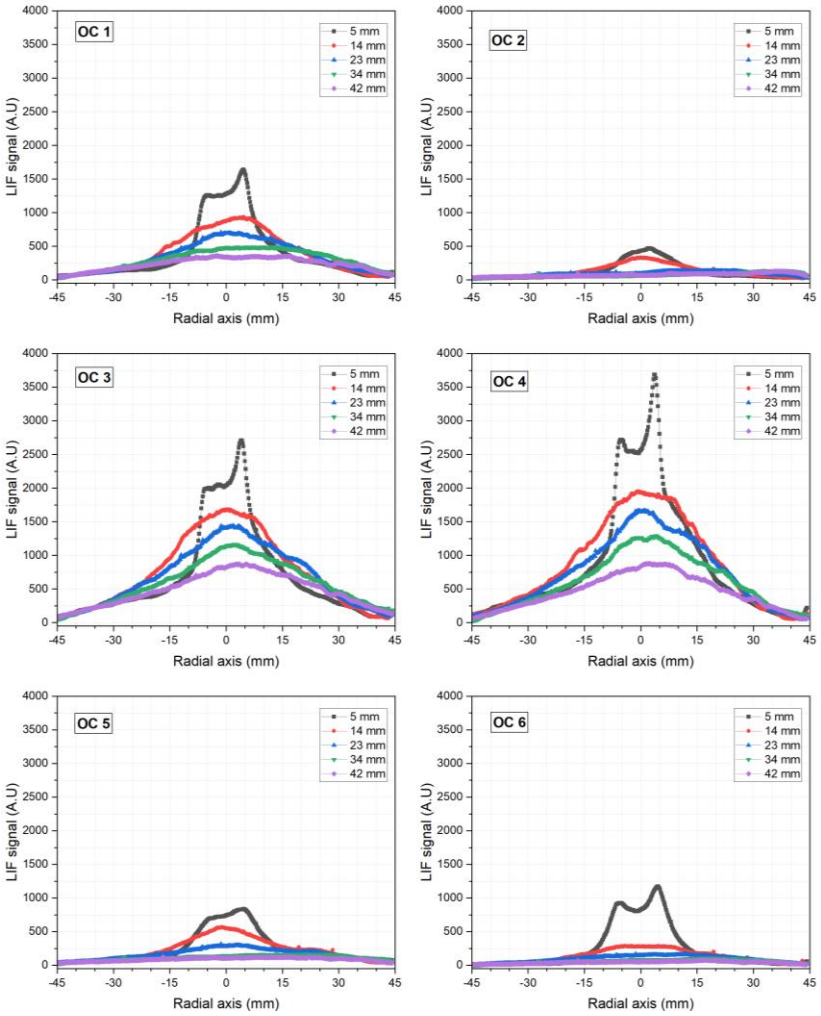

Figure 3.11 LIF signal evolution obtained at all tested conditions. The profiles were taken at the different axial positions from the injector.

As the results presented in this chapter were a joint project between different institutions, LII measurements were obtained in common with the researchers from DLR Stuttgart-Germany. Figure 3.12 shows an example of detected LII instantaneous images obtained for OC 1 and OC 4. On the instantaneous images, soot particle regions are distributed randomly over the combustion chamber with high-intensity predominance toward the inner recirculation zone compared to the PAH precursors that are seldom identified near the injector. On the instantaneous images, a significant change in the soot signal is observed from one image to another.

On OC 1, characterized by the pilot injection within the pressure value of 8.008 bar and global equivalence ratio of 0.770, the variation of soot volume fraction on instantaneous images changes from 0 ppm up to 2.7 ppm. This is 6.75 times higher than the maximum soot volume fraction obtained on the averaged signal. This range of values changes from one operating condition to another. By increasing the pressure to 10 bar and the global equivalence ratio to 0.788 on OC 4, the range of soot volume fraction on instantaneous images changes from 0 ppm up to 15.4 ppm. This condition is characterized by very high soot concentrations compared to other studied conditions, with high intermittency as well. The maximum soot volume fraction obtained on instantaneous images is almost 13 times higher than the maximum obtained on the average signal for OC 4.

Intermittency is the probability of not finding any soot at a given spatial location over a certain threshold [267]. Some studies demonstrated the high variability of soot distribution on instantaneous images strongly depends on the local gas composition history of the fluid volume moving through the combustor, combined with flow field effects causing strain and dilution [267,268].

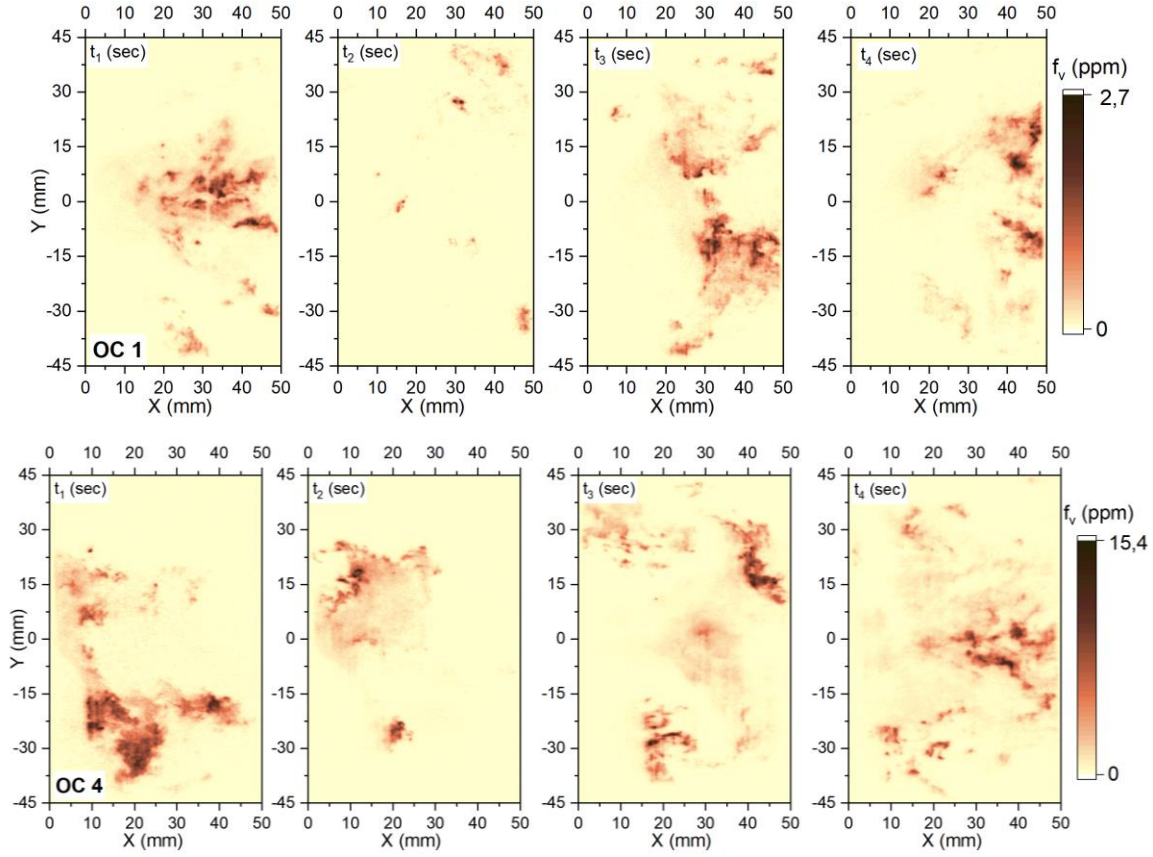

Figure 3.12 Instantaneous images with the soot volume fraction obtained from LII. The presented images represent the first sequence of recorded images on OC 1 and OC 4.

Shown instantaneous images prove that the instantaneous soot distribution differs utterly from the average values obtained on the series of 800 images. The soot concentration obtained on the averaged signal can be very different from the soot concentration detected on each sequence of images. Some conclusions on the distribution and localization of soot particles inside the combustors can be described with advanced statistical methods.

From the instantaneous images, soot clouds recirculate in the inner or outer recirculation zone based on combustion conditions. There are also diffused structures of the sharp filaments of soot that are observed in some images. Those instantaneous images are characterized by soot filaments with high temporal and spatial dynamics variation. The location of soot-containing areas within images changes significantly and the dynamics within single soot filaments are significant. Similar findings were obtained in the aero-engines studies made by Geigle et al. [265]. In contrast, the fluorescence of PAHs shown in the first instantaneous images (Figure 3.9) exhibits a more uniform intensity, with a larger coverage area per each than soot structures.

To quantify the LII signal into soot volume fraction, K.P. Geigle from DLR used an *ex-situ* calibration method performed on laboratory flames [53,268,269]. This calibration method is the same as described in the study of Geigle [53]. The levels of soot volume fractions obtained are proportional to the detected LII intensity. High LII intensity corresponds to high soot volume fractions. The calibration method used in chapter 2 on laminar diffusion flame was based on the 2C-LII calibration method. Applying this method to these measurements was not possible since the detection system belonged to them, and it was impossible to characterize it in our laboratory. As shown in chapter 2, it is necessary to apply a correction factor that takes into account the divergence of the laser sheet. This correction factor was not applied in this work because it is not sure if the correction ratio between the focal point and the extremities of the laser sheet remains the same for LII detection at high-pressure conditions. Some work is still necessary, and the raw data without the correction factor is presented in this work.

Different radial profiles were represented from the injector towards the exit of the combustion chamber to evaluate the distribution of soot on the radial profile. These radial profiles are shown in Figure 3.13, while the averaged soot volume fraction maps obtained for the six conditions are shown in Figure 3.14. Except for the OC 2, where the intensity profile is mostly distributed towards the edge of the flame, for all the other operating conditions, the maximum LII intensity is observed towards the center of the flame (IRZ). For all OCs, the lowest intensity of LII is observed at 5 mm from the injector, whereas the maximum intensity was observed at 42 mm. LIF and LII profiles show that the soot precursors are formed near the injector and once they are consumed, they are followed by soot particles.

FF/FF_{ref} mainly influences the flame dynamics that lead to the formation of soot particles in the MICADO combustor. For the OC 1 characterized by FF/FF_{ref} of 60% and the pressure of 8.08 bar, the maximum soot volume fraction obtained is 0.40 ppm. Soot particles are mainly localized toward the center of the combustor in the region with the inner recalculation zone; the soot signal is prominent after the PAHs fluorescence signal. By increasing the FF/FF_{ref} to 76% for OC 2, soot particles are mostly formed on the periphery of the combustion chamber, at 40 mm from the injector toward the exhaust. This distribution towards the walls of the combustor is mainly observed on the soot particle signal compared to the fluorescence signal. This operating condition (OC2) is characterized by

the highest air mass flow (0.486 kg s^{-1}) and highest FF/FF_{ref} (76 %) compared to the other operating conditions. Based on the obtained soot volume fraction, this condition has the lowest volume fraction of 0.08 ppm (at the maximum) compared to the other OCs. Individual spots of soot and precursors are observed on the instantaneous images of OC 2. The highest intensity observed on one side of the combustor chamber walls can be due to the laser sheet absorption or the asymmetry of the flame. This observation was obtained for all operating conditions with FF/FF_{ref} higher than 60%. The operating condition OC 3 is characterized by FF/FF_{ref} of 46 % and a pressure of 9.39 bar. This condition has a maximum soot volume fraction of 0.80 ppm. Soot particles are mainly formed in the centerline of the flame in the IRZ and towards the ORZ near the combustor backplate. The soot map has more like a transient V-like shape for the OC 3. The OC 4 is characterized by the highest tested pressure of 10.08 bar with the lowest air mass (0.25 kg.s^{-1}) and fuel (0.189 kg.s^{-1}) flows and the lowest FF/FF_{ref} of 30%. This condition resulted in the highest soot volume fraction of 1.2 ppm (at the maximum).

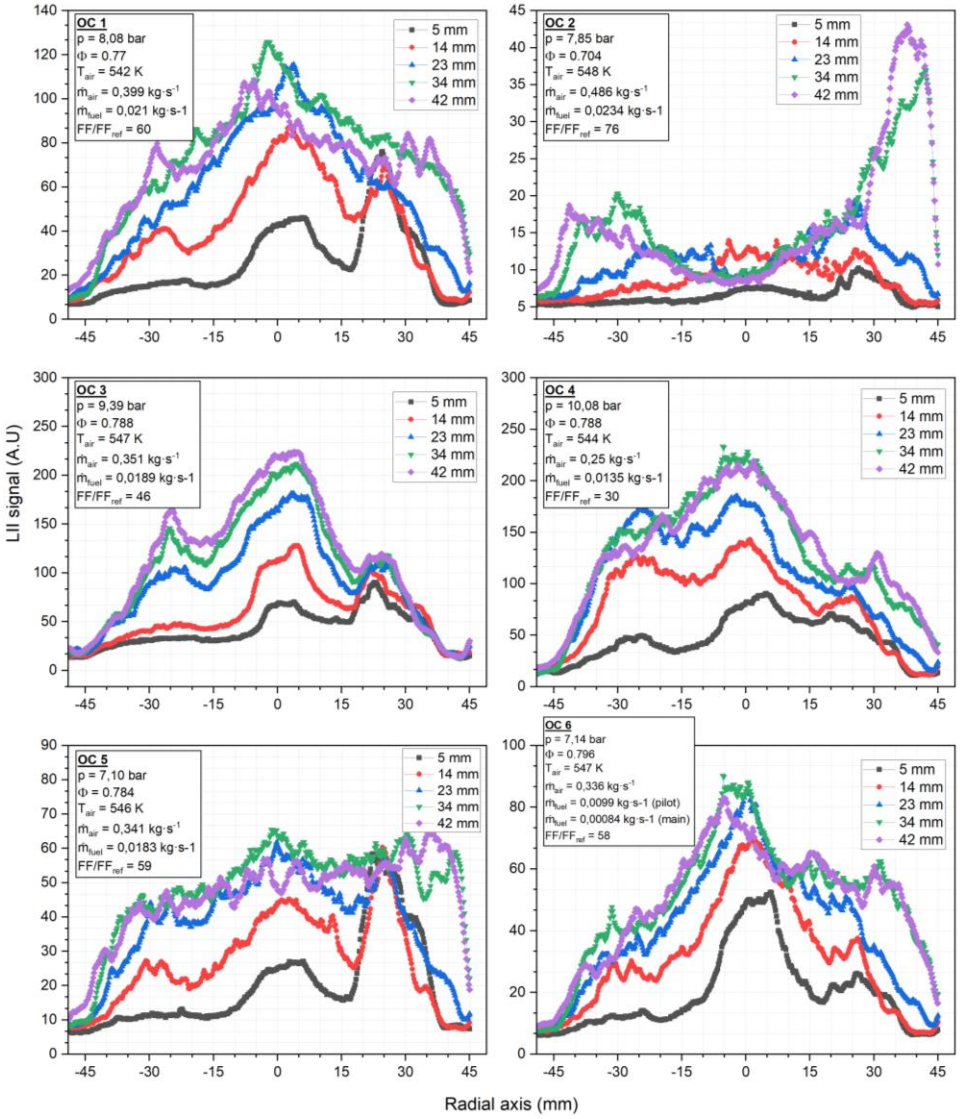

Figure 3.13 LII signal distribution profiles at the different positions in the combustion chamber. The selected profiles were averaged on 2 mm in each chosen position.

Overall the literature is stated that the LII signal increases with the pressure, but this combustion parameter cannot be decoupled from the other ones; therefore, some care has to be taken

when associating the increase of the LII with the pressure [53]. By increasing the pressure value, the decay time of the LII signal decreases due to the significant radiative cooling effects exerted on the particles from the sampled volume. However, despite the LII time decay decrease, the recorded LII signals are still prominent for OCs characterized by high-pressure values.

The operating condition OC 5 has a pressure of 7.1 bar and a global equivalence ratio of 0.784, showing that the soot particles are mostly distributed toward the center of the combustor. But high LII intensity was detected near the periphery of the combustor. The FF/FF_{ref} value is 59%, near the one of OC 1 (60 %). Besides that, FF/FF_{ref} for OC 1 and OC 4 is close, and the maximum soot volume fraction obtained on OC 4 (0.78 ppm) is almost double the value obtained on OC 1. This change can be caused by different pressure and flow rate values for these two conditions and by changing the fuel injection type from pilot to mixed pilot-main injection simultaneously on OC 6. The fuel split ratio between the pilot and main injection affects the distribution of the soot-rich regions in the combustor. The FF/FF_{ref} used for this condition is 58%; besides that, the pressure value used on OC 5 (7.10 bar) is almost the same as that of OC 6 (7.14 bar).

The maximum soot volume fraction obtained on this condition is 4.8 times lower than that of OC 5. The soot map has a V shape with high intensity in the inner recalculation zone of the flow. The study of Geigle et al. investigated the soot formation and flame characterization of an aero-engine model combustor by burning ethylene. They found that the chamber pressure and the equivalence ratio are the parameters that impact the most soot formation. Both these parameters influence soot concentrations as well as the shape and coverage area of the formed soot filaments. In addition, the air split between the inner and outer air nozzles influences the position of soot-rich regions. Increasing the mass flow rates at a given pressure and equivalence ratio improves mixing, thus reducing fuel-rich zones and decreasing soot formation.

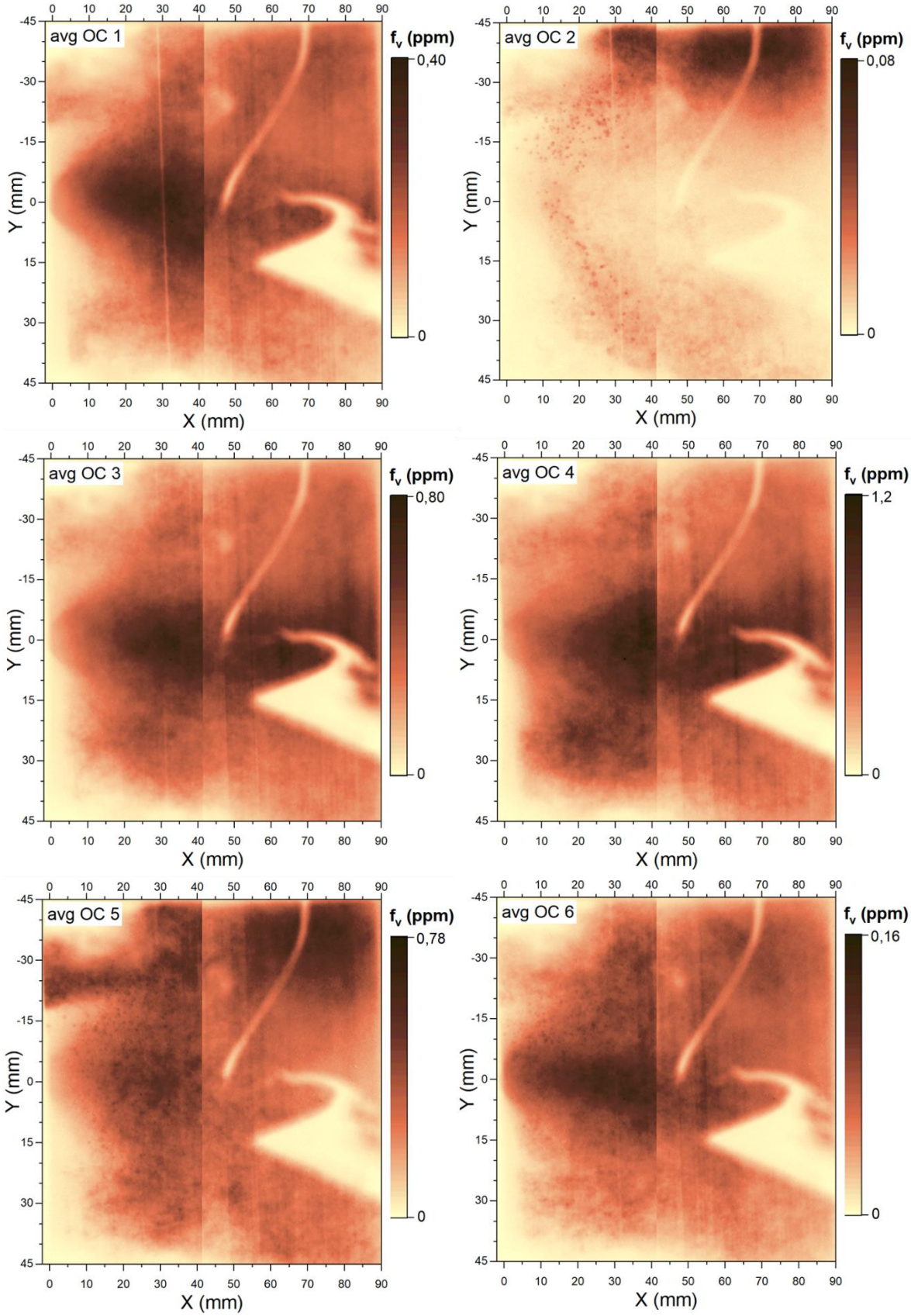

Figure 3.14 Averaged 2D soot volume fraction maps obtained for the six operating conditions.

The variation of soot inside the combustor depends on more factors. Figure 3.15 illustrates the dependence of the maximum detected values subtracted from the average image maps for the soot volume fraction and PAHs fluorescence signal inside the combustion chamber as a function of the different combustion parameters (FF/FF_{ref}, equivalence ratio, air temperature and chamber pressure) at different operating conditions.

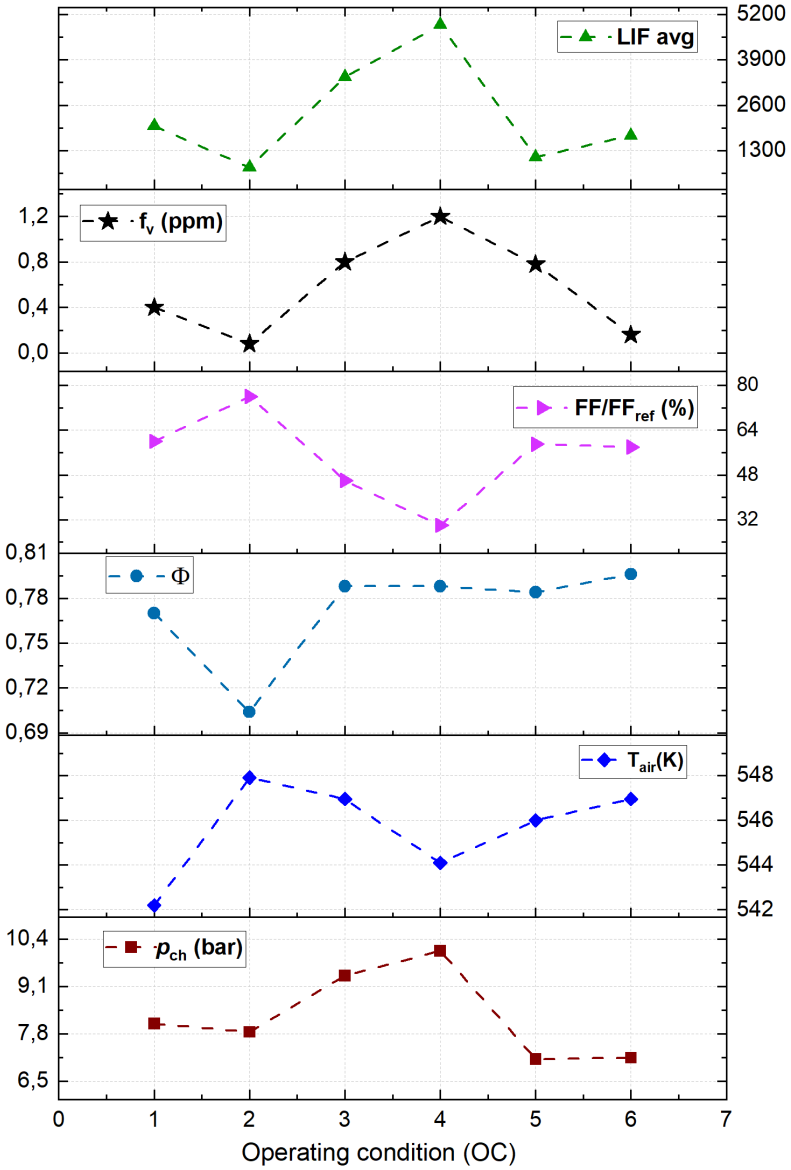

Figure 3.15 Influence of combustion condition parameters on obtained soot volume fractions and PAHs fluorescence at different operating conditions (OC).

Based on all combustion conditions' characteristics, high soot volume fraction and soot precursors correlate with **the pressure** value of the combustor. The obtained soot volume fraction is the smallest for the OC2, having the lowest pressure value. When the pressure increases, the soot volume fraction increases, and the same observation is obtained on the PAHs fluorescence signal. However, the pressure effect is proportional to the increase in the soot volume fraction only for the pilot injection of the fuel (OC 1 to OC 5). In the case of OC6, when switching to combined pilot and

main injections of the fuel, the maximum soot volume fraction decreased compared to the pressure value, but the PAHs fluorescence signal increased.

The **air temperature** (tiny variation) does not systematically affect the final soot volume fraction and PAHs fluorescence signal, but it slightly evolves as the FF/FF_{ref} values from OC 1 to OC 6. Garnayak et al. [29] investigated the effect of the preheated oxidizer (air) temperature on soot formation and flame structure in turbulent methane-air diffusion flame at 1 atm and 3 atm. They found that a rise in air temperature leads to the early appearance of soot, extending toward the exit of the combustor. In their results, the peak of soot volume fractions was observed at 293 K, a value that increased almost five times when the temperature increased to 723 K at the pressure of 1 atm. They obtained the same findings at the pressure of 3 atm, but they noticed a slight change in soot location when the pressure increased. Another key finding of their work is that the residence time of the fuel in the combustor decreases as the air temperature increases and increases with pressure elevation.

The global equivalence ratio can also influence the formation of soot particles and precursors. For example, when the global equivalence ratio decreased at OC 2, the soot volume fraction and fluorescence signal decreased. While the soot volume fraction increased when the equivalence ratio increased at OC 3. For the other operating conditions, there is no well-defined variation of the global equivalence ratio function of the soot volume fraction and PAHs fluorescence signal.

Gleason et al. [270] studied the effect of **equivalence ratio** and **temperature** on soot formation in partially premixed counterflow flames. They found that as the equivalence ratio is lowered, the premixed flame component shifts away from the diffusion flame component. The resulting broadening and local temperature increase of the soot-forming region promote soot formation, as surface growth is enhanced and oxidation is suppressed because of the lower concentration of O_2, increasing both soot volume fraction and particle sizes.

The effect of the $\mathbf{FF/FF_{ref}}$ on soot formation is observed. The importance of FF/FF_{ref} resumes the effect of the total air mass flow rate, air temperature and pressure inside the combustion chamber on soot particles and precursors. From the obtained results for all operating conditions, when the FF/FF_{ref} value increased, the soot volume fraction and PAHs fluorescence signal decreased. FF/FF_{ref} value impacts the localization of soot particles inside the combustor. For OCs where the $FF/FF_{ref} > 60\%$ (OC 1 and OC 2), the soot signal intensity is high near the walls of the combustor, and the soot map distributions (Figure 3.14) have an M-like shape. For the $60\ \% < FF/FF_{ref} < 50\ \%$ (OC 5 and OC 6), soot is formed mainly in the centerline of the flame in the zone of inner recirculation. Most of the structure of soot and precursors maps obtained with these conditions have a V shape. The last category consisted of $30\ \% < FF/FF_{ref} < 50\ \%$ (OC 3 and OC 4), which are the lowest tested values for the FF/FF_{ref}, and the operating conditions in this zone highlight high-intensity signals of soot particles and PAHs fluorescence. The effect of the combustion parameters on soot volume fraction can vary depending on the injection mode.

Figure 3.16 shows the Pearson correlation between different combustion parameters with soot and PAH results. Again, Pearson correlation was employed to determine the influence of each parameter on the maximum soot volume fraction and maximum LIF signal for each operating condition. As explained in chapter 2, Pearson correlation measures the strength of the linear relationship between two variables. It has a value between -1 to 1, with a value of -1 meaning a total

negative linear correlation, 0 being no correlation, and + 1 representing a total positive correlation [271].

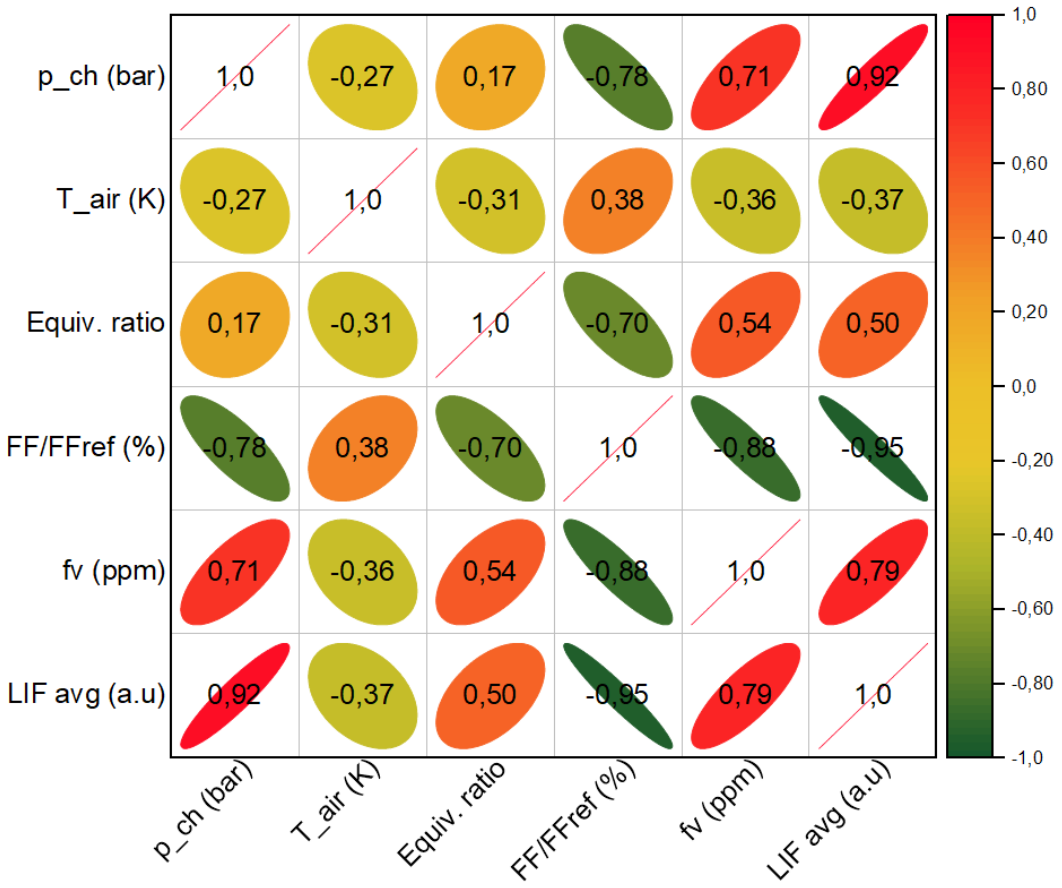

Figure 3.16 correlation map between the pressure in the combustion chamber p_{ch}, the temperature of the air T_{air}, global equivalence ratio, flow factor ratio (FF/FF_{ref}), soot volume fraction (f_v) obtained from LII detected signal and LIF averaged signal for the six operating conditions.

In other words, this correlation map summarizes how the characteristic parameters of the combustion impact the LIF and LII values. Therefore it is possible to extract a correlation factor for each parameter and its effect on one of the measured signals (LII or LIF).

A **positive correlation** exists between the **pressure** inside the combustor with soot volume fraction (0.71) and LIF averaged signal (0.92). A factor with positive correlation means that if variable one increases, variable two will also increase.

There is also a **positive correlation** between **global equivalence**, soot volume fraction (0.54), and PAHs LIF signal (0.50), but this parameter impacts less the formation of soot than the pressure.

A **weak negative correlation** is observed between inlet **air temperature**, soot volume fraction (-0.36), and PAHs LIF averaged signal (-0.37).

A strong **negative correlation** is observed between **FF/FF_{ref}** with soot volume fraction (-0.88), and PAHs LIF averaged signal (-0.95), meaning that if the FF/FF_{ref} decrease, the soot particle and precursors will increase. A strong correlation means a high probability of the described phenomena

happening, whereas a weak correlation refers to a lower probability of defined phenomena or no clear trend. For example, with inlet air temperature, it can be possible that the soot particles and precursors can increase or decrease as the temperature changes.

Since the FF/FF_{ref} extensively describes the trends of soot formation in the combustor, it is necessary to characterize the spray dynamic and the flow field for at least a few OC identified in this first part.

3.3 FLOW FIELD AND SPRAY DYNAMICS

This subchapter describes the implementation of PIV and Mie/Rayleigh scattering on the MICADO test rig for a few selected OCs already presented in the previous subchapter and one extra OC at a lower pressure value of the combustion chamber. These techniques are used as complementary techniques of LII/LIF to help identify the phenomena impacting the soot particle formation inside the combustor based on the flow velocity field and spray dynamics. The scattering technique was implemented in the framework of the Astoria project that aims to account for soot particle morphology in flame radiation and optical diagnostics in complex systems [254].

3.3.1 Particle image velocimetry PIV

The knowledge of the velocity vector fields and the orientation of the velocity vectors is one of the prime interests in combustion as it plays a crucial role in providing qualitative and quantitative information about the flow movement. Therefore, PIV is an up-and-coming technique because it can instantaneously provide comprehensive information about the flow field [272]. It is an intrusive technique relying on recording two consecutive images with tracer particles seeded into the flow. The PIV working principle is to indirectly measure the field flow velocity vectors by analyzing the motion of seeded particles in the flow. Usually, the size of seeded particles is very small compared to the flow scale; thus, the velocity of each seeded particle can be considered as the velocity of the fluid where it is located. The particles' density must be light enough to follow the flow. The images of the movement distances of all particles or ensembles of particles in a whole flow field can be measured from a series of consecutive images to derive the velocity vector field [272,273]. The seeding particles are chosen based on their melting temperature, density and sizes that can follow the flow easily [274]. The displacement of these tracers is measured from the correlation of two consecutive images [275].

One drawback of PIV in a reactive flow is particle seeding of the flow and distinguishing higher light scattering components over the flame emission background for the second recorded image. High measurement accuracy requires a sufficient number of seeded particles in the measuring volume, defined by the laser sheet [273]. The other challenge is related to the high turbulence and pressure in the combustion chamber, leading to rapid fouling of the optical access. These few points are underlined here because they were directly addressed during the implementation of PIV on the MICADO combustor. Other details about the PIV applications in high-pressure combustion chambers are presented by Chen et al. [274].

In turbulent combustion, there is some limitation that has to be taken into account during PIV measurements and attention has to be taken to these parameters. First, the time delay between the laser pulses should be long enough to capture the tracer particle displacement and short enough so

that the particles with an out-of-plane velocity component leave the laser sheet. Secondly, with the use of high-power lasers, the tracer particle size can be small. Therefore, the accuracy of the PIV measurements will drastically improve as the particles follow the flow more closely. Lastly, the interrogation window size should be small such that there is no significant velocity gradient within the interrogation area [276].

3.3.2 Experimental PIV setup

Each type of PIV setup needs fitting hardware and software for flow field measurement. Even though many types of PIV are applied today, they still include standard processes. PIV measurements consist of four main experimental parts: seeding, illuminating particles using a laser, image detection using a camera and image processing. Each stage should be rigorously performed for accurate PIV measurements in the whole experiment. The enumerated steps of PIV measurements are detailed as follows. The first one consists of seeding particles in the analysis environment.

When particles have an adapted behavior of traceability to a fluid flow, the particle velocities usually represent the local fluid velocities. The small particles seeded in the fluid to trace its flow should be distributed as homogeneous as possible in the fluid, be well reflective, accurately follow the motion of the fluid and not change the properties of the flow. Generally, particles that satisfy the four conditions have diameters of a few μm and a density that makes them almost neutrally buoyant in the fluid [272,277,278]. If the seeding concentration is appropriate, it corresponds to the density of velocity vectors desired. The second stage consists of illuminating seeded particles by using a laser. In 2D PIV measurements, a uniform laser sheet illuminated the flow field of light-scattering tracer particles. Most PIV lasers have a Gaussian beam and care has to be taken on the optics used to shape the laser beam into a laser sheet to analyze the ROI. This is because the divergence of the laser sheet change along the propagation axis, as demonstrated in chapter 2. The third step consists of the detection system. A series of images capturing the particles following the flow are recorded by high-resolution cameras. Accurate velocity measurements require a short time interval Δt between two consecutive images. The optical axis of the camera lens must be perpendicular to the plane of the light sheet. Hence, the camera should be calibrated to determine its parameters before image detection [272]. The last step in PIV measurements consists of the image processing toolbox. Some examples of image processing include removing noise, flame luminosity and smoothing. The data processing steps depend on the type of measurement. By putting some interrogation windows on consecutive images, the particle velocity vectors are calculated by various methods. The interrogation window has to be chosen wisely based on the flow dynamics.

In this study, the following experimental setup was used during PIV measurements on the MICADO test rig and a schematic of the used configuration is illustrated in Figure 3.17.

- A particle-seeding system consisting of a pressurized air supply panel and a cylindrical container with a cyclone allows the suspension of particles. During the measurements, the used particles are magnesium oxide (Mg0) with particle size distribution centered at 1 μm. They were chosen because they can withstand the reactive combustion environment (high temperature). In addition, a small quantity of Aerosil nano-particles, known as fumed silica particles, was added to fluidize the seeding particle admixture and reduce the risk for particle aggregation in the seeding line. A carrier flow of air (between 2 to 5% of the total air mass flow used for the OC) entrains the

particles after passing through a cyclone and mixes with the main air flow of the combustor via the seeding injector.

- The lighting source is a high-frequency Quantronix Darwin-dual Laser containing two Nd: YLF oscillators. Two SHG modules convert the laser fundamental into the second harmonic with a 527 nm exit wavelength. The power emitted by each cavity is 25 mJ/pulse. The laser frequency is tunable and can be changed from 1 to 10 kHz, with pulse durations between 120 and 180 ns.

- A set of mirrors is used to direct the emitted laser beams from the optical control room to the MICADO installation combustion room. The Gaussian laser beams were shaped into a laser sheet of 100 mm height and 1.2 mm width by using a set of lenses consisting of a cylindrical negative lens (f= -50 mm), two spherical lenses and a positive cylindrical lens (f= 1mm). The two overlapped laser sheets are directed transversally through the combustor and aligned with the center of the injector.

- The acquisition system comprises a Phantom camera V711, a Canon objective with a focal distance of 135 mm and a filter centered at 527 nm. The camera sensor detector has a resolution of 1280 x 800 pixels, with a maximum recording rate at the full frame of 7530 frames per second (fps) and a minimum exposure time of 1 µs. PIV measurements were performed in double-frame mode with an inter-frame time of 5 µs. A high reflective mirror positioned under the combustion chamber reflects the Mie scattered signal to the detection system.

- A computer equipped with Davis 10.1 software was used to control the camera and two laser cavities and ensure all systems synchronization.

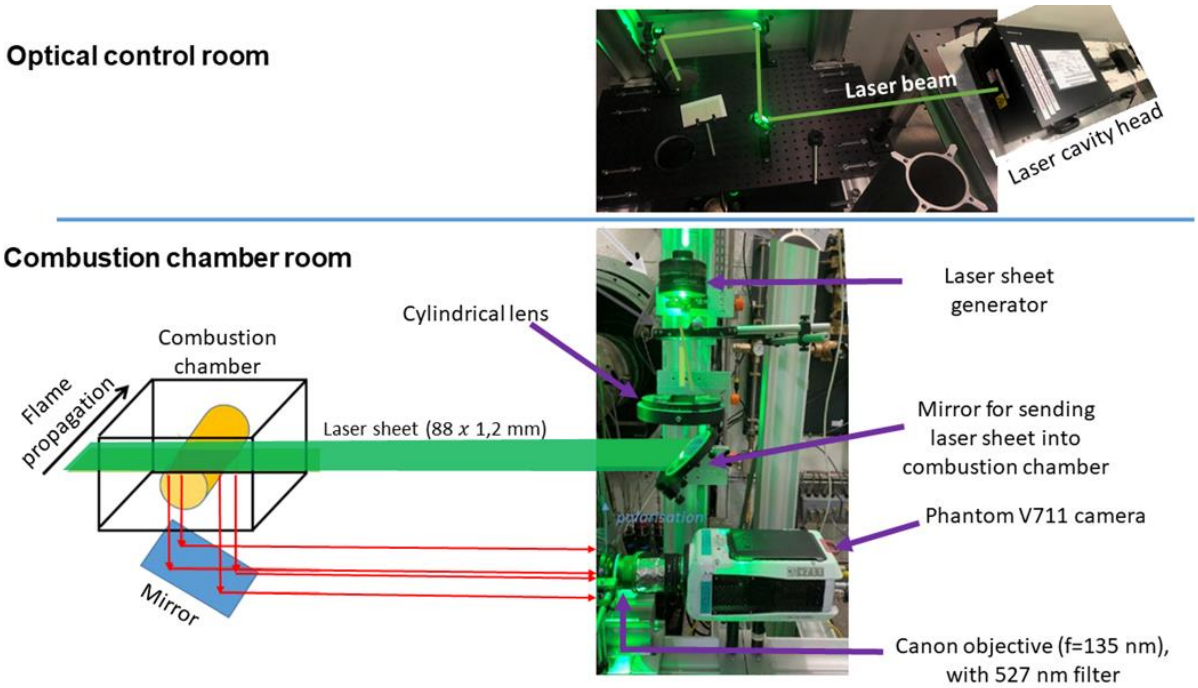

Figure 3.17 PIV and scattering experimental setup installed on MICADO (figure adapted from internal report of Astoria project, December 2020).

Applying PIV in a liquid fuel combustion chamber is challenging due to the swirled flow and mixing of particles with the non-vaporized fuel. A common problem encountered in seeding flows with solid particles is the tendency of seeding material to deposit onto access windows, rendering them optically opaque. Although the MICADO test rig uses air cooling flow near the windows, over time, seeding accumulated on the optical port views. This is why in all PIV presented results, only a 50 mm distance from the injector is covered. The flame luminosity impacts the second recorded image from the PIV series, where the exposure of the GW is longer than the first image. The recording of the first image is at the end of the camera window, while for the second image, the exposure is at the beginning of the gate width exposure. This means that higher flame luminosity is captured on the second image. In this case, the laser intensity is varied to a value where the Mie scattering from particles is superior to the luminosity of the flame. Another challenge is the interference between the Mie scattering from Jet A-1 droplets and the Mie scattering from seeded particles. The PIV analysis of images with both scattering components makes it impossible to determine the velocity field in the region near the spray. Similar challenges were identified in the study of Willert [279], which focused on planar flow field measurements in atmospheric and pressurized combustion chambers. For more details, interested readers can refer to the work of Sciacchitano [34], highlighting the different sources of uncertainties in PIV measurement.

3.3.3 Steps for PIV data analysis and results for velocities flow fields

The application of PIV measurements in pressurized combustion chambers is limited by several issues as the swirled flow, strong luminescence from the flame emission, Mie scattering from the fuel droplets and the seeding procedure. Table 5 shows the tested operating conditions during PIV measurement tests on the seeding methodology performed under similar flow conditions (total $\dot{m}_{air}$) as the ones used during LII/LIF measurements. Preliminary tests helped define the operating parameters of the seeding cyclone and particle flow rate with respect to the total air mass flow rate. Selected operating conditions OC 2 and OC 3 have the same working parameters as the ones used for LII/LIF on OC 2 and OC 3 Table 4. The seeding rate was chosen between 4% to 5% from the total air mass flow rate. A short seeding time was selected for each operating condition of the test rig.

Nevertheless, the optical accesses were covered with particles towards the combustion chamber exhaust, which led to a reduced exploitable region of interest for the obtained velocity vectors near the injector. Therefore, a supplementary operation condition (OC 1) was selected among the two common cases studied with LII/LIF, and a lower pressure value of 4.5 bar was chosen for this case.

Operating conditions	OC 1	OC 2	OC 3
p_{ch} (bar)	4,448	8,08	9.56
Φ	0,806	0,683	0,777
$T_{air\ inlet}$ (K)	563	548	543
$\dot{m}_{air}$ (kg·s-1)	0,227	0,472	0,346
$\dot{m}_{fuel}$ (kg·s-1) (pilot injection)	0,0131	0,0231	0,0193
$\dot{m}_{fuel}$ (kg·s-1) (main injection)	-	-	-
pilot: main injection	100:0	100:0	100:0
FF/FF_{ref} (%)	66	76	47

Table 5 Operating condition parameters tested during PIV measurements on MICADO test rig.

The PIV image data analysis process can be a source of error in estimating the flow field velocity. Different steps are followed by using LaVision software to deduce the velocities field. The recorded images are scaled according to the default pixel count and depend on the software settings.

The first step of data analysis consisted of setting a proper scale parameter (5 mm/pixel) and applying it to all recorded images. The second step consisted of applying an algorithmic mask that eliminates the scattering signal from non-vaporized fuel, as underlined in Figure 3.18 with red color.

The third step consisted of the calculation of the velocity vectors. As described in the previous section, these velocity vectors are calculated by overlapping the two frames with a specific interrogation window. Since the observation area is high, a (16 x 16) pixels interrogation window with a 50% 2D overlap by geometric mapping was set to calculate the vectors from the two frames with 5 µs between them. A maximum expected displacement of 8 pixels, meaning half of the interrogation window, was set, resulting in a maximum speed of 195.6 m/s.

The last data analysis step focused on the vector validation processes and noise removing. The vectors are calculated with a certain amount of uncertainty caused by various factors, such as the faint tracing of the seeding particles. The vector range was defined into a limited area of 12 pixels in all directions and a peak ratio intensity lower than 1.4. Since the particles are microscopic, the signal results in regrouping vectors of the same size.

Figure 3.18 shows two consecutive images with the seeded flow during reactive conditions on operating condition OC 1. The image set represents the complete optical access (88 x 89 mm) of the combustor. A region of 50 mm near the injector was processed with the PIV tools. The ROI near the combustor exit was not visible due to damage to the optical port view (window fouling), which hindered the laser sheet intensity across this region. The signal in the set of images represents the scattering from the fuel spray (red color) and the scattering from particles (white dots).

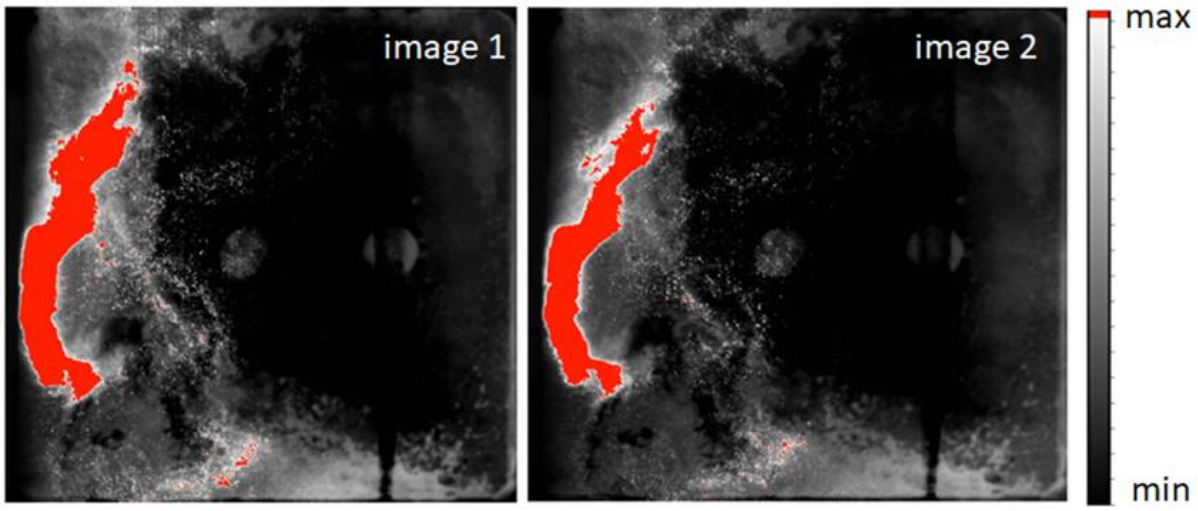

Figure 3.18 A set of two consecutive images showing the seeded flow for combustion conditions corresponding to working point OC 1.

PIV measurements are particularly difficult under these conditions. In addition, the presence of the atomized spray poses a problem in interpreting the PIV measurements. The primary sources of errors in PIV measurements in the reactive environment are demonstrated in different studies.

For 2D PIV configuration, there are two-dimensional velocity vector components: one is on the X-axis, and the other is on the Y-axis. The magnitude of the total velocity vector field length ($\mathbf{V_L}$) is obtained from the square root of the velocity fields on the X-Y axis component and is expressed by the following equation:

$$\boldsymbol{V_L = \sqrt{V_x^2 + V_y^2}} \qquad \text{Equation 3.5}$$

V_L is the magnitude of the total velocity (m/s) (expressed as vector length in Figure 3.19, Figure 3.20 and Figure 3.21). V_x and V_y are velocity components on the X and Y axes (m/s).

Figure 3.19 illustrates the 2D velocity vector maps ($\overrightarrow{v_x}$, $\overrightarrow{v_y}$ and $\overrightarrow{v_L}$) obtained for operating condition OC 1. The presented fields are averaged over 5500 images. This OC is characterized by a pressure of 4.45 bar and a global equivalence ratio of 0.806 with an FF/FF_{ref} value of 66%. The maximum average velocity on the X-axis is 76 m/s, with a fluctuation (the stdv) of 39 m/s from the maximum value (Figure 3.19). The high-velocity field on this axis is mainly on the edges of the flow with lower velocity in the inner and outer recirculation zones. The averaged velocity on the Y-axis has a maximum value of 23 m/s with a high standard error deviation compared to the X-axis. The averaged velocity field on the Y-axis is mainly distributed on the upper edge of the flame. The maximum velocity vector length for the X-Y axis is 80 m/s, distributed mainly on the edges of the flame with lower intensity in the inner and outer recirculation zones. The velocity vector fluctuation length is 45 m/s. The velocity field length has a V shape with low intensity at the injector exit. This low intensity is due to the unburned fuel and makes it difficult to deduce the velocity field in that region due to the masked zone, which was removed. On these conditions, the penetration of unburned fuel can be seen until a distance of 5 mm from the injector. OC 1 has the highest averaged velocity field values compared to the other tested conditions. These high-velocity vector values may be due to the lowest injection value

of air (0.227 kg/s) and fuel (0.0131 kg/s) flows, which allows particular sensitivity of particles to follow the flow.

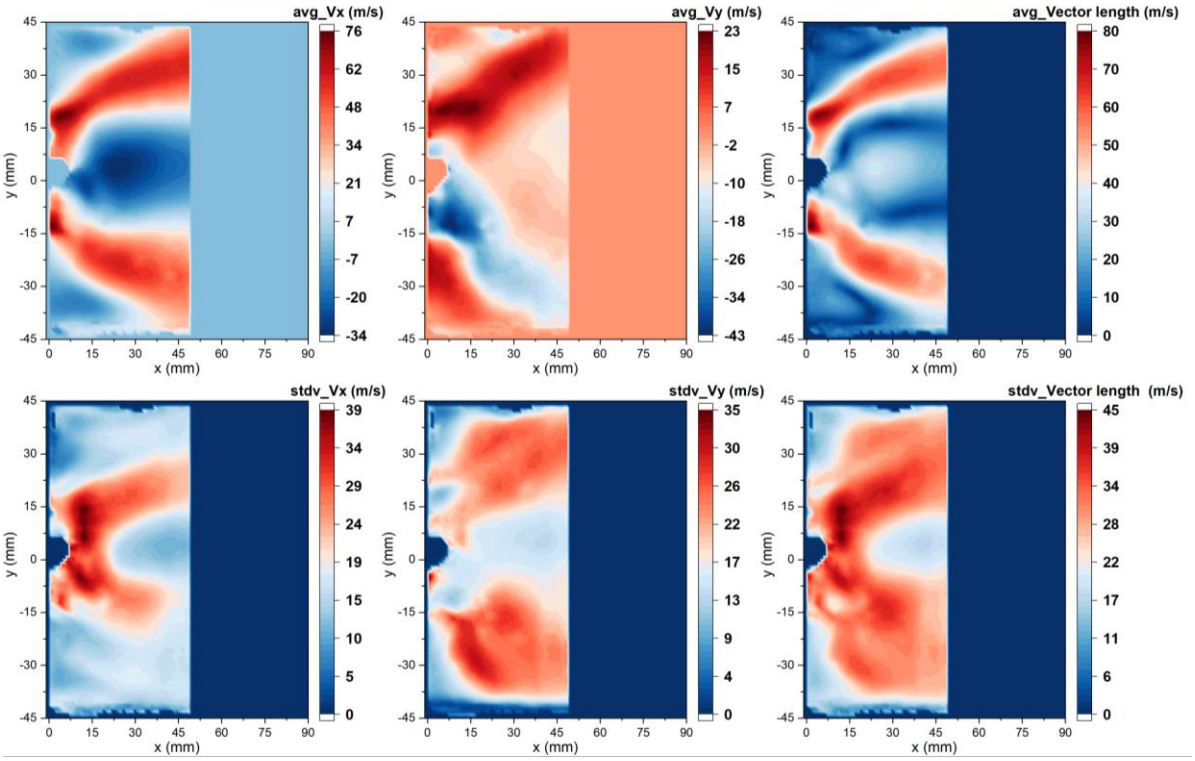

Figure 3.19 2D averaged and standard deviation (fluctuation) velocity vector field obtained on operating condition 1 (OC 1), the presented averaged velocity fields are obtained on X-axis, Y-axis and the vector length module on both X and Y.

By changing the operating condition, Figure 3.20 illustrates the velocity vector fields obtained at OC 2 with their corresponding standard error deviation (fluctuation over the recorded series of images). The presented averages resulted from over 55000 images. This operating condition is characterized by a pressure value of 8.08 with an FF/FFref of 76%. It is observed that the velocity vector fields reduced slightly on both components X-Y compared to the first operating conditions. The maximum average velocity field on the X component is 69 m/s, whereas, on the Y axis, it is 35 m/s. The vector for both components results in the maximum averaged velocity fields of 73 m/s. On the magnitude of the resultant velocity field length, a high-intensity value is observed on the edges of the flame (shear layers). The velocity intensity distribution on standard deviation (fluctuations) can also be seen in the inner recirculation zone, which is low on the averaged fields. This condition is characterized by the highest FF/FF_{ref} (76 %) and highest air mass flow (0.472 kg/s) compared to OC 1 and 2.

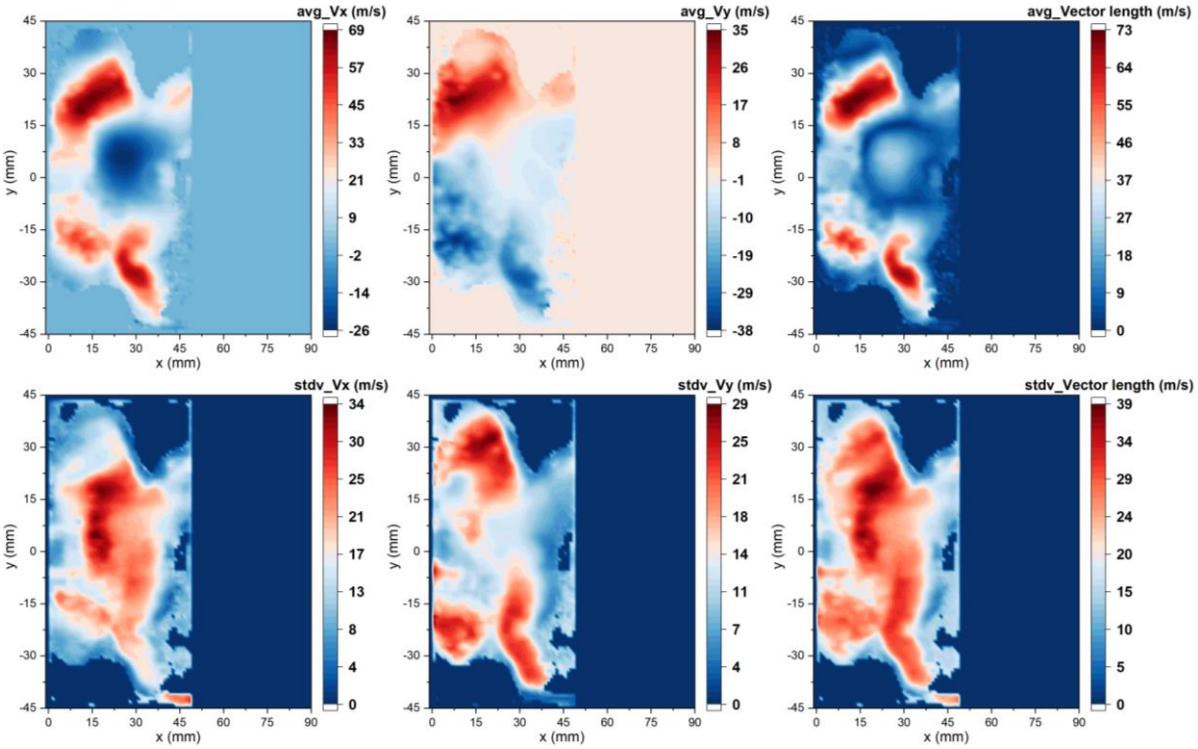

Figure 3.20 2D averaged and standard deviation (fluctuation) velocity vector fields obtained on operating condition OC 2.

The last tested conditions for PIV measurements correspond to operating condition OC 3. This OC is characterized by a pressure value of 9.56 bar and FF/FF_{ref} of 47 %. This OC has almost the same parameters in terms of pressure and FF/FF_{ref} as the OC 3 studied with LII/LIF measurement. With this condition, the maximum averaged velocity fields on X-components is 53 m/s with a maximum standard deviation of 44 m/s. This component has a high-velocity field intensity distribution in the upper and lower shear layer. On Y-component, the maximum averaged velocity field is 25 m/s with a fluctuation of 22 m/s. The high-velocity intensity on this component is mostly distributed on the upper shear layer. For X-Y components, the high-velocity intensity is mainly distributed on the upper shear layer on averaged velocity fields.

In contrast, high intensity can also be seen in the inner recirculation zone for the map with the fluctuations (stdv_V_L). The velocity field obtained on both components (V_L), the maximum velocity vector value is 54 m/s and 47 m/s for the fluctuations. On average, the high intensity is distributed on the upper shear layer, whereas on standard deviation, the high intensity is mainly in the inner recirculation zone on X components and both shear layers on Y components. Based on the findings of averaged velocity fields, it is observed that the velocity field decreases when the air mass flow increases. Therefore, this OC has the lowest velocity component compared to OC 1 and OC 2. The flow velocities changes affect the soot and PAHs formation and distribution inside the combustion chamber.

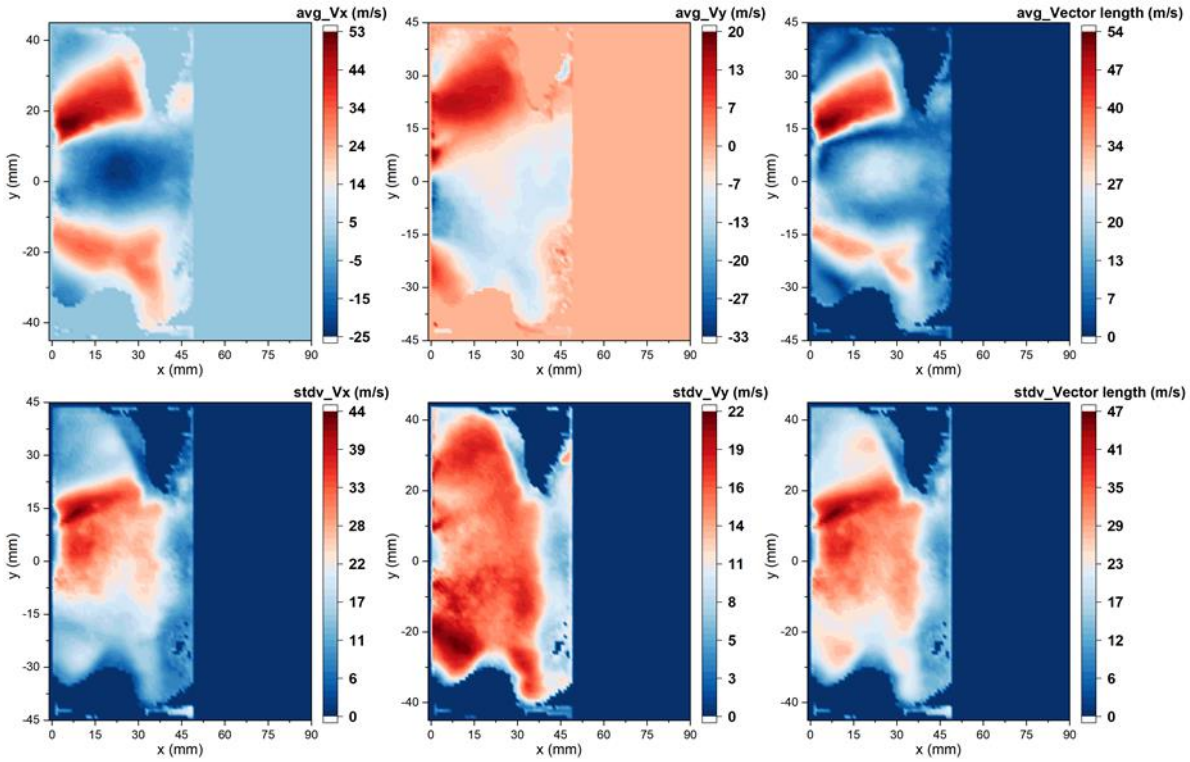

Figure 3.21 Averaged and standard deviation (fluctuation) velocity vector fields obtained on operating condition OC 3.

The aim of using PIV in this study is to understand the interaction of the flow fields and soot particles inside the combustor. Figure 3.22 illustrates the overlay of averaged velocity vector field maps and averaged soot volume fraction maps obtained for OC 2 and OC3.

The distribution of velocity fields correlates with the distribution of soot particles. At OC 2, the maximum velocity field intensity is observed near the injector on the upper and lower shear layers. However, soot particles are also distributed on the upper shear layer towards the edge of the combustor. In this condition, by analyzing instantaneous images, in some cases, soot is seen in the form of localized thick pockets that are transported by the flow and is confirmed on the averaged signals where the orientation of maximum velocity vector fields correspondent with the maximum soot intensity. This condition (OC 2) is characterized by high velocities components and the lowest soot volume fraction compared to OC 3.

On OC 3, the highest velocity vectors are mostly distributed on both shear layers with high intensity on the upper share layer. The predominant region with soot particles is mainly in the center of the inner recirculation zone. When the maximum averaged velocity vector fields decreased for these two operating conditions, the maximum averaged soot volume fraction increased.

In addition, we observe that the maximum intensity of soot particles is obtained forward after the maximum velocity fields. The limitation of correlating the averaged intensities map of flow fields and soot particles is that soot formation distribution strongly depends on the instantaneous fluid structure and flow condition (turbulence, pressure, temperature, global equivalence ratio and flow rate), and the averaged map cannot show the change in the distribution from one image to another.

Geigle et al. [280] studied the flow field characterization of pressurized sooting swirl flames and their impact on soot distributions inside the combustor. Their findings showed a spatial correlation between soot presence and mean flow field, where the maximum soot was observed on the condition with lower flow field velocities.

In this study, the result of the averaged flow field confirmed that soot presence is primarily close to the inner shear layer between the flow and recirculation zone. The findings correspond to the results obtained in Figure 3.22, where soot is primarily formed in the inner recirculation zone. From the average, the general correlation between the velocity field and soot particles can be based on the residence time. The region with **low-velocity field** value favors **high residence time** for soot particles, leading to **high concentrations of soot particles**.

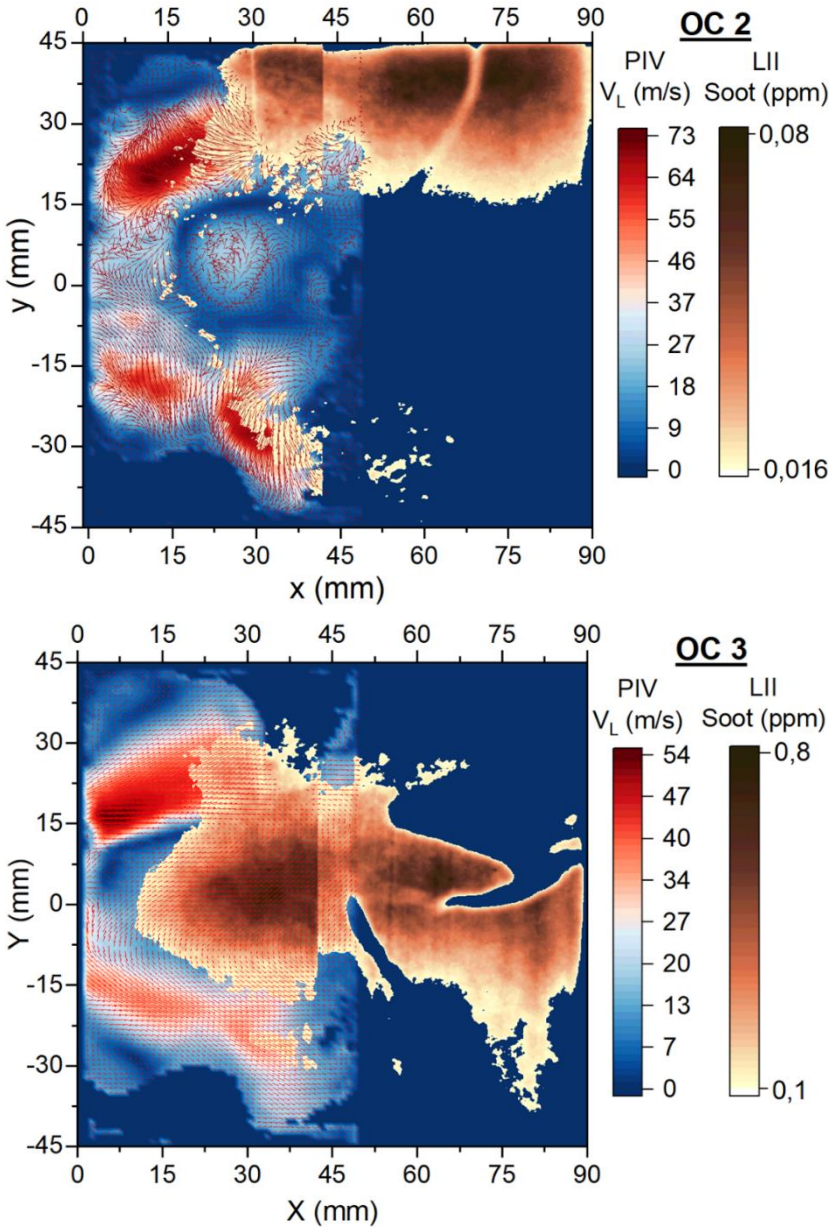

Figure 3.22 Overlay of averaged velocity vector fields with 2D LII soot volume fraction maps obtained for OC 2 and OC 3.

To enhance the understanding of the soot and PAHs localization in the combustion chamber, Figure 3.23 shows the velocity field (PIV), soot (LII), and PAHs (LIF) profiles evolution, taken at 5 mm and 34 mm radial position from the injector towards the exhaust of the combustor. From these profiles, at OC 2, the velocity field profiles near the injector (5 mm) correspond to the LIF signal where the maximum intensity is observed in the center of the recirculation zone of the injector compared to the profiles obtained at 34 mm. In comparison, LII intensity is low near the injector (5 mm) and high toward the shear layer of the upper side, where the velocity decreases. This information can be related to the residence time in the combustor, when it increases (low-velocity vectors) the soot detected signals increase with respect to the region near the injector. The distribution of PAHs that occur before the soot particles for all tested conditions shows how soot precursors participate in the formation of soot particles. The intensity of PAHs reduces as the distance from the injector increases, whereas the soot intensity increase as the distance from the injector increase.

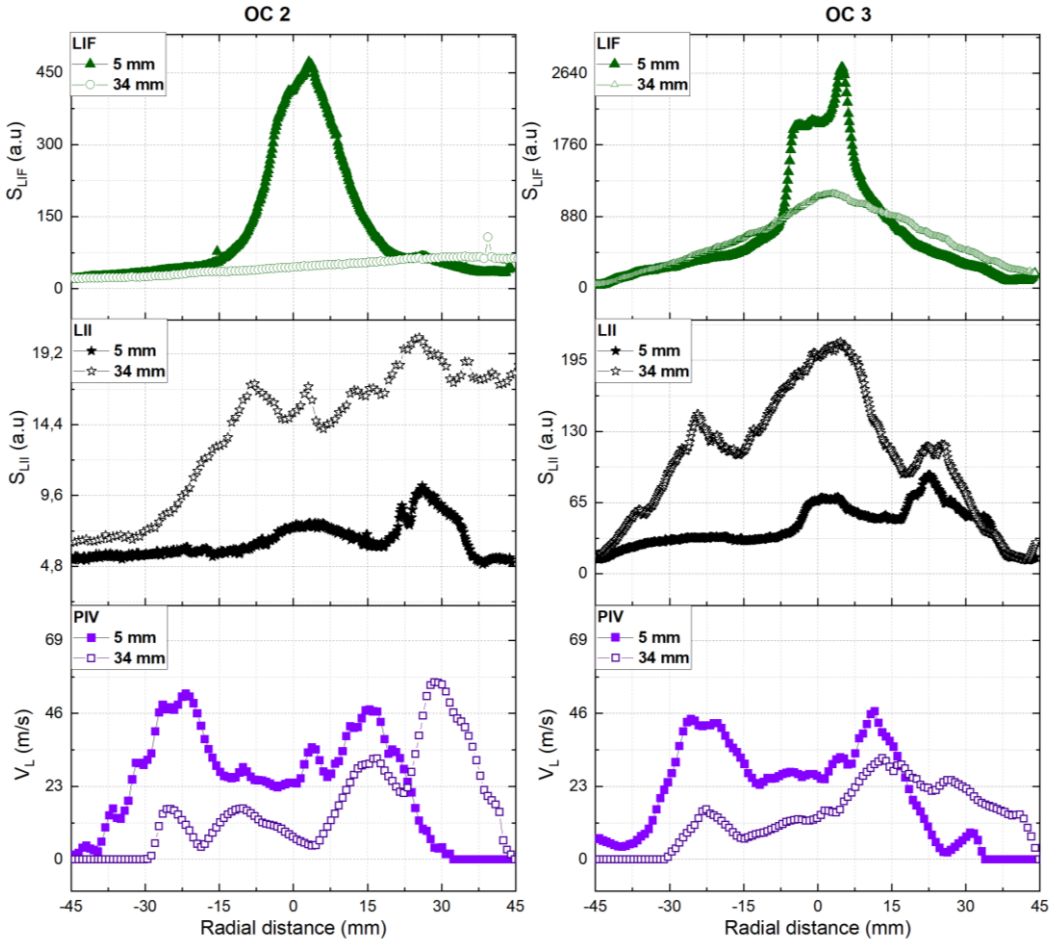

Figure 3.23 Radial profiles comparison for PIV/LII/LIF signals taken at a distance of 5 mm and 34 mm from the injector towards the combustion chamber exhaust.

PIV and LIF signals are higher toward the injector than the LII signal. At OC 3, The maximum intensity profile was also observed near the injector (5 mm) for PIV and LIF, whereas the maximum intensity for LII was observed at 34 mm. These profiles were taken in on the averaged signal; however, in the study of Bouvier et al. [147], it was observed that the time-averaged velocity distribution offers little information that can contribute to an understanding of the interaction between the aerodynamic flow and the soot formation since dynamic phenomena such as turbulence or local equivalence ratio

gradients play an important role in the production of soot. The study of Narayanaswamy [281] focused on simultaneous LII and PIV measurements in the soot formation region of turbulent non-premixed jet flames. They found that the link between soot and velocity vectors is represented by the global residence time. Still, the instantaneous fluctuations dictate where soot will be formed and how turbulent structures passively advect it.

3.3.4 Mie/Rayleigh scattering

During the combustion process of liquid fuel, the properties of the spray govern the combustion processes as they occur on a longer time scale than the other chemical reaction [282]. Therefore, spray properties like liquid phase penetration and atomization play a role in the characterization of soot particle formation in the combustor. When a laser beam with a given wavelength and frequency irradiates a sample volume, an interaction occurs between the incident laser and the matter, such as solid particles, liquid droplets, or gaseous molecules [274]. In combustion processes, Mie/Rayleigh scattering is the most non-intrusive used technique [283–285] to infer information on spray dynamics and possible soot interactions with the flow. Mie scattering corresponds to the elastically scattered light of particles with a diameter similar to or larger than the wavelength of the incident light. Whereas Rayleigh scattering is the light elastic scattering induced by particles much smaller than the wavelength of the light [58]. The challenge of applying the scattering technique in turbulent test rig flame is to differentiate Mie and Rayleigh scattering.

For example, isolated soot particles can have a diameter of a few nanometers, while they can form macro-molecular structures as large as hundred nanometers when they agglomerate. Figure 3.24 illustrates different interaction processes between the irradiating laser beam and matter present in a sample volume. The interaction cross-sections are applied to express the magnitude of achievable signal intensities in these processes. The achievable signal intensities vary tremendously in magnitude among these commonly used laser diagnostics. Therefore, it determines the choice of the best-suited diagnostics [274].

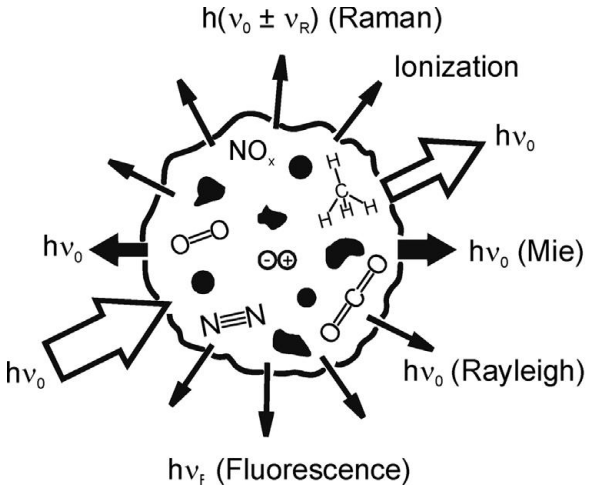

Physical Process	Cross section [cm²/sr]
Mie Scattering f (size)	10^{-7} - 10^{-13}
Fluorescence	10^{-19} – 10^{-24}
Rayleigh Scattering	10^{-27}
Linear Raman Scattering	10^{-30} - 10^{-31}

Figure 3.24 Large-scale schematic of different interaction processes between the irradiating laser beam and matter present in the sample volume. The table lists the differential interaction cross-sections of some of these processes [58].

Mie/Rayleigh scattering measurements were performed on the MICADO test rig. The experimental configuration used in this study (Figure 3.25) is similar to the one described above for the PIV measurement. The laser for scattering measurement was tuned at 10 kHz with a fluence of 3 mJ/cm^2. A fast intensifier (IRO) module was implemented in front of the camera detector to limit the exposure time to 100 ns. The measurements were performed in single-frame mode with an intensifier gate width of 2 µs. The recorded images correspond to a vertical polarization orientation (VV) between the laser sheet and the detector.

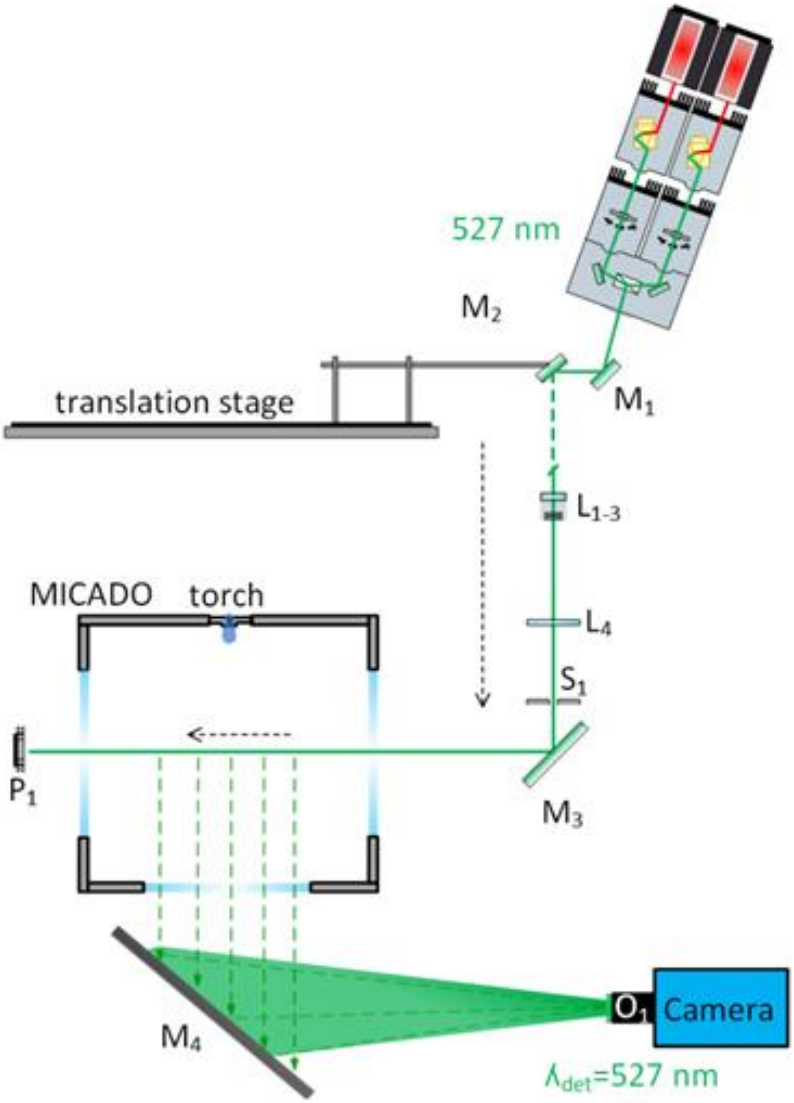

Figure 3.25 Transversal plane of the optical configuration setup for PIV and scattering measurements. L - lens, S – slit, M – mirror, P – power meter, O – objective.

The studied operating conditions are similar to the ones of PIV measurements described in Table 5. The opening and penetration depth of the spray change from one image to another. Figure 3.26 shows instantaneous images of the spray in the case of OC 3. The first series of images have a V shape with a wide-angle opening. The signal is mainly towards the outer recirculation zone. As the sequence of the images increases, the spray moves to the inner recirculation zone with a small opening angle compared to the first sequence of images. At some instant, the spray signal decreases, and it looks like all injected fuel is vaporized. The dynamics of the spray continue to change for a given series

of images, changing the opening angle and orientation of the spray either in the outer, shear layer or inner recirculation zone.

The attribute of the instantaneous spray dynamics plays a role in the transport and localization of soot and precursors in the combustion chamber. The high intermittency obtained on instantaneous images of the LII signal is relatively dependent on the spray dynamics in the combustors. The dependence of soot particles in the combustors based on spray dynamics can be due to the significant changes in the direction of a swirling flow and boundary layer separation.

Moreover, a recirculation zone arises in which a depression with local pressures below the vapor pressure of the fuel exists [286]. Different studies have shown the effect of spray penetration on soot formation and localization in the combustion chamber. Bashirnezhad et al. [287] demonstrated the effect of the fuel spray angle on soot formation in turbulent spray flames. The results show that the fuel spray cone angle significantly influences the flame structure and temperature profiles. The maximum temperature of the flame is enhanced with the fuel spray angle increased. The results showed that the nearly complete fuel dissociation depends on the fuel spray cone angle. Also, the spray angle strongly affects the soot volume fraction. The soot volume fraction measurement shows that increasing the fuel spray cone angle decreases the soot volume fraction. Their numerical and experimental results confirmed that the peak value of soot and its location are dependent on the fuel spray cone angle.

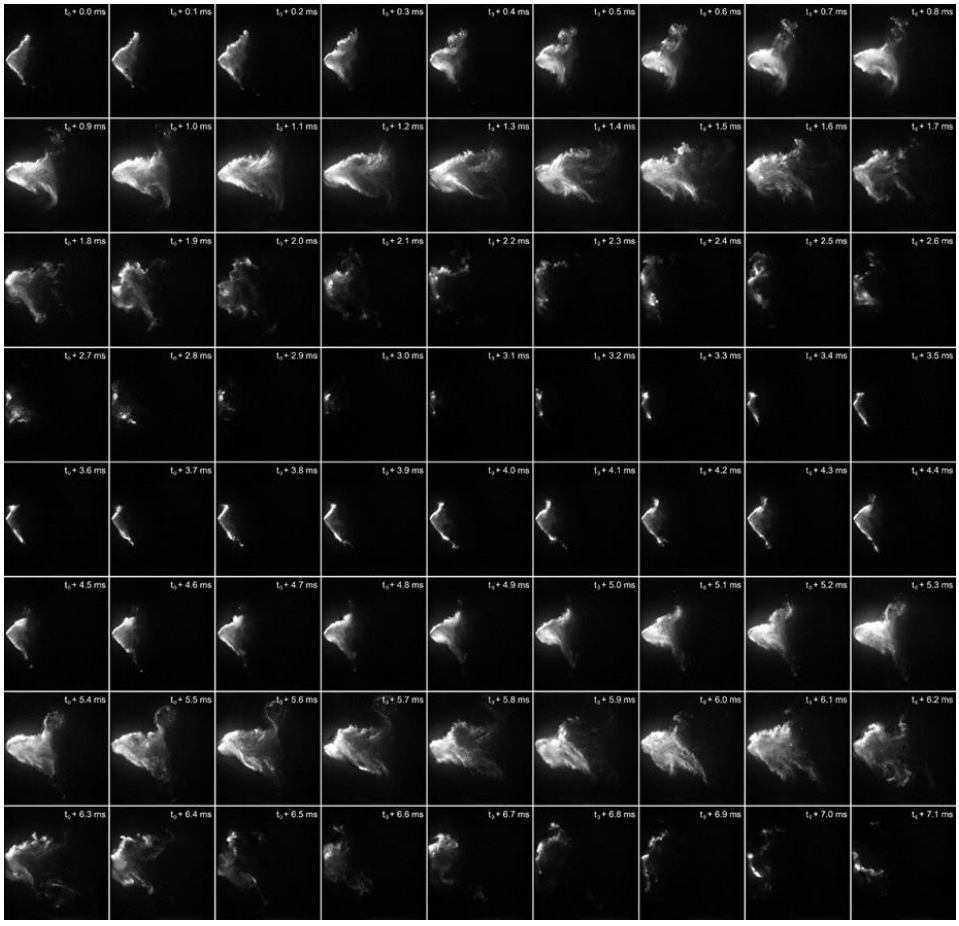

Figure 3.26 Successive instantaneous images showing the Mie scattering of the kerosene droplets at 10 kHz on OC 3.

As there is a significant change in the instantaneous images, Figure 3.27 show phase-resolved averaging of the jet A-1 spray images for the 220 Hz cycle by post-processing phase-selected images from a set of 11,000 successive images. This phase-averaged signal gives information on the evolution in shape and penetration of the spray on a given series of images. On an average of 45 frames, the opening and penetration of the spray change. The first sequences of averaged signals have a high spray opening with a low penetration level distance. When the opening angle is small, the penetration level of the spray towards the exhaust of the combustor is high.

The study of Ekaab [288] focused on the effect of fuel spray angle on the emissions of pollutants from a continuous combustion process. Their results showed that increasing the spray angles increases soot particle emission. They concluded that when the spray angle increases, the diameter of droplet size decreases, which increases the contact between fuel and air and the air-fuel mixing. In addition, the increase in the spray angle enhances the evaporating rate and peak temperature near the nozzle. Also, Mishra et al. [16] confirmed in their study on soot formation and its effect in an aero gas turbine combustor that the spray structure affects the soot formation. Their results showed that a higher spray cone angle causes higher soot concentrations at the liner front end of their combustion chamber. An increase in soot concentration in the dilution zone is more pronounced at a higher equivalence ratio.

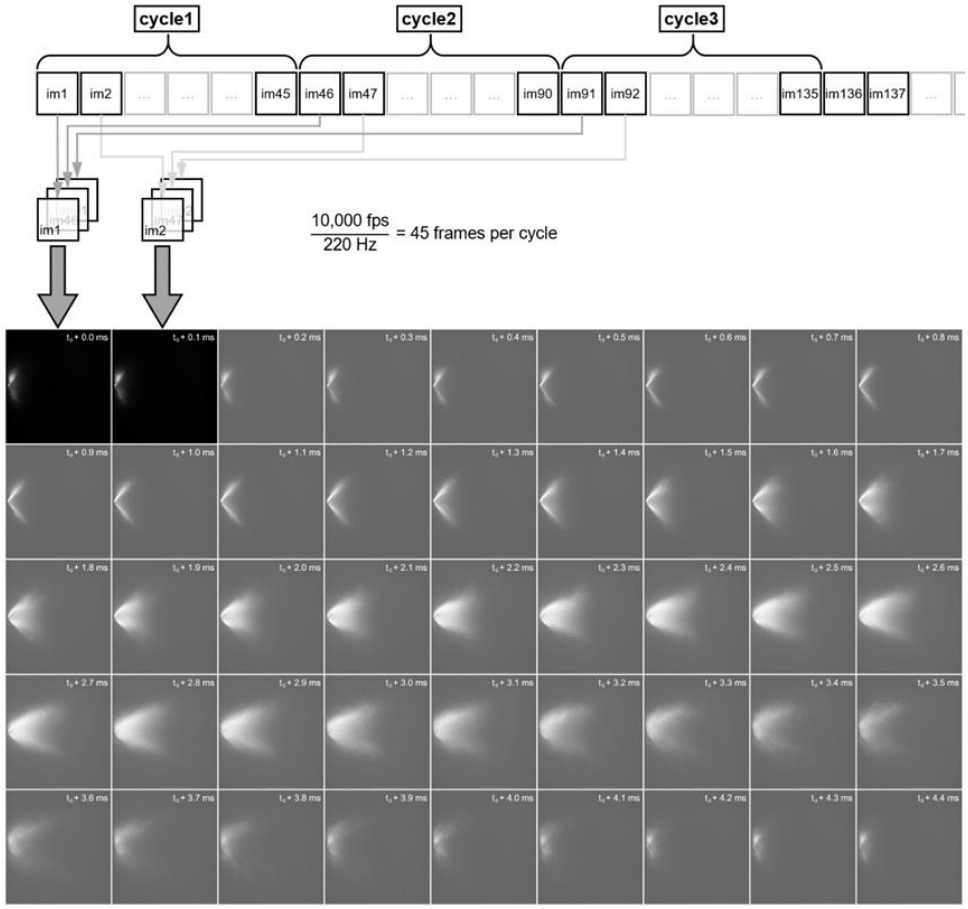

Figure 3.27 Phase-resolved averaging of the kerosene spray images for the 220 Hz cycle by post-processing phase-selected images from a set of 11,000 successive images recorded at 10 kHz for operating condition OC3.

The average scattering signal shows the general behavior of the spray in all recorded images. Figure 3.28 illustrates the average and standard deviation signals at different operating conditions.

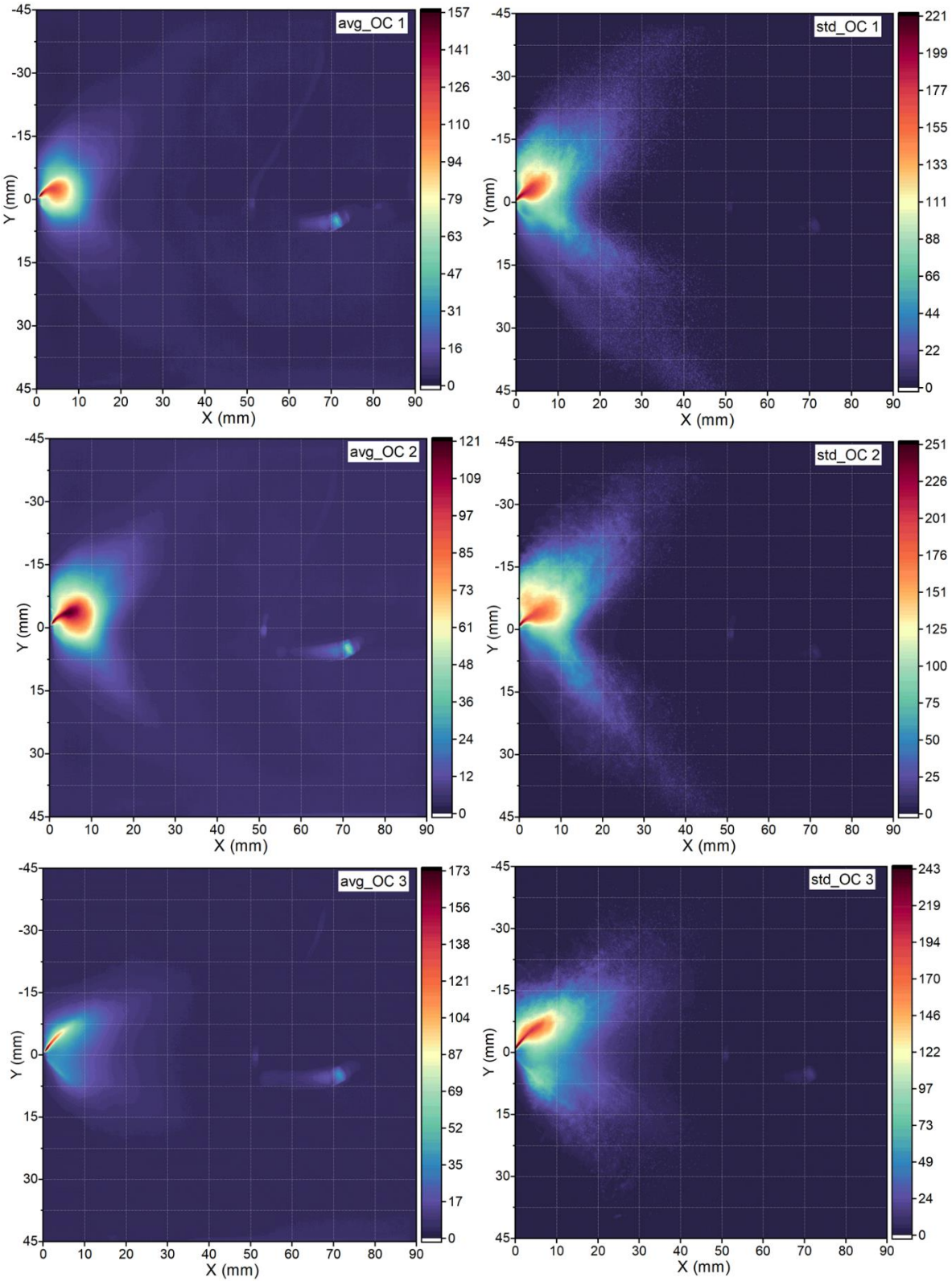

Figure 3.28 averaged spray scattering signal and their corresponding standard error deviation for OC 1, OC 2 and OC 3.

In the overall obtained averages, the high-intensity signal is near the injector and the region corresponds to the region where the maximum intensity for PAH fluorescence was obtained. For example, at OC 1, the high averaged spray signal is on the upper region of the shear layer and the intensity is distributed over 15 mm from the injector. By looking at the standard error deviation, the spray has a well-defined V shape and is distributed until 30 mm on the shear layer of the flow. The scattering intensity increased from condition OC 2 to OC 3 as the flow factor decreased and the pressure increased. The same findings were obtained on the averaged LII and LIF signal on these two conditions.

The other advantage of having information on the spray dynamics is that it can help deduce flow oscillations caused by the combustion conditions or injection mode. Figure 3.29 displays the amplitude of the frequency component obtained on the sum signal of the region of interest of 30 × 30 mm near the injector. The amplitude shows the intensity level of all pixels in the region of interest of each image and can help to follow the time evolution of the scattered signal. The summed signals show a high amplitude variation on OC 3 compared to OC 2 and OC 1.

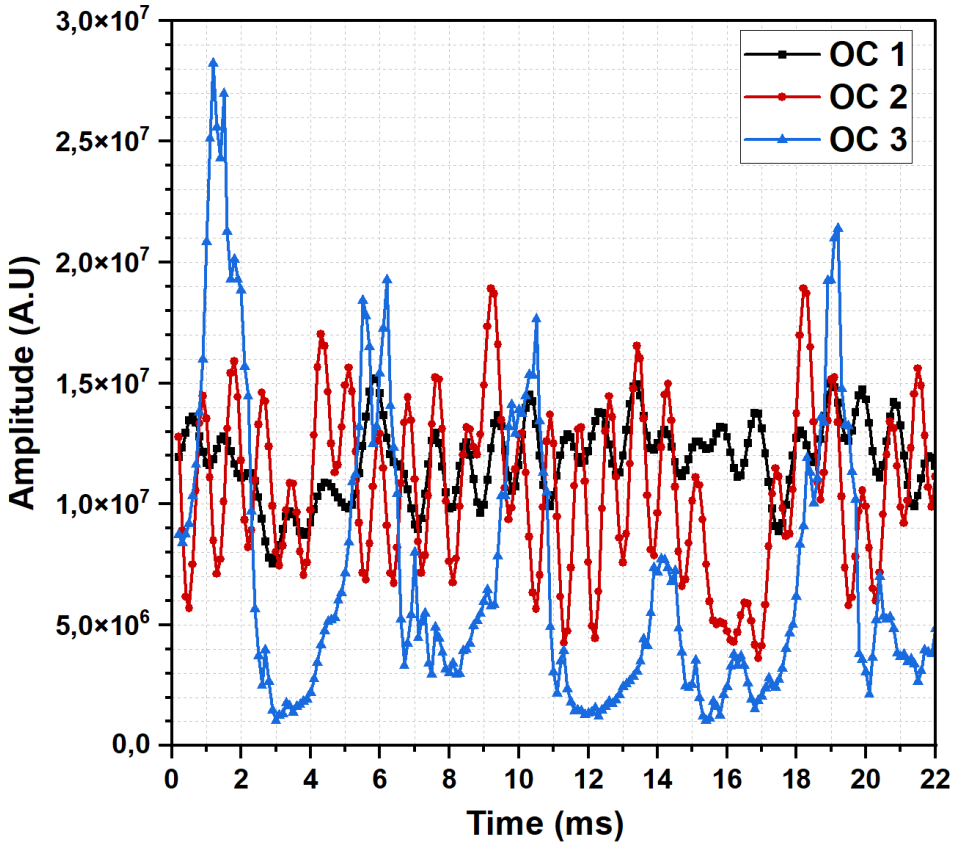

Figure 3.29 Time-evolution of the Mie scattering signal. One point is representative of the sum of intensities of the total number of pixels of a single frame recorded at OC 1, OC 2 and OC 3.

Fast Fourier transformation (FFT) helps deduce the frequency modes associated with some oscillations inside the combustor. Figure 3.30 shows the FFT of the summed amplitude signals represented in Figure 3.29 for the three OCs. At OC 1, the first dominant frequency is 233.9 Hz and the second peak is 1044 Hz. This second peak was also observed at OC 2. The dominant harmonic frequency of 229.9 Hz, 459.8 Hz, 687.7 Hz, 919.5 Hz and 1149 Hz were identified at OC 3. These

frequencies can be associated with multiple phenomena (fuel droplets flow, vaporization of the fuel and soot) that impact the thermoacoustic oscillations.

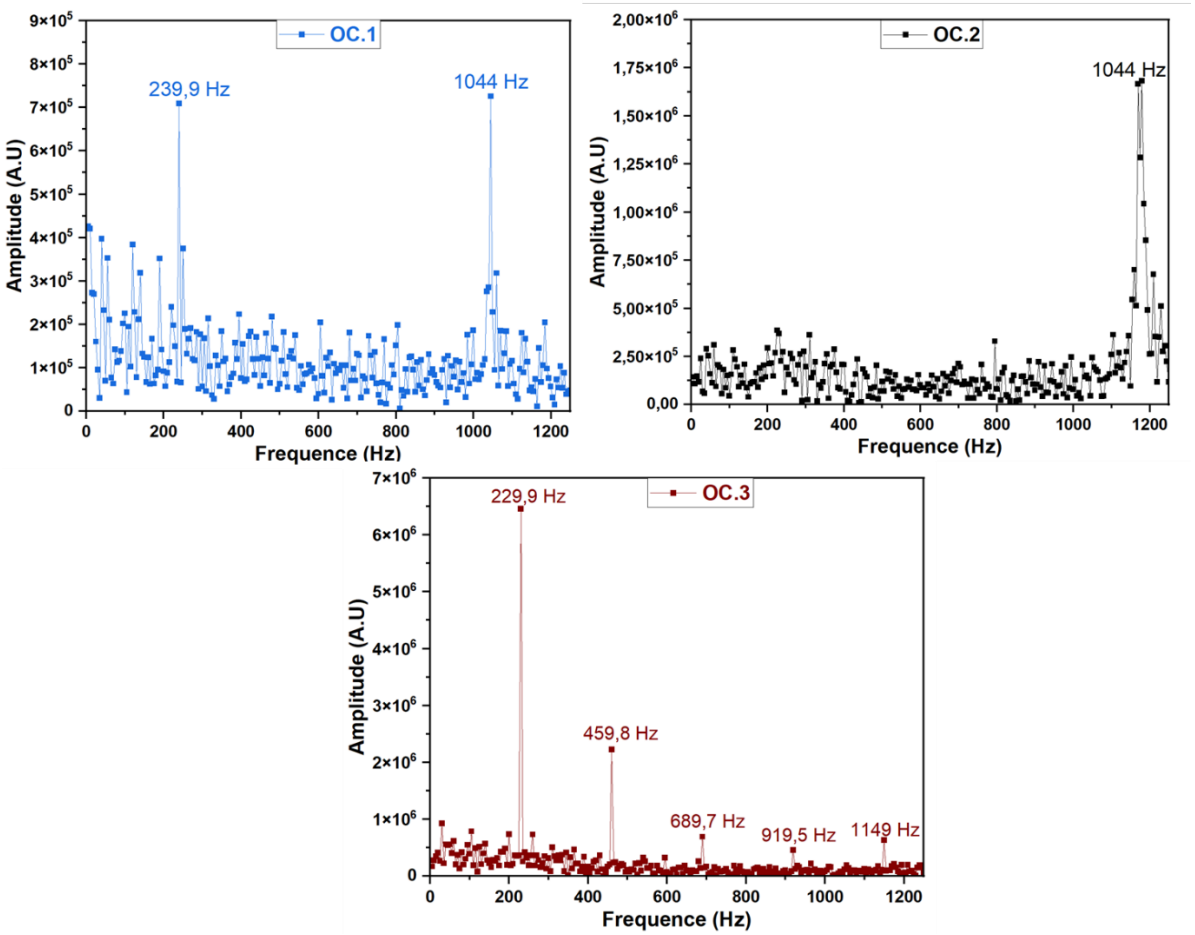

Figure 3.30 FFT spectra obtained from the sum of intensity detected on the images recorded at 10 kHz on OC 1, OC 2 and OC 3.

Additional details on possible oscillations and instabilities that can be obtained and the effect of these oscillations on soot formation and distribution inside the combustor are discussed in chapter 4.

3.4 SUMMARY OF THE CHAPTER

Multiple optical imaging diagnostics were used to investigate the soot formation in an aeronautical representative test rig for six operating conditions.

The first part of this chapter focused on the characterization of soot particles using the LII technique and soot precursors using the LIF technique. Then, different test rig operating conditions were chosen based on flow factor values referenced to conditions used in the CFM56 engine.

The overview of experimental configuration proved the feasibility of these optical techniques on high-pressure combustors, despite the limitations imposed by the complexity and operating conditions of the test rig. Furthermore, these techniques were successfully implemented in harsh combustion conditions. Selected OCs were classified depending on the injection type of the fuel (main or mixed pilot/main), global equivalence ratio, air and fuel mass flow rates, inlet air temperature and pressure inside the combustion chamber.

The LII and LIF measurements were carried out simultaneously with a delay of 1 µs between two measurements to avoid signal interference. Soot particles were heated with a laser at 1064 nm and detected at 450 nm, whereas PAHs fluorescence was excited at 532 nm and detected at 580 nm. Both signals were recorded at a frequency of 10 Hz. The LII and LIF results bring spatial and temporal information about the distribution of soot particles and aromatic precursors (PAHs) inside the combustion chamber.

The averaged signal shows high contributions of aromatic compounds near the fuel injector in all studied conditions. The high intensity was obtained in the conditions with high pressure and low FF/FF_{ref} (OC 3 and OC 4). Soot particles are located on the shear layer towards the edges of the combustion chamber with an "*M shape*" for OC 2 and towards the center with "*V shape*" for the other tested conditions. OC 2 is characterized by the highest FF/FF_{ref}, and with this condition, it has the lowest soot volume fraction (0.08 ppm). The maximum soot volume fraction was obtained for the conditions with high-pressure value and lower FF/FF_{ref} value. At OC 3, the maximum is 0.80 ppm, and for OC 4, the maximum is 1.2 ppm on the averaged images. The soot signal appears with very high spatial intermittency. Processed data were correlated with the test rig operating conditions (OC) for observing the parameters affecting the production of soot particles. Selected correlation methods identified a link between the combustion parameters and produced soot and precursors. Firstly soot and precursors signals are positively correlated, and both signals increased with the increase of pressure in the combustion chamber. The correlation between the LII signal and LIF signal inside the combustion chamber can bring insights into the role of pyrogenic aromatic compounds that participate in soot formation and evolution in the combustor.

On the other hand, the LII and LIF signals were negatively correlated with the flow factor, suggesting that the aerodynamic conditions impact the formation of these species. Therefore it is concluded that an elevated residence time is directly related to the abundance of soot and precursors in the axial direction of the combustor. Increased flow factors do not give enough time for particles/precursors to form (short residence time). For the case where the FF/FF_{ref} is higher than 60 %, the soot and precursors signals are predominant near the walls of the combustor.

Additionally, high-speed complementary techniques were implemented to identify the impact of the flow dynamics in soot formation for three selected OCs. The PIV technique was used to study the flow velocity field inside the combustion chamber. At the same time, light scattering was implemented to characterize the soot/spray dynamics. Successful results of velocity vectors were obtained despite the problems encountered with the seeding system. The velocity vector field maps show the influence of flow speed on soot and precursor formation. The high soot particle signal was obtained in the region with lower velocity fields. This can be caused by the residence time, which plays an essential role in soot formation and localization.

The scattering technique shows how the spray dynamics can influence the soot formation and localization in the combustor. The condition OC 3, characterized by high summed intensity amplitude from the spray scattering and lower oscillation frequency, is characterized by the high soot volume fraction. On the other hand, OC 2 has a lower summed signal amplitude with the high-frequency oscillation modes, resulting in conditions with lower soot volume fractions than OC 3. The spray opening angle and penetration length also influence the soot formation and localization in the combustion chamber.

CHAPTER 4

SOOT PARTICLES FORMATION IN SUSTAINABLE AERONAUTIC FUELS (SAF) – NECESSITY OF OPTICAL COMPLEMENTARY TECHNIQUES

This page is intentionally left blank

4 SOOT PARTICLES FORMATION IN SUSTAINABLE AERONAUTIC FUELS (SAF) – NECESSITY OF OPTICAL COMPLEMENTARY TECHNIQUES

This chapter continues with the application of coupled optical techniques for the characterization of soot particles produced by classical aeronautical Jet A-1 and sustainable aviation fuels (SAF) for three operation conditions (OC) stabilized on the MICADO test rig. This study aims to assess the effect of SAFs on soot production through combustion experiments. Three OC were selected based on measurements performed in Chapter 3. During the experimental campaign, the effect of Jet A-1, 50:50% vol. of F35:ATJ and neat Alcohol to Jet (ATJ) on soot levels were studied for the three OCs in which the pressure of the combustion chamber varied from 4.5 to 9 bar, while maintaining almost constant the fuel-to-air ratio. Furthermore, an investigation of spray formation, flame shape and combustion dynamics was carried out to shed light on the impact of fuel composition on soot formation. Different in-situ optical techniques were used. Laser Induced Incandescence (developed in chapter 2) was used to detect soot particles, light scattering was used as a complementary technique to have information on the possible effects of liquid fuel (spray) dynamics on soot formation and distribution, and simultaneously OH* chemiluminescence to have information on the reaction zone or possible heat release inside the combustion chamber.

The first section of this chapter focuses on the general context of alternative fuels used in propulsion, followed by the different studied OCs on the MICADO test rig and the implemented optical techniques. Finally, the last section summarizes the obtained results and compares some experimental and numerical findings. Part of the research conducted in this chapter was in the framework of the European Union Horizon 2020 project ALTERNATE [289].

4.1 CONTEXT OF ALTERNATIVE FUELS FOR AIRCRAFT PROPULSION

The aviation industry seeks competitive synthesized aviation fuels with a carbon benefit and sustainable performance to counter the effects of price spikes, competition for finite oil supplies, and high aviation profile as a greenhouse gas (GHG) and particulate emitter [290]. This decarbonization is additionally needed to meet long-term net-zero emissions goals. However, reducing jet fuel's carbon footprint reduces aviation's impact on the environment now and in the long term [291]. Therefore, aviation decarbonization is a necessary procedure that leads to developing and implementing new types of fuels that ensure sustainability. For the aviation industry, alternative fuels present an opportunity to minimize harmful emissions, and good near-term options are sustainable aviation fuels (SAF), which are non-fossil fuels produced from feedstock [292,293].

Based on the literature, the primary source of bio-jet fuels is renewable resources. This source is essential due to various advantages, like sustainability, carbon dioxide recycling, renewable and eco-friendly technology and less dependence on regions that produce petroleum [294,295]. The main bioresource used for producing sustainable fuels is camelina, algae, waste and halophytes [294,295]. Good candidates for different sustainable fuels have to fulfill additional requirements, such as limited greenhouse gas emissions, being produced from renewable resources and being compatible with classic conventional fuels. The most advanced alternative fuels are hydro-processed renewable jet

fuels that are generally paraffinic liquids fuels with a chemical formula of C_nH_{2n+2}. One of the major advantages of hydro-processed renewable jet fuels is the reduction in greenhouse gas emissions [296]. The hydro-processed renewable jet fuels have a low quantity of aromatics, sulfur and possess high cetane numbers, high thermal stability and low emission indexes [297]. These fuels are stable in storage conditions compared to other biofuels [295,298]. The second type of used sustainable fuels is Fischer Tropsch fuels produced from the catalytic conversion of syngas. The third type is Biodiesel fuels which are made mostly with alkyl esters of fatty acid and mostly produced from vegetable oils and animal fats. The energy density of biodiesel is very low compared to conventional jet fuels. However, despite the low efficiency, these biodiesels present the advantage of not requiring further modification of aircraft engines and infrastructure [299]. The fourth type of sustainable fuel is liquid bio-hydrogen and bio-methane. Liquid hydrogen produces more energy per weight compared to conventional aviation fuel but requires high storage volume [295,300,301]. The combustion of liquid hydrogen fuels causes low emissions of greenhouse gases compared to petroleum-based jet fuels. The major problem is that liquid hydrogen fuel cannot be used as such in the conventional aircraft engine, so the engine has to be modified [295,302]. The study of Midili et al. [303] identified that the other problem associated with the use of liquid hydrogen is that upon mixing with air, it can burn in low concentration, which can cause safety problems.

Moreover, storing hydrogen as a liquid is also challenging since it needs low-temperature conditions. The emission of comparatively high amounts of water vapor is a problem associated with hydrogen aircraft [295,304]. The last most used sustainable fuel is bio alcohol. These fuels are produced by the fermentation of starch and sugar or the catalytic conversion of biogas. The most known bio alcohols are ethanol and butanol. However, the use of such bio alcohols might also be problematic in aircraft engines, notably because of their high volatility, low energy density and the necessity of particular infrastructures for distribution and engine modification to be adequately used [297].

Nowadays, Alcool-to-jet (ATJ) fuel has been brought into the limelight due to its compatibility with classic aircraft engines. The production of the ATJ pathway refers to the catalytic conversion process to sustainable kerosene production from various alcohols (ethanol or iso-butanol usually). These alcohols can be obtained from biogenic feedstock (sugarcane, corn and lignocellulose) via thermochemical and biochemical processes [305–307]. These fermentation processes are well known, especially when a "classic" feedstock is used. However, the converting process is still under development for the lignocellulose resources. The produced alcohol is transformed into an iso-alkanes blend via an ATJ process that consists of dehydration, oligomerization, hydrogenation and fractionation [20,307]. After these processes, the obtained biokerosene is a mixture of iso-alkanes called ATJ-SPK (alcohol-to-jet synthetic paraffinic kerosene). The ATJ fuel is typically blended with traditional jet fuel to create a "*drop-in*" fuel that can be used in existing jet engines without needing modifications. The exact blend ratio depends on the specific characteristics of the ATJ fuel and the requirements of the aircraft. It is certified for a maximum blend of up to 50% with conventional kerosene according to the standard specification for Aviation Turbine Fuel Containing Synthesized Hydrocarbons (ASTM) standard.

The study of Kramer et al. [291] discussed the perspectives on fully synthesized sustainable aviation fuels in terms of direction and opportunities. The critical challenges to SAF adoption are primarily related to production, distribution problems, feedstock availability and sustainability, and the

necessary technical infrastructure to maximize SAF utilization [295]. Based on the report "WAYPOINT 2050" [308], it is necessary to bring together experts from across various fields of the aviation sector to contribute to the world climate action mission. Their report describes different scenarios about how to reduce carbon emissions in the aviation domain by 2050. The main proposed solution is based on reviewing traffic forecasts, innovating with technology, improving operations and infrastructure and finally deploying a sustainable aviation fuel. To summarize this, Figure 4.1 outline the scenarios of how the industry would use technology, operations, infrastructure and sustainable aviation fuels to reach net-zero CO_2 in 2050 and the years afterward. Different millistones directed by industries and governmental instutions are established to reduce carbon emission. To accomplish these objectives, replacing Jet fuel with SAF is the solution with the highest impact on the decarbonization of the aviation domain, especially in cutting down particulate (soot) emissions, which act considerably on the formation of contrails.

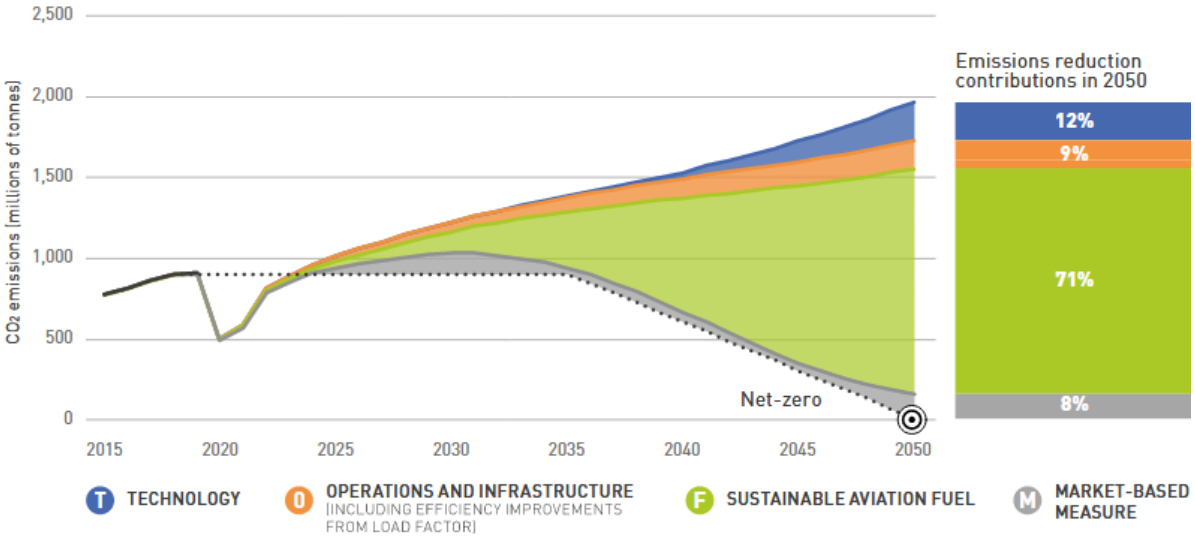

Figure 4.1 The scenarios outline how the industry would use technology, operations, infrastructure and sustainable aviation fuels to reduce CO_2 emissions in 2050 and the following years [309].

SAF is a promising technology that is expected to substitute petroleum-based fuels in aerobic propulsion. Nevertheless, many challenges arise, including the availability of feedstock, compatibility of alternative fuels with conventional fuels, environmental concerns and production and distribution issues. Nevertheless, based on the literature, different studies indicate that using SAF fuels is of great interest. As the number of flights using SAF blends increases, it is feasible to have airplane engines operating safely with neat SAF in the near future despite certain technical and certification constraints [293,295].

Still, further studies must be made to understand turbine-emitted gaseous and soot emissions when alternative fuels are used [310]. These studies must be performed directly on the combustor or at the exhaust with suitable optical metrology techniques. Lately, outstanding progress toward cleaner combustion has been achieved due to the development of lasers and fast acquisition systems and, nonetheless, due to the increased processing power of computers [311,312]. However, despite these advancements, the characterization and understanding of soot formation in industrial-scale combustors and, even more, while using SAF still need to be improved. From an experimental point of

view, the coupling of non-intrusive optical techniques, which can provide simultaneous experimental information about the involved physical phenomena (e.g., turbulent flow field, flame, spray, pollutant emissions), is becoming crucial. However, implementing extensive optical technique measurements inside aircraft engines is expensive and almost impossible.

In this work, optical diagnostics are custom-developed (Chapter 2) to characterize a highly turbulent environment. Complex phenomena such as the evaporation of the fuel, spray dynamics and pollutants formation are monitored in real-time with optical techniques such as Mie and Rayleigh scattering, OH* chemiluminescence and laser-induced incandescence (LII) for a matrix of selected fuels and blends that are burned in representative conditions of aircraft combustors operating conditions (OC) [313].

4.2 STUDIED FUELS AND MICADO OPERATING CONDITIONS

A matrix of fuels was studied to investigate the soot produced by SAF fuel. The studied fuels are Jet A-1, F35, the admixture of 50% F35:50% Isopar and the neat ISOPAR, referred to as alcohol-to-jet (ATJ). The properties of the F35 are close to the ones of Jet A-1. Due to this, the description used for jet A-1 in this chapter is related to the one of F35.

MICADO test rig adjustments for the use of SAF:

The configuration of the MICADO test rig described in chapter 3 is adapted for the use of alternative fuels and blends, as shown in Figure 4.2. Incoming air is heated with a counter-flow heat exchange, where the vitiated heating airflow is delivered by a kerosene/air burner while the ambient temperature air counter-flow is fed either from compressors ($p \leq 1$ MPa) or the high-pressure (HP) storage (22 tonnes of air at 25 MPa). As a result, the heated airflow expands to 4 MPa or less before entering the combustor. The main supply lines of air and fuel to the combustor are represented in Figure 4.2. A 20 m^3 fuel tank provides Jet A-1 for heating the air and the fuel supply of the combustor. A fuel tank of 80 L containing SAF is added (Figure 4.2) parallel to the Jet A-1 fuel tanks. The storage volume for SAF roughly allows 40 to 100 minutes of combustion for a fuel consumption between 25 and 10 $g \cdot s^{-1}$ which does not allow the supply of the combustor for the entire duration of the test session, which is around 4 hours (Figure 4.4). Therefore, Jet A-1 from the main storage is used for most of the session time to avoid the consumption of fuel blends or SAF. Measurement sequences between the Jet A-1, SAF or fuel blends were alternated to cover the OC of interest.

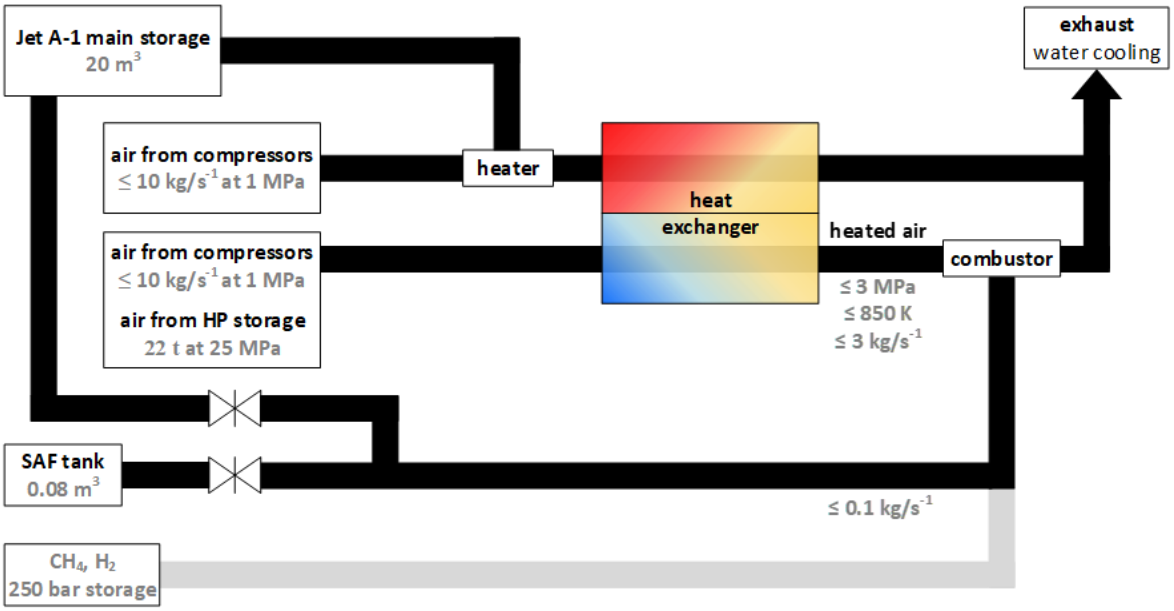

Figure 4.2 Operation principle of the MICADO test rig facility.

The chemical composition of ATJ is different from the Jet A-1. Figure 4.3 shows an example of the main organic compounds present in classic Jet A-1 fuel in ATJ. The ATJ is mainly composed of the iso-paraffins, whereas Jet A-1 mainly consists of aromatics, iso-paraffins, n-paraffins and cycloparaffins. In the context of soot studies, the ATJ does not contain aromatics as Jet A-1, and aromatic species are well known to be soot precursors; therefore, this characteristic can have a first-order impact on the soot pollutant emissions obtained.

Fuels properties:

In general, ATJ fuel may have a lower environmental impact than Jet A-1 fuel due to the lower carbon content, which can result in lower greenhouse gas emissions during combustion. However, the environmental impact of ATJ fuels can vary depending on the specific blend of alcohols and hydrocarbons used to make them, as well as the conditions of the combustion process.

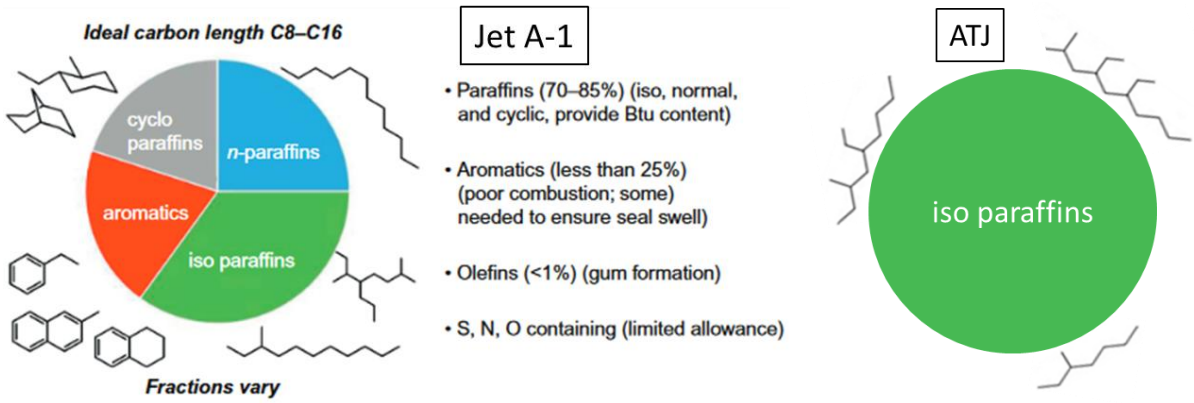

Figure 4.3 Typical example of the main organic chemical composition of Jet A-1 [305] and ATJ [307] fuels.

Here are some more physicochemical characteristic parameters showing the differences between tested ATJ and Jet A-1 fuels:

- Density: ATJ density (around 778 kg/m^3) is lower than Jet A-1 (798 kg/m^3). This can impact the atomization process during combustion.
- Freezing point: The freezing point of a fuel is the temperature at which it can solidify or freeze. ATJ fuel has a lower freezing point than Jet A-1 fuel, making it more suitable for cold climates. The freezing point of ATJ fuel is typically around -60 °C, while the freezing point of Jet A-1 fuel is around -47 °C.
- Viscosity: The viscosity of a fuel is a measure of its resistance to flow. ATJ fuel has a higher viscosity than Jet A-1 fuel, which can affect its performance in some types of aircraft engines. The viscosity of ATJ fuel is typically around 2.104 g·m^{-1}·s^{-1}, while the viscosity of Jet A-1 fuel is around 1.342 g·m^{-1}·s^{-1}.
- Lower heating value (LHV): is a measure of the energy released when the fuel is burned at a constant pressure and cooled to a reference temperature (typically 25°C). The LHV of ATJ fuel can vary depending on the specific blend of alcohols and hydrocarbons used to make it and the temperature and pressure at which it is measured. In general, ATJ fuel has a lower LHV than Jet A-1 fuel due in part to the lower energy content of the alcohols it contains. The LHV of ATJ fuel is typically around 44.06 MJ/kg at 15°C, and the LHV of Jet A-1 fuel is typically around 43.21 MJ/kg at 15°C.

Selected operating conditions:

Three operating conditions are tested based on the pressure inside the combustion chamber, global equivalence ratio, inlet air temperature, air and fuel flow rate and flow factor, as presented in chapter 3. The selected OCs correspond to the three OCs studied in subchapter 3.3. Table 6 summarizes different tested combustion conditions with the corresponding fuels. However, due to the MICADO OC system, the global equivalence ratio between Jet A-1 and alcohol to jet (ATJ) is slightly different at the same operating condition due to other combustion parameters needed to stabilize the combustors. In particular, the global equivalence ratio of Jet A-1 is slightly higher for OC 1 and OC 3, while on OC 2 is superior for ATJ fuel. A slight difference also can be observed in other operating condition parameters like air and fuel flow rate. Therefore, attention must be paid to the interpretation of obtained results, as these small differences can induce some misinterpretations by comparing tested fuels based on operating conditions. 29% of this airflow is ducted by the combustor's dome metallic plate to protect the optical windows (film cooling), while the remaining 71% is fed to the swirler (Figure 4.1). These tests resulted in nine individual OCs with specific operating parameters, as summarized in Table 6.

OC	fuel	p_{ch} (MPa)		T_{air} (K)		$\dot{m}_{air}$ (g/s)		$\dot{m}_{fuel}$ (g/s)		Φ	
		avg	std×10^{-3}	avg	std	avg	std	avg	std	avg	std×10^{-3}
OC1	Jet A-1	0.45	3.4	540.6	0.9	241.3	0.8	13.2	0.02	0.80	3.2
	Jet A-1:ATJ	0.45	1.0	523.4	0.3	245.1	0.4	12.6	0.05	0.75	3.4
	ATJ	0.45	2.2	526.1	0.4	244.0	1.4	12.4	0.08	0.77	7.4
OC2	Jet A-1	0.79	6.9	555.6	0.3	491.7	1.3	22.9	0.10	0.68	3.7
	Jet A-1:ATJ	0.79	3.8	550.4	0.1	489.8	1.1	23.5	0.08	0.70	3.4
	ATJ	0.79	1.5	549.6	0.1	491.9	1.0	24.1	0.25	0.72	7.6
OC3	Jet A-1	0.94	8.5	553.3	0.1	347.4	0.9	18.5	0.11	0.78	5.0
	Jet A-1:ATJ	0.94	3.9	543.9	0.1	351.1	1.2	19.0	0.09	0.79	4.7
	ATJ	0.93	1.8	546.8	0.7	347.2	1.7	18.3	0.10	0.77	5.7

Table 6 Studied combustion operating conditions (OC) during the ALTERNATE project on the MICADO combustion chamber.

The operating conditions (OC) are chosen based on the stability of the combustion chamber and the operating parameters referenced to real aircraft engine cycles (LTO). However, due to the test rig complexity, it is challenging to reproduce with 100% precision the same parameters of referenced OCs in Chapter 3.

Figure 4.4 displays an example of characteristic combustion parameters variation during one day of experiments. To record the parameters linked to one OC, the combustor has to be stabilized with all combustion parameters like pressure, temperature and flow rate. Once the combustor is stabilized, a session of acquisition parameters is triggered to record all data simultaneously, from temperature and pressure sensors to cameras. Different sessions were recorded based on the need, as the test rig can work in continuous mode.

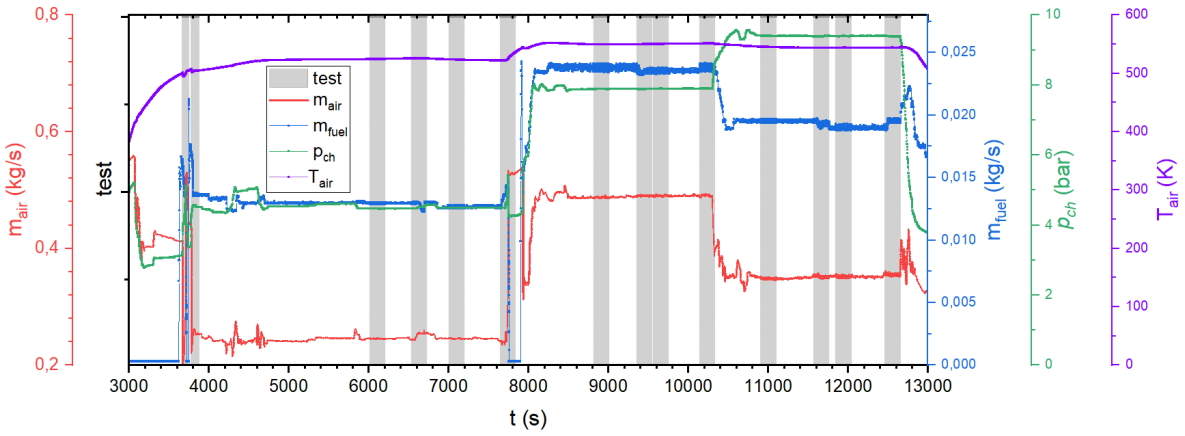

Figure 4.4 Second productive measurement sequence on MICADO test rig. Used fuels: Jet A-1 and 50:50% vol. Jet A-1:ATJ in OC1, OC2 and OC3.

All these properties can affect unburned liquid fuel dynamics, flame characteristics and pollutant soot emissions when using different fuels (Jet A-1, Blend Jet A-1/ATJ and pure ATJ).

The next section describes the implemented experimental configuration used for studying soot particles generated with different types of fuels.

4.3 APPLIED OPTICAL DIAGNOSTICS

4.3.1 LII and Mie/Rayleigh scattering coupled with OH* chemiluminescence

The LII technique developed in the laboratory (chapter 2.3) was adapted and implemented on the MICADO test rig. Test rig measurement campaigns are extensive and costly. Hence coupling optical techniques are used to obtain parameters of importance during one OC, which are further used to understand the differences between the combustion of various fuels. The LII technique alone cannot grasp all processes that govern and influence soot formation in the combustion chamber. So due to this fact, complementary high-frequency (in the order of kHz) techniques were added. The light scattering technique provides information on non-vaporized fuel, spray dynamics and, eventually, soot particles if they are in high concentration. In addition, the OH* chemiluminescence is used to get information on the possible reaction zone and heat release.

Two lasers and four cameras were used to couple in-situ optical techniques around the MICADO test rig. Figure 4.5 illustrates the schematic of the coupled diagnostics implemented on the test rig. The laser beams were directed from the upper laser laboratory to the test rig room through two ports dedicated to optical access. For LII measurements, a 1064 nm Litron laser described in chapter 2.3.2 was used to heat soot particles to a temperature higher than flame temperature. A high-frequency Quantronix Darwin-dual laser containing two Nd: YAG oscillator modules (the laser used for PIV and scattering in subchapter 3.3) was used for scattering experiments. SHG modules convert the fundamental laser wavelength into the second harmonic at 527 nm excitation, with a pulse width of 180 ns at 10 kHz. The laser beam is directed by different mirrors from the MICADO optical control room to the combustion chamber.

For the LII experiments, a laser sheet of L= 100 mm, H= 89 mm and W= 0.4 mm that covers the whole region of interest inside the combustion chamber (Figure 4.6) was formed by using a set of lenses: a negative cylindrical lens (f= -24.5 mm) and two positive cylindrical lenses (f= 200 mm and f= 1000 mm). The formed laser sheet is directed in the horizontal median plane of the combustion chamber by using a mirror. The laser fluence at the focus point is 0.25 J/cm^2. This fluence value is superior to the LII sublimation threshold of ∼0.18 J/cm^2 for mature soot and was chosen to compensate for the attenuation of the laser beam while passing through the dense pressurized sampling volume.

For scattering, a laser sheet of sheet L=100 mm, H=89 mm and W= 1.2 mm is formed by using a set of lenses consisting of a cylindrical negative lens, two spherical lenses and a positive cylindrical lens. Another mirror (M_2) is added before the entrance of the combustion chamber to combine the formed laser sheet for scattering and LII (Figure 4.5). The focal points of the formed two laser sheets were aligned in the same median plane at a known distance from the injector nozzle while covering a region of interest of 100 mm in length and 89 mm in height. Figure 4.*6* shows the view of different regions of interest covered with each optical technique. The *in-situ* measurements were implemented simultaneously with the *ex-situ* measurements that focused on sampling emissions products with the sampling probe at the exit of the combustion chamber. Only results obtained with the in-situ techniques are covered in this work.

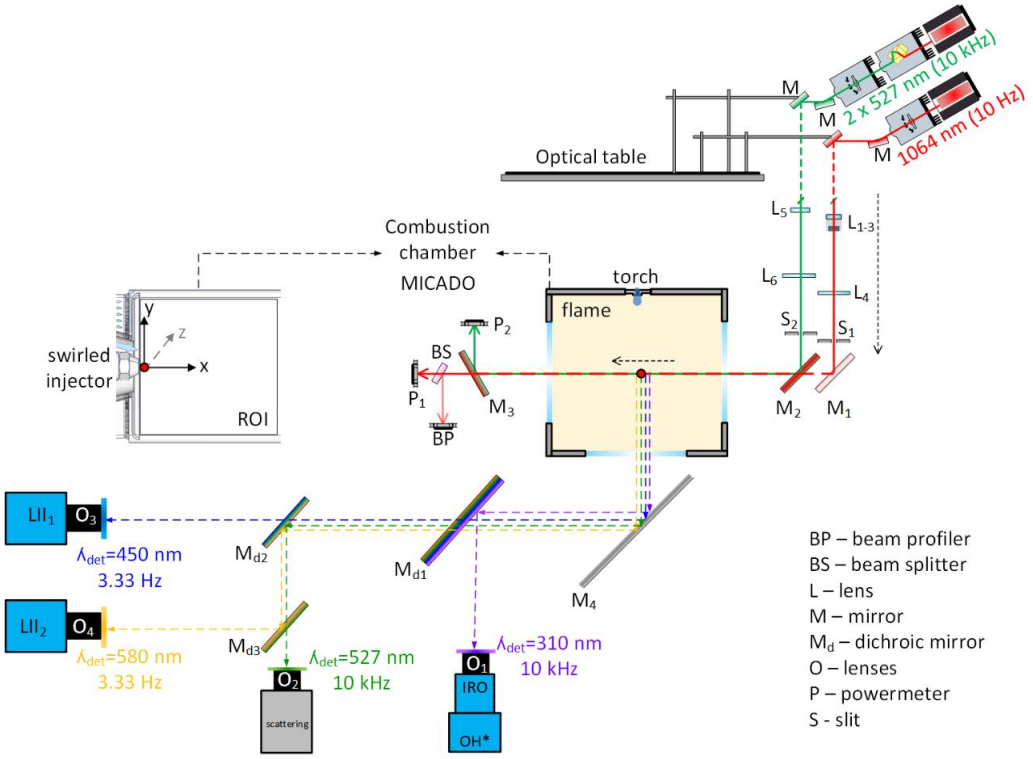

Figure 4.5 Detailed sectional front view of the experimental optical configuration for LII, Scattering and OH* chemiluminescence used during the ALTERNATE measurement campaign.

Flame emission and laser-induced signals were collected through a UV-visible, highly reflective mirror placed below the combustor (M_4). A second dichroic mirror (Md1) reflected the UV emission toward an intensified relay optics (HSIRO, LaVision) module coupled with a Phantom V710 camera (Vision Research) used to record the chemiluminescence of OH* at 10 kHz with a 4 µs gate width (GW). This camera had a 94 mm focal length CERCO UV lens set at f/4 aperture. The lenses were equipped with a short bandpass filter of 10 nm bandwidth centered at 310 nm. The scattering light was recorded simultaneously with OH* due to a third dichroic mirror (Md2), directing visible light toward a Phantom V711 camera during an exposure of 0.3 µs. The camera was equipped with 135 mm (f/8 aperture) lenses and a narrow-bandpass filter of 10 nm bandwidth centered at 527 nm.

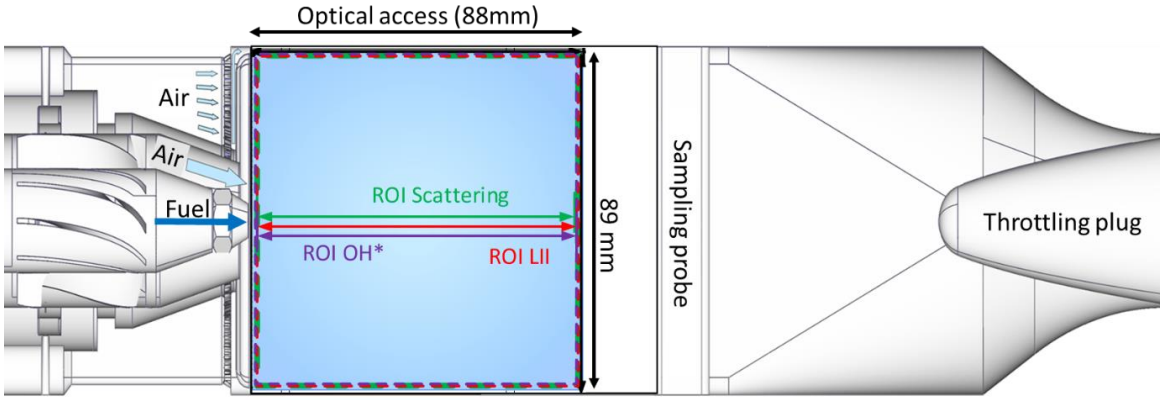

Figure 4.6 Schematic representation of the viewport of the combustion chamber defining the region of interest selected for the in-situ optical techniques: 1) chemiluminescence OH* (purple), 2) scattering (green), and 3) induced LII and flame self-emission (blue).

The LII and flame emissions signals were recorded perpendicularly to the IR excitation plane with a PIMAX4 1024f intensified camera (Teledyne Princeton Instruments) equipped with Sigma 105 mm (F2.8) lens. A narrow bandpass filter with a 10 nm bandwidth, centered at 450 nm, collected the transmitted signal through the M_{d2} dichroic mirror. The LII signal and flame emission were recorded simultaneously during 50 ns GW at a frequency of 3.33 Hz. A PIMAX2 intensified camera equipped with Sigma 23-300 mm (f/3.5-6.3) lenses collected the flame emission 80 ns before the LII signal during a GW of 50 ns. This camera only records the flame emission signal that has to be subtracted from the LII and flame emission raw signal. A narrow bandpass filter with a bandwidth of 10 nm, centered at 580 nm, collected the flame emission signal reflected by the Md3 mirror. Figure 4.7 shows the synchronization chronogram between two low-frequency cameras used for LII and flame emission signals.

All four cameras were flat field corrected, and their focal point was adjusted with a calibrated target before each measurement. Once the combustion produced in MICADO is stabilized at a given OC, a total of 10 minutes was dedicated to recording images with the coupled optical system. Each high-speed camera for OH* and scattering simultaneously recorded 15000 images at 10 kHz, while the flame emission and LII were performed at 3.33 Hz. Each PIMAX camera recorded a series of 1500 images. A correction factor was calculated for the flame emission recorded with the PIMAX2 camera to subtract from images recorded with the PIMAX4 camera. This correction factor was estimated while measuring the flame emission with the two cameras without inducing the LII signal.

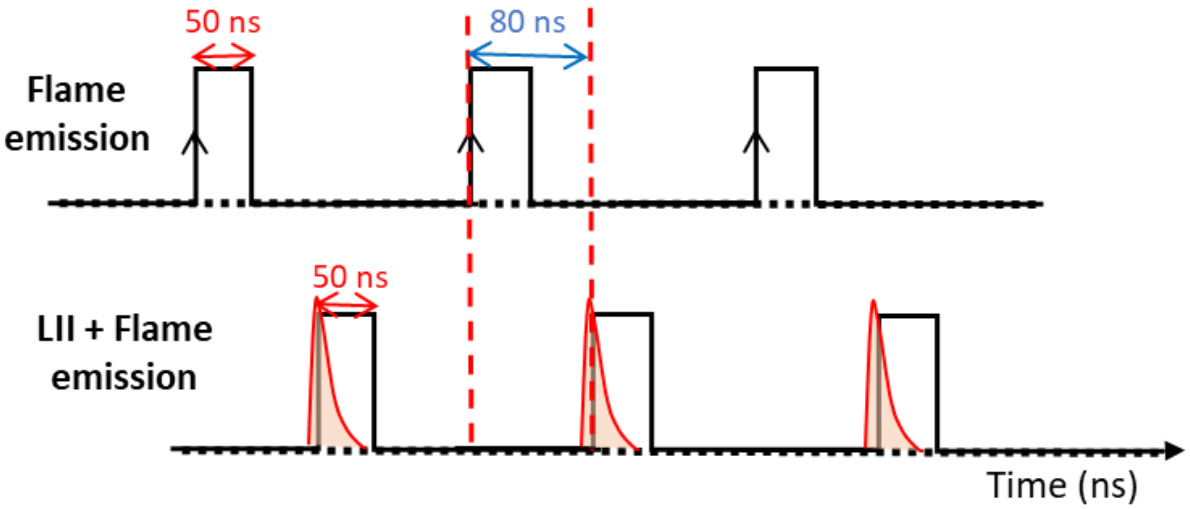

Figure 4.7 Chronogram of synchronization between the flame emission camera (PIMAX2) and the LII+Flame emission camera (PIMAX4) exposures and the LII laser pulse.

The challenges of implementing coupled optical techniques in these types of combustion environments are related to the limitation of the optical techniques. For example, implementing the LII technique (few Hz) with light scattering (in order of kHz) is not possible due to the different time recordings. Only a few frames can be captured synchronously with fast and low-frequency techniques.

Figure 4.8 shows the test rig near the combustor after installing all optical components (for detection only, as the lasers are located in the laser room above the test room).

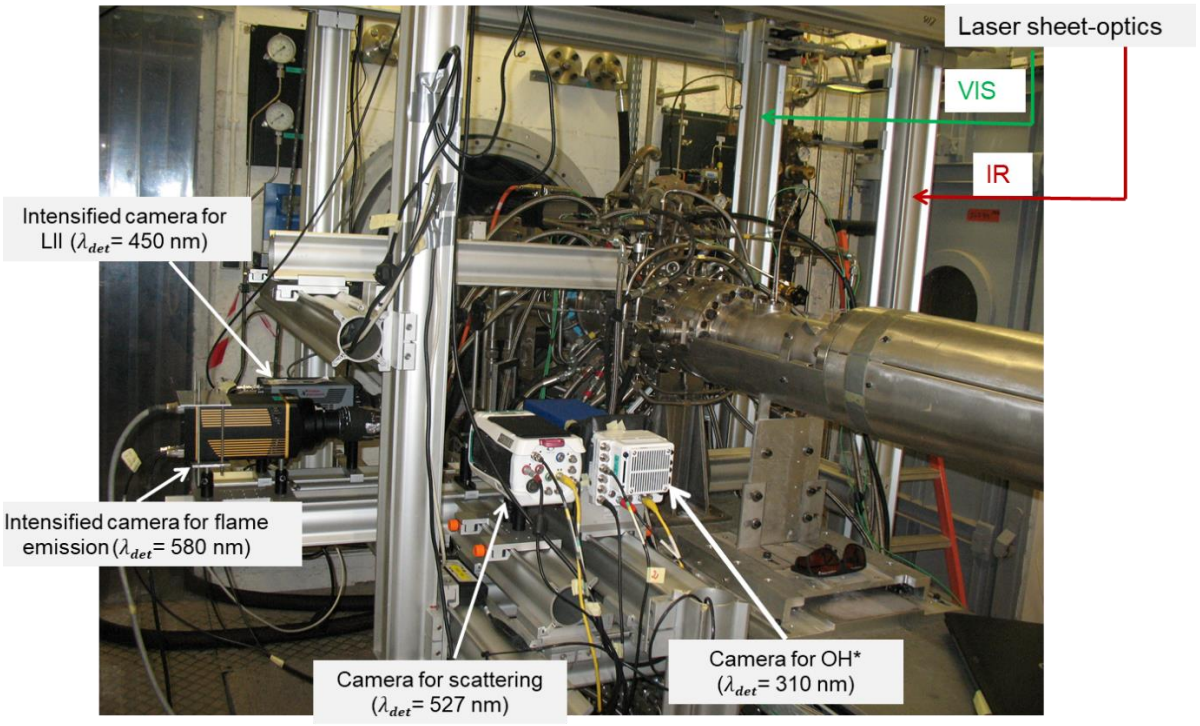

Figure 4.8 Installed optical diagnostics around the MICADO test rig combustor during the measurement campaign performed during the ALTERNATE project.

4.4 RESULTS

This section describes the results obtained after implementing the coupled optical techniques to characterize soot particles on Jet A-1, an admixture of Jet A-1 / ATJ and pure ATJ – air flames. First, spray characterization, OH* chemiluminescence and LII signals are presented to identify the main parameters leading to soot formation for the three-tested OC. Then, the comparison between experiments and simulation is proposed.

4.4.1 Mie/Rayleigh scattering: liquid fuel and soot distribution

It is necessary to have information about spray vaporization and dynamics to study soot production due to the liquid fuel that can interfere with the incandesced soot signal, as discussed at the end of Chapter 3. The general benefits of considering the effect of non-vaporized fuel in explaining soot values and regions in the combustor are:

- Enhanced understanding of soot formation and combustion processes: by studying the scattering properties of liquid fuel, it is possible to gain insights into the conditions under which soot is formed and how it evolves during combustion – correlation with the spray dynamics. Such information can provide valuable information about the parameters that influence their formation in the combustor.
- Improved modeling and prediction of soot emissions: accurate measurements of soot concentrations are critical for developing and validating soot formation and evolution models. By accounting for the contribution of liquid fuel scattering, it is possible to improve the

accuracy of these models and more accurately predict soot emissions under different conditions because the first step in a model consists of the validation of the spray shape (opening angle and penetration depth) and stabilization.

- Enhanced ability to control soot emissions: a better understanding of the factors influencing soot formation and evolution can provide strategies for reducing soot emissions. By accounting for the contribution of liquid fuel atomization and vaporization, it is possible to more accurately assess the effectiveness of different strategies for controlling soot emissions for different types of fuels.

In this study, liquid fuel dynamics are inferred from instantaneous scattering images that are exhaustively described (Figure 4.9) [173,314]. Scattered light from multi-phase combustion is attributed to non-vaporized fuel droplets (through Mie scattering interaction) or soot particles (Rayleigh scattering interaction). In turbulent combustion, like on the MICADO test rig, it is challenging to differentiate Mie/Rayleigh scattering. Rayleigh scattering signals are inferior to Mie scattering due to different scattering cross-section values, µm for liquid fuel droplets and nm for soot particles, and polarization properties. Hence, recorded signals must be pre-processed to assign them to various phases of matter in the combustor. From the observation of recorded images, two categories of signals can be differentiated based on their intensity value and sharpness, whether they are emitted from spray or soot particulates. In addition, in dark regions at the periphery of the spray were identified soot pockets trapped between the spray scattered signal and the detector, similar to shadowgraph.

These dark regions (soot pockets) were identified when soot was localized near the sampling focal point. Light scattered from soot was mainly identified for OC 3 with Jet A-1, the blended fuel and neat ATJ fuels. The separation from Mie scattering is possible when soot particulates are not interfering with the liquid fuel region, as well as in the case of high local soot concentrations on instantaneous images. Specific features are determined on the instantaneous images, which differentiate mainly the OC and less among the fuels. Similar spray angle and coverage area patterns are identified for OC 1 and OC 2. But, OC 3 spray shapes are notably different from the first two OCs due to the oscillation of the spray opening angle and penetration distance from one image to another. Several instantaneous images corresponding to OC 1 - Jet A-1 fuel are shown in Figure 4.9 (blue-colored area), where the coverage spray zone is compact near the injector and thinner towards the spray branches.

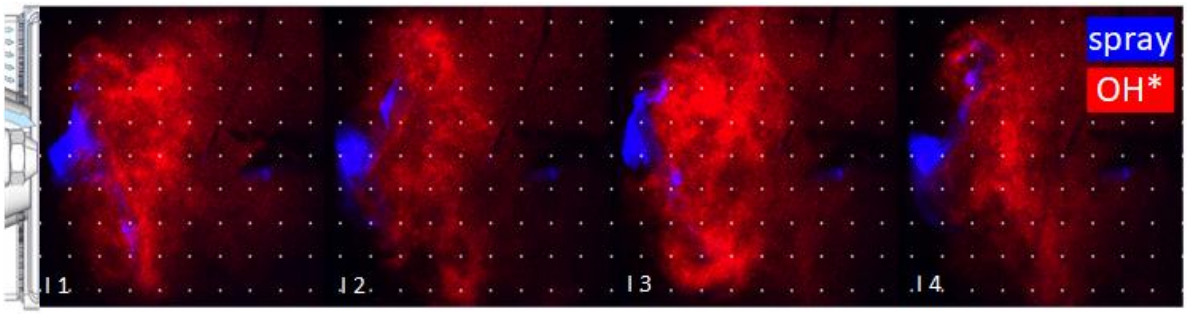

Figure 4.9 Overlay of instantaneous OH* (red color) and non-vaporized fuel (blue color) images for OC1 - Jet A-1 fuel. The dotted mesh has a 10 mm distance between each neighboring dot. Images (I1-4) were randomly selected from the dataset.

For OC 1 and OC 2, the spray is localized on a 10 mm narrow region next to the nozzle, followed by a ramified branch that expands between 10 to 20 mm from the combustor backplate. Thin droplets

of the swirling spray extend from 25 to 45 mm and then impinge on the combustor walls. The spray shape varies considerably for the OC 3 case, indicating that this condition is prone to instability. For OC 3, the spray penetration depth oscillates between 20 and 45 mm, with a synchronous spray angle oscillating between 80 and 140 degrees. High residence time is expected for soot when the spray has a large fan angle (140 degrees) and is localized near the injector; in this case, soot structures persist in the chamber for a few µs until the penetration depth of the spray increases and displaces the soot zones toward the combustor walls. This information is confirmed by the PIV measurements performed in chapter 3 on the same OC for Jet A-1. The movement can be associated with low-frequency spray dynamics. High soot formation rates are associated with regions of high equivalence ratios since the fuel is not evaporated, corresponding to regions evidenced by Mie scattering where the fuel density is high.

Spray frequency oscillations for each OC and fuel were determined after applying fast Fourier Transform (FFT) on summed scattered intensities of each frame for a series of 15000 images. Figure 4.10 shows the dominant frequencies detected at different working conditions on three tested fuels. The dominant frequency is obtained for all fuels for OC 1 at 247 Hz, 1044 Hz, 2090 Hz and 3145 Hz. Almost the same frequencies were obtained at OC 2 but 10% higher than the frequency obtained at OC 1. The OC 3 is characterized by high spray oscillation, easily observed during the measurements on the instantaneous images. OC 3 has a principal detected frequency peak at 232 Hz, followed by its harmonics at 464 Hz, 697 Hz, 929 Hz, 1160 Hz and 1393 Hz.

After the FFT analysis, several prominent frequencies were identified for each OC, with four non-harmonic modes for OC 1, two for OC 2, and six harmonics for OC 3. These modes correlate with the shape evolution of the spray, its stability and mixing with surrounding hot gas. For instance, the reverse frequency shift between the two fuels in OC 2 may be related to the global equivalence ratio role in the vaporization process rather than the operating conditions. This fact is attributed to the fuel-to-air ratio (FAR), which is smaller for Jet A-1 than ATJ in OC 2. FAR values of Jet A-1 in OC 1 and OC 3 are higher than for ATJ. Identified frequencies could be attributed to hydrodynamics or thermoacoustic oscillations.

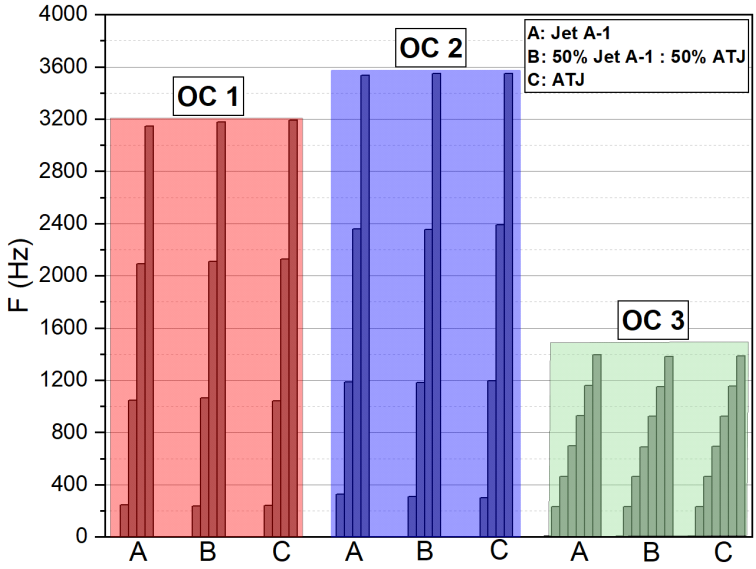

Figure 4.10 FFT on the signals summed for individual 15000 instantaneous images.

To gain more insight into overall spray images, Figure 4.11 shows the averaged non-vaporized fuel scattered signal for different OC and fuels. It has to be noted that the flame is slightly asymmetrical, and some regions of the visualization window were damaged or fouled during the experiment. Therefore, the discussion is limited to the visible regions of the flame through the optical port view. From the averaged signals, for OC 1, the spray is localized near the injector (well-defined edges over 5 mm), followed by an opening of around 45 degrees. For the OC 3 case, the spray extremities are not near the walls due to the predominant spray coverage area on the central axis of the chamber and instability. As a result, the spray angle near the injector slightly increases from OC1 to OC3. At the same time, a slight broadening in the spray fan angle is observed between Jet A-1, 50% Jet A-1: 50% ATJ and neat ATJ fuel for the three cases, as referenced in Figure 4.11, with white arrows. These changes can rely upon the physical properties of the fuel, and they may be an indicator of different vaporization processes from one fuel to another. Standard deviation images corresponding to averaged images (Figure 6.12, annex 4) display a higher spread of pure ATJ and 50% Jet A-1: 50% ATJ scattered signals on the spray region as against the Jet A-1, suggesting again that the atomization of the two fuels is diverse. Indeed highly scattered signals indicate a dense spray, while weakly scattered signals are typical of a more diluted spray. Overall, averaged intensities from the spray are higher next to the injector region for ATJ fuel and 50% Jet A-1: 50% ATJ in the three OC. Conversely, Jet A-1 spray branches are denser than ATJ cases.

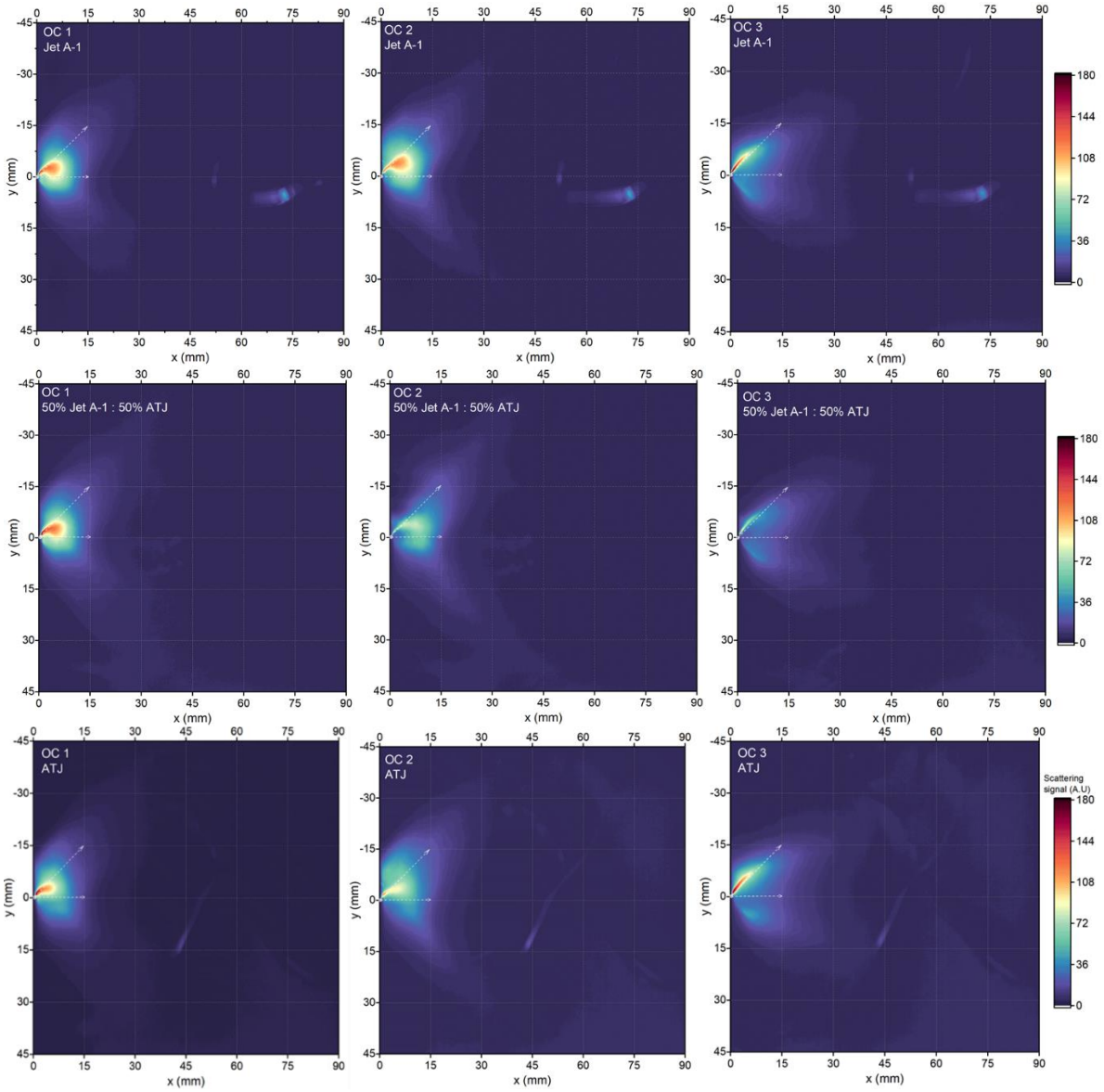

Figure 4.11 Averaged image maps of scattered signals from non-vaporized fuel. Averaged images were calculated on a series of 15000 instantaneous images.

Based on some literature findings, the opening angle and the penetration distance affect the soot formation inside the combustor. For example, the study of Bashirnezhad et al.[287] showed that spray angle strongly affects the soot volume fraction. Their online measurement of the soot volume fraction exiting the furnace indicates that an increase in the fuel spray cone angle decreases the soot volume fraction at the exhaust. The effect of spray on the combustor has also been demonstrated in the study of Zhou et al. [315]. They studied the impact of spray angle on a diesel engine's combustion and emission performance of a separated swirl combustion system. In their experiment, they tested two opening angle scenarios; the first one occurred when the lower spray angle was 105 degrees and the upper spray angle was 165 degrees. The second tested scenario is when the lower spray angle was 75 degrees and the upper spray angle was 165 degrees. Their main findings demonstrated that there is a greater reduction in fuel consumption and soot emission under spray angle in scenario one compared two the second one. Fuel consumption decreased by approximately 1.6% - 8.3%, and soot emission decreased by 16.16% - 36.64%.

In this study, the conditions with small opening angles (OC 1 and OC 2) have lower LII signals, and higher soot intensity is observed on the upper shear layer towards the walls of the combustor. Whereas the condition with a slightly higher opening angle (OC 3) has a higher LII signal, the high soot intensity is mainly formed towards the inner recalculation zone of the flow. This observation on OC 3 can be based as well on the fluctuations of the spray cone angle. Based on the observations of this study, the switch from ATJ to Jet A-1 does not significantly impact the spray distribution and the flame stabilization process. The main characteristics of the spray, like the opening angle and penetration, are not modified, and the flame shape looks similar. However, the different physical properties of the two fuels only impact locally the fuel/air mixing, thus determining a local modification of the flame heat release. The discussion on the impact of spray vaporization and dynamics on soot is detailed when presenting LII results.

4.4.2 OH* chemiluminescence: flame front, heat release and reaction zone

During the combustion process, chemiluminescence refers to the phenomenon that radicals excited by chemical reactions fall from higher to lower energy levels and emit light of a specific wavelength [316]. Chemiluminescence emission occurs in particular wavelength bands characteristic of the emitting molecules. Because the molecules responsible for the chemiluminescence change for different combustion regimes and types, chemiluminescent emissions can provide information about the reaction steps in the flame [317]. Due to this, OH* chemiluminescence emerges near the flame reaction zone and can be used to depict the flame structure (front), reaction characteristics and heat release zone [284,316,318–320].

These phenomena can help to reveal some factors influencing soot particle formation inside the combustor. However, difficulties can occur in associating OH* signal with these phenomena, as in turbulent combustion [21]. The main factors that influence the OH* in turbulent combustion are pressure and temperature; the concentration of hydroxyl radicals increases with temperature and pressure as the rate of their production through the thermal decomposition of water vapor increases [321,322]. Also, fuel types can produce different amounts of hydroxyl radicals during combustion [323]. For example, fuels with a higher hydrogen content tend to produce more hydroxyl radicals [324,325]. The concentration of OH* radicals also depends on the availability of oxygen. If the oxygen concentration is high, the rate of OH* production can be higher [326,327]. Lastly, the intensity of the turbulence in the combustion chamber can affect the production and distribution of OH*; higher turbulence levels can lead to more evenly distributed OH* concentrations [328,329].

Figure 4.9 shows an example of OH* signal distribution inside the combustor at OC 1 with the combustion of pure ATJ. From the instantaneous images, the OH* signal is distributed almost all over inside the combustor, with higher intensity formed after the spray location. The oscillation and intensity level of detected signals change from one working condition to another, with a small difference in the type of fuel used.

To have general information on the distribution and localization of the OH* signal in the combustor, Figure 4.12 illustrates the averaged OH* emission for the three OC on three tested fuels. The flame front is not changing significantly among selected fuels and OC. The flame is expanding almost identically on the vertical axis for OC 1 and OC 2.

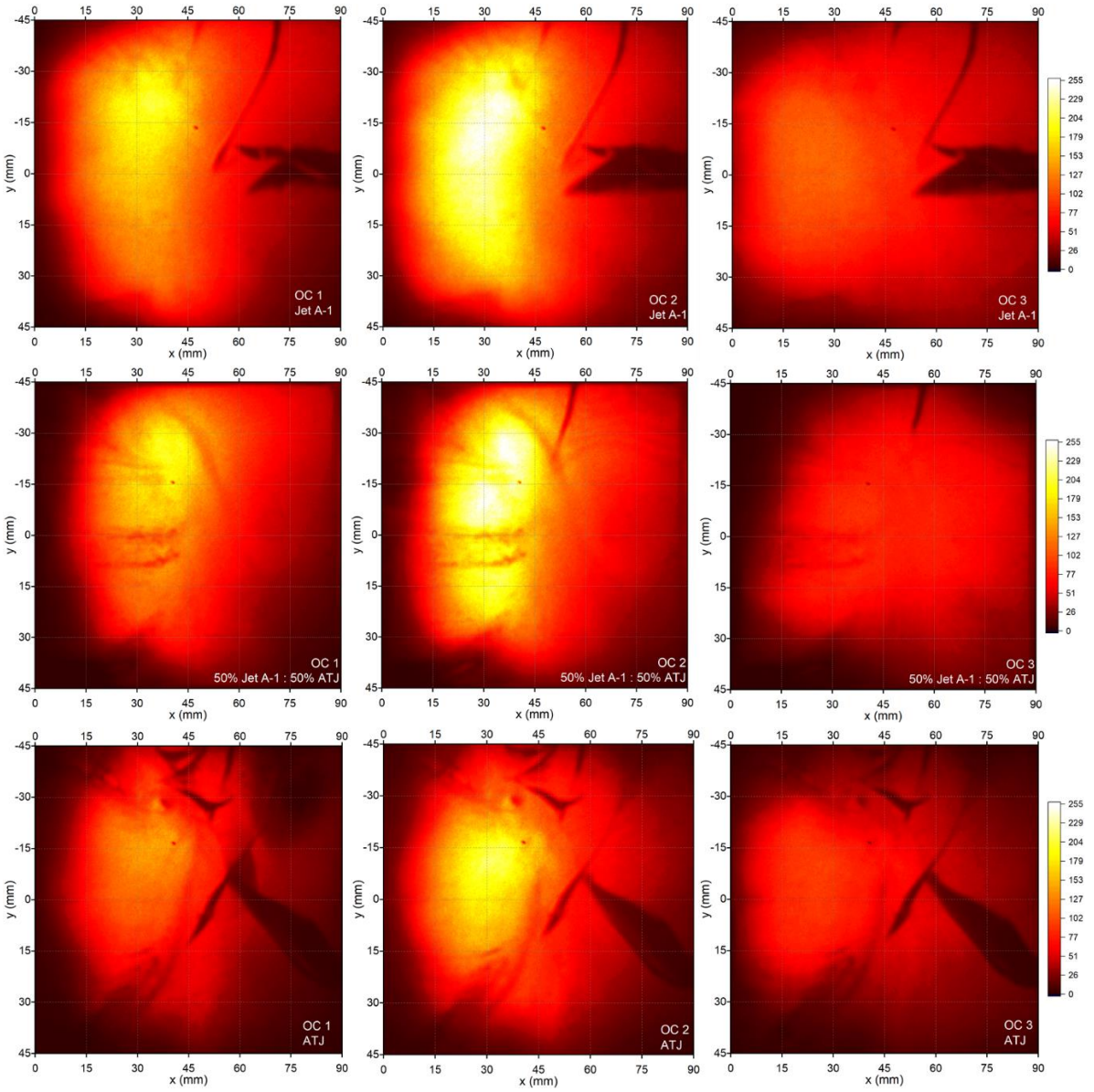

Figure 4.12 Average OH* chemiluminescence maps for the three fuels (Jet A-1, blend and ATJ) for the three OCs. Averaged images were obtained from a series of 2000 instantaneous images.

The heat release is dominant in the inner recirculation zone of the flame. On the horizontal axis, the shift of OH* intensities from the injector toward the exhaust suggests that the flame is stabilized differently for the three OCs. For OC 2 and OC 1, the flame is stabilized closer to the injector, with a peak of heat release near 30 mm, indicating a faster fuel evaporation rate and improved mixing. Unexpectedly, Jet A-1 fuel combustion is characterized by a higher OH* emission than the one displayed by ATJ in the three OCs. A positive linear correlation exists between the FAR and OH* ratio for the two fuels (Jet A-1 and pure ATJ) for OC 1 and OC 2, but this trend is changing for OC 3, the condition characterized by unsteady phenomena. Because the observed difference between the OH* signal for the three fuels cannot be explained by the fuel LHV only, it is suggested that the local mixing influences the heat release as well, which can affect the evaporation of fuel. It is suggested that differences in the local mixing, which result from the turbulence and the evaporation rate, directly affect the heat release rate and the concentration of soot precursors and soot particles.

OC 3 case is characterized by lower OH* intensities on the averaged image, with a maximum peak between 15 and 30 mm and a higher turbulence rate since the standard error deviation (Figure 6.13, annex 4) is the highest among the three OCs. Unexpectedly, an admixture of Jet A-1 and ATJ fuel combustion is characterized by a higher OH* emission than the one displayed by pure Jet A-1 or ATJ in the three OCs. A positive linear correlation exists between the FF/FF_{ref} and OH* ratio of the two fuels for OC 1 and OC 2, but this trend is changing for OC 3 on the admixture of Jet A-1 and ATJ. Because the observed difference between the heat release of the tested fuels can be caused by the difference in the LHV of the fuels, but it is possible that the local mixing influences the heat release as well, which can affect the evaporation of fuel. It is suggested that differences in the local mixing, which result from the turbulence and the evaporation rate, directly affect the heat release rate and the concentration of soot precursors and soot particles.

The study of Li et al. [330] has revealed the competitive relationship between soot formation and chemiluminescence on ethylene/air laminar diffusion flame at atmospheric combustion conditions. The results show that soot formation and chemiluminescence compete for fuel pyrolysis products because their reaction paths are opposite. CH*, C*, and OH* intensity decrease with the increase of soot volume fraction because more pyrolysis products participate in soot formation. These findings can be compared to the results obtained on MICADO combustors, as on the averaged OH* signal, the majority of OC with a lower OH* averaged signal corresponds to the condition with a higher LII signal (Figure 4.16).

The advantage of applying OH* chemiluminescence cannot be only based on heat release and reaction zone; it can also bring information on the oscillation of the flame and some possible instabilities inside the combustor. Different studies have used OH* to study the instabilities inside real engine combustors [328,331,332]. As the OH* is related to the heat release, applying Fast Fourier Transformation on the detected images can give an insight into frequencies and oscillations inside the combustor. Figure 4.13 shows the FFT spectral amplitude (spectrograms) obtained on 15000 OH* images summed on the whole visualized region of the flame. The OC 1 is characterized by the frequency with high amplitude around 247 Hz and 1043 Hz for Jet A-1 and admixture of Jet A-1 and ATJ, whereas on pure ATJ, there is one detected frequency at 1065 Hz. The OC 2 has a slight shift in frequency compared to the OC for all fuels, where for Jet A-1 and admixture of Jet A-1 and ATJ, the high amplitude frequencies are detected at 323 Hz and 1188 Hz, whereas for pure ATJ, the high amplitude is detected at 1196 Hz. These conditions are characterized by low averaged soot signal, and OH* instantaneous images do not represent high oscillation from one image to another. On the other hand, the OC 3 is characterized by more fluctuations and harmonic mode detected around 232 Hz, 464 Hz, 697 Hz and 929 Hz for all fuels. These high oscillations can be caused by the thermoacoustic effect and high pressure inside the combustion chamber compared to OC 1 and OC 2.

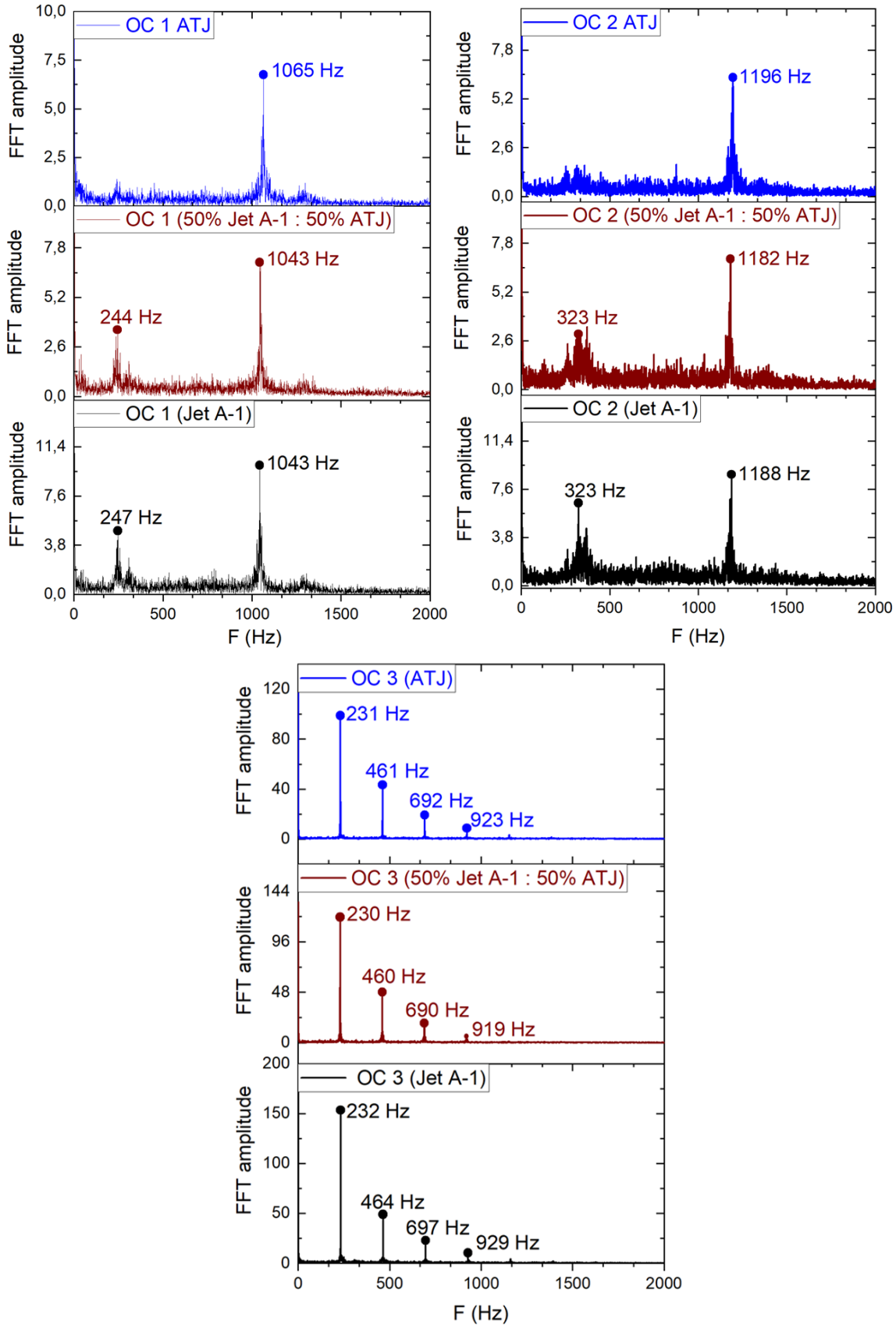

Figure 4.13 Fast Fourier Transformation (FFT) spectral amplitude obtained on 15000 summed OH* images for the three OC and three fuels.

4.4.3 Laser-Induced Incandescence – LII: soot particles detection

Laser-induced incandescence was used for detecting soot particles inside the MICADO combustor. As explained in the section on the experimental setup (subchapter 4.3), the detection system for LII is composed of two cameras (to differentiate flame emission from LII signal). Figure 4.14 illustrates an example of averaged and std flame emitted signal detected at 580 nm during the combustion of Jet A-1 fuel. The recorded flame signal represents an important percentage compared to the total detected LII signal, showing the importance of subtracting flame emission from the LII-detected signals in this turbulent environment. Detected flame emission is produced by the soot in the flame volume and other self-excited molecules.

For all OCs, the flame-emitted averaged signal maps are shown in Figure 4.14. The flame emission shape is similar to the maps with soot detected from LII (Figure 4.17). For OC 1, the highest intensity is mainly towards the upper walls of the combustor. For OC 2, the flame emission is primarily on both walls towards the exhaust, and for OC 3, the highest intensity is detected in the center of the inner recalculation zone. As the pressure in the combustion chamber increases, the averaged and std flame emitted signal increases. One of the main parameters that pressure can influence is the luminosity of a kerosene flame, but it is not the case in this study.

At higher pressures, the gases and particles can tend to flow more quickly, and the heat and mass can be transported more efficiently, leading to a higher rate of fuel burn and a more luminous flame. At lower pressures, the gases and particles can flow more slowly, and the transport of heat and mass can be less efficient, leading to a lower rate of fuel burn and a less luminous flame. Another factor that can affect the luminosity of the flame is the temperature of the flame. The higher temperature results in a higher energy release rate and a more efficient combustion process, leading to a more luminous flame. The amount of oxygen available for the combustion process can also influence the luminosity of the flame. More oxygen is typically available at higher pressures, leading to a more complete and efficient combustion process and a more luminous flame. Conversely, less oxygen may be available at lower pressures, leading to an incomplete combustion process and a less luminous flame. It is worth noting that these effects are not always linear, and the relationship between pressure and flame luminosity can depend on the specific conditions of the combustion process [333].

In our case, the observed effect of pressure on the flame luminosity can not be the only determinant parameter on the emitted flame signal; more combustion parameters have to be considered. For example, as the FF/FF_{ref} increase, the flame emitted signal also increase. This can be due to the mixing ratio between the air and the fuel and also the inlet air temperature. The localization and the structure of the flame-emitted signal from jet A-1 look almost similar to the one of 50:50 blending and pure ATJ. The only difference is seen in the level of emitted intensity; Jet A-1 has a higher flame emitted intensity compared to ATJ flame. The main reason that can lead to this difference is the chemical composition. Jet A-1 is a complex mixture of hydrocarbons, while ATJ fuel is mainly composed of iso-paraffines, which may contain other organic chemical compounds. These differences in chemical composition lead to other combustion products contributing to differences in flame intensity. Another factor that can lead to this difference is the LHV of the fuel. The flame intensity of a fuel depends on its heat of combustion, which is a measure of the heat released when the fuel burns. Jet A-1 has a higher heat of combustion than ATJ fuel, which means that it releases more heat when it burns and may produce a higher flame intensity.

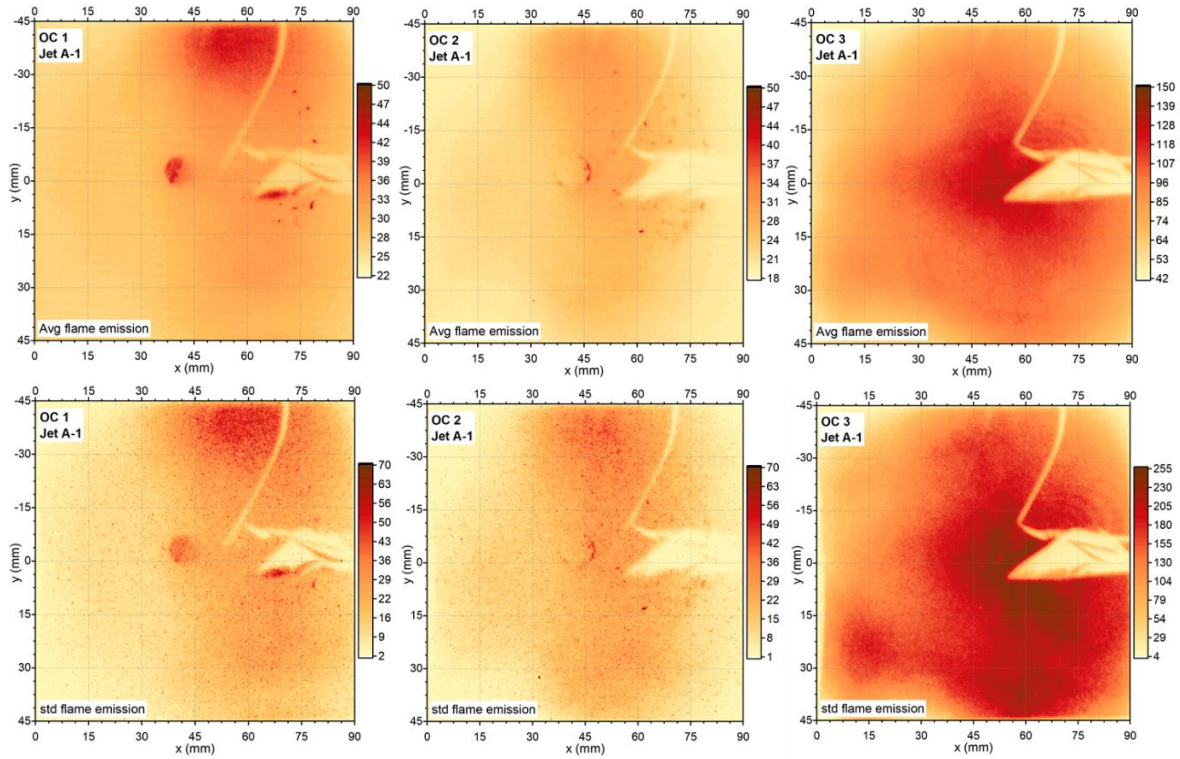

Figure 4.14 Averaged and std flame emitted signal obtained over 1500 images during the combustion of Jet A-1/air at different operating conditions.

Soot particle regions were identified with the LII technique, which is highly sensitive until a few ppb for their detection. The high intermittency observed on the LII instantaneous images in chapter 3 for Jet A-1 was almost the same, but the LII intensity on the admixture of Jet A-1 / ATJ and pure ATJ were changing compared to the one obtained on Jet A-1. On instantaneous images, soot zones identified in OC 1 and OC 2 for Jet A-1 have well-defined wrinkled structures (Figure 4.15). At the same time, for the same OCs for the admixture of Jet A-1 /ATJ and pure ATJ fuel, it is only possible to detect some soot patches with low LII signal representing only a few percent from the total of the signal detected for Jet A-1 fuel.

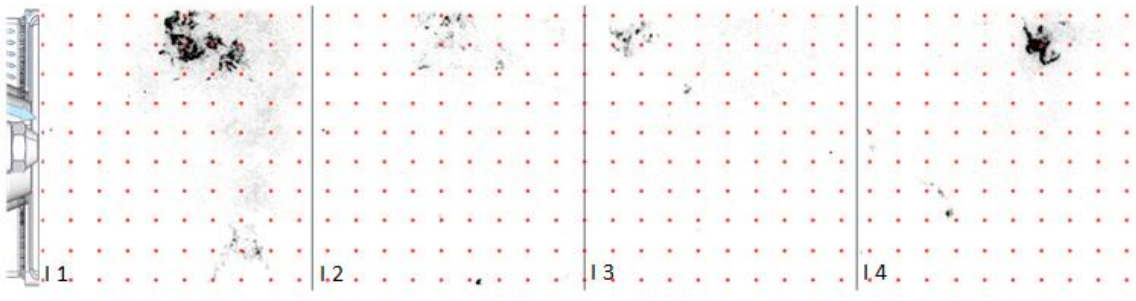

Figure 4.15 LII instantaneous images for Jet A-1 at OC 1. The dotted scale corresponds to a 10 mm distance. Images (I1-4) were randomly selected from the dataset.

Due to the high turbulence, there are large fluctuations of the LII signal from one image to another (Figure 4.16). In addition, turbulence causes fluctuations in the intensity and intensity distribution of the laser sheet used to heat soot particles. This can make it more difficult to accurately measure the LII signal, as the signal varies spatially and temporally from one image to another. Also,

MICADO turbulent flame causes fluctuations in the temperature and composition of the sample being analyzed with LII. This can lead to changes in the LII signal that are not related to the properties of the sample itself but rather to the effects of turbulence on the measurement environment.

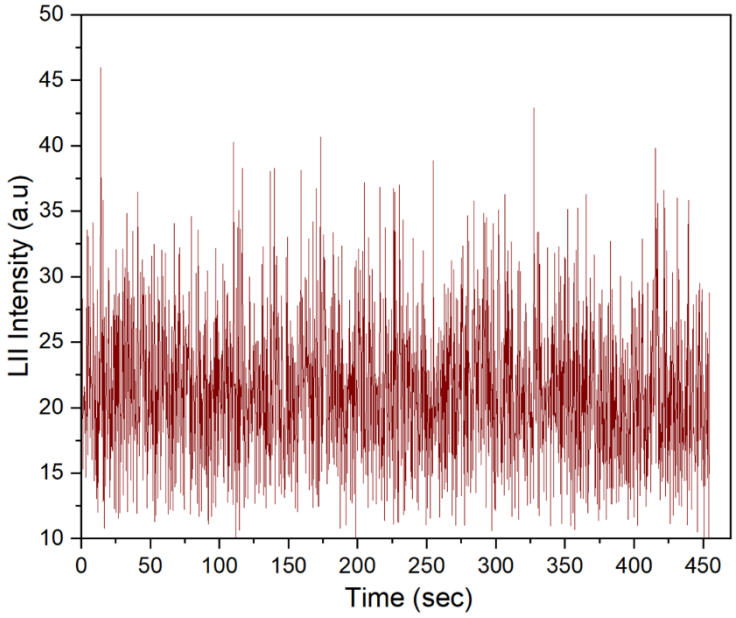

Figure 4.16 Temporal fluctuations of LII instantaneous signal (spatially averaged images). The plotted signal was recorded at the frequency of 3.33 Hz, with 1500 recorded images on each sequence at OC 3, using Jet A-1 as fuel.

The overall distribution of the LII signal is shown on the averaged signal (Figure 4.17) after the flame emission is subtracted. Spatially, soot-averaged fields are shifted toward the exhaust from the reaction zones for OC 1 and 2. High intensity is observed near the window peripheries with reduced average soot volume fractions (few ppb). For these two cases, soot is present near the walls after X= 30 mm from the combustor back plate. An outer corner recirculation zone (CRZ) is observed near the back plate region, mainly for OC 1 and less prominent for OC 2. This trend is not kept for OC 3, where soot particles are mainly detected in the inner recalculation zone, which can be due to the flame pressure, high turbulent behavior, unsteady phenomena and lower velocity vector values as measured in chapter 3.3.1.

LII signals are at their detection limit for the admixture of Jet A-1 / ATJ and pure ATJ on OC 1 and OC 2. The inner recirculation zone is not well delimited in the OC 1 and OC 2 (high std) case because the probability of identifying a soot filament in this region is low. The formation of soot is particularly interesting for OC 3. High LII signals (ppm) are identified on the instantaneous images, where soot coverage is similar to corrugated flamelets, as displayed in Figure 4.18. In this case, soot is all over the combustor, and most instantaneous images are covered with soot in the inner recirculation zone.

The soot volume fraction is estimated to be in the range of few ppm on the averaged images for Jet A-1 for OC 3 (as shown in chapters 2 and 3). The high predominant sooting behavior of OC 3 was also captured with the scattering techniques, where soot is mainly identified in the inner recirculation toward the exhaust when the spray is broader and closer to the back plate. In the literature, few studies focus on the non-intrusive characterization of soot particles by burning SAF fuels in such combustion conditions and applications. Corbin et al. [334] studied *ex-situ* measurements on

aircraft-engine particulate matter emissions from conventional and sustainable aviation fuel combustion. They found that the particle mitigation potential of SAF blends tends to decrease with increasing engine power settings. While the general trends in particle emission are well reflected by combustion kinetics and soot precursor formation at controlled conditions, the actual soot formation at a full scale of the engine is a complex interaction of fuel chemistry, spray formation, turbulent flow field and soot oxidation. From this study, soot particles emitted at lower pressure (OC 1 and OC 2) have lower LII signals for admixture and pure ATJ compared to Jet A-1. Still, by increasing the pressure at OC 3, there is a considerable difference in emitted soot signal for the three tested fuels, where Jet A- 1 has higher soot emitted intensity compared to the blend and ATJ.

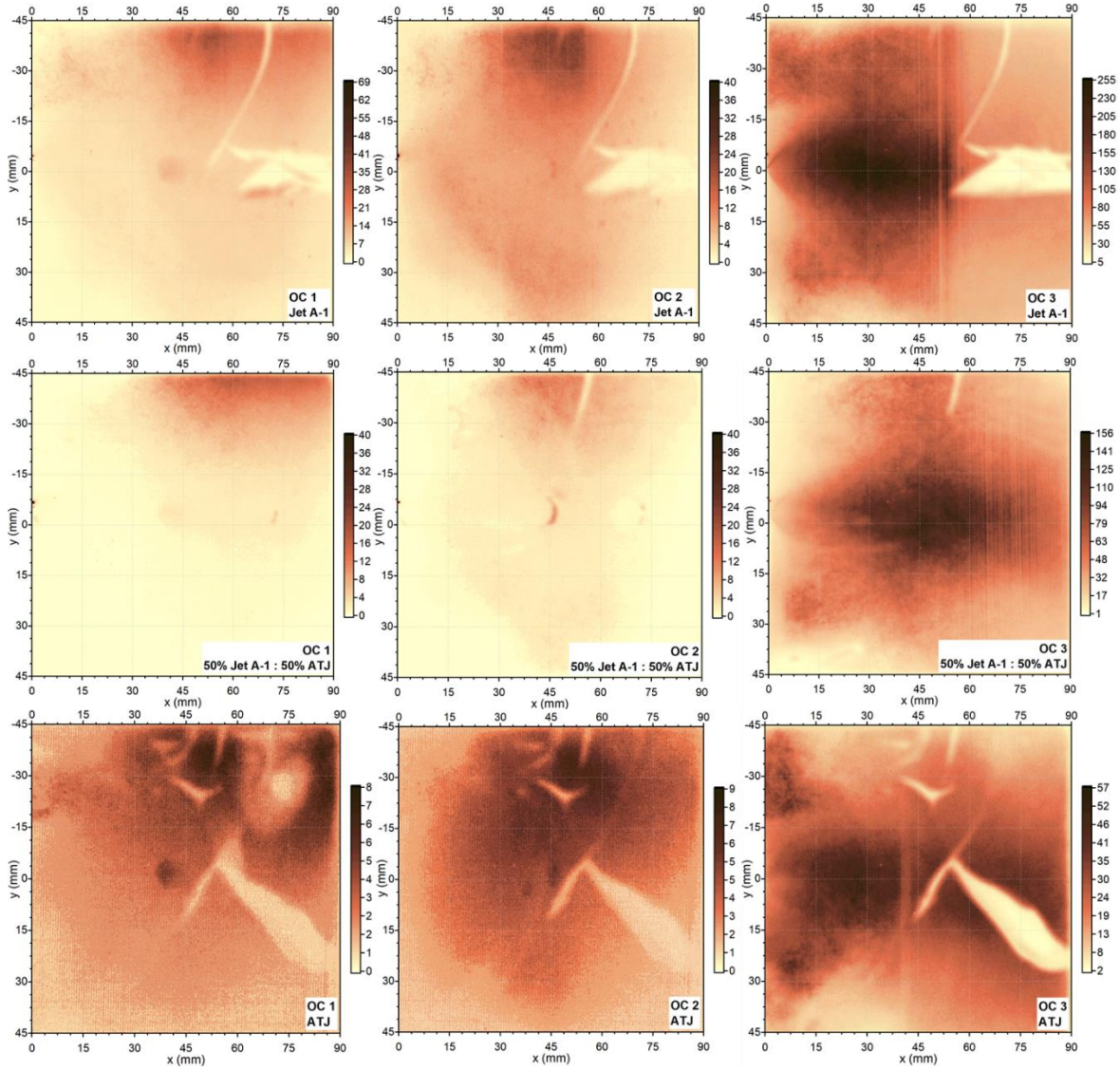

Figure 4.17 Average LII signal maps detected for the three OCs with different tested fuels. Averaged images were obtained from a series of 1500 instantaneous images.

Due to the complexity of the MICADO flame structure, six different regions of interest were selected to analyze further soot distribution and their localization inside the combustor (Figure 4.18). These regions were chosen based on the main region identified on the swirled flame obtained in the MICADO combustion chamber.

Based on the temporal and spatial evolution of the soot incandescence signal, it is possible to obtain information on the probability of detecting a certain amount of soot particles in a given region of interest, as in the work of Roussilo et al. [148]. Theoretically, the probability density function (PDF) is a function of a continuous random variable whose integral across an interval gives the probability that the value of the variable lies within the same interval. In the context of studying the distribution of soot particles in a combustor, a PDF is used to describe the probability of finding soot particles within a certain range of sizes or concentrations. This can be useful for understanding the overall distribution of soot within the combustor and identifying any potential trends or patterns in the data. By plotting the PDF (Figure 4.19), it is possible to see the distribution shape and understand how the soot particles are distributed across different size ranges (mostly soot filaments). In addition, PDFs can provide insights into the central tendency and dispersion of the distribution, which can help to understand the overall characteristics of the soot particle distribution.

There are different types of PDF; in this study, the normal distribution function is expressed by the following equation [335]:

$$f(x, \mu, \sigma^2) = \frac{1}{\sigma\sqrt{2\pi}} e^{-\frac{1}{2}\left(\frac{x-\mu}{\sigma}\right)^2} \quad \text{Equation 4.1}$$

Where μ is the mean representing the average value of the distribution in the given ROI, σ is the variance which represents the dispersion of the distribution around the mean, and x is in the range of $0 \leq x \leq 255$, which correspond to the LII images coded under 8 bits. Figure 4.18 illustrates an example of the different regions of interest (ROI) used for calculating the PDF. These regions were chosen based on the main attributed zones of the swirled flame. The ROI 1,2,5 and 6 are considered as the outer recirculation zone, and ROI 3 and 4 are the center of the inner recirculation regions.

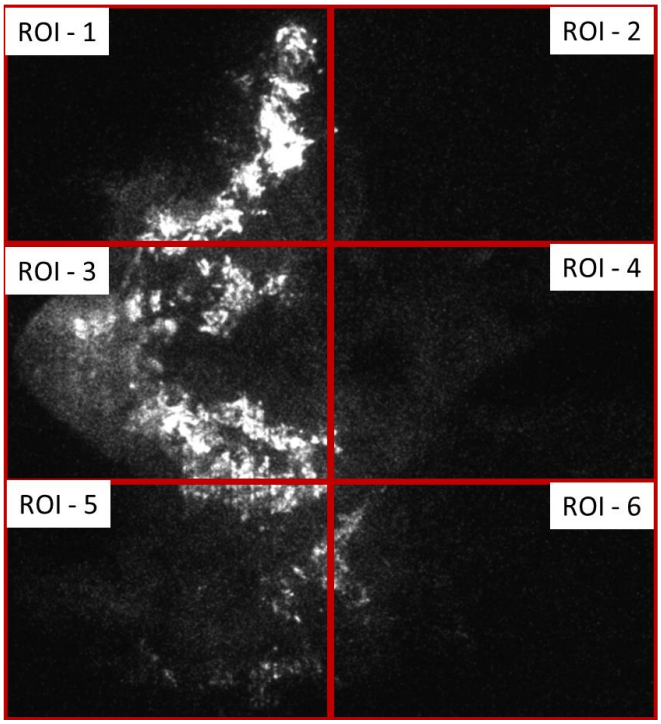

Figure 4.18 Different regions of interest selected on instantaneous LII image for OC 3 with Jet A-1 fuel.

Figure 4.19 shows the probability density function of soot distribution in the different regions of interest for three tested fuels at OC 3. The intensity is shown in counts and is coded in the images of 8-bit (the maximum count is 255). The probability of getting soot particles in the ROI 1 for this condition (OC3); on Jet A-1, the averaged intensity is 96.6 counts and is higher compared to the admixture of Jet A-1/ATJ and pure ATJ. This region covers a part of the outer recirculation zone. By looking at the ROI 2, which is toward the exhaust on the upper side of the flow, the average intensity is 74.6 counts and is two times higher compared to pure ATJ and 1.5 times higher than the one of the admixture. ROI 3, which covers the center of the inner recirculation zone, is characterized by the maximum intensity, which means that it is the region with a high probability to get the soot particles. The average LII intensity obtained is 150 for Jet A-1, almost two times more than the one obtained on ROI 1 and 2 on the same fuel. Based on the calibration carried out in chapter 3, the maximum intensity in this condition is in the order of 0.80 ppm. By changing the fuel types and using the admixture of Jet A-1 and ATJ, the average intensity was reduced by almost three times compared to the one of admixture and pure ATJ, which can be in the order of 0.25 ppm. The intensity distribution in the flow center toward the exhaust (ROI 4) decreased compared to the average intensity obtained on ROI 3. The obtained averaged LII intensity in that region is 105 counts for Jet A-1, 95 counts from the admixture of Jet A- 1 / ATJ and 50 counts for pure ATJ.

If the flame dynamic was symmetric with respect to the injection axis, the distribution of soot particles in the upper region of the flow (ROI 1 – ROI 2) and the lower region (ROI 5 – ROI 6) should be the same. But in ROI 5, the average intensity for Jet A-1 is 67 counts, almost 1.8 times higher than the one detected for the admixture of two fuels and 43 counts for pure ATJ.

To summarize this condition (OC 3), there is a high probability of detecting soot particles in the center region of the inner recirculation zone (ROI 3) for both tested fuels compared to the other analyzed ROI. However, there is a difference in the averaged LII intensity detected for the three-tested fuel. The maximum intensity was observed for Jet A-1 fuel and decreased around two times on the admixture of Jet A-1/ATJ and more than three times for pure ATJ. This high intensity detected in ROI 3 can be caused by many factors, including combustion conditions and flow dynamics.

The probability of detecting soot particles in some regions for OC 2 and OC 1 differs from that one obtained in different ROIs at OC 3. For this condition, the maximum intensity was detected in the ROI 2 for all fuels. The soot particles are more distributed on the upper side than the lower side of the flow (probably due to a problem of asymmetry of the flame). Consequently, the lowest probability of detecting soot particles is for ROI 5 and 6. The averaged LII signals obtained are the lowest ones detected with the Incandescence technique. By changing the type of fuels, sometimes on the instantaneous images, it was impossible to detect soot particles on the admixture of Jet A-1 / ATJ. The averaged LII signal for OC 1 in different ROI becomes lower compared to the one obtained on OC 2, but the localization of maximum intensity is the same for both OC. Therefore, the probability of detecting soot particles in different ROI is low for these two cases, and the detected soot filaments and pockets have an intensity that is the order of tens ppb for Jet A-1 and few ppb for pure ATJ and admixture.

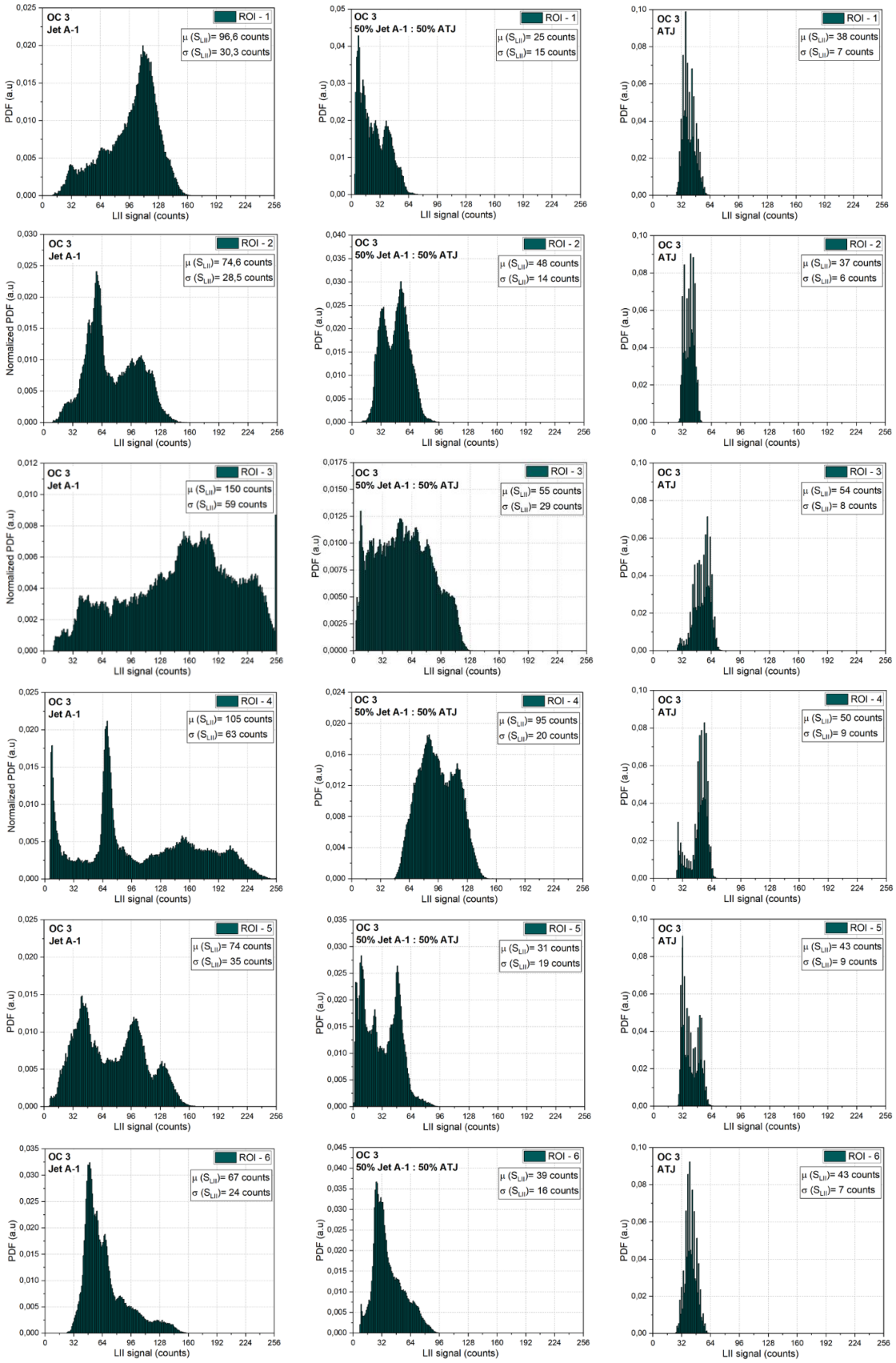

Figure 4.19 The probability density function of soot distribution on the different regions of interest for three tested fuels at OC 3.

4.4.4 Soot production for Jet A-1 and ATJ: comparison of experimental data with numerical results

The results obtained in this chapter are part of a collaboration project between different institutes. Apart from experimental studies carried out on the MICADO test rig, in parallel, Safran Tech and CERFACS worked jointly to perform Large Eddy Simulation (LES) for the OC 1 and OC 2 with Jet A-1 and pure ATJ. Semi-detailed chemistry for fuel oxidation and gaseous soot precursors together with the Lagrangian Soot Tracking model, both developed by CERFACS and Safran Tech, is applied, and a first comparison against the available experimental data in terms of spray evolution and flame shape is obtained. The work presented in this section was done in a joint article between ONERA, CERFACS and SAFRAN Tech [336]. This discussion aims to show the application of the obtained results against the numerical models. The modeling part is not in the scope of this Ph.D., but it is worth giving such a discussion since we need to commonly agree on the data to be used for comparison. The details of the used models are described in annex 4 and the article of Irimiea et al. [336].

Figure 4.20 compares the experimental and numerical simulation of the scattered signal of unburned Jet A-1 and ATJ fuel droplet at OC 1. However, both signals show almost the same penetration distance until 14 mm from the injector. In addition, the numerical results show a well-defined V shape opening compared to the experimental data. Also, on numerical results, the liquid phase penetration increases slightly, passing to semi-detailed chemistry in the downstream zone, while the near injection region is almost unchanged.

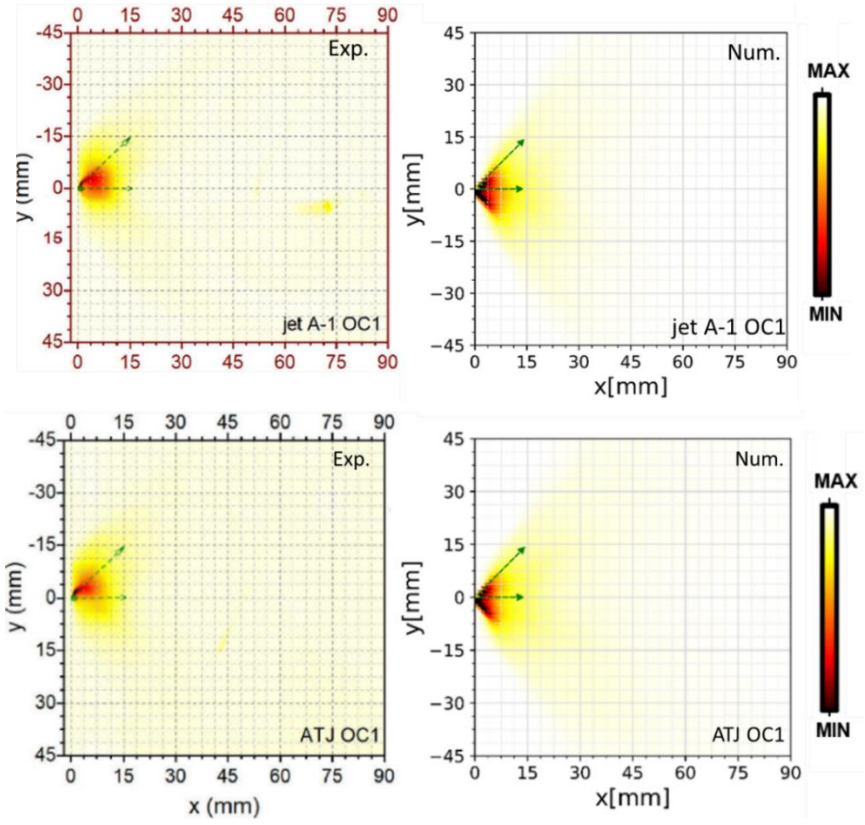

Figure 4.20 Comparison of the spray evolution for Jet A-1 AND ATJ from Mie scattering (left side) and the sight integrated liquid volume fraction line from ARC-LST-Jet-A1 and ATJ case (right side) [336].

Figure 4.21 shows the experimental and numerical results of the OH* chemiluminescence distribution signal obtained from Jet A-1 and ATJ at OC 1. For both fuels, experimental results show lower OH* signal distribution compared to numerical results. The numerical results also show a well-defined V shape for JeJ A-1, which was cut in the middle of each branch by changing to ATJ fuel. The spray shape and penetration depth was the first step to validate the used model. On the experimental side, difficulties can occur in associating the obtained OH* signal directly with the reaction zone and the heat release. In MICADO combustion conditions, many factors can affect the distribution of OH* molecules, like fuel properties, combustion temperature and pressure, turbulence level, global equivalence ratio at the injection point and the flow dynamic that can lead to the symmetry of the flame. As a result, the experimental OH* signal distribution is asymmetric, whereas the numerical result is symmetric. The spray shape and penetration depth was the first step to validate the used model.

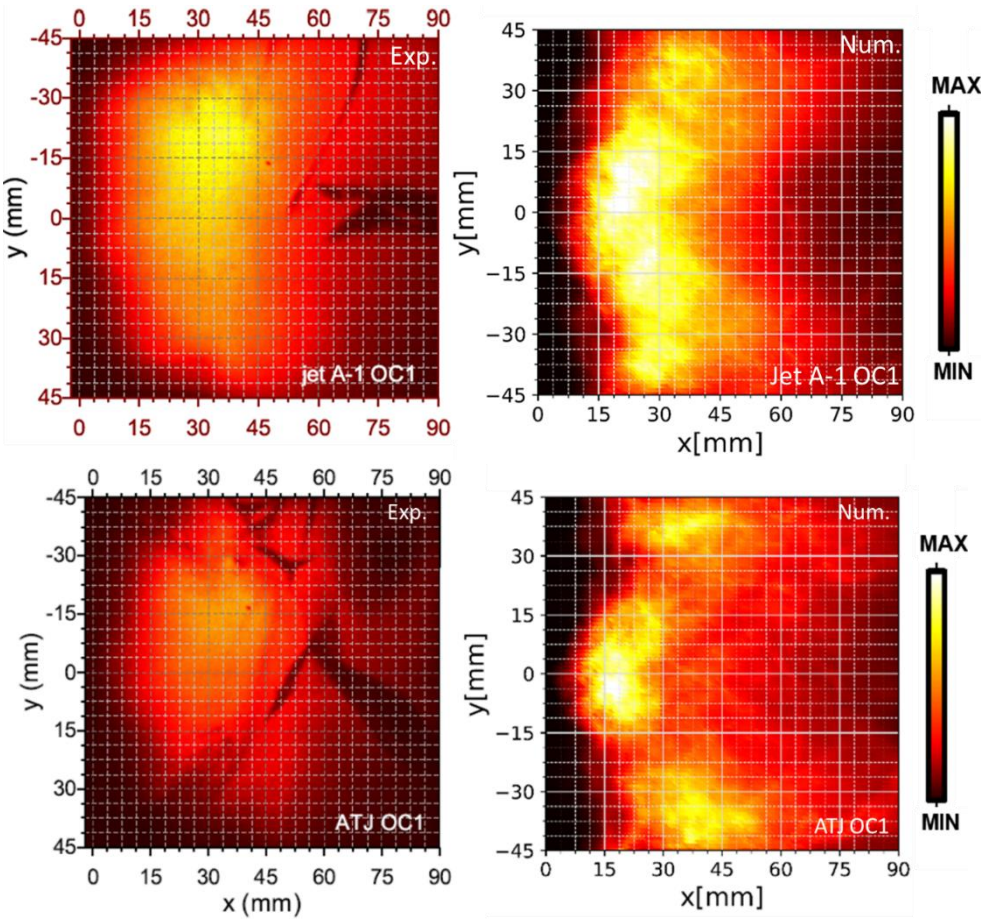

Figure 4.21 Comparison of the flame shape obtained for Jet A-1 and ATJ from OH* chemiluminescence (left side) and the line of sight integrated from the ARC-LST-Jet-A1 and ATJ case (right side) [336].

Figure 4.22 shows the averaged soot incandesced signal map obtained experimentally with the soot volume fraction map obtained numerically for jet A-1 and ATJ fuels at OC 1. From the model, it was difficult to find the mechanisms that could stabilize the flame as obtained experimentally. Furthermore, it was observed that models could not capture the same phenomena for the fluid mechanics' equations and kinetics when changing the fuel type. However, based on the obtained results, several points can be underlined as follows:

- The numerical results are coherent with experimental findings for the spatial distribution of soot zones; soot is mainly located near the wall zone, even at a slightly higher radial position. Despite the strong asymmetry of the experimental distribution, the peak of the soot volume fraction is located between 30 mm and 60 mm from the chamber backplane. LES looks able to retrieve it.
- The numerical calculations show soot produced in the near injection zone. This is related to the presence of the flame that entails strong evaporation and, therefore, the generation of pyrolysis products and soot precursors. From an experimental point of view, the collection of data on soot in that zone is a complex task because of the presence of the liquid that can trap the LII signal in emission. Nevertheless, it has been observed that a reduced amount of soot was detected (with scattering experiments) in that region, thus giving more confidence in the LES results.

The LES presented results were obtained during an average time of about 20 ms. Considering the intermittency in the soot production of the present case (OC 1), this is insufficient to ensure converged statistics on soot. As widely reported in the literature [337], soot may present averaging times much longer than the gaseous phase. This also explains the non-symmetrical distribution of soot obtained from a numerical point of view.

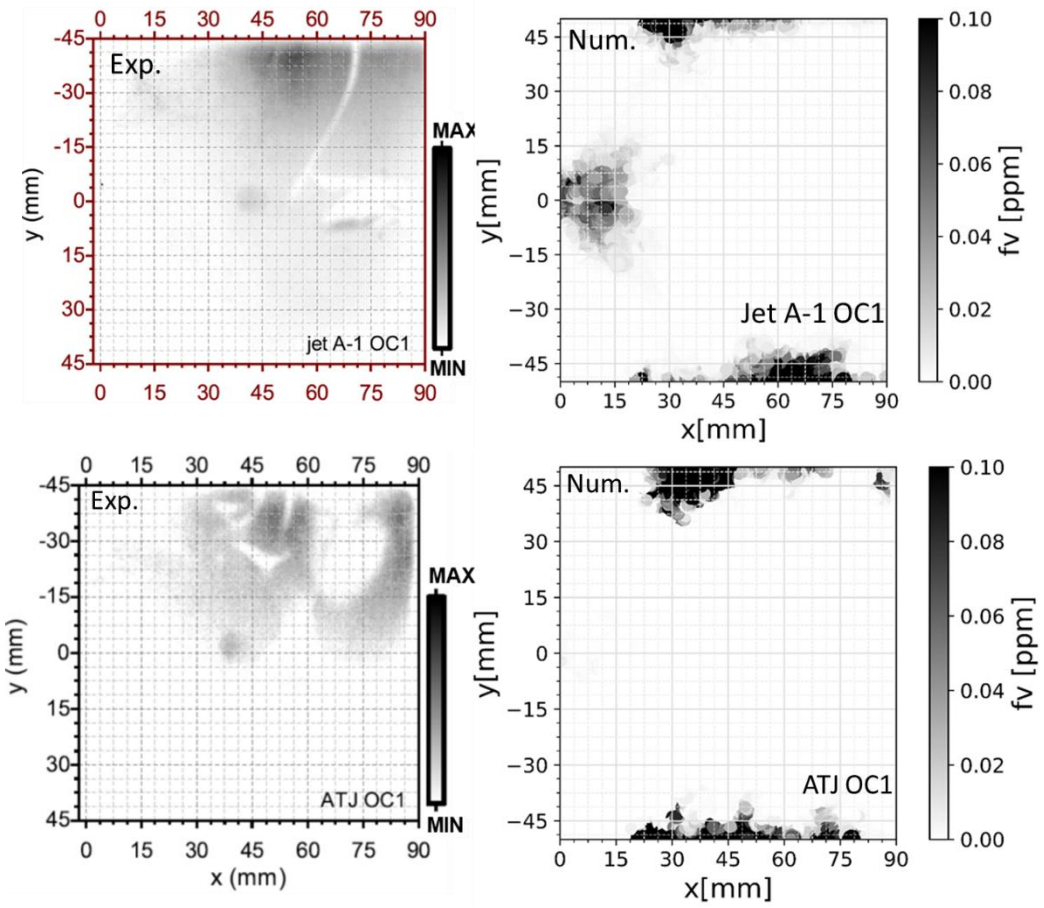

Figure 4.22 Comparison of soot volume fraction for Jet A-1 and ATJ from LII (left side) and LES (right side) [336].

However, quantitatively, the level of soot volume fraction obtained numerically from Jet A-1 and ATJ are very similar, slightly higher with ATJ than with Jet A-1. Such an outcome is in the opposite direction with respect to experiments. Several points can be envisioned to justify this:

- The differences in the chemical representation of the two fuels: in the present work, the Jet A-1 has been modeled as a mono-component fuel, while for ATJ, a multi-component formulation has been employed. This leads to a different treatment of the evaporation process and, in particular, to steeper evaporation with kerosene. This justifies why the flame obtained with Jet A-1 is shorter than the ATJ's one. To overcome this limit, the chemical representation developed during ALTERNATE, based on a multi-component formulation for kerosene, is proposed as a solution to be tested in the near future.
- The differences in the selection of the soot precursor for the LST model: Because of the different chemical representations, the same soot precursor was unavailable for the two fuels during the present work. For the ATJ case, pyrene was selected, while for Jet A-1, naphthalene was chosen. This choice has a clear impact on the zones that are interested in soot inception and its following evolution. Once again, the chemical scheme developed during the ALTERNATE project for kerosene, where pyrene has been targeted as a soot precursor, is proposed as a solution to be tested in the near future.
- The lack of a detailed understanding of the oxidation process from the carried out analyses. It is evident how oxidation has a significant role in the final soot distribution. For Jet A-1, oxidation occurs on a wide part of the combustion chamber, while for ATJ is more localized in space and higher as a time-averaged integral. This can heavily impact the soot distribution finally predicted and may justify the over-prediction obtained with ATJ. Nevertheless, state of the art, few studies have tackled the problem of a detailed study on oxidation, particularly in the presence of SAFs. This is a major axis of experimental and numerical investigation that can be pursued in the future.

The soot tends to be partially oxidized by the oxygen present in the IRZ and by the OH near the combustor walls. In that zone, fresh oxygen is also injected at the cooling slots, thus generating a further soot oxidation region. All in all, this leads to an instantaneous soot distribution with two peaks, i.e., the first one in the near injection zone and the second near the walls, similar to what is reported experimentally. Nevertheless, considering the intermittency in the soot generation and the complex flame stabilization process for this operating condition, a much longer averaging time is required on soot and on the flame structure to reinforce such results.

Therefore a joint effort has to be pursued between experimentalists and numeric experts to identify the main leading mechanisms in soot formation on such complex combustors for various fuels.

4.4.5 Summary of the chapter

This chapter showed the application of developed laser-based techniques for underlying soot behavior formed from the combustion of Jet A-1, SAF and 50:50% vol. blend fuels. These fuels were tested under three different operating conditions representative of the taxi (OC 1), approach (OC 2) cruise (OC 3) in terms of the total air mass flow rate and the pressure of the combustor. The obtained results help to improve the understanding of the complex interaction chain of various sub-processes and fuel blending effects on soot formation in turbulent environmental conditions.

The results obtained by using the LII technique show that the ATJ and an admixture of 50% Jet A-1: 50% ATJ produce lower soot particles compared to Jet A-1. However, the sooting capacity of ATJ and admixture of 50% Jet A-1: 50% ATJ is not linear with the chamber pressure. The pressure of 4.5 and 7.9 characterizes the first two tested conditions for OC 1 and OC2, with the FF/FF_{ref} of 76% and 66%, respectively. For these two conditions, averaged soot values were near the detection limit of the LII technique (few ppb) for ATJ and admixture. On the other hand, localized soot flamelets and pockets characterize instantaneous images with high intensity of soot signals (tens of ppb).

Moreover, under these conditions, the averaged soot produced from Jet A-1 is in order of hundred ppb. By changing the operating conditions to OC 3, characterized by high pressure (around 9.4 bar) and small FF/FF_{ref} (46 %), the averaged soot values are in the other of some ppm for Jet A-1 and a few ppb for ATJ. By calculating the probability of getting soot particles in different regions of interest of the swirl, it was observed that there is the lowest probability of having soot with ATJ and admixture of 50% Jet A-1: 50% ATJ on OC 1 and OC 2 (Figure 6.15 of annex 4), where soot particles are mainly formed on the edges of the flow near the optical combustion chamber window. For OC 3, soot values were high for the three fuels, but ATJ produced three times less soot than Jet A-1 and this fact can be related to both the chemical properties of the fuel and hydrodynamic conditions in the combustor.

Light scattering was applied to see the effect of fuel droplets on soot formation. It is observed that the liquid fuel distribution is different from one fuel to another, although the zones covered by the spray are similar. Based on experimental findings, the switch from ATJ to Jet A-1 does not significantly affect the spray distribution and the flame stabilization process. The main characteristics of the spray (spray opening angle and penetration) are not modified, and the flame shape looks similar. In addition, spray instability can affect the production of soot, as observed for OC 3, due to unfavorable mixing properties at the shear layer between liquid fuel and surrounding hot gas.

Finally, the OH* chemiluminescence was applied as a complementary technique to have further information on the heat release and reaction zone inside the combustor. The instantaneous OH* signal is distributed throughout the combustion chamber for all fuels and tested conditions. The averaged signal helped to localize possible maximum heat or reaction zone in the combustion, where the high intensity was mainly in the center of the flow and higher for Jet A-1 compared to the ATJ and admixture of Jet A-1 / ATJ. In addition, there is a relationship between the OH* signal and soot formation; when the OH* signal increases, the soot incandescence signal decreases and is shifted to the region with a lower OH* signal.

In parallel to experimental findings, a numerical study based on LES done by SAFRAN and CERFACS was also proposed to characterize the case OC 1 with Jet A-1 as a first step. The developed

model seems able to capture the macroscopic characteristics of the spray and the flame regions. Similarly to experiments, soot regions are identified near the injector and close to the walls. However, the models did not capture the semi-quantitative aspect of soot production between the two fuels.

CHAPTER 5

GENERAL CONCLUSION AND PERSPECTIVES

This page is intentionally left blank

5 GENERAL CONCLUSION AND PERSPECTIVES

The main objective of this Ph.D. was to develop and implement laser-based optical techniques used to characterize soot particles and their precursors in high-pressure combustion flames. Laser induced incandescence (LII) was the principal optical technique custom developed to be suitable for harsh combustion conditions applications. Laser induced fluorescence (LIF) was systematically implemented with LII technique to obtain information about a class of soot precursors that absorb the visible wavelength domain. The LII technique was chosen due to its high sensitivity to soot particles. The advantage of using LII is its ability to provide *in-situ* measurements of soot in real-world scale operating combustion conditions (engines, furnaces, burners) without interfering with the environment (flame). Therefore, this metrology technique is a "must-have" tool for understanding the behavior of soot in complex combustion systems, such as aircraft combustors. Also, LII provides high temporal and spatial resolution measurements of soot, which are important for understanding soot particle formation over time and in different flame regions. Despite all advantages provided by LII, some processes not yet understood have to be studied to reduce the uncertainty in the detection and to extend the application of the technique to even more complex combustion systems.

After a brief overview of the motivations behind this study and a literature review described in **Chapter 1**, the second chapter (**Chapter 2**) gives the first approach to developing and implementing LII/LIF on an atmospheric CH_4/Air laminar diffusion flame. All these are after a brief presentation of the theory behind the working principle of LII and LIF techniques. First experimental measurements were carried out to see the effect of the laser sheet divergence or expansion on LII and LIF signals. Different optical configurations were tested, from which a configuration with a set of one negative lens (f1= -25.4 mm) and two positive lenses (f2= 200 mm and f3 = 1000 mm) was chosen. This selection was made because it provides laser sheet dimensions that fit the need of regions of interest (ROIs) for studies of soot on an aeronautical combustor and the lowest divergence from the focal point to the extremities of the laser sheet.

Further measurements were made to see the effect of laser sheet divergence on LII and LIF signals. Soot particle incandescence signal was induced by a 1064 nm laser and detected at 450 and 650 nm. The obtained results showed that the incandesced soot signal increased more than two times from the focal point of the laser sheet (0 mm) to the propagation axis (+ 50 mm or -50 mm) and that the signal depends on the used laser fluence. Therefore, a correction factor is proposed to minimize the error due to the laser sheet divergence. For LIF, the PAHs (a class of soot precursors) were excited at 532 nm and detected at 450 and 580 nm. The LIF signal shows that different PAH classes contribute to various detection wavelengths. The fluorescence signal detected at 650 nm (Stokes detection) has a higher contribution compared to the one detected at 450 nm (anti-Stokes detection) at the selected HAB (40 mm, which represents the inception point of soot in this flame). The proposed correction factor for LIF signal depends strongly on the detection wavelength. The correction factor has to be applied cautiously, as it does not vary linearly with the sampling position and is strongly dependent on various parameters of the analyzed combustion zone. The main findings of this part are the variability of the LII correction factor, which is not a constant value as proposed in the literature [212,213] and the correction factor on the fluorescence, which seldomly is considered as a linear variation from the focal point of the laser sheet to the extremities.

The second section of this chapter focused on the quantification of the LII signal into soot volume fraction (f_v). The LII auto-compensating (2C-LII) method is used for calculating effective soot temperature (T_{eff}) and f_v. Two principal measurement configurations are used. The first configuration is the imaging mode, where the laser beam is shaped into a laser sheet to imagine the ROI. An intensified camera coupled with lenses, binocular system and filters centered at 450, 580 and 650 nm are used to detect emitted 2D LII signal. The second used configuration is spectral mode, where a top hat laser beam with a diameter of 1.04 mm was used to analyze the ROI. The detection system used for this configuration consisted of a spectrograph coupled with an intensified camera and lenses. From the main findings, it was observed that effective soot temperatures and volume fractions depend strongly on the optical properties of soot ($E_m(\lambda, T)$). It was also observed that the obtained T_{eff} value depends strongly on the chosen detection wavelength pairs in imaging mode. The two closest detection wavelengths (580-650 nm) overestimate the value of T_{eff} whereas the coupled wavelength 450-580-650 nm gave the T_{eff} with lowest std. This observation is confirmed in the spectral mode when two closed wavelengths were chosen for T_{eff} calculation. The obtained f_v were in the range of a few ppm for both configurations in the region of mature soot particles. After developing and implementing LII and LIF techniques on the CH_4/air laboratory flame, they were applied to harsh combustion conditions.

For this, the third chapter (**Chapter 3**) focused on the characterization of soot particles in a semi-industrial test rig known as MICADO. In the first step, advanced optical diagnostics (LII/LIF, PIV and scattering) were implemented to study the effects of combustion parameters on the production of soot and precursors. The used diagnostics give a complete overview of the processes involved or affecting the production of soot particles in aeronautic combustors, starting from fuel injection to particulate and gaseous emission. Soot volume fraction and soot precursors were obtained via LII/LIF techniques, whereas velocity field vectors and spray dynamics were obtained with PIV and scattering techniques. The combustion tests carried out on the newly developed MICADO test rig facility allowed the investigation of the kerosene Jet A-1 combustion process. Different operating conditions were selected based on the injection type (main or pilot mixed with main), global equivalence ratio and pressure. These studied combustion conditions are representative in terms of the total mass of air-flow rates and pressure values of the ones specific to turbo-combustors during the cruise and idle cycles.

Obtained results give interesting and complementary information about the distribution of soot particles and aromatic precursors (PAHs) inside the combustion chamber. The aromatic precursors are mostly distributed everywhere in the combustion chamber, but high contributions of aromatic compounds were detected near the injector in all studied conditions. This information can help in studying different mechanisms that participate in the formation of soot at high pressure and temperature.

Furthermore, the identified correlation between the LII signal and LIF signal inside the combustion chamber can bring insights into the role of pyrogenic aromatic compounds during the inception of soot and its evolution in the combustor. The overview of experimental configuration proved the feasibility of these optical techniques on combustors, despite the limitations imposed by the complexity and operating conditions of the test rig. Processed data were correlated with the test rig operating conditions for observing the parameters affecting the production of soot particles. Selected correlation methods identified a link between the combustion parameters and produced soot

and precursors. Soot and precursors signals are positively correlated, and both signals increase with the increase of pressure in the combustion chamber. A negative correlation was observed between LII/LIF signals with flow factor ratio FF/FF_{ref}. As FF/FF_{ref} value increased, LII/LIF signals decreased. The impact of flow field dynamics on the soot formation was investigated via PIV measurements. It was observed that the operating condition with a lower velocity vector field value promotes high residence time for soot particles which leads to higher soot particle concentration (f_v). Finally, via scattering measurements, it was observed that the high soot volume fraction characterizes the condition with high spray density and low oscillation frequency. Whereas the OC with spray high-frequency oscillation modes resulted in operating conditions with lower soot volume fractions. By also comparing with the literature findings [287], it was observed that spray opening angle and penetration length also influence the soot formation and localization. The results show that the soot volume fraction decreases as the fuel spray cone angle increases.

In the fourth chapter (**Chapter 4**), the sooting behavior of ATJ was experimentally investigated against Jet A-1, a 50:50% blend between Jet A-1 and ATJ and neat ATJ for the three operating conditions (OCs) defined in Chapter 3. LII, scattering, and OH* chemiluminescence were implemented. It was observed that for a given OC, ATJ fuel produces fewer soot particles compared to Jet A-1 and compared to the admixture of Jet A-1 /ATJ. In addition, it was observed that the sooting capacity of ATJ is not linear with the chamber pressure or the FF/FF_{ref}. The various parameters that affect the formation of soot particles are the vaporization of fuel, which differs from one fuel to another. However, the zones covered by the spray are similar in the two cases as well as (OC 1 and OC 2) the oxidation and heat release regions. In addition, flame instabilities can affect the production of soot, as observed for OC 3, due to unfavorable mixing properties in the shear layer between non-vaporized fuel and surrounding hot gases. For this case (OC 3), soot values were high for the three fuels, but ATJ produced three times less soot than Jet A-1 and this fact can be related to both the chemical properties of the fuel and hydrodynamic conditions in the combustor. For OC 1 and OC 2, averaged soot values were near the detection limit (few ppb) for ATJ; conversely, instantaneous images are characterized by localized soot flamelets and pockets with high intensities of soot signals (tens of ppb). The spray and the flame front dynamic were analyzed with FFT (Fast Fourier Transform) spectrograms to determine the frequencies that impact each OC and fuel. These findings show a stable flame for OC 1 and OC 2 and unsteady phenomena in OC 3, when increasing the pressure in the combustor and decreasing the flow factor with respect to OC 1 and OC 2. These unsteady phenomena influence the production of soot for the three tested fuels. To summarize, this chapter gives a diversified overview of the processes governing soot particle formation in aero-engine combustors, from fuel injection to particulate and gaseous emission for Jet A-1 and neat alternative fuels (SAF).

Future recommendation …

This work leaves a certain number of perspectives:

- The mechanisms leading to soot particle formation are complex and poorly understood. Using coupled *in-situ* techniques is a plus for the scientific community regarding the optical properties of soot and its formation mechanism in flames studied under harsh combustion conditions. The results presented on an extensively studied laboratory flame have a high interest in getting information on the soot refractive index (E_m) by coupling extensive data processing based on multivariate data analysis and the two LII configuration modes. Further data analysis has to be carried out from the

measured flame temperature to estimate the E_m in different regions of the flame. After that, the quantification method has to be improved to get more accurate information on 2D maps of T_{eff} and f_v. Further analysis has to be made to see the effect of laser sheet divergence on f_v. A well-defined protocol must be implemented to extend quantified LII signal from laboratory flame to test rig applications.

- The experimental results obtained on the MICADO combustor have a high potential and interest for the validation of theoretical models from the correlation of combustion-specific parameters with soot in harsh combustion conditions. However, due to the complexity and difficulties in characterizing soot in these combustion environments, further data analysis based on advanced statistical methods is needed to understand the different mechanisms and parameters (or at least some of them) that influence their formation inside the combustor. This study has created an experimental database that can be used to model similar or more complex geometries of combustors for aircraft engine purposes. It would be interesting if the obtained results were further compared with numerical model results.

- The study of alternative fuels (SAF) on the MICADO test rig presented a novelty, as there are fewer *in-situ* measurement studies regarding SAF in representative engine conditions. It will be interesting if there are more advanced developed models that can predict the soot particles in SAF fuels for better comparison with experimental results.

- All presented results obtained on the MICADO test rig are from *in-situ* measurements. However, they were also *ex-situ* measurements carried out simultaneously with *in-situ*. Therefore, future studies must compare the results obtained inside the combustor with ones performed with the sampling probe (CO, CO2, NOx, particle number, particle mass and mobility size distribution of soot particles) in the post-combustion zone.

- MICADO measurement campaigns are costly and complex due to the quantity of air, fuel, electricity and people needed to operate it. Therefore, it is necessary to have an intermediate step for developing the optical techniques and evaluating their response to the increase in pressure and temperature. A combustion chamber called PHOENIX pressurized at 20 bars is being designed for such studies (Figure 5.1).

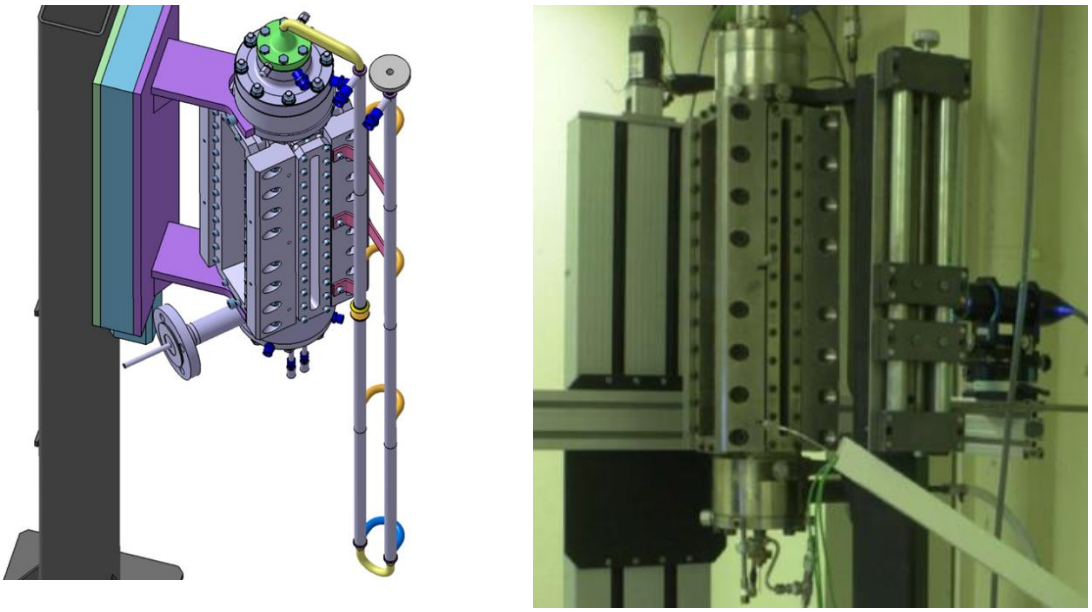

Figure 5.1 A schematic view of a high-pressure PHOENIX combustion chamber.

This page is intentionally left blank

6 ANNEX

6.1 ANNEX

6.1.1 Working principle of a laser

Based on the quantum idea used by Max Planck to explain blackbody radiation emission, in 1917, Albert Einstein proposed the processes of stimulated emission and absorption of radiation [338]. Laser stand for an acronym known as Light Amplification by the Stimulated Emission of Radiation, which was first demonstrated by Maiman in 1960 using a ruby crystal pumped with a xenon flash lamp [339]. In general, is an optical source that emits a photon that are monochromatic (of the same wavelength and frequency), coherent (in phase), highly collimated (the same direction) and uniformly polarized (all photons share the same direction) [340]. It consists of a lasing medium between optical resonators made by two mirrors forming a cavity. One of the mirrors is highly reflective and the other partially transmissive to transmit the laser light that is generated. Also, placing the active medium between two mirrors leads to the stimulated photons oscillating back and forth and being amplified each time they pass through the active medium.

On the other hand, the lasing medium determines the wavelength and gives its name to the type of Laser. The medium may be solid (ruby, Nd:YAG, Ti: sapphire), gas (Ar, CO2, He-Ne, HF), or liquid dyes (e.g. Rhodamine). Table X shows examples of some of the most important used lasers according to the nature of the active media, their typical operation wavelengths and temporal operation regimes. For stimulation of active medium, an external energy source (pump or another excitation source) is needed to provide the necessary energy, such as optical (flash lamp, continuous arc lamps), electrical discharge, and chemical [341,342].

Class	Laser Medium	Nominal Operating Wavelength (nm)	Typical Output Power or Energy	Typical Temporal Regime
Solid	Nd^{3+}:YAG	1064	10–100 W	CW
	Nd^{3+}:glass	1064	50 J	Pulsed
	$Ti^{3+}:Al_2O_3$	660–1180	10 W	CW
Semiconductor	InGaAsP	1300	10 mW	CW
Gas	He–Ne	633	5 mW	CW
	Ar^+	488	10 W	CW
	KrF	248	0.5 J	Pulsed
	CO_2	10600	100–1000 W	CW
	Kr^+	647	0.5 W	CW
	HCN	336.8×10^3	1 mW	CW
Liquid	Rhodamine-6G	560–640	100 mW	CW
Plasma	C^{6+}	18.2	2 mJ	Pulsed
FEL	Free electrons	300–4000	1 mJ	Pulsed

Figure 6.1 Representative Examples of Laser Sources

6.1.2 Nd:YAG laser

The Nd:YAG laser is one of the most frequently used high-power pulsed solid state lasers. The host medium in Nd:YAG lasers is a yttrium aluminum garnet (Y3Al5O12) crystal in which some of the Y3+ ions are replaced by neodymium Nd3+ ions. The active lasing medium is composed of the Nd3+ ions and the laser functioning as a four level laser. A fourth-level laser is when a laser beam can be achieved using atoms with two relatively stable levels between their ground state and a higher-energy excited state. As in a three-level laser, the atoms first drop to a long-lived metastable state where they can be stimulated to emit excess energy. However, instead of dropping to the ground state, they stop at another state above the ground state from which they can more easily be excited back up to the higher metastable state, thereby maintaining the population inversion needed for pulsed laser operation [343].

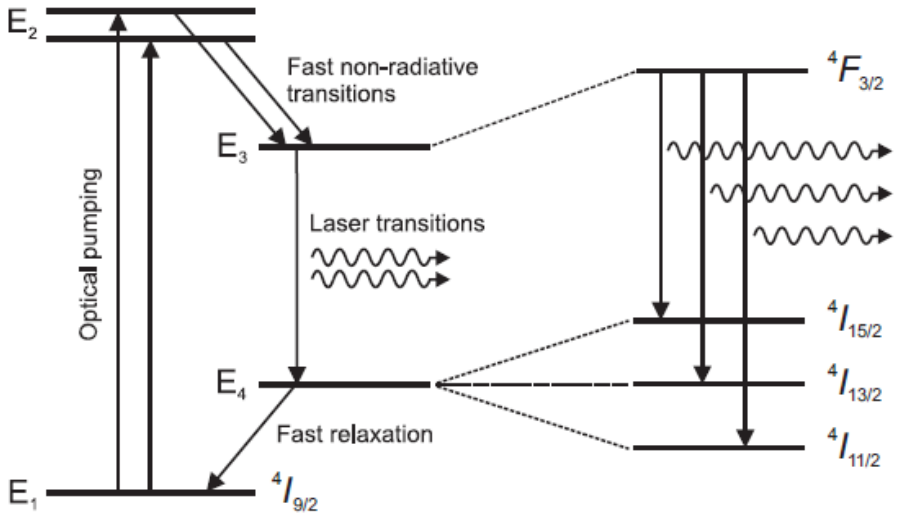

Figure 6.2 Schematic adapted from thesis of Lantz Andreas [342], energy level diagram of a four-level laser including relevant transitions for the Nd:YAG laser. The optical pumping is done by flash lamps at two absorption bands, at 730 nm and 800 nm, respectively, the lasing at 1064 nm.

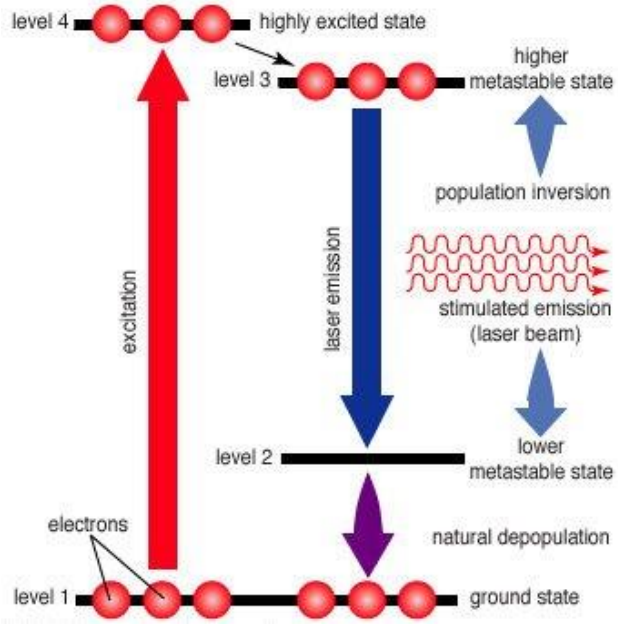

Figure 6.3 a) working principal of fourth energy lever laser.

The Nd:YAG absorbs mostly in the bands between 730 and 820 nm [343] . The Nd3+ ions are excited to higher energy levels, E2, through optical pumping, usually by use of a flash lamp. Following this excitation, electrons are rapidly coupled through fast non-radiative decay to a lower metastable state E3 (4F3/2). From this state, further deexcitations to lower levels E4 (4I11/2, 4I13/2 and 4I15/2) occur. The E3 →E4 transition is forbidden via the electronic dipole transition but is weakly allowed based on crystal-field interaction, the relaxation rate thus being slow (approximately 230 μs). Because of this relatively long period, a marked population inversion is built up in the 4F3/2 level by the flash lamp, this level thus serving as the upper level in laser radiation. Several laser transitions are possible, either between 4F3/2 and lower exited levels (4I15/2, 4I13/2 and 4I11/2) or between 4F3/2 and sublevels in the ground state, 4I9/2. The strongest transition is the 4F3/2 → 4I11/2 transition, the energy emitted by it having a wavelength of 1064 nm. This is the most frequently used lasing wavelength for Nd:YAG lasers. This wavelength can be frequency doubled by use of a non-linear crystal to obtain radiation in the green region of the visible spectrum at 532 nm. This process, which is called second harmonic generation, has an efficiency of about 40-50%. Higher harmonics, third (355 nm) and fourth (266 nm), can be obtained by introducing additional non-linear crystals [344].

For controlling output laser energy, level 4I11/2 is coupled, through a rapid relaxation, to the ground level E1, so that thermal equilibrium between these levels can be established. A large population inversion in the active laser medium can be created by limiting the buildup of stimulated emission radiation inside the cavity. This can be performed by a technique called Q switching. The term Q-switching comes from the fact that it involves switching the cavity Q factor from a low to a high value. The Q factor of a cavity is a measure of the ratio of the radiation energy stored in the cavity to the power loss involved. Here, an attenuator is placed inside the cavity to initially block the light path between the mirrors, this creating a large population inversion in the active medium, the Q factor for the cavity thus being low. As long as the attenuator blocks the light path, large gains are built up (the Q factor decreases), and when the attenuator is removed (the Q factor increases), intense lasing builds up very rapidly because of the high gain. This leads to the generation of highly intense lasing during a very short period. Laser pulses produced in this way can have a peak power of 108 W and a pulse width of about 10 ns. There are several methods of achieving Q-switching. Rotating prisms, electro-optical shutters, acoustic optical switches and saturable absorbers are a few examples of this. The different

methods employed can be divided into two categories, active and passive Q-switchers, depending on whether or not some active external operation needs to be applied to the device so as to produce the Q-switching. Most Nd:YAG lasers use an electro-optical method to Q-switch. Here, a Pockels cell is placed inside the laser cavity. A Pockels cell has different polarizing and polarization-rotating elements. If a high voltage pulse is applied to the cell, it changes the polarization rotation of the cavity radiation into a loss mode. This leads to the formation of intense and short laser pulses. It is possible to determine accurately when to release the laser pulse by means of Q-switching because of the rapid response of the Pockels cell.

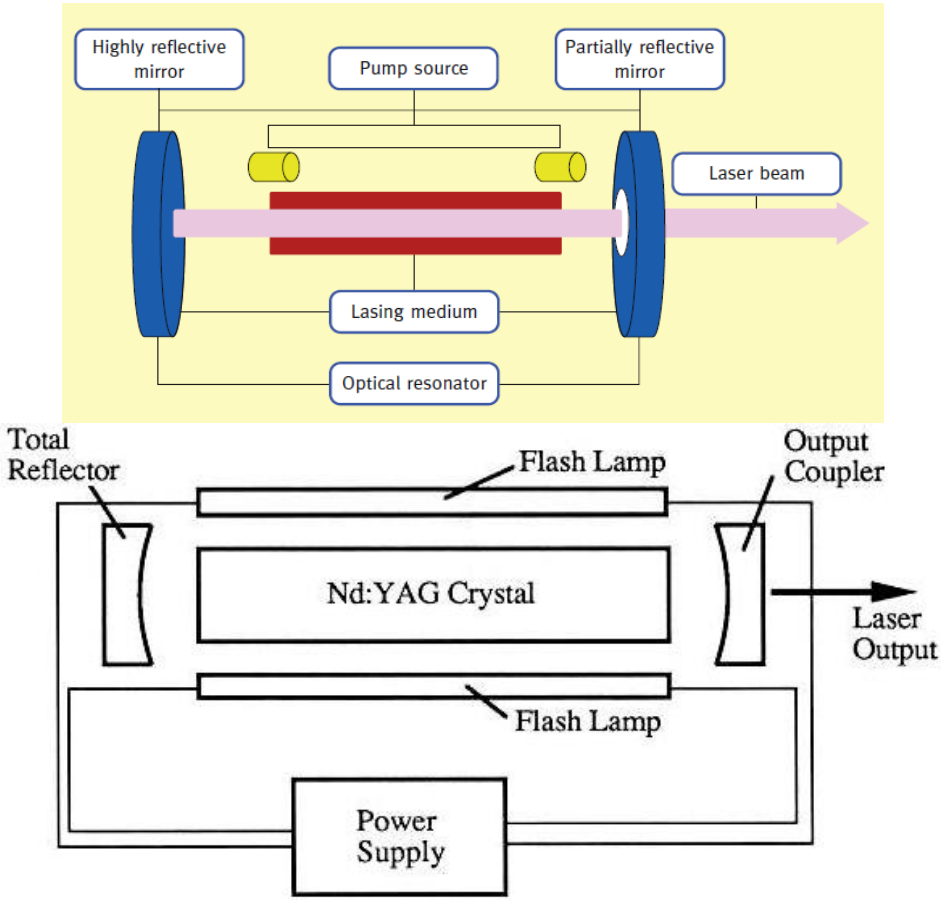

Figure 6.4 Schematic sketch of a laser cavity. The laser-active medium is placed between two mirrors that form a cavity. One of the mirrors is highly reflective and the other is partially transmissive in order to transmit the laser light.

6.1.3 Quantum efficiency of intensified Cameras used in this study

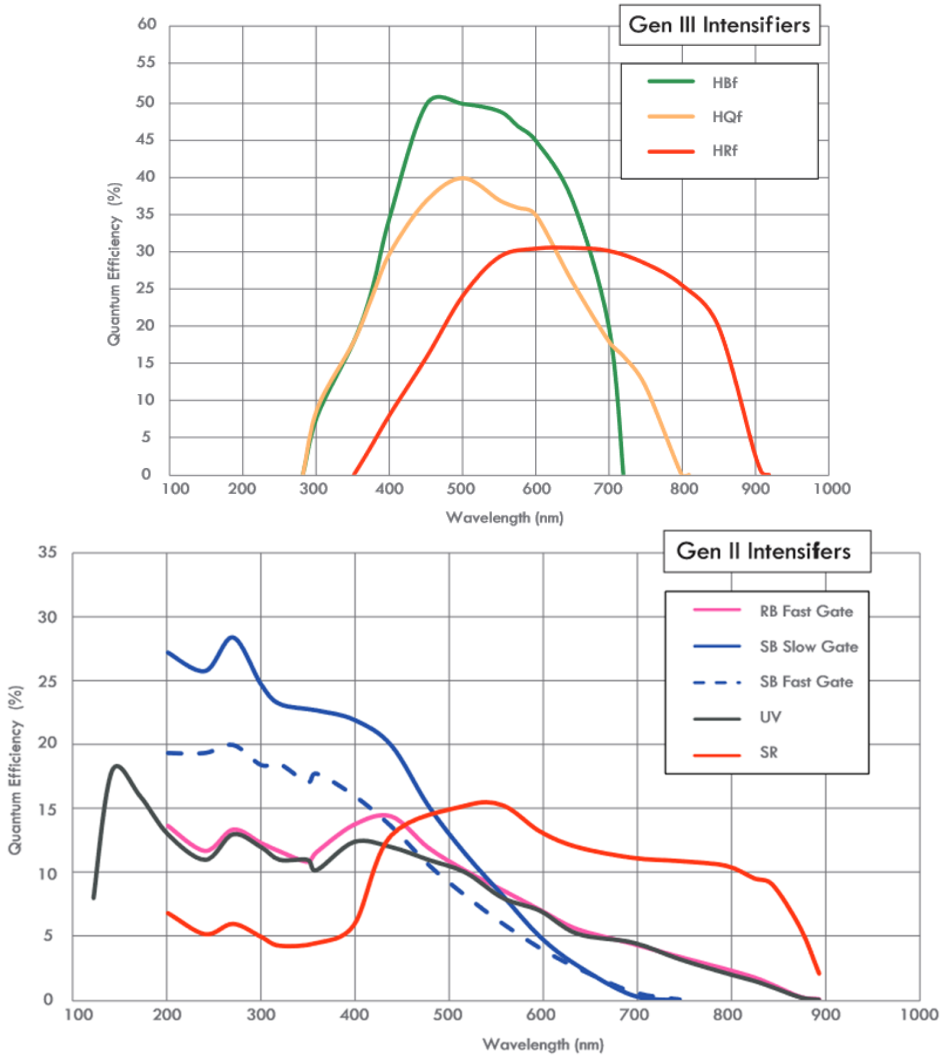

Figure 6.5 a) ICCD quantum efficiency used for LII imaging and spectral measurement mode.

6.1.4 Flame emission signal

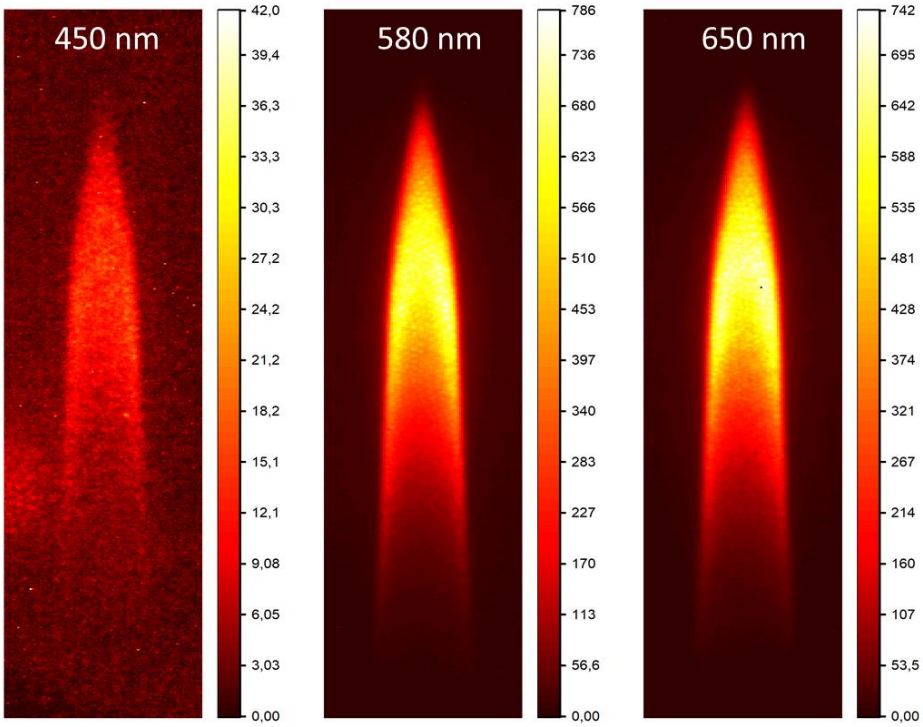

Figure 6.6 The emission of the flame at the three different detection wavelengths for the CH_4/air laminar diffusion flame.

6.1.5 Evolution of soot effective temperature in function of flame emission

To see if there is a relationship between flame emission temperature and soot effective temperature (from LII), Figure 6.7 shows the evolution of soot effective temperature function of the local emitted flame temperature in the region with mature soot particles (68 -90 mm). The correlation between effective and flame emission temperature shows that when the flame emission temperature increases, the effective soot temperature also increases. These findings need to be confirmed by looking at other combustion process factors that can influence soot temperature.

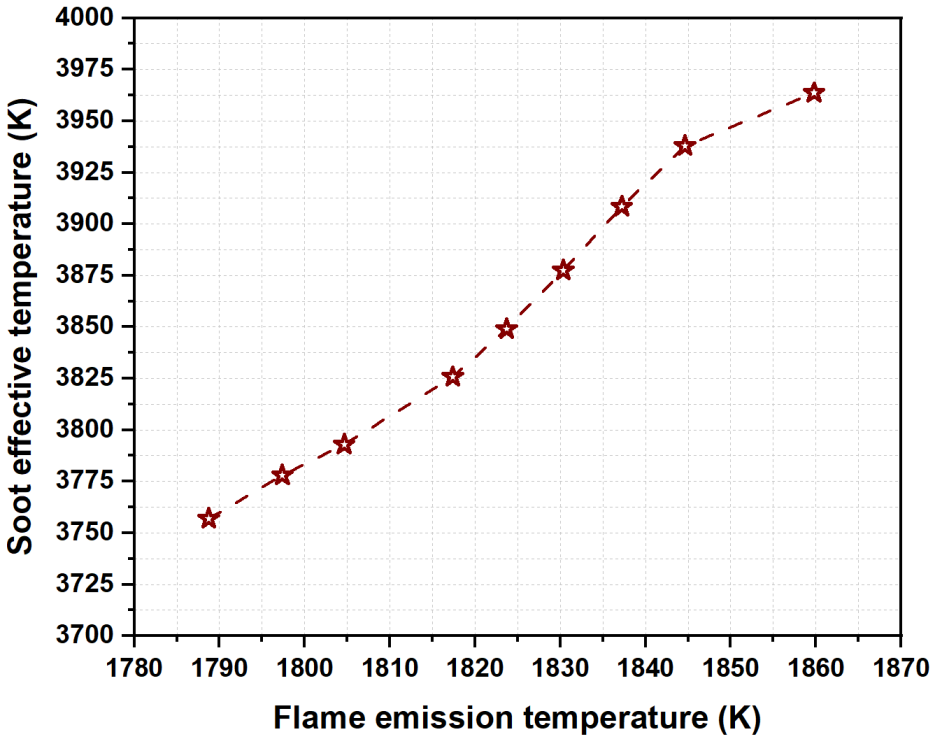

Figure 6.7 The evolution of soot effective temperature in function of flame emission temperature both obtained on detection wavelength of 450_580_650 nm.

6.1.6 TDLAS working principle

TDLAS was used to bring more information on the temperature of water vapor concentration. TDLAS is a technique that measures the wavelength-dependent absorption of laser light through a gas medium. The line-integrated absorbance is a product of the mole fraction of an absorbing gas species, its line strength, total pressure, and path length in a spatially uniform medium. A spectral absorption corresponds to a transition between two energy levels of a molecule and its line strength is correlated to the lower energy level population, which is a function of temperature. In many cases, absorption lines at two different wavenumbers interact between two energy levels and therefore have different temperature dependences [246]. In general, TDLAS helps to measure the amount of laser light absorbed as the light travels through the analyzed environment (flame). Figure 6.8 shows a simplified TDLAS experimental configuration used for measurement temperature on CH_4/air atmospheric diffusion flame. For excitation, a tunable diode analyzer consists of a laser that produces infrared light and optical lenses to focus the laser light through the flame. For detection, the detector and electronics control the laser and translate the detected signal into a signal representing evaporated water. Evaporated water molecules absorb light at a given wavelength spectrum by following Beer-Lambert law as expressed as:

$$I = I_o . e^{-E.G.L} \qquad \text{Equation 6.1}$$

Where:

I is the radiation intensity after the absorption, I_o is the initial radiation, E is the Extinction coefficient, G is the evaporated water (gas) concertation, L is the absorption path length of the measurement.

During the experiment, the laser is precisely tuned by taking care of the current of emitted light at a specific resonant water wavelength in the infrared electromagnetic spectrum domain. The laser energy causes the water molecule to vibrate and absorb energy. As the laser passes through the air (containing water vapor molecules) before arriving in the flame and before arriving on the detector, the obtained signal contains a signal background from the atmosphere (laboratory room). During signal post-processing, the size of the absorption peak in the flame is accurately measured, but to remove that background, absorption spectra are recorded without the flame and are subtracted in the final obtained signal with the flame.

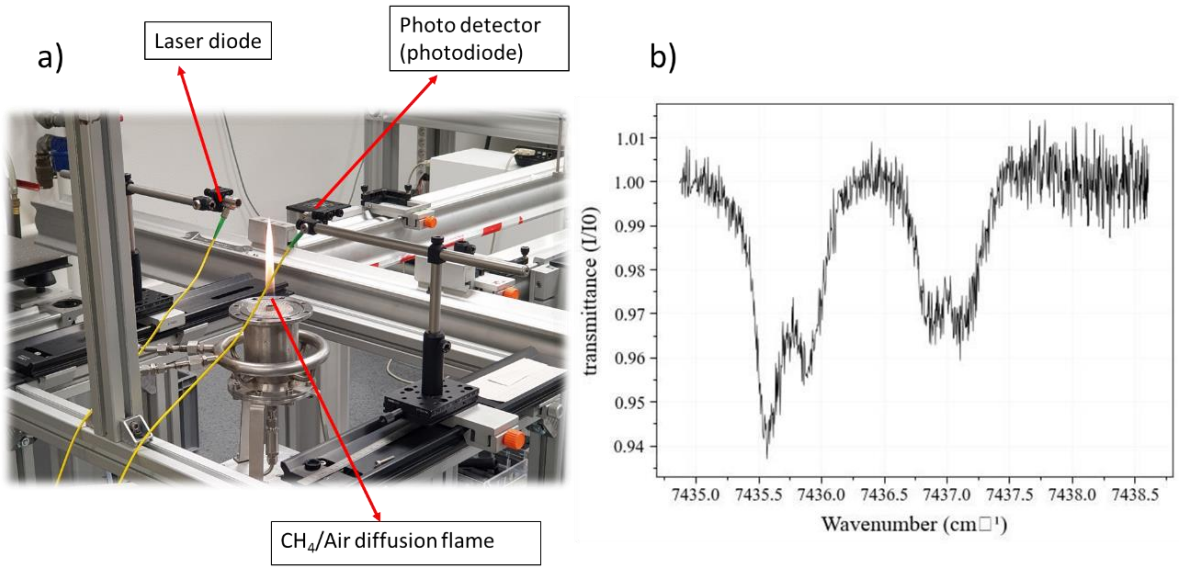

Figure 6.8 a) TDLAS experimental configuration used on laboratory laminal diffusion flame, b) Example of water vapor detected spectrum

6.1.7 Evolution soot volume fraction at different HAB, detected at 450 and 580 nm

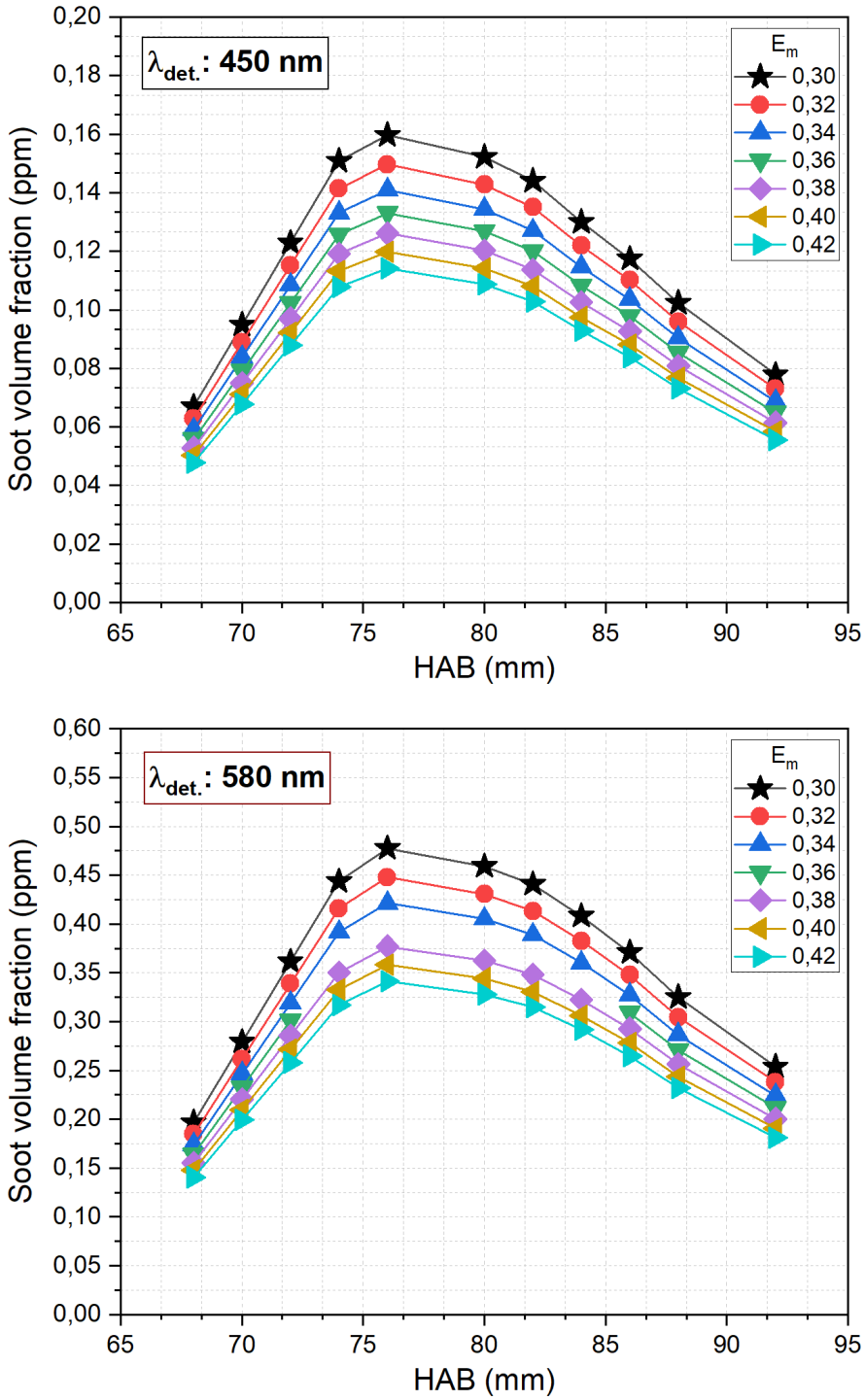

Figure 6.9 Soot volume fraction obtained at 450 and 580 nm with different HAB. The profiles were taken in the axial centerline of the flame.

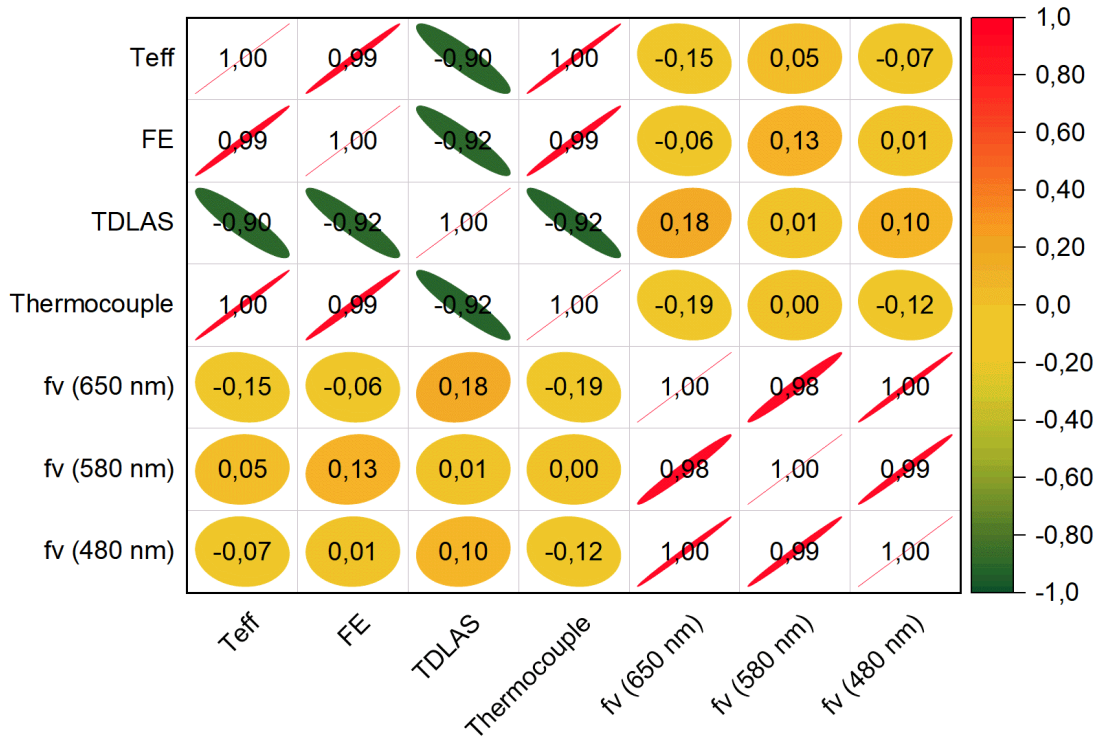

Figure 6.10 Correlation graph for all measurements made on CH_4/Air diffusion flame.

6.2 ANNEX

Evolution profiles of LII signal with different operating conditions.

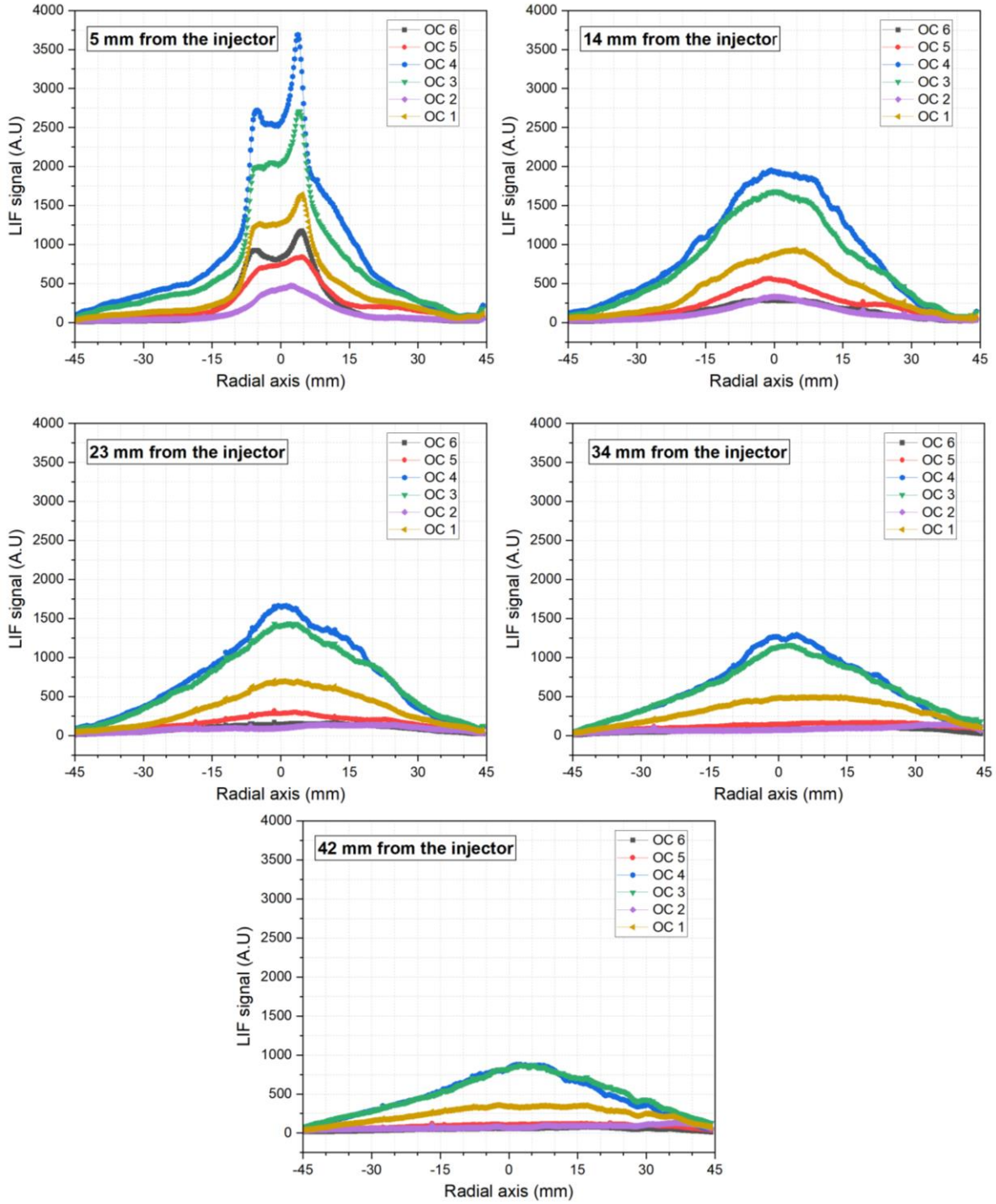

Figure 6.11 LIF signal evolution obtained at all tested conditions. The profiles were taken at different radial positions from the injector.

6.3 ANNEX

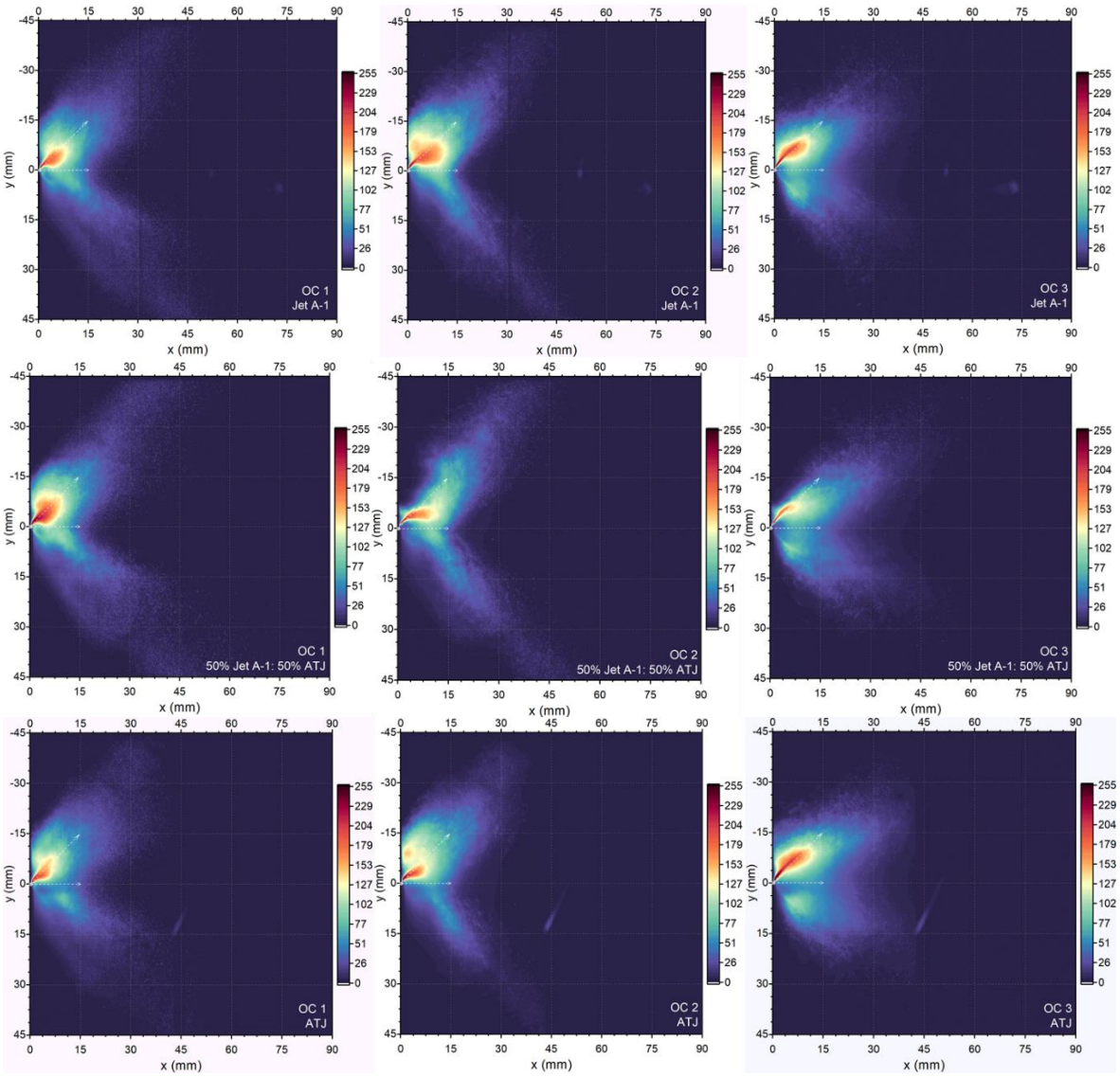

Figure 6.12 Standard deviation images of scattered signals from liquid fuel. The images were calculated on a series of 15 000 instantaneous images.

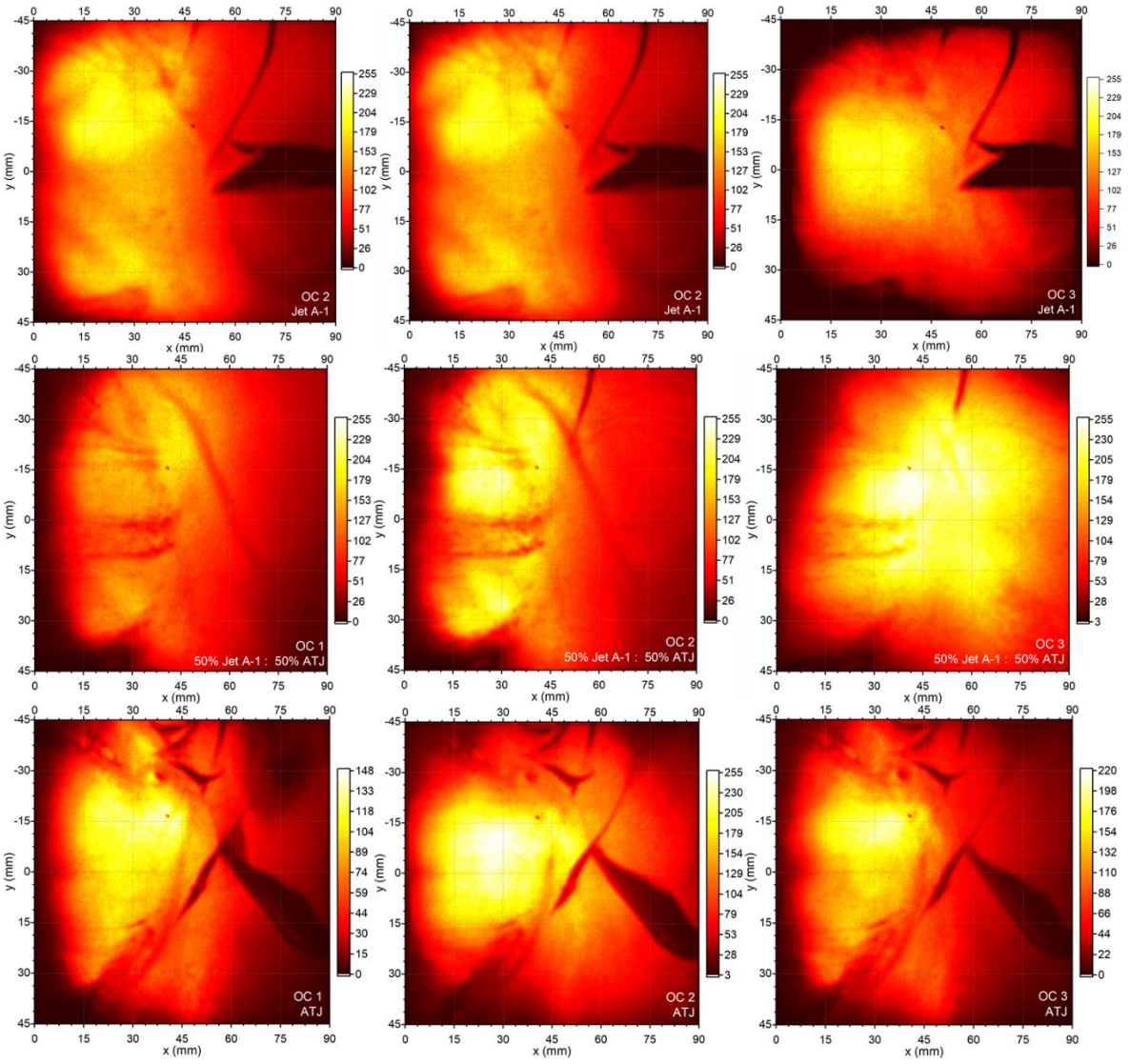

Figure 6.13 Standard deviation OH* chemiluminescence images measured for the two fuels and three OCs. Images were obtained from a series of 15 000 instantaneous images.

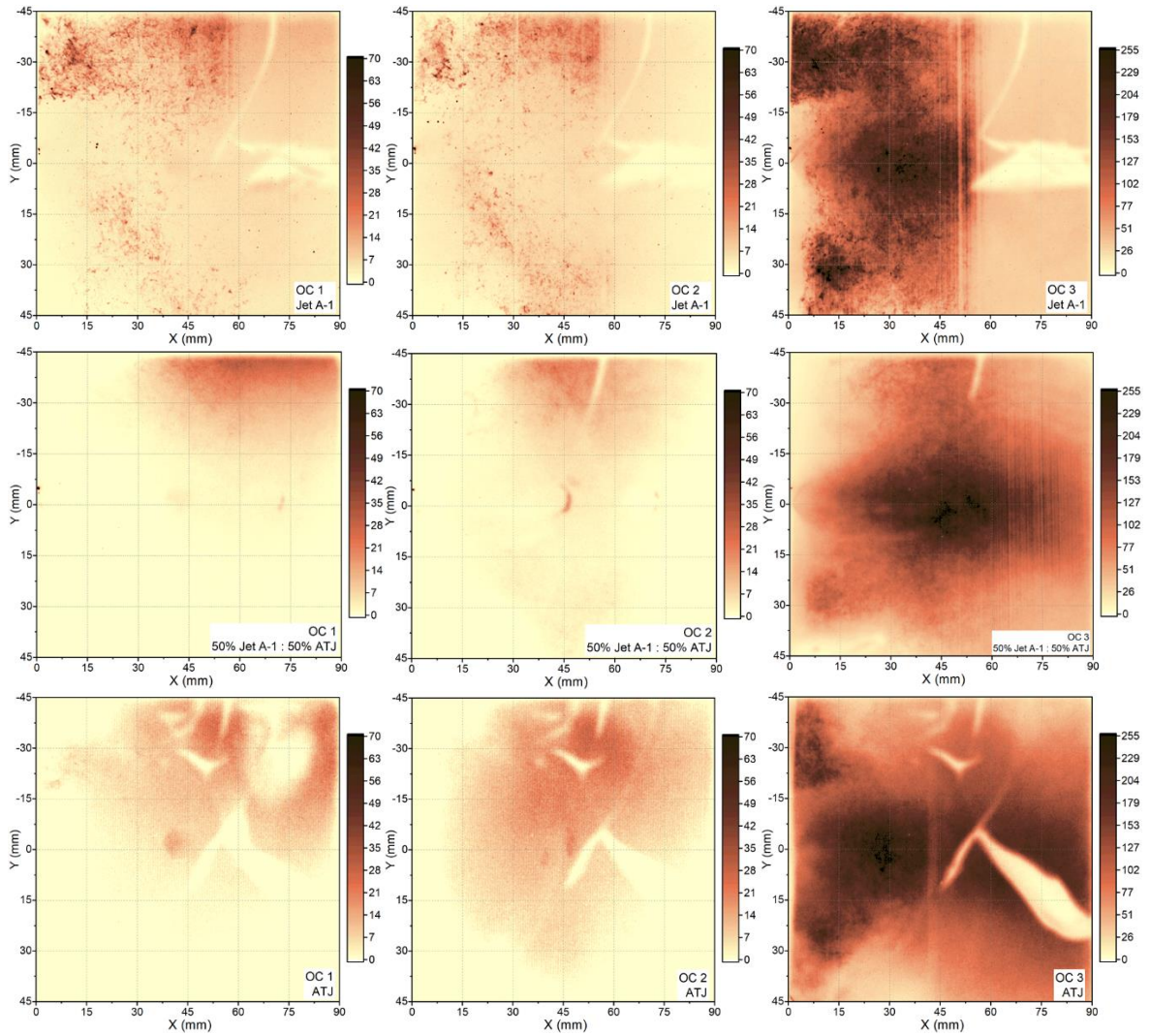

Figure 6.14 LII standard deviation images on three OCs and three tested fuels. Images were obtained from a series of 1 500 instantaneous images.

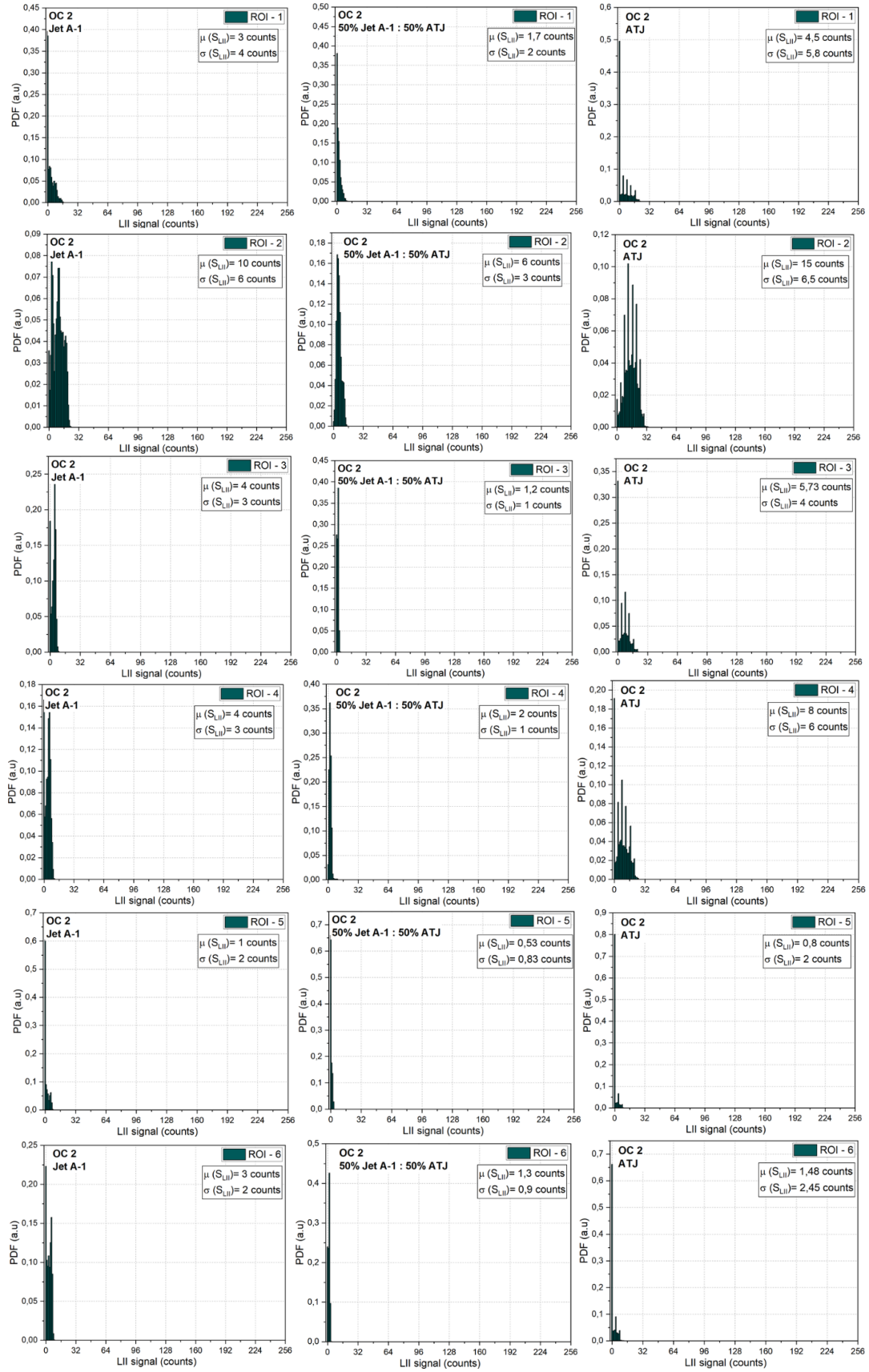

Figure 6.15 The probability density function of soot distribution in the different regions of interest for three tested fuels at OC 2

- **Simulation**

The simulations were presented using the Average Value Boundary Point (AVBP) solver developed by CERFACS [345]. AVBP solves the fully compressible multi-species Navier-Stokes equations on unstructured grids. The considered computational domain is shown in Figure 6.16 where it is possible to distinguish the air inlet which feeds the swirler, the cooling films and the outlet. The boundary conditions were fixed to be consistent with OC 1 and OC 2. The Lax-Wendroff advection scheme, second-order in space and time, was employed for all calculations.

An unstructured mesh counting 19 M elements was initially generated, imposing a uniform sizing inside the swirler channel and the combustion chamber. A first reactive simulation run using this coarse mesh to apply static mesh adaptation, similar to the one used in the thesis of Agostinelli [346]. Next, the zone to be refined was tagged based on the heat release rate field, and the local sizing was adapted to target a flame thickening factor for Dynamic Thickened Flame LES (DTFLES) of 30 in all the flame regions. This led to a mesh counting 57 M elements (unstructured grid) mainly refined in the flame zone, used for all the calculations shown in the following. The considered computational domain is shown in Figure 6.16, where the subgrid turbulent contributions were included thanks to the SIGMA model [347]. The DTFLES model [348] was used to describe the flame propagation, where the efficiency function is computed based on the formulation proposed in [349] with $\beta = 0.5$. The liquid phase was modeled with a Lagrangian approach. A standard set of modeling choices was selected for the air-fuel interactions, where the drag contribution was included in the equation for the momentum of the liquid phase with the hypothesis of a spherical shape.

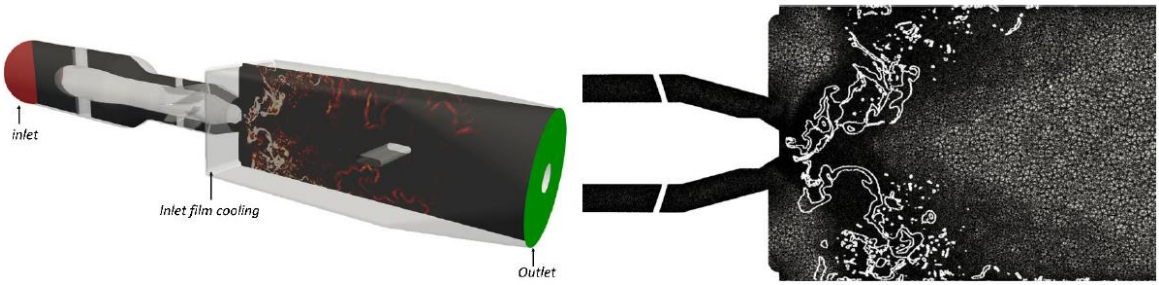

Figure 6.16 The computational domain used for LES of the MICADO test bench (left-hand side) and mesh obtained after mesh adaptation (right-hand side). The white iso-line represents an instantaneous iso-contour of heat release rate at 2×10^9 W/m^3[336].

In contrast, the evaporation rate was computed based on the model of Abramzon et al. [350]. Then, a standard correlation for pressure atomizers from Lefebvre [351] was applied to obtain a Sauter Mean Diameter (SMD) of 44 µm, used for a Rosin-Rammler distribution with a dispersion parameter q fixed to 2.5. As far as the chemical description is concerned, two sets of calculations were performed. First, a two-step globally reduced chemistry, derived from Franzelli et al. [352], was used to compute the flame main features and draw the first comparison with the experimental data. This calculation is named in the following 2S-BFER. However, although global chemistry can accurately predict global flame quantities, such as the laminar flame speed and the burnt gas state, it does not estimate pollutants, such as soot precursors. Therefore, considering the goals of the present study, the Analytically Reduced Chemistry (ARC) scheme proposed in [14] was employed to predict both the flame structure and the gaseous soot precursors. This simulation with ARC started from the 2S-BFER solution. The ARC scheme counts 29 transported species and 15 species in a Quasi Steady State. After

the first computational step to flush out the 2S-BFER initialization, the Lagrangian Soot Tracking (LST) model proposed by Gallen [353] was activated to compute soot levels. The LST method, developed by CERFACS, considers soot particles as point sources with their characteristic properties (e.g., temperature, size, velocity). Soot particles are considered spherical at the nucleation stage; their surface evolves depending on their history (collisions, surface reactions). The reader is referred to the study of Gallen [353] for a complete description of the LST approach.

Soot particles are considered spherical at the nucleation stage; then their surface evolves depending on their history: Firstly, the surface growth where the soot encounters C_2H_2 and then its size increases through Hydrogen Abstraction Carbon Addition (HACA) process. Secondly during the condensation, a dimer (e.g., C_2H_2) coagulates on the soot surface, generating a larger soot particle. Lastly during the oxidation process the soot particle encounters O_2 or OH, which reduces their size.

This page is intentionally left blank

LIST OF FIGURES

LIST OF TABLE

REFERENCES

[1] Education.psu.edu. Global Energy Sources 2022. https://www.e-education.psu.edu/earth104/node/1345.

[2] Ahmad T, Zhang D. A critical review of comparative global historical energy consumption and future demand: The story told so far. Energy Reports 2020;6:1973–91. https://doi.org/10.1016/j.egyr.2020.07.020.

[3] Tvaronavičienė M, Baublys J, Raudeliūnienė J, Jatautaitė D. Global energy consumption peculiarities and energy sources: Role of renewables. 2019. https://doi.org/10.1016/B978-0-12-817688-7.00001-X.

[4] Jonsdottir HR, Delaval M, Leni Z, Keller A, Brem BT, Siegerist F, et al. Non-volatile particle emissions from aircraft turbine engines at ground-idle induce oxidative stress in bronchial cells. Commun Biol 2019;2:1–11. https://doi.org/10.1038/s42003-019-0332-7.

[5] Herndon SC, Onasch TB, Frank BP, Marr LC, Jayne JT, Canagaratna MR, et al. Particulate emissions from in-use commercial aircraft. Aerosol Sci Technol 2005;39:799–809. https://doi.org/10.1080/02786820500247363.

[6] Fuzzi S, Baltensperger U, Carslaw K, Decesari S, Denier Van Der Gon H, Facchini MC, et al. Particulate matter, air quality and climate: Lessons learned and future needs. Atmos Chem Phys 2015;15:8217–99. https://doi.org/10.5194/acp-15-8217-2015.

[7] Kennedy IM. The health effects of combustion-generated aerosols. Proc Combust Inst 2007;31 II:2757–70. https://doi.org/10.1016/j.proci.2006.08.116.

[8] Oberdörster G, Sharp Z, Atudorei V, Elder A, Gelein R, Kreyling W, et al. Translocation of inhaled ultrafine particles to the brain. Inhal Toxicol 2004;16:437–45. https://doi.org/10.1080/08958370490439597.

[9] Niranjan R, Thakur AK. The toxicological mechanisms of environmental soot (black carbon) and carbon black: Focus on Oxidative stress and inflammatory pathways. Front Immunol 2017;8:1–20. https://doi.org/10.3389/fimmu.2017.00763.

[10] Owen B, Anet JG, Bertier N, Christie S, Cremaschi M, Dellaert S, et al. Review: Particulate Matter Emissions from Aircraft. Atmosphere (Basel) 2022;13:1–19. https://doi.org/10.3390/atmos13081230.

[11] Tait KN, Khan MAH, Bullock S, Lowenberg MH, Shallcross DE. Aircraft Emissions, Their Plume-Scale Effects, and the Spatio-Temporal Sensitivity of the Atmospheric Response: A Review. Aerospace 2022;9. https://doi.org/10.3390/aerospace9070355.

[12] Perathoner S, Centi G. Advanced nanocarbon materials for future energy applications. Elsevier Inc.; 2018. https://doi.org/10.1016/B978-0-12-813794-9.00009-0.

[13] Itami K, Maekawa T. Molecular Nanocarbon Science: Present and Future. Nano Lett 2020;20:4718–20. https://doi.org/10.1021/acs.nanolett.0c02143.

[14] Khare P, Kumar Patel R, Shankar R. Recent Developments in Nanocarbon-Polymer Composites for Environmental and Energy Applications, 200AD.

[15] Nanotubes C, Oxides G. Nano-Carbon Materials. J Inst Electr Eng Japan 2007;127:340–3. https://doi.org/10.1541/ieejjournal.127.340.

[16] Mishra RK, Chandel S. Soot formation and its effect in an aero gas turbine combustor. Int J Turbo Jet Engines 2019;36:61–73. https://doi.org/10.1515/tjj-2016-0062.

[17] Abdulqadir LB. Investigation of the Effects of Soot on the Wear of Automotive Engine Components. 2017.

[18] Chterev I, Rock N, Ek H, Emerson B, Seitzman J, Jiang N, et al. Simultaneous imaging of fuel, OH, and three component velocity fields in high pressure, liquid fueled, swirl stabilized flames at 5 kHz. Combust Flame 2017;186:150–65. https://doi.org/10.1016/j.combustflame.2017.07.021.

[19] Meier U, Heinze J, Magens E, Schroll M, Hassa C, Bake S, et al. Optically accessible multisector combustor: application and challenges of laser techniques at realistic operating conditions. Proc ASME Turbo Expo 2015 Turbine Tech Conf Expo GT2015 2015:1–11.

[20] Popovicheva OB, Persiantseva NM, Lukhovitskaya EE, Shonija NK, Zubareva NA, Demirdjian B, et al. Aircraft engine soot as contrail nuclei. Geophys Res Lett 2004;31:1–4. https://doi.org/10.1029/2003GL018888.

[21] Masri AR. Challenges for turbulent combustion. Proc Combust Inst 2021;38:121–55. https://doi.org/10.1016/j.proci.2020.07.144.

[22] Giusti A, Mastorakos E. Turbulent Combustion Modelling and Experiments : Flow, Turbul Combust 2019;103:847–69.

[23] Martin JW, Salamanca M, Kraft M. Soot inception: Carbonaceous nanoparticle formation in flames. Prog Energy Combust Sci 2022;88:100956. https://doi.org/10.1016/j.pecs.2021.100956.

[24] Frenklach M. Reaction mechanism of soot formation in flames. Phys Chem Chem Phys 2002;4:2028–37. https://doi.org/10.1039/b110045a.

[25] Yamamoto T, Shimodaira K, Yoshida S, Kurosawa Y. Emission reduction of fuel-staged aircraft engine combustor using an additional premixed fuel nozzle. J Eng Gas Turbines Power 2013;135:1–8. https://doi.org/10.1115/1.4007868.

[26] Ranasinghe K, Guan K, Gardi A, Sabatini R. Review of advanced low-emission technologies for sustainable aviation. Energy 2019;188:115945. https://doi.org/10.1016/j.energy.2019.115945.

[27] Schripp T, Anderson BE, Bauder U, Rauch B, Corbin JC, Smallwood GJ, et al. Aircraft engine particulate matter emissions from sustainable aviation fuels: Results from ground-based measurements during the NASA/DLR campaign ECLIF2/ND-MAX. Fuel 2022;325. https://doi.org/10.1016/j.fuel.2022.124764.

[28] CAEP. Committee on Aviation Environmental Protection 2023. https://www.icao.int/environmental-protection/pages/caep.aspx.

[29] Gardi A, Sabatini R, Ramasamy S. Multi-objective optimisation of aircraft flight trajectories in the ATM and avionics context. Prog Aerosp Sci 2016;83:1–36. https://doi.org/10.1016/j.paerosci.2015.11.006.

[30] ICAO. International Civil Aviation Organization 2022. https://www.icao.int/Pages/default.aspx.

[31] Zaporozhets O, Synylo K. Improvements on aircraft engine emission and emission inventory asesessment inside the airport area. Energy 2017;140:1350–7. https://doi.org/10.1016/j.energy.2017.07.178.

[32] Richard JR, Majthoub M Al, Aho MJ, Pirkonen PM. The effect of pressure on the formation of

nitrogen oxides from coal char combustion in a small fixed-bed reactor. Fuel 1994;73:1034–8. https://doi.org/10.1016/0016-2361(94)90233-X.

[33] Nicol D, Malte PC, Lai J, Marinov NN, Pratt DT, Corr RA. NOx sensitivities for gas turbine engines operated on lean-premixed combustion and conventional diffusion flames. ASME 1992 Int Gas Turbine Aeroengine Congr Expo GT 1992 1992;3. https://doi.org/10.1115/92-GT-115.

[34] Glarborg P, Miller JA, Ruscic B, Klippenstein SJ. Modeling nitrogen chemistry in combustion. Prog Energy Combust Sci 2018;67:31–68. https://doi.org/10.1016/j.pecs.2018.01.002.

[35] Zajemska M, Poskart A, Musiał D. The kinetics of nitrogen oxides formation in the flame gas. Econ Environ Stud 2015;15:445–60.

[36] Yang J, Golovitchev VI, Redón Lurbe P, López Sánchez JJ. Chemical kinetic study of nitrogen oxides formation trends in biodiesel combustion. Int J Chem Eng 2012;2012. https://doi.org/10.1155/2012/898742.

[37] Chaparala SV, Raj A, Chung SH. Reaction Mechanism for the Formation of Nitrogen Oxides (NOx) During Coke Oxidation in Fluidized Catalytic Cracking Units. Combust Sci Technol 2015;187:1683–704. https://doi.org/10.1080/00102202.2015.1059328.

[38] Maloney CM, Portmann RW, Ross MN, Rosenlof KH. The Climate and Ozone Impacts of Black Carbon Emissions From Global Rocket Launches. J Geophys Res Atmos 2022;127:1–17. https://doi.org/10.1029/2021JD036373.

[39] Tollefson J. Soot a major contributor to climate change. Nature 2013;50171:50171. https://doi.org/10.1038/nature.2013.12225.

[40] Intergovernmental Panel on Climate Change. Climate Change 2022 - Mitigation of Climate Change - Full Report. 2022.

[41] Colket MB. Particulate Formation. 2013. https://doi.org/10.1017/cbo9781139015462.009.

[42] Kholghy M, Saffaripour M, Yip C, Thomson MJ. The evolution of soot morphology in a laminar coflow diffusion flame of a surrogate for Jet A-1. Combust Flame 2013;160:2119–30. https://doi.org/10.1016/J.COMBUSTFLAME.2013.04.008.

[43] Desgroux P, Mercier X, Thomson KA. Study of the formation of soot and its precursors in flames using optical diagnostics. Proc Combust Inst 2013;34:1713–38. https://doi.org/10.1016/j.proci.2012.09.004.

[44] Okyay G. Impact of the morphology of soot aggregates on their radiative properties and the subsequent radiative heat transfer through sooty gaseous mixtures. PhD, Cent Univ Paris-Saclay 2016.

[45] Mansurov ZA. Soot Formation in Combustion Processes (Review). Transl from Fiz Goreniya i Vzryva 2005;41:137–56.

[46] Glassman I. Soot formation in combustion processes. Symp Combust 1989;22:295–311. https://doi.org/10.1016/S0082-0784(89)80036-0.

[47] Wang Y, Chung SH. Soot formation in laminar counterflow flames. Prog Energy Combust Sci 2019;74:152–238. https://doi.org/10.1016/j.pecs.2019.05.003.

[48] Bartok W, Kuriskin RJ. Formation of Soot Precursors in Diffusion Flames. Combust Sci Technol 1988;58:281–95. https://doi.org/10.1080/00102208808923968.

[49] Roditcheva O V., Bai XS. Pressure effect on soot formation in turbulent diffusion flames. Chemosphere 2001;42:811–21. https://doi.org/10.1016/S0045-6535(00)00255-1.

[50] Davis J, Molnar E, Novosselov I. Nanostructure transition of young soot aggregates to mature soot aggregates in diluted diffusion flames. Carbon N Y 2020;159:255–65. https://doi.org/10.1016/J.CARBON.2019.12.043.

[51] Veshkini A. Understanding Soot Particle Growth Chemistry and Particle Sizing Using a Novel Soot Growth and Formation Model. 2015.

[52] Amann CA, Siegla DC. Diesel particulates—What they are and why. Aerosol Sci Technol 1982;1:73–101. https://doi.org/10.1080/02786828208958580.

[53] Geigle KP, Zerbs J, Hadef R, Guin C. Laser-induced incandescence for soot measurements in an aero-engine combustor at pressures up to 20 bar. Appl Phys B Lasers Opt 2019;125:1–8. https://doi.org/10.1007/s00340-019-7211-2.

[54] Kholghy MR, Weingarten J, Sediako AD, Barba J, Lapuerta M, Thomson MJ. Structural effects of biodiesel on soot formation in a laminar coflow diffusion flame. Proc Combust Inst 2017;36:1321–8. https://doi.org/10.1016/j.proci.2016.06.119.

[55] Geigle KP, Köhler M, O'Loughlin W, Meier W. Investigation of soot formation in pressurized swirl flames by laser measurements of temperature, flame structures and soot concentrations. Proc Combust Inst 2015;35:3373–80. https://doi.org/10.1016/j.proci.2014.05.135.

[56] H. Bockhorn, A. D'Anna, A. F. Sarofim HW. Combustion Generated Fine Carbonaceous Particles. 2009.

[57] Michelsen HA, Colket MB, Bengtsson PE, D'Anna A, Desgroux P, Haynes BS, et al. A review of terminology used to describe soot formation and evolution under combustion and pyrolytic conditions. ACS Nano 2020;14:12470–90. https://doi.org/10.1021/acsnano.0c06226.

[58] Putnam A, Faulkner L. An Overview of Combustion Diagnostics. vol. 7. 2010. https://doi.org/10.2514/3.62684.

[59] Botero ML, Sheng Y, Akroyd J, Martin J, Dreyer JAH, Yang W, et al. Internal structure of soot particles in a diffusion flame. Carbon N Y 2019;141:635–42. https://doi.org/10.1016/j.carbon.2018.09.063.

[60] Xi J, Yang G, Cai J, Gu Z. A Review of Recent Research Results on Soot: The Formation of a Kind of Carbon-Based Material in Flames. Front Mater 2021;8. https://doi.org/10.3389/fmats.2021.695485.

[61] Karataş AE, Gülder ÖL. Soot formation in high pressure laminar diffusion flames. Prog Energy Combust Sci 2012;38:818–45. https://doi.org/10.1016/j.pecs.2012.04.003.

[62] Karataş AE, Gülder ÖL. Soot formation in high pressure laminar diffusion flames. Prog Energy Combust Sci 2012;38:818–45. https://doi.org/10.1016/j.pecs.2012.04.003.

[63] Lima ALC, Farrington JW, Reddy CM. Combustion-derived polycyclic aromatic hydrocarbons in the environment - A review. Environ Forensics 2005;6:109–31. https://doi.org/10.1080/15275920590952739.

[64] June A. PAH formation in acetylene – benzene pyrolysis 1999:3775–81.

[65] Wang H, Frenklach M. Transport properties of polycyclic aromatic hydrocarbons for flame modeling. Combust Flame 1994;96:163–70. https://doi.org/10.1016/0010-2180(94)90167-8.

[66] Kennish MJ. Polycyclic aromatic hydrocarbons. Encycl Earth Sci Ser 2016:495. https://doi.org/10.1007/978-94-017-8801-4_25.

[67] Dipple A, Cheng SC, Bigger CA. Polycyclic aromatic hydrocarbon carcinogens. Prog Clin Biol Res

1990;347:109–27.

[68] Wikipedia. Polycyclic aromatic hydrocarbon 2022. https://en.wikipedia.org/wiki/Polycyclic_aromatic_hydrocarbon.

[69] Bladh H, Olofsson N-E, Mouton T, Simonsson J, Mercier X, Faccinetto A, et al. Probing the smallest soot particles in low-sooting premixed flames using laser-induced incandescence. Proc Combust Inst 2015;35:1843–50. https://doi.org/10.1016/j.proci.2014.06.001.

[70] Betrancourt C, Liu F, Desgroux P, Mercier X, Faccinetto A, Salamanca M, et al. Investigation of the size of the incandescent incipient soot particles in premixed sooting and nucleation flames of n-butane using LII, HIM, and 1 nm-SMPS. Aerosol Sci Technol 2017;51:916–35. https://doi.org/10.1080/02786826.2017.1325440.

[71] Kuo KK, Acharya R. Applications of Turbulent and Multiphase Combustion. 2012. https://doi.org/10.1002/9781118127575.

[72] Michelsen HA, Schulz C, Smallwood GJ, Will S. Laser-induced incandescence: Particulate diagnostics for combustion, atmospheric, and industrial applications. Prog Energy Combust Sci 2015;51:2–48. https://doi.org/10.1016/j.pecs.2015.07.001.

[73] Busch S. The Theory and Application of Optical Diagnostic Techniques in the Combustion Chamber of a Diesel Engine 2013.

[74] Köylü ÜÖ, Faeth GM. Structure of overfire soot in buoyant turbulent diffusion flames at long residence times. Combust Flame 1992;89:140–56. https://doi.org/10.1016/0010-2180(92)90024-J.

[75] Chen HX, Dobbins RA. Crystallogenesis of particles formed in hydrocarbon combustion. Combust Sci Technol 2000;159:109–28. https://doi.org/10.1080/00102200008935779.

[76] Ticich TM, Stephens AB, VanderWal RL. Can soot primary particle size be determined using laser induced incandescence? ACS Div Fuel Chem Prepr 1998;43:305–8.

[77] Bambha RP, Dansson MA, Schrader PE, Michelsen HA. Effects of volatile coatings and coating removal mechanisms on the morphology of graphitic soot. Carbon N Y 2013;61:80–96. https://doi.org/10.1016/j.carbon.2013.04.070.

[78] Bambha RP, Michelsen HA. Effects of aggregate morphology and size on laser-induced incandescence and scattering from black carbon (mature soot). J Aerosol Sci 2015;88:159–81. https://doi.org/10.1016/J.JAEROSCI.2015.06.006.

[79] Leschowski M, Thomson KA, Snelling DR, Schulz C, Smallwood GJ. Combination of LII and extinction measurements for determination of soot volume fraction and estimation of soot maturity in non-premixed laminar flames. Appl Phys B Lasers Opt 2015;119:685–96. https://doi.org/10.1007/s00340-015-6092-2.

[80] Charalampopoulos TT, Felske JD. Refractive indices of soot particles deduced from in-situ laser light scattering measurements. Combust Flame 1987;68:283–94. https://doi.org/10.1016/0010-2180(87)90005-8.

[81] Williams TC, Shaddix CR, Jensen KA, Suo-Anttila JM. Measurement of the dimensionless extinction coefficient of soot within laminar diffusion flames. Int J Heat Mass Transf 2007;50:1616–30. https://doi.org/10.1016/j.ijheatmasstransfer.2006.08.024.

[82] Jung Y, Bae C. Immaturity of soot particles in exhaust gas for low temperature diesel combustion in a direct injection compression ignition engine. Fuel 2015;161:312–22. https://doi.org/10.1016/j.fuel.2015.08.068.

[83] Alexandrino K, Salinas J, Millera Á, Bilbao R, Alzueta MU. Sooting propensity of dimethyl carbonate, soot reactivity and characterization. Fuel 2016;183:64–72. https://doi.org/10.1016/j.fuel.2016.06.058.

[84] Tree DR, Svensson KI. Soot processes in compression ignition engines. Prog Energy Combust Sci 2007;33:272–309. https://doi.org/10.1016/j.pecs.2006.03.002.

[85] NAGLE J, STRICKLAND-CONSTABLE RF. Oxidation of Carbon Between 1000–2000°C. Proc Fifth Conf Carbon 1962;348:154–64. https://doi.org/10.1016/b978-0-08-009707-7.50026-1.

[86] Von Gersum S, Roth P. Soot oxidation in high temperature N2O/Ar and NO/Ar mixtures. Symp Combust 1992;24:999–1006. https://doi.org/10.1016/S0082-0784(06)80118-9.

[87] Sato H, Tree DR, Hodges JT, Foster DE. A study on the effect of temperature on soot formation in a jet stirred combustor. Symp Combust 1991;23:1469–75. https://doi.org/10.1016/S0082-0784(06)80415-7.

[88] Song J, Peng P. Characterisation of black carbon materials by pyrolysis-gas chromatography-mass spectrometry. J Anal Appl Pyrolysis 2010;87:129–37. https://doi.org/10.1016/j.jaap.2009.11.003.

[89] Dec JE. Advanced compression-ignition engines - Understanding the in-cylinder processes. Proc Combust Inst 2009;32 II:2727–42. https://doi.org/10.1016/j.proci.2008.08.008.

[90] Omer L, Kevin A, Elizabeth J, Roydon A, Gregory J, David R. In fl uence of Pressure on Soot Formation in Laminar 2005.

[91] Steinmetz SA, Fang T, Roberts WL. Soot particle size measurements in ethylene diffusion flames at elevated pressures. Combust Flame 2016;169:85–93. https://doi.org/10.1016/j.combustflame.2016.02.034.

[92] Ellzey JL, Berbee JG, Tay ZF, Foster DE. Total Soot Yield from a Propane Diffusion Flame in Cross-Flow. Combust Sci Technol 1990;71:41–52. https://doi.org/10.1080/00102209008951623.

[93] Bönig M, Feldermann CR, Jander H, Lüers B, Rudolph G, Wagner HG. Soot formation in premixed C2H4 flat flames at elevated pressure. Symp Combust 1991;23:1581–7. https://doi.org/10.1016/S0082-0784(06)80429-7.

[94] Xu L, Yan F, Zhou M, Wang Y, Chung SH. Experimental and soot modeling studies of ethylene counterflow diffusion flames: Non-monotonic influence of the oxidizer composition on soot formation. Combust Flame 2018;197:304–18. https://doi.org/10.1016/J.COMBUSTFLAME.2018.08.011.

[95] Mahmoud NM, Yan F, Wang Y. Effects of fuel inlet boundary condition on aromatic species formation in coflow diffusion flames. J Energy Inst 2019;92:288–97. https://doi.org/10.1016/J.JOEI.2018.01.007.

[96] Chu C, Naseri A, Mitra T, Dadsetan M, Sediako A, Thomson MJ. The effect of elevated reactant temperatures on soot nanostructures in a coflow diffusion ethylene flame. Proc Combust Inst 2021;38:2525–32. https://doi.org/10.1016/j.proci.2020.06.348.

[97] Qi S, Sun Z, Wang Z, Liu Y, He Y, Liu S, et al. Effects of gas preheat temperature on soot formation in co-flow methane and ethylene diffusion flames. Proc Combust Inst 2021;38:1225–32. https://doi.org/10.1016/J.PROCI.2020.08.034.

[98] Ibrahim F, Wan Mahmood WMF, Abdullah S, Abu Mansor MR. Soot particle measurement in engine cylinder: A review. J Teknol 2016;78:187–95. https://doi.org/10.11113/jt.v78.5140.

[99] Viskup R. Comparison of different techniques for measurement of soot and PM emission from Diesel engine. CEUR Workshop Proc 2012;865:1–19.

[100] He X, Ma X, Wu F, Wang J, Shuai S. Investigation of soot formation in laminar diesel diffusion flame by two-color laser induced incandescence. SAE Tech Pap 2008;2008. https://doi.org/10.4271/2008-01-1064.

[101] Yu Z, Ziemba LD, Onasch TB, Herndon SC, Albo SE, Miake-Lye R, et al. Direct measurement of aircraft engine soot emissions using a cavity-attenuated phase shift (CAPS)-based extinction monitor. Aerosol Sci Technol 2011;45:1319–25. https://doi.org/10.1080/02786826.2011.592873.

[102] Lou C, Chen C, Sun Y, Zhou H. Review of soot measurement in hydrocarbon-air flames. Sci China Technol Sci 2010;53:2129–41. https://doi.org/10.1007/s11431-010-3212-4.

[103] Schäfer K, Heland J, Lister DH, Wilson CW, Howes RJ, Falk RS, et al. Nonintrusive optical measurements of aircraft engine exhaust emissions and comparison with standard intrusive techniques. Appl Opt 2000;39:441. https://doi.org/10.1364/ao.39.000441.

[104] C. Richard Brundle Charles A. Evans JSW. Encyclopedia of materials characterization. 1992.

[105] Bergamaschi A, Iavicoli I, Savolainen K. Exposure Assessment. Elsevier Inc.; 2012. https://doi.org/10.1016/B978-0-12-386940-1.00002-7.

[106] Ortega IK, Delhaye D, Ouf FX, Ferry D, Focsa C, Irimiea C, et al. Measuring Non-Volatile Particle Properties in the Exhaust of an Aircraft Engine. J AerospaceLab 2016:1–14. https://doi.org/10.12762/2016.AL11-08.

[107] Bonnamy S, Oberlin A. Transmission Electron Microscopy. 2016. https://doi.org/10.1016/B978-0-12-805256-3.00004-0.

[108] Jia DE. Heat and mass transfer. Essentials Fluid. Technol., 2007, p. 291–331. https://doi.org/10.1002/9783527699483.ch14.

[109] Bennett A. Fundamental Studies of Soot Formation and Diagnostic Development in Nonpremixed Combustion Environments. 2020.

[110] Wan K, Chen D, Wang H. On imaging nascent soot by transmission electron microscopy. Combust Flame 2018;198:260–6. https://doi.org/10.1016/j.combustflame.2018.09.021.

[111] Hwang J, Hirner FS, Bae C, Patel C, Gupta T, Agarwal AK. HRTEM evaluation of primary soot particles originated in a small-bore biofuel compression-ignition engine. Appl Therm Eng 2019;159:113899. https://doi.org/10.1016/j.applthermaleng.2019.113899.

[112] Sigle W. Analytical transmission electron microscopy. Annu Rev Mater Res 2005;35:239–314. https://doi.org/10.1146/annurev.matsci.35.102303.091623.

[113] Mathews JP, Fernandez-Also V, Daniel Jones A, Schobert HH. Determining the molecular weight distribution of Pocahontas No. 3 low-volatile bituminous coal utilizing HRTEM and laser desorption ionization mass spectra data. Fuel 2010;89:1461–9. https://doi.org/10.1016/j.fuel.2009.10.014.

[114] Parent P, Laffon C, Marhaba I, Ferry D, Regier TZ, Ortega IK, et al. Nanoscale characterization of aircraft soot: A high-resolution transmission electron microscopy, Raman spectroscopy, X-ray photoelectron and near-edge X-ray absorption spectroscopy study. Carbon N Y 2016;101:86–100. https://doi.org/10.1016/j.carbon.2016.01.040.

[115] Delhaye D, Ouf FX, Ferry D, Ortega IK, Penanhoat O, Peillon S, et al. The MERMOSE project:

Characterization of particulate matter emissions of a commercial aircraft engine. J Aerosol Sci 2017;105:48–63. https://doi.org/10.1016/j.jaerosci.2016.11.018.

[116] Saggese C, Cuoci A, Frassoldati A, Ferrario S, Camacho J, Wang H, et al. Probe effects in soot sampling from a burner-stabilized stagnation flame. Combust Flame 2016;167:184–97. https://doi.org/10.1016/j.combustflame.2016.02.013.

[117] Mustafi NN, Raine RR. Electron microscopy investigation of particulate matter from a dual fuel engine. Aerosol Sci Technol 2009;43:951–60. https://doi.org/10.1080/02786820903067210.

[118] Faith Mokobi. Scanning Electron Microscope (SEM)- Definition, Principle 2022. https://microbenotes.com/scanning-electron-microscope-sem/.

[119] Macrovision. Scanning electron microscope imaging. October 2022:208–208. https://microvisionlabs.com/service/sem/.

[120] Baldelli A, Trivanovic U, Sipkens TA, Rogak SN. On determining soot maturity: A review of the role of microscopy- and spectroscopy-based techniques. Chemosphere 2020;252:126532. https://doi.org/10.1016/j.chemosphere.2020.126532.

[121] Schnaiter M, Linke C, Ibrahim I, Kiselev A, Waitz F, Leisner T, et al. Specifying the light-absorbing properties of aerosol particles in fresh snow samples, collected at the Environmental Research Station Schneefernerhaus (UFS), Zugspitze. Atmos Chem Phys 2019;19:10829–44. https://doi.org/10.5194/acp-19-10829-2019.

[122] Schuler B, Meyer G, Peña D, Mullins OC, Gross L. Unraveling the Molecular Structures of Asphaltenes by Atomic Force Microscopy. J Am Chem Soc 2015;137:9870–6. https://doi.org/10.1021/jacs.5b04056.

[123] Bionity. Atomic force microscope 2022. https://www.bionity.com/en/encyclopedia/Atomic_force_microscope.html (accessed December 20, 2022).

[124] Schulz F, Commodo M, Kaiser K, De Falco G, Minutolo P, Meyer G, et al. Insights into incipient soot formation by atomic force microscopy. Proc Combust Inst 2019;37:885–92. https://doi.org/10.1016/j.proci.2018.06.100.

[125] Commodo M, Kaiser K, De Falco G, Minutolo P, Schulz F, D'Anna A, et al. On the early stages of soot formation: Molecular structure elucidation by high-resolution atomic force microscopy. Combust Flame 2019;205:154–64. https://doi.org/10.1016/j.combustflame.2019.03.042.

[126] Sadezky A, Muckenhuber H, Grothe H, Niessner R, Pöschl U. Raman microspectroscopy of soot and related carbonaceous materials: Spectral analysis and structural information. Carbon N Y 2005;43:1731–42. https://doi.org/10.1016/j.carbon.2005.02.018.

[127] Schmid J, Grob B, Niessner R, Ivleva NP. Multiwavelength raman microspectroscopy for rapid prediction of soot oxidation reactivity. Anal Chem 2011;83:1173–9. https://doi.org/10.1021/ac102939w.

[128] Faccinetto A, Irimiea C, Minutolo P, Commodo M, D'Anna A, Nuns N, et al. Evidence on the formation of dimers of polycyclic aromatic hydrocarbons in a laminar diffusion flame. Commun Chem 2020;3:1–8. https://doi.org/10.1038/s42004-020-00357-2.

[129] Liu F, Yon J, Fuentes A, Lobo P, Smallwood GJ, Corbin JC. Review of recent literature on the light absorption properties of black carbon: Refractive index, mass absorption cross section, and absorption function. Aerosol Sci Technol 2020;54:33–51. https://doi.org/10.1080/02786826.2019.1676878.

[130] Quay B, Lee TW, Ni T, Santoro RJ. Spatially resolved measurements of soot volume fraction using laser-induced incandescence. Combust Flame 1994;97:384–92. https://doi.org/10.1016/0010-2180(94)90029-9.

[131] Commodo M. Diagnostic for the characterization of nanometric structures in high temperature reactive systems. 2007.

[132] Modest MF. Radiative Heat Transfer. 2013. https://doi.org/10.1016/C2010-0-65874-3.

[133] Lambert B. Beer–Lambert law 1913.

[134] Liu F, Wong C, Snelling DR, Smallwood GJ. Investigation of absorption and scattering properties of soot aggregates of different fractal dimension at 532 nm Using RDG and GMM. Aerosol Sci Technol 2013;47:1393–405. https://doi.org/10.1080/02786826.2013.847525.

[135] Sorensen CM, Yon J, Liu F, Maughan J, Heinson WR, Berg MJ. Light scattering and absorption by fractal aggregates including soot. J Quant Spectrosc Radiat Transf 2018;217:459–73. https://doi.org/10.1016/j.jqsrt.2018.05.016.

[136] Thomson KA, Johnson MR, Snelling DR, Smallwood GJ. Diffuse-light two-dimensional line-of-sight attenuation for soot concentration measurements. Appl Opt 2008;47:694–703.

[137] Barbosa S, Onofri FRA, Couëdel L, Wozniak M, Montet C, Pelcé C, et al. An introduction to light extinction spectrometry as a diagnostic for dust particle characterisation in dusty plasmas. J Plasma Phys 2016;82:1–24. https://doi.org/10.1017/S0022377816000714.

[138] Liu F, Thomson KA, Smallwood GJ. Soot temperature and volume fraction retrieval from spectrally resolved flame emission measurement in laminar axisymmetric coflow diffusion flames: Effect of self-absorption. Combust Flame 2013;160:1693–705. https://doi.org/10.1016/j.combustflame.2013.02.007.

[139] Snelling DR, Thomson KA, Smallwood GJ, Gülder L, Weckman EJ, Fraser RA. Spectrally resolved measurement of flame radiation to determine soot temperature and concentration. AIAA J 2002;40:1789–95. https://doi.org/10.2514/2.1855.

[140] Jain PK. On blackbody radiation. Phys Educ 1991;26:190–4. https://doi.org/10.1088/0031-9120/26/3/011.

[141] Michelsen HA. Understanding and predicting the temporal response of laser-induced incandescence from carbonaceous particles. J Chem Phys 2003;118:7012–45. https://doi.org/10.1063/1.1559483.

[142] Lefevre G. Caractérisation des propriétés radiatives des nanoparticules de suie en présence de composés organiques. 2019.

[143] Dufitumukiza JP, Fdida N, Geigle KP, Yin Z, Vincent A, Barrellon-vernay R, et al. Development of coupled optical techniques for the measurements of soot and precursors in laboratory flame and aero-engine technical combustors. ODAS, BRAUNSCHWEIG, Germany: 2020.

[144] Köhler M, Geigle KP, Meier W, Crosland BM, Thomson KA, Smallwood GJ. Sooting turbulent jet flame: Characterization and quantitative soot measurements. Appl. Phys. B Lasers Opt., vol. 104, 2011, p. 409–25. https://doi.org/10.1007/s00340-011-4373-y.

[145] Johansson KO, El Gabaly F, Schrader PE, Campbell MF, Michelsen HA. Evolution of maturity levels of the particle surface and bulk during soot growth and oxidation in a flame. Aerosol Sci Technol 2017;51:1333–44. https://doi.org/10.1080/02786826.2017.1355047.

[146] Kim GB, Shim JY, Cho SW, Chang YJ, Jeon CH. A comparison of LII analysis results from numerical

model and experiment at elevated surrounding pressures. J Mech Sci Technol 2008;22:1154–62. https://doi.org/10.1007/s12206-008-0120-7.

[147] Bouvier M, Cabot G, Yon J, Grisch F. On the use of PIV, LII, PAH-PLIF and OH-PLIF for the study of soot formation and flame structure in a swirl stratified premixed ethylene/air flame. Proc Combust Inst 2020;000:1–8. https://doi.org/10.1016/j.proci.2020.10.002.

[148] Roussillo M, Scouflaire P, Candel S, Franzelli B. Experimental investigation of soot production in a confined swirled flame operating under perfectly premixed rich conditions. Proc Combust Inst 2019;37:893–901. https://doi.org/10.1016/j.proci.2018.06.110.

[149] William D, Bachalo D, Smallwood J, Snelling R. Development of the Laser-Induced Incandescence Method for the Reliable Characterization of Diesel Particulate Emissions n.d.:1–20.

[150] Axelsson B, Collin R, Bengtsson P-E. Laser-induced incandescence for soot particle size measurements in premixed flat flames. Appl Opt 2000;39:3683. https://doi.org/10.1364/ao.39.003683.

[151] Hadef R, Geigle KP, Meier W, Aigner M. Soot characterization with laser-induced incandescence applied to a laminar premixed ethylene-air flame. Int J Therm Sci 2010;49:1457–67. https://doi.org/10.1016/j.ijthermalsci.2010.02.014.

[152] Michelsen HA, Schulz C, Smallwood GJ, Will S. Laser-induced incandescence: Particulate diagnostics for combustion, atmospheric, and industrial applications. Prog Energy Combust Sci 2015;51:2–48. https://doi.org/10.1016/j.pecs.2015.07.001.

[153] De Iuliis S, Migliorini F, Cignoli F, Zizak G. 2D soot volume fraction imaging in an ethylene diffusion flame by two-color laser-induced incandescence (2C-LII) technique and comparison with results from other optical diagnostics. Proc Combust Inst 2007;31 I:869–76. https://doi.org/10.1016/j.proci.2006.07.149.

[154] Geigle KP, Hadef R, Meier W. Soot Formation and flame characterization of an aero-engine model combustor burning ethylene at elevated pressure. J Eng Gas Turbines Power 2014;136:1–7. https://doi.org/10.1115/1.4025374.

[155] Mouton T, Mercier X, Wartel M, Lamoureux N, Desgroux P. Laser-induced incandescence technique to identify soot nucleation and very small particles in low-pressure methane flames. Appl Phys B Lasers Opt 2013;112:369–79. https://doi.org/10.1007/s00340-013-5446-x.

[156] Lakowicz JR. Principles of Fluorescence Spectroscopy. 1999. https://doi.org/10.1007/978-1-4757-3061-6.

[157] Edinburgh Instruments. What is a Jablonski Diagram (Perrin-Jablonski Diagram) n.d. https://www.edinst.com/us/blog/jablonski-diagram/.

[158] Valeur B. Molecular Fluorescence: Principles and Applications. vol. 8. 2001.

[159] Zacharioudaki DE, Fitilis I, Kotti M. Review of Fluorescence Spectroscopy in Environmental Quality Applications. Molecules 2022;27. https://doi.org/10.3390/molecules27154801.

[160] Bernard Valeur J-CB. New Trends in Fluorescence Spectroscopy Applications to Chemical and Life Sciences. vol. 15. 2001. https://doi.org/DOI 10.1007/978-3-642-56853-4.

[161] McPhie P. Principles of Fluorescence Spectroscopy, Second ed. Joseph R. Lakowicz. vol. 287. 2000. https://doi.org/10.1006/abio.2000.4850.

[162] Dreeskamp H, Koch E, Zander M. On the Fluorescence Quenching of Polycyclic Aromatic

Hydrocarbons by Nitromethane. Zeitschrift Fur Naturforsch - Sect A J Phys Sci 1975;30:1311–4. https://doi.org/10.1515/zna-1975-1017.

[163] Tedder S, Hicks Y. OH Planar Laser Induced Fluorescence (PLIF) Measurements for the Study of High Pressure Flames : An Evaluation of a New Laser and a New Camera System. Nasa Tech Memo 2012.

[164] Desgroux P, Faccinetto A, Mercier X, Mouton T, Aubagnac Karkar D, El Bakali A. Comparative study of the soot formation process in a “nucleation” and a “sooting” low pressure premixed methane flame. Combust Flame 2017;184:153–66. https://doi.org/10.1016/j.combustflame.2017.05.034.

[165] Legros S, Brunet C, Domingo-Alvarez P, Malbois P, Salaun E, Godard G, et al. Combustion for aircraft propulsion: Progress in advanced laser-based diagnostics on high-pressure kerosene/air flames produced with low-NOx fuel injection systems. Combust Flame 2021;224:273–94. https://doi.org/10.1016/j.combustflame.2020.12.036.

[166] Kohse-Höinghaus K, Barlow RS, Aldén M, Wolfrum J. Combustion at the focus: Laser diagnostics and control. Proc Combust Inst 2005;30:89–123. https://doi.org/10.1016/j.proci.2004.08.274.

[167] Bejaoui S, Mercier X, Desgroux P, Therssen E. Laser induced fluorescence spectroscopy of aromatic species produced in atmospheric sooting flames using UV and visible excitation wavelengths. Combust Flame 2014;161:2479–91. https://doi.org/10.1016/J.COMBUSTFLAME.2014.03.014.

[168] Berlman IB. Handbook of Fluorescence Spectra of Aromatic Molecules. Handb Fluoresc Spectra Aromat Mol 1971. https://doi.org/10.1016/b978-0-12-092656-5.x5001-1.

[169] Sgro LA, Minutolo P, Basile G, D’Alessio A. UV-visible spectroscopy of organic carbon particulate sampled from ethylene/air flames. Chemosphere 2001;42:671–80. https://doi.org/10.1016/S0045-6535(00)00241-1.

[170] Singh P, Sung CJ. PAH formation in counterflow non-premixed flames of butane and butanol isomers. Combust Flame 2016;170:91–110. https://doi.org/10.1016/j.combustflame.2016.05.009.

[171] Bejaoui S. Étude spectroscopique des suies et de leurs précurseurs par Incandescence et Fluorescence Induite par laser. Lille, 2012.

[172] Mercier X, Carrivain O, Irimiea C, Faccinetto A, Therssen E. Dimers of polycyclic aromatic hydrocarbons: The missing pieces in the soot formation process. Phys Chem Chem Phys 2019;21:8285–94. https://doi.org/10.1039/c9cp00394k.

[173] Espey C, Dec JE, Litzinger TA, Santavicca DA. Planar laser Rayleigh scattering for quantitative vapor-fuel imaging in a diesel jet. Combust Flame 1997;109:65–78. https://doi.org/10.1016/S0010-2180(96)00126-5.

[174] Melton LA. Soot Diagnostics Based on Laser Heating. Chem Phys Process Combust Fall Tech Meet East States Sect 1983. https://doi.org/10.1364/ao.23.002201.

[175] Roth P, Filippov A V. In situ ultrafine particle sizing by a combination of pulsed laser heatup and particle thermal emission. J Aerosol Sci 1996;27:95–104. https://doi.org/10.1016/0021-8502(95)00531-5.

[176] Johnsson J. Laser-induced incandescence for soot diagnostics : theoretical investigation and experimental development. Division of Combustion Physics, Department of Physics, Lund University; 2012.

[177] Desgroux P, Mercier X, Thomson KA. Study of the formation of soot and its precursors in flames using optical diagnostics. Proc Combust Inst 2013;34:1713–38. https://doi.org/10.1016/j.proci.2012.09.004.

[178] Cléon G, Amodeo T, Faccinetto A, Desgroux P. Laser induced incandescence determination of the ratio of the soot absorption functions at 532 nm and 1064 nm in the nucleation zone of a low pressure premixed sooting flame. Appl Phys B Lasers Opt 2011;104:297–305. https://doi.org/10.1007/s00340-011-4372-z.

[179] Planck M. The theory of heat radiation. 1914.

[180] Michelsen HA, Linne MA, Kock BF, Hofmann M, Tribalet B, Schulz C. Modeling laser-induced incandescence of soot: Enthalpy changes during sublimation, conduction, and oxidation. Appl Phys B Lasers Opt 2008;93:645–56. https://doi.org/10.1007/s00340-008-3181-5.

[181] Lemaire R, Mobtil M. Modeling laser-induced incandescence of soot: a new approach based on the use of inverse techniques. Appl Phys B Lasers Opt 2015;119:577–606. https://doi.org/10.1007/S00340-015-6032-1/FIGURES/15.

[182] Bodor AL, Agnes M, Bodor L. Numerical modelling of soot formation and evolution in laminar flames with detailed kinetics To cite this version : Numerical modeling of soot formation and evolution in laminar flames with detailed kinetics 2019.

[183] Xu L, Yan F, Zhou M, Wang Y, Chung SH. Experimental and soot modeling studies of ethylene counterflow diffusion flames: Non-monotonic influence of the oxidizer composition on soot formation. Combust Flame 2018;197:304–18. https://doi.org/10.1016/j.combustflame.2018.08.011.

[184] Thomson MJ. Modeling soot formation in flames and reactors : Recent progress and current challenges. Proc Combust Inst 2022;000:1–19. https://doi.org/10.1016/j.proci.2022.07.263.

[185] Michelsen HA, Liu F, Kock BF, Bladh H, Boiarciuc A, Charwath M, et al. Modeling laser-induced incandescence of soot: A summary and comparison of LII models. Appl Phys B Lasers Opt 2007;87:503–21. https://doi.org/10.1007/s00340-007-2619-5.

[186] Hiers R. A control volume derivation of the energy equation for LII modeling. Appl Phys B Lasers Opt 2008;92:635–41. https://doi.org/10.1007/s00340-008-3122-3.

[187] Potenza M, Naccarato F, de Risi A. Two-dimensional measurements of primary soot diameter in diffusion flames by two-dimensional time resolved laser induced incandescence. IET Sci Meas Technol 2014;8:107–15. https://doi.org/10.1049/iet-smt.2013.0134.

[188] Mansmann RA. Multi-color time-resolved laser-induced incandescence for the measurement of soot and nanoparticle aerosols. 2019.

[189] Michelsen HA. Understanding and predicting the temporal response of laser-induced incandescence from carbonaceous particles. J Chem Phys 2003;118:7012–45. https://doi.org/10.1063/1.1559483.

[190] Bambha RP, Michelsen HA. Effects of aggregate morphology and size on laser-induced incandescence and scattering from black carbon (mature soot). J Aerosol Sci 2015;88:159–81. https://doi.org/10.1016/j.jaerosci.2015.06.006.

[191] Bladh H, Johnsson J, Olofsson NE, Bohlin A, Bengtsson PE. Optical soot characterization using two-color laser-induced incandescence (2C-LII) in the soot growth region of a premixed flat flame. Proc Combust Inst 2011. https://doi.org/10.1016/j.proci.2010.06.166.

[192] Kuhlmann SA, Reimann J, Will S. On heat conduction between laser-heated nanoparticles and

a surrounding gas. J Aerosol Sci 2006;37:1696–716. https://doi.org/10.1016/j.jaerosci.2006.06.009.

[193] Sébastien M. Analysis of the Influence of the Conduction Sub-Model Formulation on the Modeling of Laser-Induced Incandescence of Diesel Soot Aggregates. Entropy 2019.

[194] Mitrani JM, Shneider MN, Stratton BC, Raitses Y. Modeling thermionic emission from laser-heated nanoparticles. Appl Phys Lett 2016;108:1–6. https://doi.org/10.1063/1.4940992.

[195] Liu F, Stagg BJ, Snelling DR, Smallwood GJ. Effects of primary soot particle size distribution on the temperature of soot particles heated by a nanosecond pulsed laser in an atmospheric laminar diffusion flame. Int J Heat Mass Transf 2006;49:777–88. https://doi.org/10.1016/J.IJHEATMASSTRANSFER.2005.07.041.

[196] Santoro RJ, Semerjian HG, Dobbins RA. Soot particle measurements in diffusion flames. Combust Flame 1983;51:203–18. https://doi.org/10.1016/0010-2180(83)90099-8.

[197] Hepp H, Siegmann K. Mapping of Soot Particles in a Weakly Sooting Diffusion Flame by Aerosol Techniques. Combust Flame 1998;115:275–83. https://doi.org/10.1016/S0010-2180(97)00346-5.

[198] Irimiea C, Faccinetto A, Mercier X, Ortega IK, Nuns N, Therssen E, et al. Unveiling trends in soot nucleation and growth: When secondary ion mass spectrometry meets statistical analysis. Carbon N Y 2019;144:815–30. https://doi.org/10.1016/J.CARBON.2018.12.015.

[199] Smallwood GJ. A Critique of Laser-Induced Incandescence for the Measurement of Soot. Cranf Univ 2008.

[200] Ruschin S, Yaakobi E, Shekel E. Gaussian content as a laser beam quality parameter. Appl Opt 2011;50:4376–81. https://doi.org/10.1364/AO.50.004376.

[201] Alda J. Laser and Gaussian Beam Propagation and Transformation. Encycl Opt Eng 2011. https://doi.org/10.1081/e-eoe.

[202] RadhaKrishna MVV, Venkata Govindh M, Krishna Veni P. A review on image processing sensor. J Phys Conf Ser 2021;1714. https://doi.org/10.1088/1742-6596/1714/1/012055.

[203] Mercier X. Mesure de Concentrations Absolues d'Espèces Réactives Minoritaires dans les Flammes par la Technique d'Absorption Cavity Ring-Down Spectroscopy. 2019.

[204] Geipel G. Laser-Induced Fluorescence Spectroscopy. Handb Appl Solid State Spectrosc 2007;4:577–93. https://doi.org/10.1007/0-387-37590-2_13.

[205] Török S, Mannazhi M, Bergqvist S, Le KC, Bengtsson PE. Influence of rapid laser heating on differently matured soot with double-pulse laser-induced incandescence. Aerosol Sci Technol 2022;56:488–501. https://doi.org/10.1080/02786826.2022.2046689.

[206] Johnson RC, Trans P, Lond RS. The structure and origin of the Swan band spectrum of carbon. Philos Trans R Soc London Ser A, Contain Pap a Math or Phys Character 1927;226:157–230. https://doi.org/10.1098/rsta.1927.0005.

[207] Liu F, Snelling DR, Thomson KA, Smallwood GJ. Sensitivity and relative error analyses of soot temperature and volume fraction determined by two-color LII. Appl Phys B Lasers Opt 2009;96:623–36. https://doi.org/10.1007/s00340-009-3560-6.

[208] Liu F, Smallwood GJ. Effects of Detection Wavelengths on Soot Volume Fraction Measurements Using the Auto-Compensating LII Technique. Combust Sci Technol 2022;194:144–58. https://doi.org/10.1080/00102202.2019.1678837.

[209] Snelling DR, Smallwood GJ, Liu F, Gülder ÖL, Bachalo WD. A calibration-independent laser-induced incandescence technique for soot measurement by detecting absolute light intensity. Appl Opt 2005;44:6773–85. https://doi.org/10.1364/AO.44.006773.

[210] Sandra Török·, Manu Mannazhi PB. Laser-induced incandescence (2λ and 2C) for estimating absorption efficiency of differently matured soot. Appl Phys B 2021.

[211] Mannazhi M, Bengtsson PE. Two-dimensional laser-induced incandescence for soot volume fraction measurements: issues in quantification due to laser beam focusing. Appl Phys B Lasers Opt 2020;126. https://doi.org/10.1007/s00340-020-07547-9.

[212] Hult J, Mayer S. Adjustable focus laser sheet module for generating constant maximum width sheets for use in optical flow diagnostics. Meas Sci Technol 2011;22. https://doi.org/10.1088/0957-0233/22/11/115305.

[213] Shaddix CR, Williams TC. Analysis of laser focusing effect on quantification of LII images. Proc Combust Inst 2020;000:1–8. https://doi.org/10.1016/j.proci.2020.07.015.

[214] Lavision. Image Doubler n.d.:48197. https://www.lavision.de/en/download.php?id=453.

[215] Stockham A, Smith JG. Comparison between a super Gaussian and a “true” top hat. Laser Beam Shap. IX, vol. 7062, SPIE; 2008, p. 70620I. https://doi.org/10.1117/12.796074.

[216] Bladh H, Johnsson J, Bengtsson PE. Influence of spatial laser energy distribution on evaluated soot particle sizes using two-colour laser-induced incandescence in a flat premixed ethylene/air flame. Appl Phys B Lasers Opt 2009;96:645–56. https://doi.org/10.1007/s00340-009-3523-y.

[217] Mannazhi M, Bengtsson PE. Two-dimensional laser-induced incandescence for soot volume fraction measurements: issues in quantification due to laser beam focusing. Appl Phys B Lasers Opt 2020;126:1–10. https://doi.org/10.1007/s00340-020-07547-9.

[218] Serwin M, Karataş AE. A calibration-free two-dimensional spectral soot emission platform for temperature and soot measurements. Exp Therm Fluid Sci 2022;130. https://doi.org/10.1016/J.EXPTHERMFLUSCI.2021.110493.

[219] Zhao H, Ladommatos N. Optical diagnostics for soot and temperature measurement in diesel engines. Prog Energy Combust Sci 1998;24:221–55. https://doi.org/10.1016/S0360-1285(97)00033-6.

[220] Chang H, Charalampopoulos TT. Determination of the wavelength dependence of refractive indices of flame soot. Proc R Soc London Ser A Math Phys Sci 1990;430:577–91. https://doi.org/10.1098/rspa.1990.0107.

[221] Yon J, Lemaire R, Therssen E, Desgroux P, Coppalle A, Ren KF. Examination of wavelength dependent soot optical properties of diesel and diesel/rapeseed methyl ester mixture by extinction spectra analysis and LII measurements. Appl Phys B Lasers Opt 2011;104:253–71. https://doi.org/10.1007/s00340-011-4416-4.

[222] Bouvier Y, Therssen E, Desgroux P. Wavelength-dependence of refractive index function of soot particle by two-color laser-induced incandescence. CEUR Workshop Proc 2005;195:16.

[223] Irimiea C. Characterization of soot particles and their precursors by coupling laser-based techniques. 2017.

[224] Thi Linh Dan N, Dreier Professeur T, Duisburg-Essen U, Barbara AD. Characterization of soot particles and their precursors produced during the combustion of conventional and alternative fuels: an in-situ laser diagnostics and ex-situ mass spectrometry investigation devant la commission d’examen. 2019.

[225] Mercier X, Desgroux P. Cavity ring-down spectroscopy : techniques and applications. Wiley; 2009.

[226] Vander Wal RL. Laser-induced incandescence: detection issues. Appl Opt 1996;35:6548. https://doi.org/10.1364/ao.35.006548.

[227] Thomson KA, Gülder ÖL, Weckman EJ, Fraser RA, Smallwood GJ, Snelling DR. Soot concentration and temperature measurements in co-annular, nonpremixed CH4/air laminar flames at pressures up to 4 MPa. Combust Flame 2005;140:222–32. https://doi.org/10.1016/j.combustflame.2004.11.012.

[228] Bejaoui S, Batut S, Therssen E, Lamoureux N, Desgroux P, Liu F. Measurements and modeling of laser-induced incandescence of soot at different heights in a flat premixed flame. Appl Phys B Lasers Opt 2015;118:449–69. https://doi.org/10.1007/s00340-015-6014-3.

[229] Leider HR, Krikorian OH, Young DA. Thermodynamic properties of carbon up to the critical point. Carbon N Y 1973;11:555–63. https://doi.org/10.1016/0008-6223(73)90316-3.

[230] Johansson KO, El Gabaly F, Schrader PE, Campbell MF, Michelsen HA. Evolution of maturity levels of the particle surface and bulk during soot growth and oxidation in a flame. Aerosol Sci Technol 2017;51:1333–44. https://doi.org/10.1080/02786826.2017.1355047.

[231] Hofmann M, Bessler WG, Schulz C, Jander H. Laser-induced incandescence for soot diagnostics at high pressures. Appl Opt 2003;42:2052. https://doi.org/10.1364/ao.42.002052.

[232] Bladh H, Johnsson J, Bengtsson PE. On the dependence of the laser-induced incandescence (LII) signal on soot volume fraction for variations in particle size. Appl Phys B Lasers Opt 2008;90:109–25. https://doi.org/10.1007/s00340-007-2826-0.

[233] Schulz C, Kock BF, Hofmann M, Michelsen H, Will S, Bougie B, et al. Laser-induced incandescence: Recent trends and current questions. Appl Phys B Lasers Opt 2006;83:333–54. https://doi.org/10.1007/s00340-006-2260-8.

[234] Williams TC, Shaddix CR. Simultaneous correction of flat field and nonlinearity response of intensified charge-coupled devices. Rev Sci Instrum 2007;78:1–7. https://doi.org/10.1063/1.2821616.

[235] Schulz C, Kock BF, Hofmann M, Michelsen H, Will S, Bougie B, et al. Laser-induced incandescence: Recent trends and current questions. Appl Phys B Lasers Opt 2006;83:333–54. https://doi.org/10.1007/s00340-006-2260-8.

[236] Lab O. 2D FFT Filters n.d. https://www.originlab.com/doc/Origin-Help/2D-FFT-Filter.

[237] Eremin A V., Gurentsov E V., Kolotushkin RN. The change of soot refractive index function along the height of premixed ethylene/air flame and its correlation with soot structure. Appl Phys B Lasers Opt 2020;126:1–11. https://doi.org/10.1007/s00340-020-07426-3.

[238] Bladh H. On the Use of Laser-Induced Incandescence for Soot Diagnostics : From Theoretical Aspects to Applications in Engines. Lund university, 2007.

[239] Habib ZG, Vervisch P. On The Refractive Index of Soot at Flame Temperature. Combust Sci Technol 1988;59:261–74. https://doi.org/10.1080/00102208808947100.

[240] Snelling DR, Liu F, Smallwood GJ, Gülder ÖL. Determination of the soot absorption function and thermal accommodation coefficient using low-fluence LII in a laminar coflow ethylene diffusion flame. Combust Flame 2004;136:180–90. https://doi.org/10.1016/j.combustflame.2003.09.013.

[241] Köylü UO, Faeth GM. Optical properties of soot in buoyant laminar diffusion flames. J Heat Transfer 1994;116:971–9. https://doi.org/10.1115/1.2911473.

[242] Charalampopoulos TT, Chang H, Stagg B. The effects of temperature and composition on the complex refractive index of flame soot. Fuel 1989;68:1173–9. https://doi.org/10.1016/0016-2361(89)90191-9.

[243] Wu JS, Krishnan SK, Faeth GM. Refractive indices at visible wavelengths of soot emitted from buoyant turbulent diffusion flames. Am Soc Mech Eng Heat Transf Div HTD 1996;325:83–93.

[244] Irimiea C. Characterization of soot particles and their precursors by coupling laser-based techniques. 2017.

[245] Yon J, Therssen E, Liu F, Bejaoui S, Hebert D. Influence of soot aggregate size and internal multiple scattering on LII signal and the absorption function variation with wavelength determined by the TEW-LII method. Appl Phys B Lasers Opt 2015;119:643–55. https://doi.org/10.1007/s00340-015-6116-y.

[246] Bong C, Lee J, Sun H, Yoo J, Bak MS. TDLAS measurements of temperature and water vapor concentration in a flameless MILD combustor. Meas Sci Technol 2021;32. https://doi.org/10.1088/1361-6501/abd8ff.

[247] Behrendt T, Hassa C, Mohamed A, Faleni JP. In situ measurement and validation of gaseous species concentrations of a gas turbine model combustor by tunable diode laser absorption spectroscopy (TDLAS). Proc ASME Turbo Expo 2008;2:273–82. https://doi.org/10.1115/GT2008-51258.

[248] Mohamed A, Messineo J, Lestrade JY, Ferrier M, Defoort S, Soutadé J, et al. Tunable diode laser absorption spectroscopy of co2 and h2o at 2.7 µm in a scramjet combustor and in exhaust gases of a hybrid rocket motor. 32nd AIAA Aerodyn Meas Technol Gr Test Conf 2016:1–10. https://doi.org/10.2514/6.2016-3548.

[249] Naegeli DW, Dodge LG, Moses CA. Effects of flame temperature and fuel composition on soot formation in gas turbine combustors. Combust Sci Technol 1983;35:117–31. https://doi.org/10.1080/00102208308923706.

[250] Elias J, Faccinetto A, Batut S, Carrivain O, Sirignano M, D'Anna A, et al. Thermocouple-Based Thermometry for Sooting Flames: Implementation of a Fast and Simple Methodology. SSRN Electron J 2022:1–16. https://doi.org/10.2139/ssrn.4154074.

[251] Martin JW, Bowal K, Menon A, Slavchov RI, Akroyd J, Mosbach S, et al. Polar curved polycyclic aromatic hydrocarbons in soot formation. Proc Combust Inst 2019;37:1117–23. https://doi.org/10.1016/J.PROCI.2018.05.046.

[252] Wey C, Powell EA, Jagoda JI. The Effect of Temperature on the Sooting Behavior of Laminar Diffusion Flames. Combust Sci Technol 1984;41:173–90. https://doi.org/10.1080/00102208408923828.

[253] www.soprano-h2020.eu n.d.

[254] Recherche A nationale de l. ASTORIA project n.d. https://anr.fr/Project-ANR-18-CE05-0015.

[255] Cochet A, Bodoc V, Brossard C, Dessornes O, Guin C, Lecourt R, et al. ONERA test Facilities for Combustion in Aero Gas Turbine Engines, and Associated Optical Diagnostics. Aerosp Lab 2016:1–16.

[256] Klein M, McDonell V. Ground-Based Gas Turbine Combustion: Metrics, Constraints, and System Interactions. Gas Turbine Emiss 2013:24–80.

[257] Banga N, Kanika K. Design and Study of Swirl Injector of Pulse Detonation Engine. Int J Adv Eng Res Sci 2017;4:79–82. https://doi.org/10.22161/ijaers.4.4.9.

[258] Rajasegar R, Mitsingas CM, Mayhew EK, Liu Q, Lee T, Yoo J. Development and Characterization of Additive-Manufactured Mesoscale Combustor Array. J Energy Eng 2018;144. https://doi.org/10.1061/(asce)ey.1943-7897.0000527.

[259] Grinstein FF, Wachtor AJ, Ristorcelli JR. Coarse grained simulation and turbulent material mixing. 2016. https://doi.org/10.1007/978-3-319-41217-7_21.

[260] Dupoirieux F, Bertier N, Guin C, Henry L-H, Geigle K, Eberle C, et al. Methodology for the numerical prediction of pollutant formation in gas turbine combustors and associated validation experiments. Aerosp Lab 2016;11:1–20. https://doi.org/10.12762/2016.AL11-07.

[261] Bladh H, Johnsson J, Rissler J, Abdulhamid H, Olofsson NE, Sanati M, et al. Influence of soot particle aggregation on time-resolved laser-induced incandescence signals. Appl Phys B Lasers Opt 2011;104:331–41. https://doi.org/10.1007/s00340-011-4470-y.

[262] Beretta F, Cincotti V, D'Alessio A, Menna P. Ultraviolet and visible fluorescence in the fuel pyrolysis regions of gaseous diffusion flames. Combust Flame 1985;61:211–8. https://doi.org/10.1016/0010-2180(85)90102-6.

[263] Boyette WR, Bennett AM, Cenker E, Guiberti TF, Roberts WL. Effects of pressure on soot production in piloted turbulent non-premixed jet flames. Combust Flame 2021;227:271–82. https://doi.org/10.1016/j.combustflame.2021.01.013.

[264] Frederickson K, Kearney SP, Grasser TW. Laser-induced incandescence measurements of soot in turbulent pool fires. Appl Opt 2011;50:49–59. https://doi.org/10.1364/AO.50.000A49.

[265] Geigle KP, O'Loughlin W, Hadef R, Meier W. Visualization of soot inception in turbulent pressurized flames by simultaneous measurement of laser-induced fluorescence of polycyclic aromatic hydrocarbons and laser-induced incandescence, and correlation to OH distributions. Appl Phys B Lasers Opt 2015;119:717–30. https://doi.org/10.1007/s00340-015-6075-3.

[266] Cenker E, Bruneaux G, Dreier T, Schulz C. Sensitivity analysis for soot particle size imaging with laser-induced incandescence at high pressure. Appl Phys B Lasers Opt 2015;119:745–63. https://doi.org/10.1007/s00340-015-6009-0.

[267] Qamar NH, Alwahabi ZT, Chan QN, Nathan GJ, Roekaerts D, King KD. Soot volume fraction in a piloted turbulent jet non-premixed flame of natural gas. Combust Flame 2009;156:1339–47. https://doi.org/10.1016/j.combustflame.2009.02.011.

[268] Geigle KP, Hadef R, Meier W. Soot Formation and flame characterization of an aero-engine model combustor burning ethylene at elevated pressure. J Eng Gas Turbines Power 2014;136. https://doi.org/10.1115/1.4025374.

[269] Zerbs J, Geigle KP, Lammel O, Hader J, Stirn R, Hadef R, et al. The influence of wavelength in extinction measurements and beam steering in laser-induced incandescence measurements in sooting flames. Appl Phys B Lasers Opt 2009;96:683–94. https://doi.org/10.1007/s00340-009-3550-8.

[270] Gleason K, Carbone F, Gomez A. Effect of equivalence ratio and temperature on soot formation in partially premixed counterflow flames. Combust Flame 2022;242. https://doi.org/10.1016/j.combustflame.2022.112088.

[271] Nettleton D. Selection of Variables and Factor Derivation. Commer Data Min 2014:79–104. https://doi.org/10.1016/B978-0-12-416602-8.00006-6.

[272] Abdulmouti H, Mansour TM. The technique of PIV and its applications. 10th Int Conf Liq At Spray Syst ICLASS 2006 2006:1–10.

[273] Chen F, Liu H, Yang Z, Hu H. Tracking characteristics of tracer particles for PIV measurements in supersonic flows. Chinese J Aeronaut 2017;30:577–85. https://doi.org/10.1016/j.cja.2016.12.033.

[274] CHEN F, LIU H. Particle image velocimetry for combustion measurements: Applications and developments. Chinese J Aeronaut 2018;31:1407–27. https://doi.org/10.1016/j.cja.2018.05.010.

[275] Willert C, Schroll M, Heinze J, Soworka T. High-speed PIV at the exit of a lean-burn combustion chamber operated at elevated pressure 2019.

[276] Velocimetry knowledge united. Particle Image Velocimetry n.d. https://velocimetry.net/principle.htm.

[277] CHEN F, LIU H. Particle image velocimetry for combustion measurements: Applications and developments. Chinese J Aeronaut 2018;31:1407–27. https://doi.org/10.1016/j.cja.2018.05.010.

[278] Rosalik DLR& M. PIV Measurements During Combustion in a Reciprocating Internal Combustion Engine. 2000. https://doi.org/10.1007/978-3-642-56963-0_22.

[279] Willert C, Jarius M. Planar Flow Field Measurements in Atmospheric and Pressurized Combustion Chambers. DLR-Mitteilung 2001:239–49.

[280] Geigle KP, Hadef R, Stöhr M, Meier W. Flow field characterization of pressurized sooting swirl flames and relation to soot distributions. Proc Combust Inst 2017;36:3917–24. https://doi.org/10.1016/j.proci.2016.09.024.

[281] Narayanaswamy V, Clemens NT. Simultaneous LII and PIV measurements in the soot formation region of turbulent non-premixed jet flames. Proc Combust Inst 2013;34:1455–63. https://doi.org/10.1016/j.proci.2012.06.018.

[282] Westlye Fredrik Ree. Experimental Study of Liquid Fuel Spray Combustion. 2016.

[283] Desclaux A, Thuillet S, Zuzio D, Senoner JM, Sebbane D, Bodoc V, et al. Experimental and Numerical Characterization of a Liquid Jet Injected into Air Crossflow with Acoustic Forcing. vol. 105. Springer Netherlands; 2020. https://doi.org/10.1007/s10494-020-00126-0.

[284] Kheirkhah S, Cirtwill JDM, Saini P, Venkatesan K, Steinberg AM. Dynamics and mechanisms of pressure, heat release rate, and fuel spray coupling during intermittent thermoacoustic oscillations in a model aeronautical combustor at elevated pressure. Combust Flame 2017;185:319–34. https://doi.org/10.1016/j.combustflame.2017.07.017.

[285] Vignat G, Lo Schiavo E, Laera D, Renaud A, Gicquel L, Durox D, et al. Dynamics of spray and swirling flame under acoustic oscillations: A joint experimental and LES investigation. Proc Combust Inst 2021;38:6015–24. https://doi.org/10.1016/j.proci.2020.05.054.

[286] Payri R, García JM, Salvador FJ, Gimeno J. Using spray momentum flux measurements to understand the influence of diesel nozzle geometry on spray characteristics. Fuel 2005;84:551–61. https://doi.org/10.1016/j.fuel.2004.10.009.

[287] Bashirnezhad K, Moghiman M, Amoli MJ, Tofighi F, Zabetnia S. Effect of Fuel Spray Angle on Soot Formation in Turbulent Spray Flames 2008;31:339–44.

[288] Ekaab NS. Experimental Study of The Effect of Fuel Spray Angle on Emissions of pollutants from

a continuous Combustion Process. 2017.

[289] ALTERNATE Consortium. ALTERNATE project n.d. https://www.alternateproject.com/.

[290] ATAG. Aviation Benefits beyond borders-Covid 19 analysis Fact sheet. vol. 3. 2020.

[291] Kramer S, Andac G, Heyne J, Ellsworth J, Herzig P, Lewis KC. Perspectives on Fully Synthesized Sustainable Aviation Fuels: Direction and Opportunities. Front Energy Res 2022;9. https://doi.org/10.3389/fenrg.2021.782823.

[292] Braun-Unkhoff M, Riedel U, Wahl C. About the emissions of alternative jet fuels. CEAS Aeronaut J 2017;8:167–80. https://doi.org/10.1007/s13272-016-0230-3.

[293] Marszałek N, Lis T. The future of sustainable aviation fuels. Combust Engines 2022;191:29–40. https://doi.org/10.19206/ce-146696.

[294] Bozell JJ. The Use of Renewable Production of Chemicals and Materials - A brief overview of Concepts. Ppoint 2011.

[295] Kandaramath Hari T, Yaakob Z, Binitha NN. Aviation biofuel from renewable resources: Routes, opportunities and challenges. Renew Sustain Energy Rev 2015;42:1234–44. https://doi.org/10.1016/j.rser.2014.10.095.

[296] Gong Y, Kaario O, Tilli A, Larmi M, Tanner FX. A computational investigation of hydrotreated vegetable oil sprays using RANS and a modified version of the RNG k - ε model in openFOAM. SAE Tech Pap 2010:1–11. https://doi.org/10.4271/2010-01-0739.

[297] Hileman JI, Ortiz DS, Bartis JT, Wong HM, Donohoo, Pearl E, Weiss MA, et al. Near-Term Feasibility of Alternative Jet Fuels -Technical Report. RAND Corp MIT 2009:1–152.

[298] Aatola H, Larmi M, Sarjovaara T, Mikkonen S. Hydrotreated vegetable Oil (HVO) as a renewable diesel fuel: Trade-off between NOx, particulate emission, and fuel consumption of a heavy duty engine. SAE Int J Engines 2009;1:1251–62. https://doi.org/10.4271/2008-01-2500.

[299] Wardle DA. Global sale of green air travel supported using biodiesel. Renew Sustain Energy Rev 2003;7:1–64. https://doi.org/10.1016/S1364-0321(03)00002-9.

[300] Balat M, Balat M. Political, economic and environmental impacts of biomass-based hydrogen. Int J Hydrogen Energy 2009;34:3589–603. https://doi.org/10.1016/j.ijhydene.2009.02.067.

[301] Charles MB, Barnes P, Ryan N, Clayton J. Airport futures: Towards a critique of the aerotropolis model. Futures 2007;39:1009–28. https://doi.org/10.1016/j.futures.2007.03.017.

[302] Airbus Deutschland GmbH. Liquid Hydrogen Fuelled Aircraft - System Analysis. Cryoplane 2003:1–80.

[303] Midilli A, Ay M, Dincer I, Rosen MA. On hydrogen and hydrogen energy strategies I : Current status and needs. Renew Sustain Energy Rev 2005;9:255–71. https://doi.org/10.1016/j.rser.2004.05.003.

[304] Saynor B, Bauen A, Leach M. The Potential for Renewable Energy Sources in Aviation. Imp Coll Cent Energy Policy Technol 2003:6–63.

[305] Pechstein J, Neuling U, Gebauer J, Kaltschmitt M. Alcohol-to-Jet (AtJ). Biokerosene Status Prospect., 2017, p. 1–758. https://doi.org/10.1007/978-3-662-53065-8.

[306] Kurzawska P, Jasiński R. Overview of sustainable aviation fuels with emission characteristic and particles emission of the turbine engine fueled ATJ blends with different percentages of ATJ fuel. Energies 2021;14. https://doi.org/10.3390/en14071858.

[307] Brooks KP, Snowden-Swan LJ, Jones SB, Butcher MG, Lee GSJ, Anderson DM, et al. Low-Carbon Aviation Fuel Through the Alcohol to Jet Pathway. Biofuels Aviat. Feed. Technol. Implement., Elsevier Inc.; 2016, p. 109–50. https://doi.org/10.1016/B978-0-12-804568-8.00006-8.

[308] Air Transport Action Group (ATAG). Waypoint 2050 Second Edition 2021:108.

[309] Abrantes I, Ferreira AF, Silva A, Costa M. Sustainable aviation fuels and imminent technologies - CO2 emissions evolution towards 2050. J Clean Prod 2021;313. https://doi.org/10.1016/j.jclepro.2021.127937.

[310] Blakey S, Rye L, Wilson CW. Aviation gas turbine alternative fuels: A review. Proc Combust Inst 2011;33:2863–85. https://doi.org/10.1016/j.proci.2010.09.011.

[311] Giusti A, Mastorakos E. Turbulent Combustion Modelling and Experiments: Recent Trends and Developments. Flow, Turbul Combust 2019;103:847–69. https://doi.org/10.1007/s10494-019-00072-6.

[312] Dreizler A, Pitsch H, Scherer V, Schulz C, Janicka J. The role of combustion science and technology in low and zero impact energy transformation processes. Appl Energy Combust Sci 2021;7:100040. https://doi.org/10.1016/J.JAECS.2021.100040.

[313] Irimiea C, Vincent-Randonnier A, Dufitumukiza JP, Treleaven N, Lesaffre T, Coudray A, et al. ALTERNATE : Experimental and modeling study of soot formation in high-pressure kerosene and SAF combustion. Towar. Sustain. Aviat. Summit 2022, 2022, p. 1–13.

[314] Stone R, Williams B, Ewart P. Optical Techniques that can be Applied to Investigate GDI Engine Combustion. SAE Tech Pap 2017;2017-Septe. https://doi.org/10.4271/2017-24-0046.

[315] Zhou H, Li X, Chen Y, Kang Y, Liu D, Liu F. The effect of spray angle on the combustion and emission performance of a separated swirl combustion system in a diesel engine. Energy 2020;190:116481. https://doi.org/10.1016/j.energy.2019.116481.

[316] Liu Y, Tan J, Wang H, Lv L. Characterization of heat release rate by OH* and CH* chemiluminescence. Acta Astronaut 2019;154:44–51. https://doi.org/10.1016/J.ACTAASTRO.2018.10.022.

[317] Tinaut F V., Reyes M, Giménez B, Pastor J V. Measurements of OH* and CH* chemiluminescence in premixed flames in a constant volume combustion bomb under autoignition conditions. Energy and Fuels 2011;25:119–29. https://doi.org/10.1021/ef1013456.

[318] Li X, Liu W, Pan Y, Yang L, An B, Zhu J. Characterization of ignition transient processes in kerosene-fueled model scramjet engine by dual-pulse laser-induced plasma. Acta Astronaut 2018;144:23–9. https://doi.org/10.1016/j.actaastro.2017.12.018.

[319] Sardeshmukh S, Bedard M, Anderson W. The use of OH* and CH* as heat release markers in combustion dynamics. Int J Spray Combust Dyn 2017;9:409–23. https://doi.org/10.1177/1756827717718483.

[320] Lv L, Tan J, Zhu J. Visualization of the heat release zone of highly turbulent premixed jet flames. Acta Astronaut 2017;139:258–65. https://doi.org/10.1016/j.actaastro.2017.07.005.

[321] Liu Y, Tan J, Wan M, Zhang L, Yao X. Quantitative Measurement of OH∗ and CH∗ Chemiluminescence in Jet Diffusion Flames. ACS Omega 2020;5:15922–30. https://doi.org/10.1021/acsomega.0c01093.

[322] Nori V, Seitzman J. Evaluation of chemiluminescence as a combustion diagnostic under varying operating conditions. 46th AIAA Aerosp Sci Meet Exhib 2008:1–14. https://doi.org/10.2514/6.2008-953.

[323] Trabold J, Hartl S, Walther S, Johchi A, Dreizler A, Geyer D. Fuel Effects in Turbulent Premixed Pre-vaporised Alcohol/Air Jet Flames. Flow, Turbul Combust 2021;106:547–73. https://doi.org/10.1007/s10494-020-00166-6.

[324] Reyes M, Tinaut F V., Giménez B, Pastor J V. Effect of hydrogen addition on the OH* and CH* chemiluminescence emissions of premixed combustion of methane-air mixtures. Int J Hydrogen Energy 2018;43:19778–91. https://doi.org/10.1016/j.ijhydene.2018.09.005.

[325] Hu G, Zhang S, Li QF, Pan XB, Liao SY, Wang HQ, et al. Experimental investigation on the effects of hydrogen addition on thermal characteristics of methane/air premixed flames. 2014. https://doi.org/10.1016/j.fuel.2013.07.024.

[326] He L, Guo Q, Gong Y, Wang F, Yu G. Investigation of OH* chemiluminescence and heat release in laminar methane–oxygen co-flow diffusion flames. Combust Flame 2019;201:12–22. https://doi.org/10.1016/j.combustflame.2018.12.009.

[327] Yang J, Gong Y, Wei J, Guo Q, Wang F, Yu G. Chemiluminescence diagnosis of oxygen/fuel ratio in fuel-rich jet diffusion flames. Fuel Process Technol 2022;232:107284. https://doi.org/10.1016/j.fuproc.2022.107284.

[328] Lauer M, Sattelmayer T. On the adequacy of chemiluminescence as a measure for heat release in turbulent flames with mixture gradients. J Eng Gas Turbines Power 2010;132:1–8. https://doi.org/10.1115/1.4000126.

[329] Lauer MRW. Determination of the Heat Release Distribution in Turbulent Flames by Chemiluminescence Imaging. 2011.

[330] Li Z, Lou C, Kumfer BM. Revealing the competitive relationship between soot formation and chemiluminescence. Combust Flame 2022;245:112335. https://doi.org/10.1016/j.combustflame.2022.112335.

[331] Poinsot T. Prediction and control of combustion instabilities in real engines. Proc Combust Inst 2017;36:1–28. https://doi.org/10.1016/j.proci.2016.05.007.

[332] Deng K, Zhong Y, Wang M, Zhong Y, Luo KH. Effects of acoustic excitation on the combustion instability of hydrogen−methane lean premixed swirling flames. ACS Omega 2020;5:8744–53. https://doi.org/10.1021/acsomega.0c00287.

[333] Gottenberg WG, Olson DR, Best HW. Flame quenching during high pressure, high turbulence combustion 1962.

[334] Corbin JC, Schripp T, Anderson BE, Smallwood GJ, Leclercq P, Crosbie EC, et al. Aircraft-engine particulate matter emissions from conventional and sustainable aviation fuel combustion: Comparison of measurement techniques for mass, number, and size. Atmos Meas Tech 2022;15:3223–42. https://doi.org/10.5194/amt-15-3223-2022.

[335] Wikipedia. Probability density function pdf 2022. https://en.wikipedia.org/wiki/Probability_density_function.

[336] Irimiea C, Vincent-randonnier A, Dufitumukiza JP, Treleaven N, Lesaffre T, Coudray A, et al. ALTERNATE : Experimental and modeling study of soot formation in high-pressure kerosene and SAF combustion. TSAS2022 2022:18–22.

[337] Tardelli LP. Investigating the LES strategy for the prediction of soot production in an aero-engine combustor Investigating the LES strategy for the prediction of soot. 2021.

[338] Becker FG, Cleary M, Team RM, Holtermann H, The D, Agenda N, et al. Advanced Optical Instruments and Techniques Volume 2. vol. 7. 2015.

[339] Maiman TH. Stimulated Optical Radiation in Ruby. Nature 1960;187, 493.

[340] Black S, Jobling L. Physical principles of LASER. Anaesth Intensive Care Med 2014;15:530–2. https://doi.org/10.1016/j.mpaic.2014.08.003.

[341] Svelto O. Principles of Lasers. 1998.

[342] Lantz A. Application of Laser Techniques in Combustion Environments of Relevance for Gas Turbine Studies. 2012.

[343] Koechner W, Bass M. Solid-State Lasers: A Graduate Text (Advanced Texts in Physics). 2003.

[344] Sune Svanberg. Atomic and Molecular Spectroscopy, Basic Aspects and Practical Applications. 2004.

[345] CERFACS. CERFACS AVBP website n.d. https://www.cerfacs.fr/avbp7x/.

[346] AGOSTINELLI PW. Assessment of Large Eddy Simulation in the Conjugate Heat Transfer context for engine operability: application to Hydrogen enrichment and Spinning Combustion Technology. 2022.

[347] Nicoud F, Toda HB, Cabrit O, Bose S, Lee J. Using singular values to build a subgrid-scale model for large eddy simulations. Phys Fluids 2011;23:0–12. https://doi.org/10.1063/1.3623274.

[348] Wang G, Boileau M, Veynante D. Implementation of a dynamic thickened flame model for large eddy simulations of turbulent premixed combustion. Combust Flame 2011;158:2199–213. https://doi.org/10.1016/j.combustflame.2011.04.008.

[349] Charlette F, Meneveau C, Veynante D. A power-law flame wrinkling model for LES of premixed turbulent combustion Part I: Non-dynamic formulation and initial tests. Combust Flame 2002;131:159–80. https://doi.org/10.1016/S0010-2180(02)00400-5.

[350] ABRAMZON B, SIRIGNANO W. Droplet vaporization model for spray combustion calculations 1988;32:1605–18. https://doi.org/10.2514/6.1988-636.

[351] Lefebvre AH, McDonell VG. Atomization and Sprays. 2017. https://doi.org/10.1201/9781315120911-4.

[352] Franzelli B, Riber E, Sanjosé M, Poinsot T. A two-step chemical scheme for kerosene-air premixed flames. Combust Flame 2010;157:1364–73. https://doi.org/10.1016/j.combustflame.2010.03.014.

[353] Gallen L, Felden A, Riber E, Cuenot B. Lagrangian tracking of soot particles in les of gas turbines. Proc Combust Inst 2019;37:5429–36. https://doi.org/10.1016/j.proci.2018.06.013.

ABSTRACT

The growth of air traffic urges the combustion research community to get a detailed understanding of the physical and chemical processes occurring in the aircraft engine, with two main objectives: first, to ameliorate the combustion process and second, to lower gaseous and particulate emissions. A solution to the first issue lies in the combustion at higher pressure and temperature, but this can impact the second issue, particularly concerning the production of soot and NO_x emissions. The solution relies on the development of suitable experimental tools for representative combustion conditions of those encountered in aircraft engines to capture their characteristic complex phenomena. As a result, during this research, coupled optical techniques were developed and implemented for characterizing soot particles in aeronautical engine-relevant combustors. Laser Induced Incandescence (LII) is the primary technique on which efforts are directed due to its high sensitivity for detecting soot particles and flexibility to be implemented around semi-industrial combustion installations. In addition, the coupling of LII with other optical techniques presents a high interest in understanding the mechanisms and parameters leading to soot formation. First, Laser Induced Fluorescence (LIF) is added as a complementary technique to detect soot precursors known as polycyclic aromatic hydrocarbons (PAHs). The development of LII/LIF was made in accordance with the application on test rigs and they were first tested on a CH_4/air laminar diffusion flame. The main findings are related to the planar configuration of the LII/LIF systems regarding the correction factors for the use of a laser sheet plane to scan a large region of interest during the measurement. Additionally, two optical configurations (imaging and spectral) proposed for the LII technique were studied to evaluate the uncertainty induced in the conversion step from the recorded LII signal to soot volume fraction. These studies allowed the application of planar LII/LIF and complementary optical techniques on a semi-industrial test rig representative of combustion conditions identified in aircraft combustors. Particle image velocimetry and Mie scattering are used as complementary techniques to LII/LIF. Six operating conditions of the test rig are characterized by the coupled optical techniques to identify the main parameters that affect soot formation in such environment. An exhaustive characterization of the various OC and their correlation with the Landing/Take-Off (LTO) Cycle is proposed. This work narrows down three OC of interest for in-depth studies with sustainable aviation fuels (SAF). These applications are subject to studies on the effect of SAF on soot formation that were evaluated with LII, OH* and Mie scattering. A matrix of three fuels (Jet A-1, 50:50% vol. Jet A 1: Alcohol-to-jet (ATJ) and pure ATJ) was selected to evaluate the fuel impact on soot production for the three selected OC. High-frequency ($\sim 10\ \mathrm{kHz}$) techniques (OH* and Mie scattering) were implemented to obtain information about the spray dynamics and flame front inside the combustor. The coupled optical techniques identify the parameters leading to soot formation and relate them to the operating conditions or fuel properties.

Keywords: Combustion, soot, optical metrology, laser-induced incandescence/fluorescence, light scattering, particle image velocimetry, OH* chemiluminescence, semi-industrial aeronautic combustor

RÉSUMÉ

La croissance du trafic aérien pousse la communauté de recherche sur la combustion à vouloir une compréhension détaillée des processus physiques et chimiques qui ont lieu dans un moteur d'avion, avec deux objectifs principaux : premièrement, améliorer le processus de combustion et deuxièmement, réduire les émissions gazeuses et particulaires. Une solution au premier problème réside dans la combustion à une pression et une température plus élevées, mais cela peut avoir un impact sur la seconde problématique, notamment en ce qui concerne la production de suie et les émissions de NO_x. La solution repose sur le développement d'outils expérimentaux appropriés pour des conditions de combustion représentatives de celles rencontrées dans les moteurs d'avion afin de capturer leurs phénomènes complexes caractéristiques. Ainsi, au cours de cette recherche, des techniques optiques couplées ont été développées et mises en œuvre pour caractériser les particules de suie dans des chambres de combustion similaires à celles des moteurs aéronautiques. L'incandescence induite par laser (LII) est la principale technique sur laquelle les efforts sont dirigés en raison de sa haute sensibilité pour la détection des particules de suie et de sa flexibilité de mise en œuvre autour des installations de combustion semi-industrielles. De plus, le couplage de la LII avec d'autres techniques optiques présente un grand intérêt pour la compréhension des mécanismes et des paramètres conduisant à la formation de la suie. Tout d'abord, la fluorescence induite par laser (LIF) est ajoutée comme technique complémentaire pour détecter les précurseurs de suie connus sous le nom d'hydrocarbures aromatiques polycycliques (HAP). Le développement de la LII/LIF a été fait en fonction de l'application sur des bancs d'essai et ont été testés pour la première fois sur une flamme à diffusion laminaire CH_4/air. Les principaux résultats sont liés à la configuration planaire des systèmes LII/LIF concernant les facteurs de correction pour l'utilisation d'une nappe laser afin d'analyser une grande région d'intérêt pendant la mesure. De plus, deux configurations optiques (imagerie et spectrale) proposées pour la technique LII ont été étudiées pour évaluer l'incertitude induite par l'étape de conversion du signal LII enregistré en fraction de volume de suie. Ces études ont permis l'application des techniques LII/LIF planaires ainsi que des techniques optiques complémentaires sur un banc d'essai semi-industriel représentatif des conditions de combustion identifiées dans les chambres de combustion aéronautiques. La vélocimétrie par image de particules et la diffusion de Mie sont utilisées comme techniques complémentaires au couple LII/LIF. Six points de fonctionnement du banc d'essai sont caractérisés par les techniques optiques couplées afin d'identifier les principaux paramètres qui affectent la formation de suie dans un tel environnement. Une caractérisation exhaustive des différents points de fonctionnement et leur corrélation avec le cycle normalisé d'atterrissage/décollage (LTO) est proposée. Ce travail permet d'identifier trois points de fonctionnement d'intérêt pour des études approfondies avec les carburants aéronautiques durables (SAF). Ces applications font l'objet d'études sur l'effet des SAF sur la formation de suie qui ont été évaluées par LII, chemilunescence OH* et la diffusion. Une matrice de trois carburants (Jet A-1, 50:50% vol. Jet A-1:ATJ et ATJ) a été sélectionnée pour évaluer l'impact du carburant sur la production de suie pour les trois points de fonctionnement sélectionnés. Des techniques à haute cadance (OH* et diffusion) ont été mises en œuvre pour obtenir des informations sur la dynamique du spray et le front de flamme à l'intérieur de la chambre de combustion. Les techniques optiques couplées permettent d'identifier les paramètres conduisant à la formation de suie et les relient aux conditions de fonctionnement ou aux propriétés du combustible.

Mots-clés : Combustion, suie, métrologie optique, incandescence/fluorescence induite par laser, diffusion de la lumière, vélocimétrie par imagerie de particules, chimiluminescence OH*, chambre de combustion aéronautique semi-industrielle.